How to verify the precision of density-functional-theory implementations via reproducible and universal workflows

Emanuele Bosoni[1], Louis Beal[2], Marnik Bercx[3], Peter Blaha[4], Stefan Blügel[5], Jens Bröder[5,6], Martin Callsen[7,8,9], Stefaan Cottenier[7,8], Augustin Degomme[2], Vladimir Dikan[1], Kristjan Eimre[3], Espen Flage-Larsen[10,11], Marco Fornari[12], Alberto Garcia[1], Luigi Genovese[2], Matteo Giantomassi[13], Sebastiaan P. Huber[3,14], Henning Janssen[5], Georg Kastlunger[15], Matthias Krack[16], Georg Kresse[17,18], Thomas D. Kühne[19,20], Kurt Lejaeghere[8,21], Georg K. H. Madsen[4], Martijn Marsman[17,18], Nicola Marzari[3,16], Gregor Michalicek[5], Hossein Mirhosseini[22], Tiziano M. A. Müller[23], Guido Petretto[13], Chris J. Pickard[24,25], Samuel Poncé[13], Gian-Marco Rignanese[13], Oleg Rubel[26], Thomas Ruh[4,8], Michael Sluydts[7,8,27], Danny E.P. Vanpoucke[7,28], Sudarshan Vijay[15], Michael Wolloch[17,18], Daniel Wortmann[5], Aliaksandr V. Yakutovich[29], Jusong Yu[3,16], Austin Zadoks[3], Bonan Zhu[30,31], and Giovanni Pizzi[3,16,*]

[1]Institut de Ciència de Materials de Barcelona, ICMAB-CSIC, Campus UAB, 08193 Bellaterra, Spain
[2]Univ. Grenoble-Alpes, CEA, IRIG-MEM-L_Sim, 38000 Grenoble, France
[3]Theory and Simulation of Materials (THEOS) and National Centre for Computational Design and Discovery of Novel Materials (MARVEL), École Polytechnique Fédérale de Lausanne (EPFL), CH-1015 Lausanne, Switzerland
[4]Institute for Materials Chemistry, Technical University of Vienna, Getreidemarkt 9/165-TC, A-1060 Vienna, Austria
[5]Peter Grünberg Institut and Institute for Advanced Simulation, Forschungszentrum Jülich and JARA, D-52425 Jülich, Germany
[6]Institute for Advanced Simulation, Materials Data Science and Informatics (IAS-9), Forschungszentrum Jülich, D-52425 Jülich, Germany
[7]Department of Electromechanical, Systems and Metal Engineering, Ghent University, Belgium
[8]Center for Molecular Modeling (CMM), Ghent University, Belgium
[9]Institute of Atomic and Molecular Sciences, Academia Sinica, Taipei 10617, Taiwan
[10]Norwegian EuroHPC Competence Center, Sigma2 AS, Norway
[11]SINTEF Industry, Materials Physics, Oslo, Norway
[12]Department of Physics and Science of Advanced Materials Program, Central Michigan University, Mount Pleasant, Michigan 48859, USA
[13]Institut de la Matière Condensée et des Nanosciences (IMCN), Université catholique de Louvain, Chemin des Étoiles 8, Louvain-la-Neuve 1348, Belgium
[14]National Centre of Competence in Research (NCCR) Catalysis, École Polytechnique Fédérale de Lausanne (EPFL), CH-1015, Lausanne, Switzerland
[15]Center for Catalysis Theory (Cattheory), Department of Physics, Technical University of Denmark (DTU), 2800 Kongens Lyngby, Denmark
[16]Laboratory for Materials Simulations (LMS), Paul Scherrer Institut (PSI), CH-5232 Villigen PSI, Switzerland
[17]University of Vienna, Faculty of Physics and Center for Computational Materials Science, Kolingasse 14-16, A-1090 Vienna, Austria
[18]VASP Software GmbH, Sensengasse 8, A-1090 Vienna, Austria
[19]Center for Advanced Systems Understanding (CASUS) and Helmholtz-Zentrum Dresden-Rossendorf, D-02826 Görlitz, Germany
[20]Paderborn Center for Parallel Computing (PC2) and Center for Sustainable Systems Design, University of Paderborn, D-33098 Paderborn, Germany
[21]OCAS NV/ArcelorMittal Global R&D Gent, Pres. J. F. Kennedylaan 3, Zelzate B-9060, Belgium
[22]Dynamics of Condensed Matter, Chair of Theoretical Chemistry, University of Paderborn, D-33098 Paderborn, Germany
[23]HPE HPC EMEA Research Lab, CH-4051 Basel, Switzerland
[24]Department of Materials Science & Metallurgy, University of Cambridge, 27 Charles Babbage Road, Cambridge

CB3 0FS, United Kingdom
[25]Advanced Institute for Materials Research, Tohoku University 2-1-1 Katahira, Aoba, Sendai, 980-8577, Japan
[26]Department of Materials Science and Engineering, McMaster University, 1280 Main Street West, Hamilton, Ontario L8S 4L8, Canada
[27]ePotentia, Frans van Dijckstraat 59, 2100 Deurne Antwerpen, Belgium
[28]Institute for Materials Research (IMO-IMOMEC), UHasselt - Hasselt University, Belgium
[29]Swiss Federal Laboratories for Materials Science and Technology (Empa), nanotech@surfaces laboratory, CH-8600 Dübendorf, Switzerland
[30]Department of Chemistry, University College London, 20 Gordon St, Bloomsbury, London WC1H 0AJ, United Kingdom
[31]The Faraday Institution, Didcot OX11 0RA, United Kingdom
[*]e-mail: giovanni.pizzi@psi.ch

ABSTRACT

In the past decades many density-functional theory methods and codes adopting periodic boundary conditions have been developed and are now extensively used in condensed matter physics and materials science research. Only in 2016, however, their precision (i.e., to which extent properties computed with different codes agree among each other) was systematically assessed on elemental crystals: a first crucial step to evaluate the reliability of such computations. We discuss here general recommendations for verification studies aiming at further testing precision and transferability of density-functional-theory computational approaches and codes. We illustrate such recommendations using a greatly expanded protocol covering the whole periodic table from Z=1 to 96 and characterizing 10 prototypical cubic compounds for each element: 4 unaries and 6 oxides, spanning a wide range of coordination numbers and oxidation states. The primary outcome is a reference dataset of 960 equations of state cross-checked between two all-electron codes, then used to verify and improve nine pseudopotential-based approaches. Such effort is facilitated by deploying AiiDA (https://www.aiida.net) workflows that perform automatic input parameter selection, provide identical input/output interfaces across codes, and ensure full reproducibility. Finally, we discuss the extent to which the current results for total energies can be reused for different goals (e.g., obtaining formation energies).

***Note**: This version of the article has been accepted for publication, after peer review but is not the Version of Record and does not reflect post-acceptance improvements, or any corrections. The Version of Record is available online on Nature Review Physics at: https://doi.org/10.1038/s42254-023-00655-3. Use of this Accepted Version is subject to the publisher's Accepted Manuscript terms of use: https://www.springernature.com/gp/open-research/policies/accepted-manuscript-terms.*

Key points:

- Verification efforts are critical to assess the reliability of density-functional theory (DFT) simulations and provide results with properly quantified uncertainties.
- Developing standard computation protocols to perform verification studies and publishing curated and FAIR reference datasets can significantly facilitate their use to improve codes and computational approaches.
- The use of fully automated workflows with common interfaces between codes can guarantee uniformity, transferability, and reproducibility of results.
- A careful description of the numerical and methodological details needed to compare with the reference datasets is essential; we discuss and illustrate this point with a dataset of 960 all-electron equations of state.
- Reference datasets should always include an explanation of the target property for which they were generated, and a discussion of their limits of applicability.
- Further extensions of DFT verification efforts are needed to cover more functionals, more computational approaches, and the treatment of magnetic and relativistic (spin-orbit) effects. They should also aim at concurrently delivering optimized protocols that, not only target ultimate precision, but also optimize the computational cost for a target accuracy.

Website summary: Verification efforts of DFT calculations are of crucial importance to evaluate the reliability of simulation results. We discuss general recommendations for performing such studies and illustrate them with an all-electron reference dataset of 960 equations of state covering the whole periodic table (hydrogen to curium). The importance of verification for the improvement of pseudopotential codes is also demonstrated.

The fast improvement of hardware, methods, and tools for density-functional theory (DFT) calculations in periodic boundary conditions has greatly advanced the field of condensed matter physics and computational materials science, paving the way for an effective use of the "materials design process" that accelerates the discovery, development and deployment of new materials thanks to the aid of simulations[1,2]. Efficient software infrastructures[3–13] facilitate, nowadays, large high-throughput calculations of a panoply of material properties which are often made available to the public in large repositories[14–21]. Most datasets aspire to be findable, accessible, interoperable, and reusable (FAIR)[22] in order to accelerate materials discovery, possibly with the aid of machine learning. They are queryable with *ad hoc* application programming interfaces (APIs) or, for many of them, via a single common API thanks to the recent efforts of the OPTIMADE[23] consortium. However, full integration of different data is often limited by considerations related to uncertainty quantification[1,24–27]. In this work, we discuss recommendations on how to quantify to which extent properties (total energies and derived quantities) obtained by different DFT codes agree among each other.

In principle, DFT applies the fundamental laws of quantum physics to predict properties of a material, with no other inputs than the chemical composition and the crystal structure. In reality, the electronic-structure calculations involve a variety of choices to solve the equations prescribed by DFT and introduce several levels of approximation. Those choices, reflected in the resulting data, range from the specific flavor of DFT (e.g., the approach used for the exchange-correlation functional) to the discretization assumptions (e.g., the basis set), to the specific computational parameters needed by the codes. Some approaches are more reliable, and therefore often slower, while others make more substantial approximations in order to gain computational speed and enable the study of systems with more atoms. Furthermore, even when formally the same choices have been made in different codes, these may provide slightly different results due to the details of their implementations. The importance of verifying the precision of codes has been long recognized[28]. Despite this, when considering DFT codes adopting periodic boundary conditions, a first systematic assessment of their precision was performed in 2016, where the consistency of 40 computational approaches was assessed by calculating the equation of state (EOS) (i.e., the energy-versus-volume curve) for a test set of 71 elemental crystals[29,30]. This so-called "Δ-project" led to the conclusion that the mainstream codes were in very good agreement with each other, which was not the case a decade before. Despite being already a large project by itself, the "Δ-project" was only the first step towards a careful verification of DFT calculations, which requires a much larger diversity of structural and chemical variables, as also discussed in the outlook of Ref. 29.

In this Expert Recommendation, we list a set of guiding principles to perform new verification studies of DFT calculations (see Box 1), as well as a recommendation (see Box 2) for users of DFT codes, encouraging them to refer to quantitative sources on the reliability and precision of the codes and computational approaches used in their publications. In order to illustrate these recommendations, we create a curated reference set of highly converged results for the EOS of 960 crystals, using two independent state-of-the-art all-electron (AE) DFT codes (FLEUR[31,32] and WIEN2k[33,34]). These 960 crystals cover all elements and a wide variety of structural and chemical environments in the form of four unary compounds and six oxides. The resulting data are shared on the Materials Cloud[19] according to the FAIR[22] principles. A key feature of our work is that the thousands of computations performed are implemented within a reproducible and automatic infrastructure. Specifically, the launching and management of all the DFT calculations is carried out using AiiDA[3,4,35]. The choice of code-specific inputs and numerical parameters (called "protocols" in the following) are implemented in the publicly available `aiida-common-workflows` (ACWF) package[36,37] together with a number of error handlers to recover automatically from typical failure modes of each code. This setup enables to easily generate new datasets and to extend the current work for the verification of other computational approaches (see also Box 4).

As we discuss later, some choices of numerical parameters (such as the smearing type and size, or the k-point integration mesh) must be performed consistently in order to make correct use of the dataset. The suggestions regarding how to use our reference dataset are summarized in Box 3. One of our recommendations for verification efforts is to develop metrics to quantify discrepancies between codes that depend on physically measurable quantities. We implement this recommendation by defining two new metrics (in addition to the Δ metric introduced in Ref. 38) to facilitate quantitative comparison of EOS results for pairs of codes or computational approaches, and we discuss their benefits.

Using these metrics, we then compare the EOS results of our reference dataset to the results obtained by a number of pseudopotential codes. The latter are designed to enhance computational efficiency by considering explicitly only "valence"

Expert Recommendation Box 1, Summary of recommendations to perform verification studies of DFT calculations

- Quantitatively estimate the precision of DFT computational approaches and implementations with respect to exact numerical results. Provide adequate details of the verification protocols to ensure reproducibility of the results and a correct reuse in data-driven research, e.g., clarifying their range of applicability and specifying which parameters need to be fixed — independent of the approach — to ensure comparable results.
- Develop fully automated workflows to guarantee uniformity and transferability of parameters between computational approaches. This includes the definition and use of "standard protocols", i.e., automated selection of numerical parameters — often specific to each computational approach — that can ensure numerically precise results.
- Publish curated reference datasets from systematic verification studies. Facilitate their use to improve other codes by making the datasets FAIR: findable and accessible on open repositories, interoperable by using standard formats and clear annotations, and reusable by specifying all parameters needed to reproduce the results. See Box 3 for an example.
- Organize the reference data in appropriate subsets by recognizing the diversity of focus and the non-uniform capabilities of available computational approaches (e.g., if some systems require additional effort to be supported by all codes).

Expert Recommendation Box 2, Summary of recommendations for users of DFT codes

- When publishing research that makes use of DFT codes, refer as much as possible to quantitative sources that document the precision of the numerical implementation (all-electron vs. pseudopotential, basis-set type and size, ...).
- Equally important is a validation statement that refers to the accuracy of the chosen exchange–correlation functional to correctly and accurately address the physics at hand. Note that, however, this is beyond the scope of the current Expert Recommendation focusing on the precision of numerical implementations.
- Always cite the exact pseudopotentials that are used in published simulations, including the exchange–correlation functional, the library from which they were obtained and the exact library version, together with all the essential numerical parameters of the calculations (e.g., k-point integration mesh and smearing, basis set type and size or plane-wave cutoffs, ...). Lack of this information results in essentially non-reproducible simulations.

electrons, which contribute to bonding[39–41]. The codes considered here are: ABINIT[13,42,43], BigDFT[44], CASTEP[45], CP2K[46,47], GPAW[48,49], QUANTUM ESPRESSO[50,51], SIESTA[52,53], the SIRIUS[54] library (via its CP2K interface) and VASP[55,56]. The numerical basis sets implemented in these codes include plane waves, Gaussians combined with plane waves, Daubechies wavelets, and atomic orbitals. For this reason, we do not label our results simply with the code name, but with a short string also indicating a few additional relevant parameters to better specify the details of the computational approach. We stress that the aim of this study is not to provide a ranking or to evaluate the quality of different codes, but to illustrate with a few examples the value of curated datasets generated following our recommendations. In particular, we illustrate its use to improve existing pseudopotentials and to assess the consistency of results of several computational approaches to compute the EOS within DFT.

Finally, in our Outlook, we discuss a set of recommendations (summarized in Box 4) on future extensions of verification efforts. On the one hand, we suggest to cover more exchange–correlation functionals, computational approaches, and treatment of magnetic and relativistic (spin-orbit) effects. On the other hand, we highlight how future studies should not only target ultimate precision, but also aim at delivering protocols that optimize the computational cost for a target accuracy. We stress that, in this Expert Recommendation, we limit all discussions to verification efforts: i.e., investigating code precision, that is, how codes reproduce the ideal theoretical results given by DFT (e.g., with a given choice of exchange–correlation functional). We do not discuss validation, i.e., accuracy with respect to the experimental results. While this is also an highly relevant topic (and we briefly mention it in Box 2), it is beyond the scope of this Expert Recommendation.

AE reference dataset for EOS parameters

In this section we discuss our reference dataset of EOS calculations, that we use to illustrate, with a practical example, how to implement the recommendations of Box 1. The results are obtained with the AE codes FLEUR and WIEN2k, using the PBE[57]

exchange-correlation functional, and considering the scalar-relativistic approximation (no spin-orbit coupling) for the orbitals treated as valence states (including the heavy elements). The two codes use the linearized augmented plane waves plus local orbitals method, but differ in details of the basis set and some computational setup parameters.

Crystal-structures dataset

We compute the EOS on a dataset of 960 cubic crystal structures. In order to provide a chemically comprehensive dataset, we consider all elements in the periodic table from $Z = 1$ (hydrogen) to $Z = 96$ (curium). Furthermore, we systematically scan structural diversity and investigate the transferability to more complex chemical environments by examining, for each element, 4 mono-elemental cubic crystals ("unaries dataset") and six cubic oxides ("oxides dataset").

Specifically, the unaries dataset considers all elements in the face-centered cubic (FCC), body-centered cubic (BCC), simple cubic (SC) and diamond crystal structure, thus covering a wide range of coordination numbers (12, 8, 6, and 4, respectively); a total of 384 systems. More information about the crystal structures are presented in the Supplementary Information (SI) Table S1.1. The oxides dataset is composed of six cubic oxides for each of the 96 elements X, with chemical formula X_2O, XO, X_2O_3, XO_2, X_2O_5 and XO_3, thus totaling 576 additional structures, whose crystal structures are detailed in SI Table S1.2. The oxide stoichiometries are chosen such that the formal oxidation state of the element considered varies from +1 to +6. We note that the actual oxidation state is typically different (see the discussion with a Hirshfeld-I[58–60] analysis in SI Sec. S2), but shows a good correlation with calculated charges being on average about half the formal oxidation state. The X-O distance varies rather systematically over these 6 oxides (see SI Fig. S1.3), typically with the smallest distance for XO_3 and the largest for X_2O. This indicates that XO_3 could be a proxy for systems with very short bond lengths, such as in high-pressure studies. The two datasets of unaries and oxides (jointly called "full dataset"; a total of 960 systems) complement each other in covering chemical and structural variety for each element.

In addition to the criteria above, all structures have been chosen to be cubic and such that forces on all atoms are zero by symmetry. Therefore, the only free parameter is the unit cell volume V or, equivalently, the lattice parameter. As a consequence, the EOS results can be compared with any code able to compute total energies, with no requirement on the capability of computing forces and stresses.

It is important to note that most structures are not stable in nature (in particular under our constraint of cubic spacegroup symmetry). Still, they can be used to assess that all codes reproduce the same DFT result, with the advantage of providing a consistent set across the whole periodic table.

Computation of EOS parameters and comparison between AE codes

The EOS has been traditionally used to determine the computational parameters and study convergence of DFT calculations. By fitting the DFT energy vs. cell volume to an EOS, it is possible to extract the theoretical predictions of the equilibrium volume V_0, the bulk modulus B_0, and its derivative with respect to the pressure, B_1. The Birch–Murnaghan EOS[61]

$$E(V) = E_0 + \frac{9V_0B_0}{16}\left\{\left[\left(\frac{V_0}{V}\right)^{\frac{2}{3}} - 1\right]^3 B_1 + \left[\left(\frac{V_0}{V}\right)^{\frac{2}{3}} - 1\right]^2 \left[6 - 4\left(\frac{V_0}{V}\right)^{\frac{2}{3}}\right]\right\} \tag{1}$$

was used in the Δ-project[29,30] and we follow the same approach by performing a fit of $E(V)$ of Eq. (1) using calculations of the total energy corresponding to 7 equidistant constant volumes between 94% and 106% of a reference central volume $\tilde{V}_0$ (for each Structure). We emphasize that the results are quite sensitive to the precise choice of volume range, reference central volume, and even of fitting algorithm, as we discuss in SI Sec. S3. In this work, the reference central volumes $\tilde{V}_0$ for each of the 960 crystals have been chosen after an iterative process of performing more and more accurate simulations with the two AE codes considered here, until the difference between the reference central volume and the equilibrium volume of the EOS fit was smaller than the 2% volume spacing between total-energy calculations. These central reference volumes are tabulated in SI Sec. S1 and the corresponding crystal-structure files are available in the data entry associated to this Recommendation[62]. These volumes have no physical significance, but for precise comparison between computational approaches, each of them should use the same reference volumes.

The results obtained with the AE codes FLEUR and WIEN2k constitute our reference data. Figure 1 shows the distributions of the percentage difference between FLEUR and WIEN2k for V_0, B_0 and B_1 with respect to their average, for instance the V_0 difference (in %) is given by:

$$100 \cdot \frac{V_0^{\text{WIEN2k}} - V_0^{\text{FLEUR}}}{(V_0^{\text{WIEN2k}} + V_0^{\text{FLEUR}})/2}. \tag{2}$$

Although the histograms do not carry material-specific information, they clearly highlight the agreement between the two AE codes. The relative difference on the equilibrium volume is below 0.3% for all the materials except for 5 oxides (see SI Sec. S4

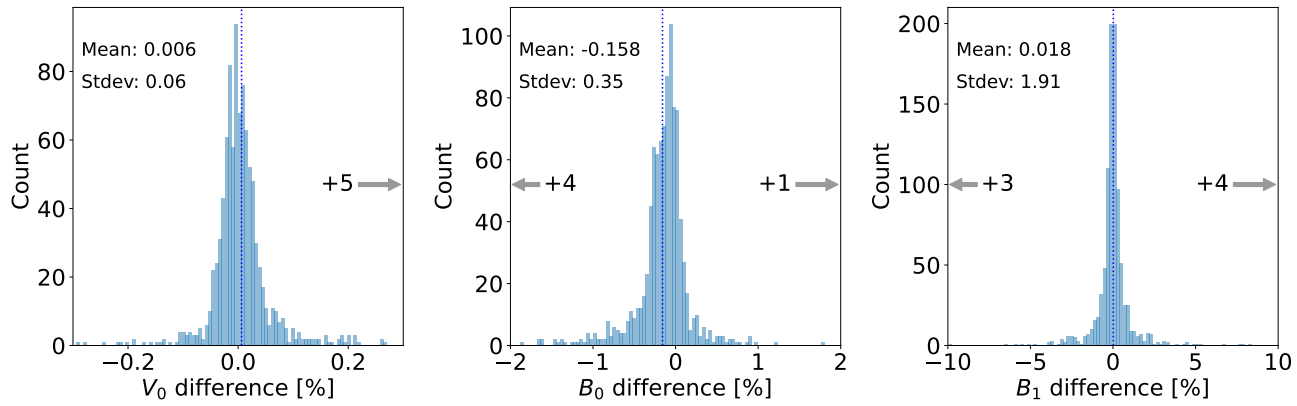

Figure 1. Histograms of the percentage difference between the results of the two all-electron codes (FLEUR and WIEN2k) with respect to their average for the three parameters of the EOS: V_0, B_0 and B_1, for the full dataset of unaries and oxides. Positive values indicate larger values for WIEN2k with respect to FLEUR. Mean and standard deviation (stdev) of the distributions are reported on the top left of each panel. The number near the arrows indicate the number of outliers outside of the x-axis range. The relative difference on V_0 is below 0.1% for 93% of all structures in our dataset; the relative difference on B_0 is below 1% for 97% of the structures; and the relative difference on B_1 is below 2% for 92% of the structures. The 5 outliers for V_0 are NeO_3 (0.302%), RbO_3 (0.343%), Cs_2O_5 (0.323%), Fr_2O_5 (0.645%) and Ra_2O_5 (0.333%), corresponding to lattice parameters for FLEUR/WIEN2k of 4.320/4.324Å, 4.783/4.789Å, 6.247/6.254Å, 6.120/6.133Å and 6.238/6.244Å, respectively.

and the raw data in Ref. 62 for the full dataset). The discrepancies for B_0 and B_1 are larger; this is not surprising, because they originate from higher derivatives of the EOS curves (see also discussion in SI Sec. S3). We emphasize that these values, obtained after careful convergence of all numerical parameters related to the basis-set choices in the two codes, are of extremely high precision, with a spread that can even be an order of magnitude smaller than the typical discrepancies that we observe between pseudopotential codes (see discussion later).

The complete list of numerical parameters used for the AE calculations is presented in SI Sec. S5. We highlight here that the exact choice of the electronic-state smearing and of the k-point integration mesh, as well as the specific quantity considered as the energy $E(V)$ (internal energy, or free energy including the entropic smearing contribution as we do here), are of crucial importance for a reliable comparison among codes and must be fully consistent; therefore, we discuss those in detail in section "Using the All-Electron Reference Dataset" and in Box 3.

Average AE dataset: the reference for further studies

In addition to the data for each of the two codes and in order to provide a single comparison reference, we also provide a "reference average all-electron dataset" obtained by averaging the values of V_0, B_0, and B_1 for each of the 960 systems in the full dataset. The corresponding values are in SI Sec. S4 and published according to the FAIR principles in Ref. 62. Considering the very good agreement between the two codes, this average dataset constitutes an excellent reference, and we use this average to compare with the pseudopotential codes in Section "Comparison with Pseudopotential-based Computational Approaches". In addition, if error bars are desired, the spread between the results of the two AE codes can be used as an estimate of our dataset precision.

Metrics for EOS comparison

In Refs. 29, 30, the "Δ" metric was used to compare the EOS computed with two different DFT computational approaches a and b. There, $\Delta = \Delta(a,b)$ was defined as:

$$\Delta(a,b) = \sqrt{\frac{1}{V_M - V_m}\int_{V_m}^{V_M} [E_a(V) - E_b(V)]^2 \, dV}, \tag{3}$$

where $E_a(V)$ and $E_b(V)$ are the Birch–Murnaghan fits of the data points obtained from approaches a and b respectively, the two EOS have been lined up with respect to their minimum energy, and as discussed earlier the integral spans a ±6% volume range centered at a central volume $\tilde{V}_0$ (with $\tilde{V}_0$ values tabulated in SI Sec. S1), i.e., $V_m = 0.94\tilde{V}_0$ and $V_M = 1.06\tilde{V}_0$.

The use of a single metric to compare two EOS curves simplifies the data analysis, since it can be used instead of the difference of the Birch–Murnaghan parameters V_0, B_0, and B_1, as we did in Fig. 1. However the value of $\Delta(a,b)$, that has the units of energy, has the shortcoming of being too sensitive to the value of the bulk modulus of the material: visually similar discrepancies between two curves result in larger Δ values for materials with larger B_0. This was already recognized in Ref. 63, where a modified metric Δ_1 was suggested, renormalized to a reference value of V_0 and B_0. In addition, the $E_a(V)$ and $E_b(V)$ quantities in Eq. (3) are typically renormalized by the number of atoms in the unit cell, to provide a "Δ/atom" metric, independent of the choice of the simulation cell size. Since we expand our analysis to two-component oxides, generalizations might be required (e.g., by normalizing instead per formula unit).

We propose and recommend here two new metrics that we label ε and ν, and we discuss their pros and cons. We first define the following shorthand notation for the integral average of a quantity $f(V)$ over the volume range $[V_m, V_M]$:

$$\langle f \rangle = \frac{1}{V_M - V_m} \int_{V_m}^{V_M} f(V)\, dV. \tag{4}$$

Using this notation, we can simply write $\Delta(a,b) = \sqrt{\langle [E_a(V) - E_b(V)]^2 \rangle}$. The first metric $\varepsilon(a,b)$ that we define is a renormalized dimensionless version of Δ:

$$\varepsilon(a,b) = \sqrt{\frac{\langle [E_a(V) - E_b(V)]^2 \rangle}{\sqrt{\langle [E_a(V) - \langle E_a \rangle]^2 \rangle \langle [E_b(V) - \langle E_b \rangle]^2 \rangle}}}. \tag{5}$$

This metric, similarly to the Δ_1 of Ref. 63 or the subsequently defined Δ_{rel} available in the DeltaCodesDFT package[30], is insensitive to the magnitude of the bulk modulus (see SI Sec. S6). In addition, it is independent of the use of a "per-formula-unit" or "per-atom" definition of the EOS (see SI Sec. S6). Therefore, $\varepsilon(a,b)$ provides a uniform metric across the variety of structural and chemical environments under investigation, given the requirement that it must be calculated with the same relative volume range for every material. As the list of central reference volumes has been fixed (see SI Sec. S1), and as we use the same $\pm 6\%$ volume range as in Ref. 29, 30, the 960 intervals $[V_m, V_M]$ are unambiguously defined. We highlight, in passing, that the discrete form of Eq. (5), i.e.:

$$\varepsilon(a,b) = \sqrt{\frac{\sum_i [E_a(V_i) - E_b(V_i)]^2}{\sqrt{\sum_i [E_a(V_i) - \langle E_a \rangle]^2 \sum_i [E_b(V_i) - \langle E_b \rangle]^2}}} \tag{6}$$

where the index i runs over the explicit calculations of $E(V)$ from DFT, provides a reasonably good approximation to the value of Eq. (5) as long as the minima of the $E_a(V_i)$ and $E_b(V_i)$ data points are aligned on the energy scale, with the advantage that it can be used to directly compare raw DFT total energy data without requiring an EOS fitting. Nevertheless, we stress that in the rest of this work we use the expression of Eq. (5) and not its discrete version of Eq. (6). Eq. (6) is grounded in the definition of the coefficient of determination (or R^2) in statistics[64] as a fraction of variance unexplained. We can interpret the value of $1-\varepsilon^2$ as the coefficient of determination (i.e. $1-\varepsilon^2 \approx R^2$) in a situation when one EOS $E_a(V)$ is treated as a fit for the other EOS $E_b(V)$. More precisely, since we want to define a symmetric metric $\varepsilon(a,b) = \varepsilon(b,a)$, our ε^2 is the $1-R^2$ value that one would obtain treating $E_a(V)$ as a fit for $E_b(V)$ and vice versa with the geometric mean of both data variances. We note that the interpretation $R^2 \approx 1-\varepsilon^2$ holds in very good approximation when the value of ε is much smaller than one (i.e., for very similar $E(V)$ curves).

We discuss the sensitivity of ε to perturbations of the Birch–Murnaghan parameters in SI Sec. S7. The main outcome is that ε is mostly sensitive to the variations of V_0, and much less of B_0 and B_1. For some applications, however, some of the parameters are more relevant than others (e.g., if one is mostly interested in accurate bulk moduli). For these cases, we recommend (see also Box 4) to define metrics of discrepancy that depend directly on physically measurable quantities. Since an EOS is very well described by the three parameters V_0, B_0 and B_1, we suggest a second metric ν that directly captures the relative difference of these three parameters between two computational approaches a and b, using appropriate weights w_{V_0}, w_{B_0}, w_{B_1}:

$$\nu_{w_{V_0},w_{B_0},w_{B_1}}(a,b) = 100 \sqrt{\sum_{Y=V_0,B_0,B_1} \left[w_Y \cdot \frac{Y_a - Y_b}{(Y_a+Y_b)/2} \right]^2}, \tag{7}$$

where, for instance, $(V_0)_a$ indicates the value of V_0 obtained by fitting the data of approach a, and so on. The (arbitrary) prefactor 100 is chosen to obtain values with similar order of magnitude to those of ε. Furthermore, it also helps in interpreting the value of ν as an estimate of percentage errors (rather than relative errors) on the fit parameters. We highlight that ν depends on the

weights (w_Y), that in turn could be chosen to satisfy particular applications. Here, since we aim to be application-agnostic, we choose weights based only on the sensitivity of our fitting procedure to random numerical noise applied to the energy values of the EOS data points. The detailed procedure to determine the weights is described in SI Sec. S3; we just report here the final choice $w_{V_0} = 1$, $w_{B_0} = 1/20$ and $w_{B_1} = 1/400$. Intuitively, the reduced weights are consistent with the expected increase of numerical uncertainty propagated in the fit when estimating higher-order derivatives of the EOS. Similarly to ε, also these weights depend on the volume range of the datapoints used for the EOS fit, as well as the specific choice of the fitting algorithm (see details in SI Sec. S3). In the rest of the manuscript, we refer to ν assuming this specific choice of weights, i.e., $\nu \equiv \nu_{1,1/20,1/400}$. In SI Sec. S7 we also discuss an intuitive interpretation of the ν metric: it is the percentage error on the equilibrium volume between the two approaches a and b, when B_0 and B_1 are the same in the two approaches; otherwise, when B_0 and B_1 differ, it corresponds to an equivalent percentage error on V_0 that would result in quantitatively similar changes to the EOS curve, within the $\pm 6\%$ volume range considered here.

The metrics ε and ν allow to compare a pair of codes for each material in the dataset. Fig. 2 reports the results for the pair (FLEUR, WIEN2k) across the entire set of structures under investigation in the form of periodic tables, enabling a quick identification of the most problematic elements in each set. For instance, as one might expect the agreement is generally worse for noble gases: weakly bonded systems with a very small bulk modulus and thus more susceptible to numerical errors due to the choice of the basis set and of other computational parameters.

We emphasize that with our choice of the volume range and weights for ν, the two metrics provide very consistent information, highlighting the importance of properly defining metrics based on physically measurable quantities, and on careful analysis of the error propagation of the fitting procedure, as we recommend in Box 4 (see also SI Sec. S7, where we discuss quantitatively the effect of perturbations on the EOS parameters to the values of ε, ν and Δ). Indeed, although ε and ν are constructed according to quite different principles, they turn out to contain nearly identical information (in SI Sec. S8 we show that they are to a good extent linearly correlated for $\nu \lesssim 1$, with $\nu \approx 1.65\varepsilon$). This has the consequence that periodic tables for ε or ν will be almost identical if the range of the color scale is taken according to this linear correlation (as it is the case, e.g., in Fig. 2 and is discussed in more detail in SI Sec. S9).

Finally, we identify (and report in Box 3, see also discussion in SI Sec. S7) indicative thresholds on ε and ν to represent an excellent agreement between two EOS curves if $\varepsilon \lesssim 0.06$ or $\nu \lesssim 0.1$, or a good agreement (noticeable, but still relatively small) if $\varepsilon \lesssim 0.2$ or $\nu \lesssim 0.33$. As discussed earlier, we can interpret the two thresholds $\varepsilon = 0.06$ ($\varepsilon = 0.2$) approximately as a determination coefficient $R^2 \approx 1 - 0.06^2 = 0.9964$ ($R^2 \approx 1 - 0.2^2 = 0.96$) if one EOS is treated as a fit for the other. The data from the two AE codes shows an overall excellent agreement: only four systems out of 960 have one or both metrics outside of the "good-agreement" range (Cs_2O_5, Fr_2O_5, Ra_2O_5 and RbO_3) when comparing the two AE codes of our reference dataset, and 883 out of 960 systems have an excellent agreement for both ε and ν according to the thresholds discussed above.

Using the AE reference dataset

In this section we detail several aspects that must be carefully considered when using the reference dataset presented in the previous section. We then show how the dataset has been used to evaluate the precision of several computational approaches based on pseudopotentials and to improve a number of pseudopotential libraries.

Recommendations on how to use the dataset

When comparing our reference dataset with results from other codes, either for verification purposes or as a reference to improve basis sets and pseudopotentials, it is essential to use the same approximations (such as the exchange–correlation functional or the treatment of spin) and numerical choices (smearing and k-point integration mesh), as these parameters significantly affect the EOS results. Therefore, we discuss here (and summarize in Box 3) specific recommendations on which parameters should not be changed when generating new data to compare with.

All calculations are performed in periodic boundary conditions using the PBE[57] exchange-correlation functional, without including spin-polarization effects (non-magnetic calculations) and within a scalar-relativistic approximation (no spin-orbit coupling) for the orbitals treated as valence states. The reciprocal-space integration is performed with a Monkhorst–Pack uniform k-point grid including the Γ point, chosen as the smallest integration mesh guaranteeing a linear spacing of at most 0.06 $Å^{-1}$ in each of the three reciprocal-space directions for the smallest volume, and the same set of k-points (in scaled units) for all other volumes. For instance, this corresponds to a grid of $21 \times 21 \times 21$ k-points for a simple-cubic primitive cell with lattice parameter of 5 Å. A Fermi–Dirac smearing of electronic states with a broadening of 0.0045 Ry (≈ 61.2 meV) is used in all cases, requiring the high-density k-points sampling mentioned above. In addition, the quantity $E(V)$ that is fitted with the Birch–Murnaghan expression of Eq. (1) is not the internal energy, but the free energy that includes the entropic contribution $-TS$ introduced by the smearing (where T is the effective temperature given by the smearing broadening). This corresponds to considering isothermal quantities for B_0 and B_1 (we stress, however, that the temperature effect in these simulations do not mimic a physical temperature, but a fictitious temperature due to the electronic smearing).

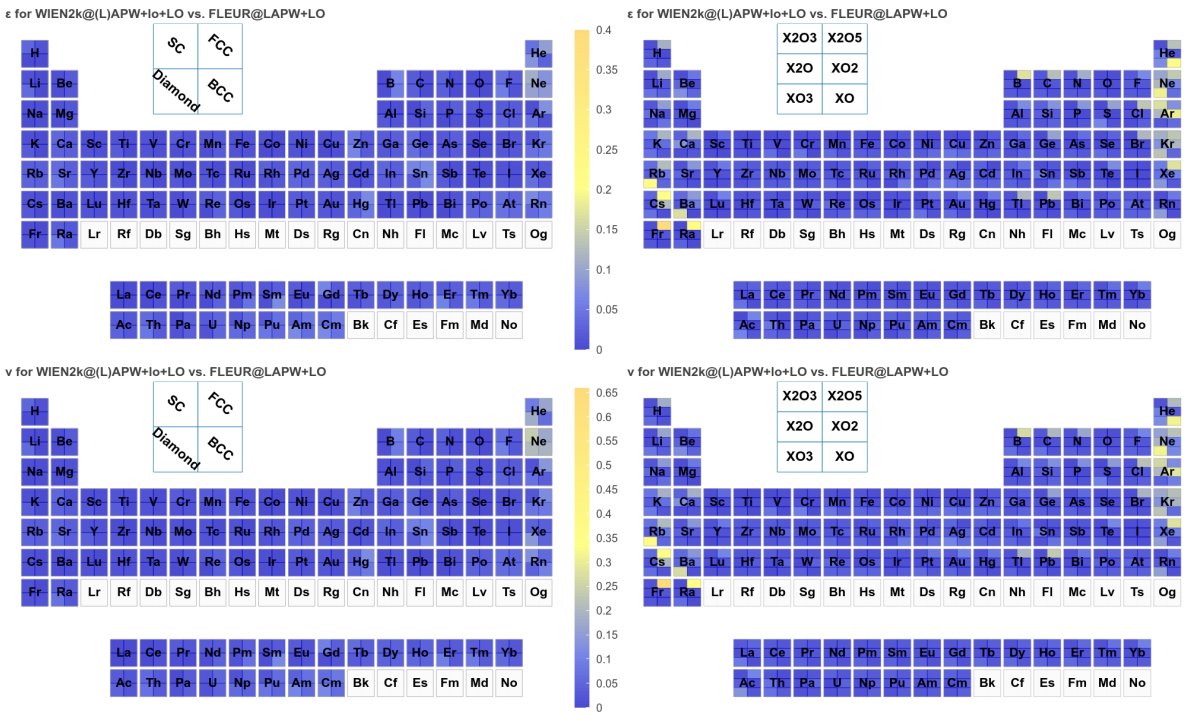

Figure 2. Discrepancy between the AE results (obtained with WIEN2k and FLEUR) in our reference dataset, measured either with the ε metric (top panels) or the ν metric (bottom panels), for all 96 elements considered. Each square for a given element is subdivided in 4 (6) in the left (right) panel, each referring to one of the unary (oxide) structures, as indicated in the legend presented in each panel. The color scale is the same for each pair (unaries and oxides) of periodic tables for the same metric (ε or ν). All structures are within our threshold for good agreement except Cs_2O_5 ($\varepsilon = 0.20$, $\nu = 0.33$), Fr_2O_5 ($\varepsilon = 0.40$, $\nu = 0.66$), Ra_2O_5 ($\varepsilon = 0.21$, $\nu = 0.33$) and RbO_3 ($\varepsilon = 0.21$, $\nu = 0.37$).

We stress that, in general, two codes using a different smearing distribution are expected to return comparable results only in the limit of an infinite number of k-points and an infinitesimal smearing. However, for the purpose of verification, we do not need to reach this computationally expensive limit, provided that the same parameters among codes are chosen. As a consequence, our results should not be considered a prediction of the zero-temperature (i.e., no smearing) limit. We still highlight, however, that our choice of the k-point density results in a very dense and almost converged integration mesh (for fixed broadening): e.g., all values of V_0 computed with WIEN2k change by less than 0.07% when comparing with a denser k-point integration mesh with linear spacing of 0.045 $Å^{-1}$, except in two cases (RbO_3: 3.7% change, and HeO, 0.16% change). More details are reported in SI Sec. S10.

To emphasize the sensitivity of the EOS to the choice of smearing, we show in Fig. 3 one of the most pathological cases of our dataset, erbium in the diamond crystal structure. In this case, the EOS does not have a simple shape but displays instead, for the case of Fermi–Dirac and Gaussian smearing, two minima at very different volumes. Which one is favored in energy depends on the type of smearing and the value of the broadening. This behavior can be explained by the presence of a set of narrow f bands close to the Fermi level, shown in SI Sec. S11, whose filling strongly depends on the smearing. If we are after an improved erbium pseudopotential, trying to optimize it with a different smearing (and thus possibly for a different minimum) will result in an incorrect pseudopotential. A similar reasoning holds for the choice of using the free energy instead of the internal energy for the EOS (see SI Sec. S12). We also highlight that we adopted a scalar-relativistic treatment of valence electrons for our dataset. In most pseudopotential codes, this is obtained by simply using scalar-relativistic pseudopotentials, and the treatment is applied only for the valence electrons that are considered explicitly, while the treatment for the core electrons is implicitly included in the pseudopotential used. Even for AE codes, electrons are typically partitioned into a core (treated fully relativistically) and a valence set (treated scalar relativistically). We highlight that the two AE codes used in this work do not adopt the same core/valence assignment for all crystals (see SI Sec. S5), yet they agree very well, illustrating that the core/valence assignment might not lead to ambiguities in the calculated results, provided all other numerical parameters are chosen consistently.

Finally, we note that many additional code-specific parameters exist, such as the type and size of the basis set or the

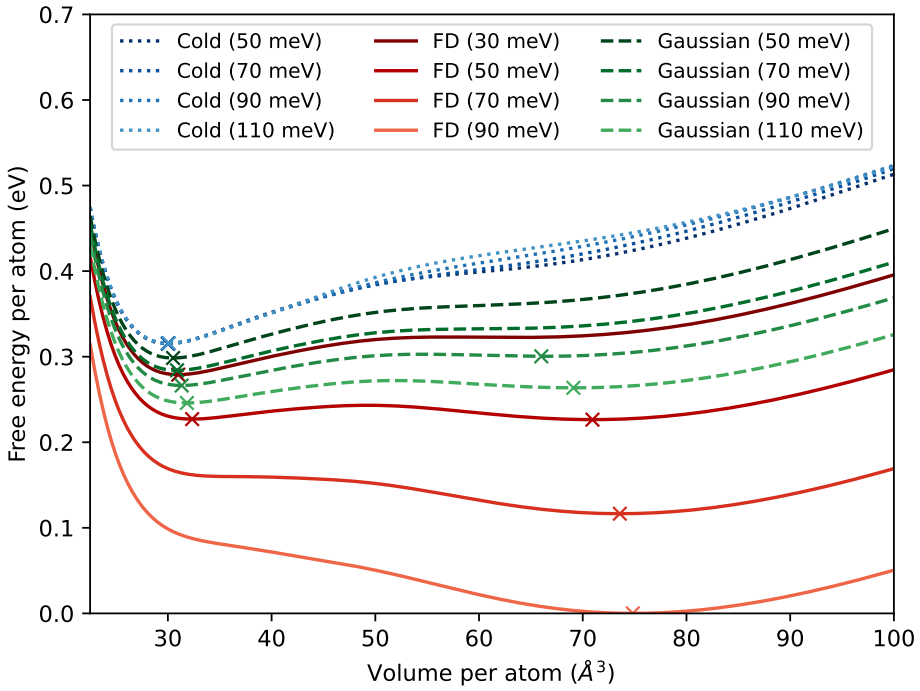

Figure 3. Effect of different choices of smearing on the EOS of the artificial diamond structure of erbium computed with the QUANTUM ESPRESSO code. Er in the diamond structure is one of the systems in which the effect of smearing is most pronounced. In the legend, "Cold", "FD" and "Gaussian" indicate, respectively, cold smearing[65], Fermi–Dirac smearing and Gaussian smearing. Two alternative minimum-energy solutions can exist for the FD and Gaussian smearings at very different volumes (as indicated by the crosses, when local minima exist in the curves); which one is selected depends on the choice of smearing and broadening. Note also the much reduced sensitivity of the cold smearing to the broadening temperature, and how FD and Gaussian smearings are essentially equivalent after a renormalisation of the FD broadening by a factor ≈ 2.565, as discussed in Ref. 66.

pseudopotential family. These choices are implemented in our automated common workflows[36] and can be selected using a new protocol defined for this work and named `verification-PBE-v1`. Specific details for each code are reported in SI Sec. S5 for the AE codes, and in SI Sec. S13 for all the other codes.

Before showing an example of the comparison of our reference AE dataset with nine computational approaches based on pseudopotentials, we discuss an additional recommendation. Our dataset was generated to provide reference EOS for each of the 960 structures. One might be tempted to reuse our dataset for different purposes. For instance, since the values of the minimum energy of the EOS curves are also available from the fits, one could imagine using them to compare total energies of various oxides of the same element X, estimating their relative stability and the corresponding formation energies. However, while this approach often results in sensible values, some notable cases lead to significantly off results, even by 1 eV/atom (see results in SI Sec. S18). The reason is that we designed our workflows and protocols for the EOS, in order to guarantee that simulation parameters are chosen consistently for all volumes of a given material, but this is not necessarily true among different materials. As an example, since oxides of the same element might have very different interatomic spacings, the choices of atomic radii (and the corresponding core/valence separation) for the AE codes might be different in different systems, which precludes direct comparison between total energies. From a more general point of view, one needs to be aware of the context in which data was produced, and consider implications and limitations when using them for different applications, as we discuss in the Outlook section.

Comparison with pseudopotential-based computational approaches

Using the recommendations of the previous section and of Box 3, we now compare our reference dataset with the results obtained with nine computational approaches based on pseudopotentials. As discussed earlier, each approach is not only defined by the choice of the code, but also by the pseudopotentials used (and, where applicable, by the type of basis set).

Expert Recommendation Box 3, Summary of details to properly compare with the reference dataset presented in this work

- Use the PBE exchange–correlation functional, do not include spin-polarization effects, and consider a scalar-relativistic treatment of (valence) electrons.
- Use Fermi–Dirac smearing with a value of 0.0045 Ry. While this choice does not lead to zero-smearing results (which would require extrapolation and extremely dense k-point integration meshes), using the same values ensures that results are comparable. In extreme cases, using a different smearing may affect significantly the equilibrium volume and the overall shape of the EOS.
- Compute the equations of state (EOS) using as the proper variational functional the free energy $E - TS$, where E is the internal energy and $-TS$ is the smearing-energy entropic contribution. Other choices, such as the internal energy E, or the extrapolated energy for zero smearing (e.g., the expression $E - TS/2$, valid for Fermi–Dirac or Gaussian smearings[66,67]) can result in significant changes of the EOS, including large variations of the minimum-energy volume.
- Use the same protocol to fit the EOS curves: 7 equally spaced points in a volume range of $\pm 6\%$ around the specified central volume. With these choices, values $\varepsilon \lesssim 0.06$ or $v \lesssim 0.1$ can be considered to indicate an excellent agreement, and $\varepsilon \lesssim 0.2$ or $v \lesssim 0.33$ a good agreement (with a noticeable, but still relatively small discrepancy between them). A different volume range will affect these thresholds and require a different choice of weights for v to capture differences that are not purely statistical in nature. In addition, a different volume range will affect the k-point integration mesh (see next point).
- Use the exact same choice of the k-point integration mesh: regular grid including the Γ point and the smallest mesh guaranteeing a spacing between points of at most 0.06 Å^{-1} along each of the three reciprocal-space directions for the smallest volume, and the same set of k-points (in scaled units) for all other volumes. This is typically converged for most systems and ensures that results can be compared even in the rare case of an unconverged k-point integration mesh.
- Do not transfer the choices performed for this reference dataset to a different context, since it might lead to incorrect conclusions. For instance, extracting formation energies from our reference dataset can provide inaccurate results, since the parameters used in our simulations are guaranteed to be consistent only for different volumes of the same material, but not necessarily among different materials.

Therefore, we summarize here briefly the meaning of the labels used for every computational approach. The two AE codes, FLEUR and WIEN2k, are labeled with their code name, followed by an indication of the basis set they use: `FLEUR@LAPW+LO` and `WIEN2k@(L)APW+lo+LO`, respectively (see SI Sec. S5 for more details). All other labels also include, at the end, the name of the pseudopotential library that was used. In particular: `ABINIT@PW|PseudoDojo-v0.5` indicates the ABINIT code, adopting a plane-wave (PW) basis set, using norm-conserving pseudopotentials from the PseudoDojo standard library version 0.5[68,69]; `BigDFT@DW|HGH-K(Valence)` indicates a (partial) set of structures with valence-only Hartwigsen–Goedecker–Hutter pseudopotentials[70] calculated with the BigDFT code, adopting a basis set of Daubechies wavelets (DW), `CASTEP@PW|C19MK2` indicates the CASTEP code using on-the-fly generated core-corrected ultrasoft pseudopotentials from the `C19` library with updated settings for the f block elements, `CP2K/Quickstep@TZV2P|GTH` indicates the CP2K Quickstep code using Goedecker–Teter–Hutter pseudopotentials[71,72] and a molecularly optimized TZV2P-type basis set[73], `GPAW@PW|PAW-v0.9.20000` indicates the GPAW[48,49] code used in its plane-wave mode using GPAW's PAW pseudopotentials included in the setup release 0.9.20000[74], `Quantum ESPRESSO@PW|SSSP-prec-v1.3` indicates the QUANTUM ESPRESSO code using the Standard Solid-State Pseudopotentials (SSSP) library (PBE precision version 1.3)[75,76], `SIESTA@AtOrOptDiamond|PseudoDojo-v0.4` indicates the SIESTA code using norm-conserving pseudopotentials from the PseudoDojo standard library version 0.4 in psml format[68,69,77] and localized basis sets in which the orbitals for each element are taken from a partial optimization, considering just the unary Diamond structure for that element (therefore no optimization for the chemical environment of each material has been performed), `SIRIUS/CP2K@PW|SSSP-prec-v1.2` indicates the SIRIUS library code (run via its interface to CP2K) using the SSSP pseudopotential library (PBE precision version 1.2)[75] and `VASP@PW|GW-PAW54*` indicates the VASP code (v6.3) using the PAW GW PBE pseudopotentials released in the dataset `potpaw_PBE.54`, except for the lanthanides (see Section "Pseudopotentials Improvement"). The exact versions of the codes and libraries, together with the other code-specific choices implemented in the `verification-PBE-v1` protocol, are detailed in SI Sec. S13. The choices of computational approaches (for each code) listed above have been selected by the

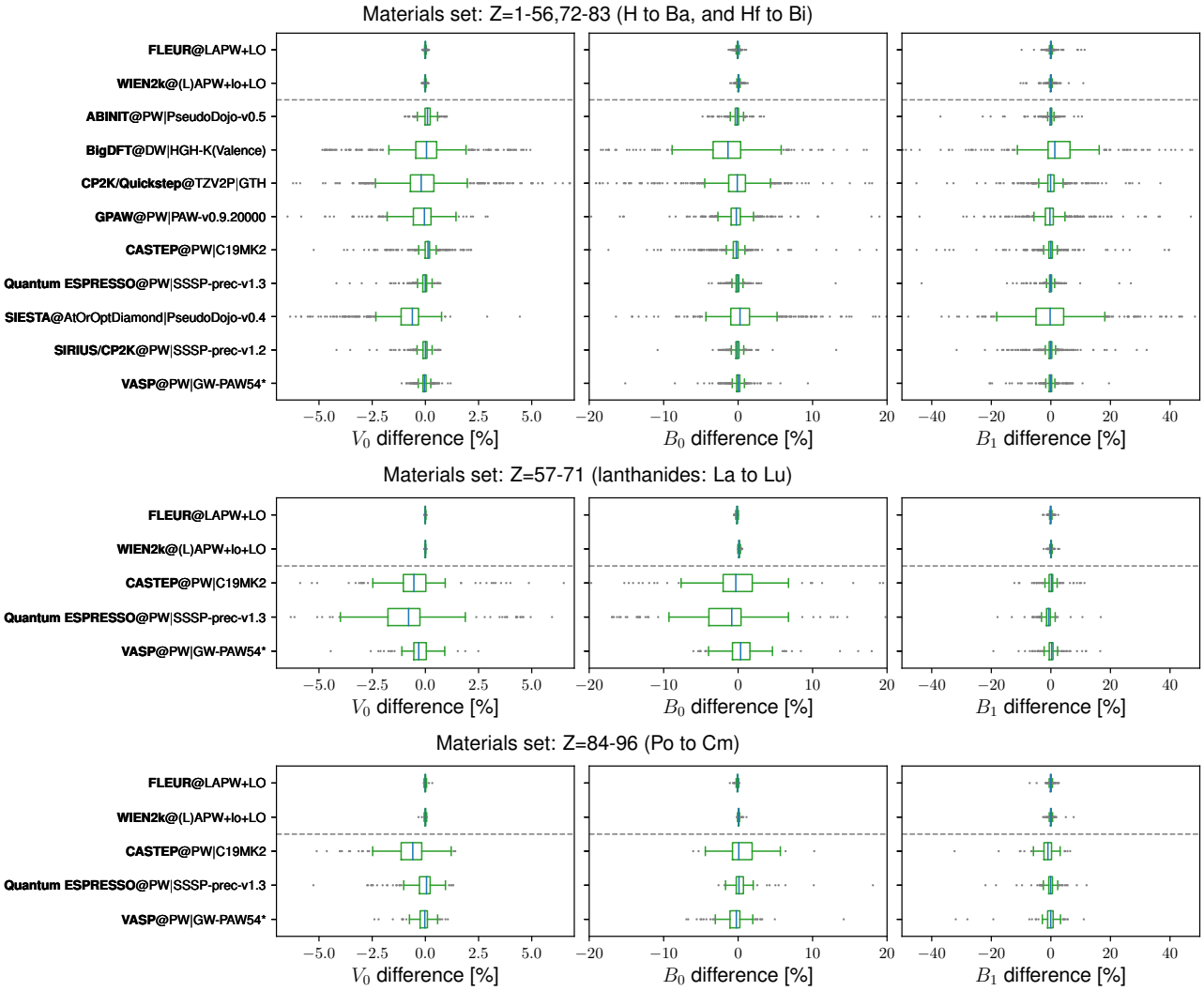

Figure 4. Box-and-whisker plots comparing the V_0, B_0 and B_1 discrepancy of each computational approach involved in this work with respect to the average all-electron reference dataset. The two AE codes are also reported at the top of the plot above the dashed line, for comparison. In the box-and-whisker plots, the central blue line represents the median and the box extends between the first quartile $Q1$ and the third quartile $Q3$. The "whiskers" extend between the first point greater than $Q1 - 1.5 \cdot \text{IQR}$ and the last point smaller than $Q3 + 1.5 \cdot \text{IQR}$ (where IQR is the inter-quartile range $Q3 - Q1$). Outliers beyond the wiskers are represented as grey points. Note that some of the outliers are outside of the visible axis range in order to facilitate comparison between codes on the same axis range. Each row corresponds to a different subset of materials, where only the computational approaches that could compute those materials are included (since not all approaches include pseudopotentials for rare-earths). Specifically, the top row includes all materials from H to Bi excluding the lanthanide elements from La to Lu (68 elements in total). For this set, 295 crystals are missing for `BigDFT@DW|HGH-K(Valence)`, Na (FCC) is missing for `CP2K/Quickstep@TZV2P|GTH`, Hg (FCC) and RbO_3 are missing for `SIESTA@AtOrOptDiamond|PseudoDojo-v0.4`, and all 10 crystals containing Tc are missing for `GPAW@PW|PAW-v0.9.20000`. The central row reports the results for lanthanides only (from La to Lu), and the bottom row for all materials from Po to Cm (i.e., heavy elements, including actinides up to Cm).

workflow developers of each code, trying to identify converged parameters and limiting to choices commonly available to users (or in some cases improving upon them, as we discuss later in the section "Pseudopotentials improvement").

The results are presented in Fig. 4 in the form of box-and-whisker plots for the percentage error of V_0, B_0 and B_1, with respect to the reference average AE dataset. Applying one of our general recommendations of Box 1, we partition our results in three groups (considering separately rare earths and/or heavy elements), in order to highlight the non-uniform capabilities of the various computational approaches. Indeed, the narrow bands originating from the localized f electrons are very challenging to be described accurately with plain DFT[78]. Therefore, often pseudopotentials for these elements are not available and thus several approaches cannot produce data for rare earths. Even when available, those pseudopotentials might be less tested and thus deliver a lower precision. By separating the results, we also enable a fairer comparison of approaches for the common set of elements (from H to Bi excluding the lanthanide elements from La to Lu).

Our results show that different numerical approaches have different precision; in general, the spread of the parameters of pseudopotential approaches are significantly larger than those between our two AE codes. In addition, the results indicate that additional work is required to obtain a high precision with approaches employing localized basis sets (that, on the other hand, are typically faster and scale better with system size) with respect to those using a plane-wave basis set (in the present case, the approaches listed above using the ABINIT, CASTEP, GPAW, QUANTUM ESPRESSO, VASP and SIRIUS/CP2K codes). Indeed, while a plane-wave basis set can be tuned with a single numerical parameter (the energy cutoff), systematically improving localized basis sets (and the associated pseudopotentials) requires dedicated efforts, that we recommend in Box 4. Verification projects such as this will facilitate these efforts by providing appropriate benchmarks. Another example of verification is presented in SI Sec. S14, where we discuss the agreement of different codes adopting the same computational approach, in particular with the same plane-wave basis set and the same pseudopotential library. In this case, the results show an agreement that is similar in precision to the one between the two AE codes. We finally stress that the choice of the energy cutoff is specific to plane-wave codes, and in addition it depends on the pseudopotentials adopted. Therefore, for the goal of this Expert Recommendation, we do not provide reference values for the energy cutoffs (as we instead do for other code-agnostic parameters such as the k-point integration mesh or the energy smearing, see Box 3). Instead, the cutoffs are determined in the protocols of each code, together with all other code-specific numerical parameters; each code is responsible for verifying that the cutoff choice is converged for the goal of computing the equations of state illustrating our Expert Recommendation.

Periodic tables (similar to Fig. 2) for each code are provided in SI Sec. S9, allowing for a closer inspection of the results resolved per chemical element and crystal-structure type. These tables also show that using a larger crystal-structure set (960 systems here) with respect to the set of 71 of Ref. 29 helps in highlighting possible shortcomings of pseudopotentials, as we discuss in more detail in SI Sec. S15. The results of each code are also available in Ref. 62, and can be visually displayed and compared directly online on the Materials Cloud[19] at `https://acwf-verification.materialscloud.org`.

Pseudopotentials improvement

Curated datasets such as the one presented in this Recommendation can drive efforts to improve pseudopotentials, ultimately delivering more precise computational approaches. To illustrate this, we briefly summarize examples of pseudopotential enhancements that we performed to improve the comparison with our AE results (more technical details are discussed in SI Sec. S16) and used in the generation of the data of Fig. 4.

The results for `ABINIT@PW|PseudoDojo-v0.5` for elements around the $4f$ block (from Te to Ba, and from Tl to Rn) were not giving ideal agreement using available pseudopotentials from PseudoDojo (version 0.4). In almost all cases, we found that the accuracy of the pseudopotentials is significantly improved by including a projector for the unbound f state, at the expense of an increase of the computational cost when applying the non-local part of the Hamiltonian V_{nl} (this can, however, be mitigated by the use of Legendre polynomials). Without this projector, the local part of the pseudopotential cannot reproduce the all-electron scattering properties of the f angular momentum (see SI Sec. S16.1). This led to the creation of a new PseudoDojo table (version 0.5), used here.

For `CASTEP@PW|C19MK2`, starting from the on-the-fly pseudopotential generation settings for the built-in `C19` library, pseudopotentials for the lanthanide and actinide elements were improved by systematically changing the core radii, adding additional projectors, and adding fractional occupations of states that are empty in the reference atomic configurations. While making these changes did result in improvements, we note that no iterative optimization has been carried out to fit to the AE results.

For `Quantum ESPRESSO@PW|SSSP-prec-v1.3`, the pseudopotentials of SSSP PBE Precision version 1.1.2[79] have been updated for elements Na, Cu, Cs, Cd, Ba, As, Te, I, Hg, Ne, Ar, Kr, Xe, Rn; these new pseudopotentials have been released in the new SSSP PBE Precision 1.2[80]. The new pseudopotentials have been selected by re-verifying the precision of pseudopotentials from various external libraries against the AE reference dataset discussed in this Recommendation, and replacing those displaying significant discrepancies with pseudopotentials from other libraries that displayed a better agreement (lower ε and v). Moreover, in SSSP PBE Precision version 1.3[76] (used here) new pseudopotentials have been included for

actinides (Th-Lr) from Ref. 81, as well as for Ac, At, Ra, and Fr from PSlibrary[82].

For VASP@PW|GW-PAW54*, the latest available PAW potential set (version 5.4) was improved by reducing by about 20% the core radii for lanthanides (other than La, Ce, and Lu). Furthermore, placing two electrons in the 6*s* shell, half an electron in the 5*d* shell and the rest in the *f* shell led to the most balanced description. For Tm, Er, and Yb, three *f* projectors were required to accurately describe the *f* scattering properties. The optimization was continued until very accurate scattering properties were obtained and agreement with very small core potentials was excellent, in turn resulting in a significant improvement of the agreement with the AE reference dataset.

Outlook

This work constitutes a next step in a grand scheme of actions aiming at controlling the numerical aspects of electronic structure calculations, where the diversity of computational approaches and codes provides an opportunity for pairwise verification. Compared to earlier work[29,30], we define here more discriminative metrics (crystals where two approaches would agree according to Δ might agree less according to ε or ν, see SI Fig. S8.1a,b) and consider many more crystals, leading to more stringent testing. While major conclusions based on previous work remain valid (see SI Sec. S15 and SI Sec. S17), the dataset presented here—together with the clear set of recommendations on how to reuse the data—provides a more refined and valuable reference for verification, uncertainty quantification and pseudopotential optimization.

Additionally, by formulating recommendations on how to perform further validation studies, and by providing and sharing universal common workflow interfaces (based on the AiiDA workflow infrastructure) to reproduce our calculations and perform new ones, we facilitate the community in taking new steps towards a better control of the uncertainty quantification in electronic structure calculations. There are several directions in which those steps could be taken. First, we recommend the creation of similar datasets for other commonly used exchange–correlation functionals (such as LDA and PBEsol, but possibly also a selection of hybrid and meta-GGA functionals), as well as for fully relativistic simulations. For these studies, we recommend to use the same initial set of crystal structures discussed here, possibly only adapting the central point of the volume interval $[V_m, V_M]$ if the equilibrium volume V_0 for the functional does not lie anymore roughly in the middle of the interval. Indeed, the set is fairly complete and systematic, and using the same structures facilitates the comparison between different computational approaches and approximations. In addition, we recommend to test and verify codes also for magnetic materials.

Once such datasets are available, efforts to further improve pseudopotentials (and basis sets) should be initiated or continued, with the aim of making the results easily available to the broad simulation community. One useful outcome could be, for instance, the generation of new reliable fully relativistic pseudopotential datasets for rare-earths (especially of the norm-conserving type, often required by many codes computing advanced materials properties). Another relevant example, involving also the generation of additional bespoke AE reference datasets, is the generation of pseudopotentials with a hole in the core, needed to predict the outcome of X-ray photoelectron spectroscopy (XPS) or X-ray absorption spectroscopy (XAS) experiments.

As a note, we highlight here that some of our structures are unrealistic. When generating a new pseudopotential for a given chemical element, one might want to accept a compromise and not reproduce precisely the EOS of all 10 unaries and oxides, in order to obtain a computationally cheaper pseudopotential (e.g., with less projectors, more electrons in the core, or requiring a smaller energy cutoff), as long as the results are precise enough for the intended applications.

Other properties beyond the EOS are relevant to characterize materials and might benefit from tailored verification efforts; these include, e.g., formation energies, electronic band structures and phonon frequencies. As we already highlighted, the simulation protocols might be significantly different for each property. We therefore recommend that these protocols are well designed, documented and discussed, together with their limit of applicability. In particular, especially if limiting to a scalar-relativistic approach as we did here, we recommend to further investigate the relevance of the choice of which electrons are included in the core or in the valence, as this can be of higher relevance than for the EOS (e.g., for formation energies, see also SI Sec. S18). Moreover, new metrics should be designed to quantitatively compare results, ideally directly dependent on physically measurable quantities. Error propagation through any fitting procedure or data analysis should be carefully assessed, as we did in SI Sec. S3, to be able to define appropriate error bars.

Finally, we emphasize that while the goal here was ultimate precision in order to provide a reference dataset and obtain the best agreement possible between computational approaches, in real simulations one needs to optimize also the computational cost for a target accuracy, to obtain "good-enough data" for their scientific purpose. This is especially true for high-throughput runs or when the DFT simulations are the first step of more expensive post-DFT methods. We thus encourage to develop protocols to automatically define or select optimally converged parameters that at the same time minimize energy and CPU time, and then disseminate these to the whole community, so that they become easily accessible and usable by a broad range of users.

Expert Recommendation Box 4, Summary of recommendations to extend the verification effort presented in this work

- Extend the current study to more computational approaches (codes, basis or pseudopotential sets, etc.), adopting the same reference crystal-structure set presented here.
- Investigate whether there are advantages in using a different crystal-structure set as the one presented here. E.g., whether lower-symmetry environments (low-symmetry structures, vacancies, surfaces, ...) might highlight further differences between DFT implementations; or considering only compounds for which experimental data is available, for studies focusing instead on validation against experiments.
- Extend the current study to more properties (forces, phonons, Kohn–Sham band structures, formation energies, ...). Choose properties (and materials) that maximize the number of codes that can compute them (e.g., here for the EOS, only single-point DFT simulations are required; forces and stresses were not used).
- Investigate the generality of optimal protocols and develop new ones for each property being computed, generalizing how to select a consistent set of parameters for multiple runs. For instance, for the EOS it is important to use the same k-point integration mesh at all volumes, but for a formation energy one wants a mesh that has reached a threshold accuracy for each component. In addition, use the same core/valence assignment, core radii and any other approach-specific precaution needed to compare total energies of different crystals.
- Create additional curated sets needed to generate improved pseudopotentials. E.g., extend to fully relativistic simulations and consider other exchange–correlation functionals in addition to PBE, such as the local-density approximation (LDA) and PBEsol, but also a selection of hybrids and meta-generalized-gradient approximations (meta-GGAs) for instance. Provide also curated sets needed to generate core-hole pseudopotentials for the simulation of core-level spectroscopies.
- Beside targeting improved pseudopotentials, develop dedicated efforts to optimize localized basis sets when these cannot be systematically improved by just tuning one or a few numerical parameters.
- Develop new protocols aiming at "good-enough data": i.e., not only targeting ultimate numerical precision (needed for verification), but also optimizing the computational cost for a target accuracy.
- Disseminate these protocols to the broad simulation community to optimize energy and CPU time and to expand the computational feasibility of DFT computational approaches in high-throughput studies or for expensive post-DFT methods (e.g., many-body perturbation theory).
- For new verification protocols, define metrics (such as ε and ν discussed here for the EOS) that depend on physically measurable quantities. Using such metrics, that condense in a single quantity the precision of computational approaches on a property of interest, one can easily define precision thresholds, compare approaches quantitatively, and evaluate the uniformity of results in a dataset. If fitting procedures are needed, assess the robustness of the chosen algorithms and estimate the uncertainty on the fitted parameters, using the results to define error bars.

References

1. Alberi, K. *et al.* The 2019 materials by design roadmap. *J. Phys. D: Appl. Phys.* **52**, 013001, DOI: 10.1088/1361-6463/aad926 (2018).
2. Marzari, N., Ferretti, A. & Wolverton, C. Electronic-structure methods for materials design. *Nat. Mater.* **20**, 736–749, DOI: 10.1038/s41563-021-01013-3 (2021).
3. Pizzi, G., Cepellotti, A., Sabatini, R., Marzari, N. & Kozinsky, B. AiiDA: automated interactive infrastructure and database for computational science. *Comput. Mater. Sci.* **111**, 218–230, DOI: 10.1016/j.commatsci.2015.09.013 (2016).
4. Huber, S. P. *et al.* AiiDA 1.0, a scalable computational infrastructure for automated reproducible workflows and data provenance. *Sci. Data* **7**, DOI: 10.1038/s41597-020-00638-4 (2020).
5. Ong, S. P. *et al.* Python materials genomics (pymatgen): A robust, open-source python library for materials analysis. *Comput. Mater. Sci.* **68**, 314–319, DOI: https://doi.org/10.1016/j.commatsci.2012.10.028 (2013).
6. Jain, A. *et al.* Fireworks: a dynamic workflow system designed for high-throughput applications. *Concurr. Comput. Pract. Exp.* **27**, 5037–5059, DOI: 10.1002/cpe.3505 (2015).
7. Mathew, K. *et al.* Atomate: A high-level interface to generate, execute, and analyze computational materials science workflows. *Comput. Mater. Sci.* **139**, 140–152, DOI: 10.1016/j.commatsci.2017.07.030 (2017).
8. Bahn, S. R. & Jacobsen, K. W. An object-oriented scripting interface to a legacy electronic structure code. *Comput. Sci. Eng.* **4**, 56–66, DOI: 10.1109/5992.998641 (2002).
9. Hjorth Larsen, A. *et al.* The atomic simulation environment—a Python library for working with atoms. *J. Physics: Condens. Matter* **29**, 273002, DOI: 10.1088/1361-648X/AA680E (2017).
10. Curtarolo, S. *et al.* Aflow: An automatic framework for high-throughput materials discovery. *Comput. Mater. Sci.* **58**, 218–226, DOI: https://doi.org/10.1016/j.commatsci.2012.02.005 (2012).
11. Janssen, J. *et al.* pyiron: An integrated development environment for computational materials science. *Comput. Mater. Sci.* **163**, 24 – 36, DOI: https://doi.org/10.1016/j.commatsci.2018.07.043 (2019).
12. Armiento, R. *Database-Driven High-Throughput Calculations and Machine Learning Models for Materials Design*, 377–395 (Springer International Publishing, Cham, 2020).
13. Gonze, X. *et al.* The Abinit project: Impact, environment and recent developments. *Comput. Phys. Commun.* **248**, 107042, DOI: 10.1016/j.cpc.2019.107042 (2020).
14. Jain, A. *et al.* Commentary: The Materials Project: A materials genome approach to accelerating materials innovation. *APL Mater.* **1**, 011002, DOI: 10.1063/1.4812323 (2013).
15. Landis, D. D. *et al.* The Computational Materials Repository. *Comput. Sci. & Eng.* **14**, 51–57, DOI: 10.1109/MCSE.2012.16 (2012).
16. Kirklin, S. *et al.* The open quantum materials database (oqmd): assessing the accuracy of dft formation energies. *npj Comput. Mater.* **1**, 15010, DOI: 10.1038/npjcompumats.2015.10 (2015).
17. Merkys, A. *et al.* A posteriori metadata from automated provenance tracking: Integration of AiiDA and TCOD. *J. Cheminformatics* **9**, 56, DOI: 10.1186/s13321-017-0242-y (2017). 1706.08704v3.
18. Stevanović, V., Lany, S., Zhang, X. & Zunger, A. Correcting density functional theory for accurate predictions of compound enthalpies of formation: Fitted elemental-phase reference energies. *Phys. Rev. B* **85**, 115104, DOI: 10.1103/PhysRevB.85.115104 (2012).
19. Talirz, L. *et al.* Materials cloud, a platform for open computational science. *Sci. Data* **7**, DOI: 10.1038/s41597-020-00637-5 (2020).
20. Draxl, C. & Scheffler, M. Nomad: The fair concept for big data-driven materials science. *MRS Bull.* **43**, 676–682, DOI: 10.1557/mrs.2018.208 (2018).
21. Curtarolo, S. *et al.* Aflowlib.org: A distributed materials properties repository from high-throughput ab initio calculations. *Comput. Mater. Sci.* **58**, 227–235, DOI: https://doi.org/10.1016/j.commatsci.2012.02.002 (2012).
22. Wilkinson, M. D. *et al.* The FAIR guiding principles for scientific data management and stewardship. *Sci. Data* **3**, DOI: 10.1038/sdata.2016.18 (2016).
23. Andersen, C. W. *et al.* OPTIMADE, an API for exchanging materials data. *Sci. Data* **8**, DOI: 10.1038/s41597-021-00974-z (2021).

24. IEEE Standard for System, Software, and Hardware Verification and Validation. *IEEE Std 1012-2016 (Revision IEEE Std 1012-2012/ Incorporates IEEE Std 1012-2016/Cor1-2017)* 1–260, DOI: 10.1109/IEEESTD.2017.8055462 (2017).

25. Wang, A. *et al.* A framework for quantifying uncertainty in dft energy corrections. *Sci. Reports* **11**, 15496, DOI: 10.1038/s41598-021-94550-5 (2021).

26. Carbogno, C. *et al.* Numerical quality control for dft-based materials databases. *npj Comput. Mater.* **8**, 69, DOI: 10.1038/s41524-022-00744-4 (2022).

27. Poncé, S. *et al.* Verification of first-principles codes: Comparison of total energies, phonon frequencies, electron–phonon coupling and zero-point motion correction to the gap between abinit and qe/yambo. *Comput. Mater. Sci.* **83**, 341–348, DOI: https://doi.org/10.1016/j.commatsci.2013.11.031 (2014).

28. Pople, J. Nobel Lecture. NobelPrize.org, https://www.nobelprize.org/prizes/chemistry/1998/pople/lecture/.

29. Lejaeghere, K. *et al.* Reproducibility in density functional theory calculations of solids. *Science* **351**, aad3000, DOI: 10.1126/science.aad3000 (2016).

30. 71-crystal benchmark results from ref. 29 plus data collected later on, https://molmod.ugent.be/deltacodesdft.

31. The FLEUR project. https://www.flapw.de/.

32. Wortmann, D. *et al.* Fleur. Zenodo, DOI: 10.5281/zenodo.7576163 (2023).

33. Blaha, P. *et al.* Wien2k: An augmented plane wave plus local orbitals program for calculating crystal properties. http://www.wien2k.at/.

34. Blaha, P. *et al.* Wien2k: An apw+lo program for calculating the properties of solids. *J. Chem. Phys.* **152**, 074101, DOI: 10.1063/1.5143061 (2020).

35. Uhrin, M., Huber, S. P., Yu, J., Marzari, N. & Pizzi, G. Workflows in AiiDA: Engineering a high-throughput, event-based engine for robust and modular computational workflows. *Comput. Mater. Sci.* **187**, 110086, DOI: 10.1016/j.commatsci.2020.110086 (2021).

36. Huber, S. P. *et al.* Common workflows for computing material properties using different quantum engines. *npj Comput. Mater.* **7**, 136, DOI: 10.1038/s41524-021-00594-6 (2021).

37. Huber, S. P. *et al.* AiiDA common workflows (ACWF) package (2021). https://github.com/aiidateam/aiida-common-workflows.

38. Lejaeghere, K., Speybroeck, V. V., Oost, G. V. & Cottenier, S. Error Estimates for Solid-State Density-Functional Theory Predictions: An Overview by Means of the Ground-State Elemental Crystals. *Critical Rev. Solid State Mater. Sci.* **39**, 1–24, DOI: 10.1080/10408436.2013.772503 (2013).

39. Grosso, G. & Pastori Parravicini, G. *Solid State Physics* (Academic Press, Amsterdam, 2013), second edn.

40. Martin, R. M. *Electronic Structure: Basic Theory and Practical Methods* (Cambridge University Press, Cambridge, 2013), second edn.

41. Cohen, M. L. & Louie, S. G. *Fundamentals of Condensed Matter Physics* (Cambridge University Press, Cambridge, 2016).

42. Gonze, X. *et al.* Recent developments in the ABINIT software package. *Comput. Phys. Commun.* **205**, 106–131, DOI: 10.1016/j.cpc.2016.04.003 (2016).

43. Romero, A. H. *et al.* ABINIT: Overview and focus on selected capabilities. *The J. Chem. Phys.* **152**, 124102, DOI: 10.1063/1.5144261 (2020).

44. Ratcliff, L. E. *et al.* Flexibilities of wavelets as a computational basis set for large-scale electronic structure calculations. *The J. Chem. Phys.* **152**, 194110, DOI: 10.1063/5.0004792 (2020).

45. Clark, S. J. *et al.* First principles methods using CASTEP. *Zeitschrift für Kristallographie - Cryst. Mater.* **220**, DOI: 10.1524/zkri.220.5.567.65075 (2005).

46. The CP2K simulation package. https://www.cp2k.org.

47. Kühne, T. D. *et al.* CP2k: An electronic structure and molecular dynamics software package - quickstep: Efficient and accurate electronic structure calculations. *The J. Chem. Phys.* **152**, 194103, DOI: 10.1063/5.0007045 (2020).

48. Mortensen, J. J., Hansen, L. B. & Jacobsen, K. W. Real-space grid implementation of the projector augmented wave method. *Phys. Rev. B* **71**, 035109, DOI: 10.1103/PhysRevB.71.035109 (2005).

49. Enkovaara, J. *et al.* Electronic structure calculations with GPAW: a real-space implementation of the projector augmented-wave method. *J. Physics: Condens. Matter* **22**, 253202 (2010).

50. Giannozzi, P. *et al.* QUANTUM ESPRESSO: a modular and open-source software project for quantum simulations of materials. *J. Physics: Condens. Matter* **21**, 395502, DOI: 10.1088/0953-8984/21/39/395502 (2009).

51. Giannozzi, P. *et al.* Advanced capabilities for materials modelling with quantum ESPRESSO. *J. Physics: Condens. Matter* **29**, 465901, DOI: 10.1088/1361-648x/aa8f79 (2017).

52. Soler, J. M. *et al.* The SIESTA method for ab initio order-N materials simulation. *J. Physics: Condens. Matter* **14**, 2745–2779, DOI: 10.1088/0953-8984/14/11/302 (2002).

53. García, A. *et al.* Siesta: Recent developments and applications. *The J. Chem. Phys.* **152**, 204108, DOI: 10.1063/5.0005077 (2020).

54. The SIRIUS domain-specific library for electronic-structure calculations. https://github.com/electronic-structure/SIRIUS.

55. Kresse, G. & Furthmüller, J. Efficient iterative schemes for ab initio total-energy calculations using a plane-wave basis set. *Phys. Rev. B* **54**, 11169–11186, DOI: 10.1103/physrevb.54.11169 (1996).

56. Kresse, G. & Joubert, D. From ultrasoft pseudopotentials to the projector augmented-wave method. *Phys. Rev. B* **59**, 1758–1775, DOI: 10.1103/physrevb.59.1758 (1999).

57. Perdew, J. P., Burke, K. & Ernzerhof, M. Generalized gradient approximation made simple. *Phys. Rev. Lett.* **77**, 3865–3868, DOI: 10.1103/physrevlett.77.3865 (1996).

58. Vanpoucke, D. E. P., Bultinck, P. & Van Driessche, I. Extending Hirshfeld-I to bulk and periodic materials. *J. Comput. Chem.* **34**, 405–417, DOI: 10.1002/jcc.23088 (2013).

59. Vanpoucke, D. E. P., Van Driessche, I. & Bultinck, P. Reply to 'Comment on "Extending Hirshfeld-I to bulk and periodic materials" '. *J. Comput. Chem.* **34**, 422–427, DOI: 10.1002/jcc.23193 (2013).

60. Bultinck, P., Van Alsenoy, C., Ayers, P. W. & Carbó-Dorca, R. Critical analysis and extension of the hirshfeld atoms in molecules. *J. Chem. Phys.* **126**, 144111, DOI: 10.1063/1.2715563 (2007).

61. Birch, F. Finite elastic strain of cubic crystals. *Phys. Rev.* **71**, 809–824, DOI: 10.1103/PhysRev.71.809 (1947).

62. Bosoni, E. *et al.* How to verify the precision of density-functional-theory implementations via reproducible and universal workflows. *Mater. Cloud Arch.* DOI: https://doi.org/10.24435/materialscloud:s4-3h (2023). https://doi.org/10.24435/materialscloud:s4-3h.

63. Jollet, F., Torrent, M. & Holzwarth, N. Generation of projector augmented-wave atomic data: A 71 element validated table in the XML format. *Comput. Phys. Commun.* **185**, 1246–1254, DOI: 10.1016/j.cpc.2013.12.023 (2014).

64. Glantz, S. A., Slinker, B. K. & Neilands, T. B. *Selecting the "Best" Regression Model, in Primer of Applied Regression and Analysis of Variance, third edition* (McGraw-Hill Education, New York, 2017).

65. Marzari, N., Vanderbilt, D., De Vita, A. & Payne, M. C. Thermal Contraction and Disordering of the Al(110) Surface. *Phys. Rev. Lett.* **82**, 3296–3299, DOI: 10.1103/PhysRevLett.82.3296 (1999).

66. dos Santos, F. J. & Marzari, N. Fermi energy determination for advanced smearing techniques. *arXiv* **2212.07988**, DOI: 10.48550/ARXIV.2212.07988 (2022).

67. Gillan, M. J. Calculation of the vacancy formation energy in aluminium. *J. Phys.. Cond. Matter* **1**, 689, DOI: 10.1088/0953-8984/1/4/005 (1989).

68. van Setten, M. *et al.* The PseudoDojo: Training and grading a 85 element optimized norm-conserving pseudopotential table. *Comput. Phys. Commun.* **226**, 39–54, DOI: 10.1016/j.cpc.2018.01.012 (2018).

69. The PseudoDojo website. http://www.pseudo-dojo.org/.

70. Hartwigsen, C., Goedecker, S. & Hutter, J. Relativistic separable dual-space Gaussian pseudopotentials from H to Rn. *Phys. Rev. B* **58**, 3641–3662, DOI: 10.1103/PhysRevB.58.3641 (1998).

71. Goedecker, S., Teter, M. & Hutter, J. Separable dual-space Gaussian pseudopotentials. *Phys. Rev. B* **54**, 1703 (1996).

72. Krack, M. Pseudopotentials for H to Kr optimized for gradient-corrected exchange-correlation functionals. *Theor. Chem. Accounts* **114**, 145–152 (2005).

73. VandeVondele, J. & Hutter, J. Gaussian basis sets for accurate calculations on molecular systems in gas and condensed phases. *The J. chemical physics* **127**, 114105 (2007).

74. GPAW atomic PAW setups. https://wiki.fysik.dtu.dk/gpaw/setups/setups.html#atomic-paw-setups.

75. Prandini, G., Marrazzo, A., Castelli, I. E., Mounet, N. & Marzari, N. Precision and efficiency in solid-state pseudopotential calculations. *npj Comput. Mater.* **4**, DOI: 10.1038/s41524-018-0127-2 (2018).

76. Prandini, G. *et al.* A standard solid state pseudopotentials (sssp) library optimized for precision and efficiency. *Mater. Cloud Arch.* **2023.65** (2022). Version v11, https://doi.org/10.24435/materialscloud:f3-ym.

77. García, A., Verstraete, M. J., Pouillon, Y. n. & Junquera, J. The psml format and library for norm-conserving pseudopotential data curation and interoperability. *Comput. Phys. Commun.* **227**, 51 – 71, DOI: https://doi.org/10.1016/j.cpc.2018.02.011 (2018).

78. Topsakal, M. & Wentzcovitch, R. Accurate projected augmented wave (paw) datasets for rare-earth elements (re=la–lu). *Comput. Mater. Sci.* **95**, 263–270, DOI: https://doi.org/10.1016/j.commatsci.2014.07.030 (2014).

79. Prandini, G. *et al.* A standard solid state pseudopotentials (sssp) library optimized for precision and efficiency. *Mater. Cloud Arch.* **2021.76** (2021). Version v7, https://doi.org/10.24435/materialscloud:rz-77.

80. Prandini, G. *et al.* A standard solid state pseudopotentials (sssp) library optimized for precision and efficiency. *Mater. Cloud Arch.* **2022.159** (2022). Version v8, https://doi.org/10.24435/materialscloud:3v-xt.

81. Sachs, M. *et al.* Dft-guided crystal structure redetermination and lattice dynamics of the intermetallic actinoid compound uir. *Inorg. Chem.* **60**, 16686–16699 (2021).

82. Dal Corso, A. Pseudopotentials periodic table: From H to Pu. *Comput. Mater. Sci.* **95**, 337–350 (2014).

83. Thörnig, P. JURECA: Data Centric and Booster Modules implementing the Modular Supercomputing Architecture at Jülich Supercomputing Centre. *J. large-scale research facilities JLSRF* **7**, 182, DOI: 10.17815/jlsrf-7-182 (2021).

Acknowledgments

This work was inspired and is supported in part by the European Union's Horizon 2020 research and innovation programme under grant agreement No. 676598 and grant agreement No. 824143 (European MaX Centre of Excellence "Materials design at the Exascale") and by NCCR MARVEL, a National Centre of Competence in Research, funded by the Swiss National Science Foundation (grant number 205602). For the purpose of Open Access, a CC BY public copyright licence is applied to any Author Accepted Manuscript (AAM) version arising from this submission.

We acknowledge Flaviano José dos Santos for useful discussions on the analysis of the smearing types and k-point convergence, and Xavier Gonze, Marc Torrent, and François Jollet for useful discussions on PAW pseudopotentials.

M.F. and N.M. acknowledge the contribution of Sadasivan Shankar in early discussions about the use of 6 prototype oxides as general platform to explore the transferability of pseudopotentials.

Work at ICMAB (E.B., A.G., V.D.) is supported by the Severo Ochoa Centers of Excellence Program (MCIN CEX2019-000917-S), by grant PGC2018-096955-B-C44 of MCIN/AEI/10.13039/501100011033, "ERDF A way of making Europe", and by GenCat 2017SGR1506. We also thank the Barcelona Supercomputer Center for computational resources. V.D. acknowledges support from DOC-FAM, European Union's Horizon 2020 research and innovation programme under the Marie Sklodowska-Curie grant agreement No 754397.

O.R. acknowledges travel support from WIEN2k (Technical University of Vienna).

The Jülich team (S.B., J.B., H.J., G.M., D.W) acknowledges support by the Joint Lab Virtual Materials Design (JL-VMD) of the Forschungszentrum Jülich, the Helmholtz Platform for Research Software Engineering - Preparatory Study (HIRSE_PS), the Joint Virtual Laboratory AI, Data Analytics and Scalable Simulation (AIDAS) of the Forschungszentrum Jülich and the French Alternative Energies and Atomic Energy Commission, and we gratefully acknowledge the computing time granted through JARA on the supercomputers JURECA[83] at Forschungszentrum Jülich and CLAIX at RWTH Aachen University.

H.M and T.D.K (University of Paderborn) gratefully acknowledge the Gauss Centre for Supercomputing e.V. (www.gauss-centre.eu) for funding this project by providing computing time on the GCS Supercomputer JUWELS at Jülich Supercomputing Centre (JSC).

S.P. and G.-M.R. (Université catholique de Louvain) acknowledge support from the F.R.S.-FNRS. Computational resources have been provided by the PRACE-21 resources MareNostrum at BSC-CNS and by the Consortium des Équipements de Calcul Intensif (CÉCI), funded by the Fonds de la Recherche Scientifique de Belgique (F.R.S.-FNRS) under Grant No. 2.5020.11 and by the Walloon Region as well as computational resources awarded on the Belgian share of the EuroHPC LUMI supercomputer.

G.Ka. and S.V. received funding from the VILLUM Centre for the Science of Sustainable Fuels and Chemicals (9455) from VILLUM FONDEN. Computational resources were provided by the Niflheim supercomputing cluster at the Technical University of Denmark (DTU). They also thank Jens Jørgen Mortensen and Ask H. Larsen for the valuable discussions on optimizing the workflow for the GPAW code.

S.C. acknowledges financial support from OCAS NV by an OCAS-endowed chair at Ghent University. The computational resources and services used at Ghent University were provided the VSC (Flemish Supercomputer Center), funded by the Research Foundation Flanders (FWO) and the Flemish Government – department EWI.

M.W. gratefully acknowledges computational resources provided by the Vienna Scientific Cluster (VSC). This research was funded in part by the Austrian Science Fund (FWF) [P 32711].

E.F.L. would like to acknowledge resources provided by Sigma2 - the National Infrastructure for High Performance Computing and Data Storage in Norway and support from the Norwegian Research Infrastructure Services (NRIS).

B.Z. is grateful to the UK Materials and Molecular Modelling Hub for computational resources, which is partially funded by EPSRC (EP/P020194/1 and EP/T022213/1) and acknowledge the use of the UCL Myriad and Kathleen High Performance Computing Facility (Myriad@UCL, Kathleen@UCL), and associated support services, in the completion of this work.

N.M., G.Pi., and A.G. acknowledge support from the European Union's Horizon 2020 research and innovation programme under grant agreement No. 957189 (BIG-MAP), also part of the BATTERY 2030+ initiative under grant agreement No. 957213.

G.P., J.Y. and G.-M.R. acknowledge support by the Swiss National Science Foundation (SNSF) and by the Fonds de la Recherche Scientifique de Belgique (F.R.S.-FNRS) through the "FISH4DIET" Project (SNSF grant 200021E_206190 and F.R.S.-FNRS grant T.0179.22).

G.P. acknowledges support by the Open Research Data Program of the ETH Board, under the Establish project "PREMISE".

J.Y. acknowledges support from the European Union's Horizon 2020 research and innovation programme under grant agreement No. 760173 (MARKETPLACE).

Author contributions

S.C. and K.L. developed an initial early design of this research topic, and analyzed together with M.C. the first exploratory datasets. M.S. was responsible for job, queue and data management in the first exploratory phase. E.B. and G.Pi. contributed the idea to use the AiiDA and `aiida-common-workflow` infrastructure to carry on the thousands of DFT simulations required by the project. E.B. and G.Pi. coordinated the whole project.

M.F. and N.M. devised the protocol of using six oxides to test pseudopotentials across different coordinations and chemistries. P.B., G.M., and O.R. performed the iterative refinement of the input parameters for the AE calculations, that ultimately resulted in the generation of the central volumes of our dataset. O.R. proposed the ε metric. N.M. proposed the ν metric. S.P. raised the issue of the smearing selection, that ultimately led to the decision of a fixed k-point integration mesh and smearing broadening. K.E. contributed to the data analysis and the conversion of the data into a dynamic website. D.E.P.V. contributed the Hirshfeld-I calculated charges and their analysis. E.B., M.W. and G.Pi. performed the analysis of the error propagation in the fit and the estimation of the parameters of the ν metric. E.B., S.C., O.R., and G.Pi. analyzed in detail the dependency and sensitivity of the metrics Δ, ε and ν.

A.Z. and S.P. developed the ABINIT implementation of the common workflow which relies on the `aiida-abinit` plugin developed and maintained by A.Z., G.Pe. and S.P. M.G. created new pseudopotentials used for ABINIT and improved the parameter profile. A.Z. and S.P. performed the ABINIT calculations, including verification tests. The work on ABINIT was supervised by G.M.R. and S.P.

L.B., A.D. and L.G. contributed to the BigDFT-related parts of the work. A.D. developed the BigDFT implementation of the common workflows. L.B. and A.D. generated the BigDFT results under the supervision of L.G.

B.Z. developed the CASTEP implementation of the common workflow which relies on the `aiida-castep` plugin which is also maintained by B.Z., and performed all CASTEP simulations. C.J.P. created new on-the-fly generated pseudopotentials using the verification tests performed by B.Z.

M.K., T.D.K., H.M., T.M.A.M. and A.V.Y. contributed to all CP2K-related parts of this work. A.V.Y. implemented the workflows and performed preliminary calculations. The workflows rely on the `aiida-cp2k` plugin developed by A.V.Y., T.M.A.M., and others. M.K. performed preliminary calculations, created new pseudopotentials and contributed to the design of the protocol, T.D.K. contributed to the CP2K setup, discussion of the results and supervised the calculations, H.M. conducted all AiiDA calculations and analyzed the results, T.M.A.M. provided implementations of CP2K input and output parsers.

S.B., J.B., H.J., G.M. and D.W. contributed the FLEUR-related parts of this work[1]. G.M. hereby developed the parameter profile and performed the calculations. J.B. and H.J. adapted and extended the AiiDA-FLEUR plugin and the related parts of the AiiDA common-workflows package. S.B. and D.W. contributed to the analysis and discussion of the FLEUR results.

G.Ka. and S.V. contributed to the GPAW-related parts of the work. S.V. developed the GPAW implementation of the common workflows, which relies on the `aiida-ase` plugin and ran the calculations. G.Ka. and S.V. analyzed the GPAW calculations.

M.B., S.P.H., N.M., J.Y. and G.Pi. contributed to all QUANTUM ESPRESSO-related parts of this work. M.B. and S.P.H. developed the QUANTUM ESPRESSO implementation of the common workflow which relies on the `aiida-quantumespresso` plugin developed and maintained by M.B., S.P.H., G.Pi. and others. J.Y. generated and tested new pseudopotentials used for QUANTUM ESPRESSO. The work on QUANTUM ESPRESSO was supervised by G.Pi. and N.M.

[1] Corresponding contact person for the FLEUR contributions: Gregor Michalicek, g.michalicek@fz-juelich.de

H.M. and T.D.K. contributed to all SIRIUS/CP2K-related parts of this work. The workflows rely on the `aiida-cp2k` plugin developed by A.V.Y., T.M.A.M., and others. H.M. conducted all AiiDA calculations and analyzed the results. T.D.K. contributed to the SIRIUS/CP2K setup, discussion of the results and supervised the calculations.

E.B., V.D. and A.G. contributed to the SIESTA-related parts of the work. E.B. developed the SIESTA implementation of the common workflows, that relies on the `aiida-siesta` plugin developed by E.B., A.G., V.D. and others. E.B. generated the SIESTA results in collaboration with A.G.

M.W., M.M. and E.F.L. performed the execution and analysis of the VASP-related workflows used to generate the data for this work. G.Kr. generated updated potentials for the lanthanides. E.F.L. maintains the VASP implementation of the common workflows project and the `aiida-vasp` plugin (developed by a community of contributors, see full contributor list in the plugin documentation) which is used to execute the VASP calculations.

P.B., G.K.H.M., O.R. and T.R. contributed the WIEN2k-related parts of this work. T.R. performed preliminary calculations, P.B. created the setup of the WIEN2k calculations and supervised and analyzed the results, G.K.H.M. contributed the conversion of AiiDA structures to a WIEN2k struct file, and O.R. developed the `aiida-wien2k` plugin and performed all AiiDA-WIEN2k calculations.

E.B., M.F. and G.Pi. wrote the first version of the manuscript, and all authors contributed to the editing and revision of the manuscript.

Competing interests

G.Pe. and G.-M.R. are shareholders and Directors of Matgenix SRL. G.Kr. is shareholder of the VASP Software GmbH, and M.W. and M.M. are part-time employees of the VASP Software GmbH. C.J.P. is an author of the CASTEP code and receives income from its commercial sales.

Publisher's note

Code availability

The source code of the common workflows is released under the MIT open-source license and is made available on GitHub (https://github.com/aiidateam/aiida-common-workflows). It is also distributed as an installable package through the Python Package Index (https://pypi.org/project/aiida-common-workflows). The source code of the scripts to generate the plots is released under the MIT open-source license and is made available on GitHub (https://github.com/aiidateam/acwf-verification-scripts). All codes to generate the figures of this paper are available in the data entry of Ref. 62.

Data availability

The data and the scripts used to create all the images in this work are available on the Materials Cloud Archive[62]. Note that the data includes the entire AiiDA provenance graph of each workflow execution presented in the main text (including therefore all input files and output files of all simulations, as well as their logical relationship, in AiiDA format), as well as the curated data that is extracted from that database in order to produce the images.

Supplementary information for "How to verify the precision of density-functional-theory implementations via reproducible and universal workflows"

Emanuele Bosoni, Louis Beal, Marnik Bercx, Peter Blaha, Stefan Blügel, Jens Bröder, Martin Callsen, Stefaan Cottenier, Augustin Degomme, Vladimir Dikan, Kristjan Eimre, Espen Flage-Larsen, Marco Fornari, Alberto Garcia, Luigi Genovese, Matteo Giantomassi, Sebastiaan P. Huber, Henning Janssen, Georg Kastlunger, Matthias Krack, Georg Kresse, Thomas D. Kühne, Kurt Lejaeghere, Georg K. H. Madsen, Martijn Marsman, Nicola Marzari, Gregor Michalicek, Hossein Mirhosseini, Tiziano M. A. Müller, Guido Petretto, Chris J. Pickard, Samuel Poncé, Gian-Marco Rignanese, Oleg Rubel, Thomas Ruh, Michael Sluydts, Danny E. P. Vanpoucke, Sudarshan Vijay, Michael Wolloch, Daniel Wortmann, Aliaksandr V. Yakutovich, Jusong Yu, Austin Zadoks, Bonan Zhu, Giovanni Pizzi

S1 Structures under investigation

This section reports some details on the crystal structures used in the verification study. As already explained in the main text, we consider two subsets: the "unaries dataset" and the "oxides dataset".

The "unaries dataset" consists of 4 monoelemental cubic crystals for every element from Z=1 (hydrogen) to Z=96 (curium), in the well-known structures face-centered cubic, body-centered cubic, simple cubic and in the diamond structure. The details of each of the 4 monoelemental cubic crystals are described in Table S1.1, together with the indication of a prototype belonging to each category. A visualization of the crystal structures is reported in SI Fig. S1.1.

Table S1.1. Description of the four unary crystals under investigation, with a prototypical crystalline example and the corresponding ID from the ICSD database[84]. The quantity l is the length of the primitive-cell lattice vectors, a the cubic conventional-cell side, and d_{nn} is the nearest-neighbor distance.

	Prototype (ICSD number)	Space group	Wyckoff site (site symmetry)	Coordination number	l	d_{nn}
FCC	Al (43423)	$Fm\bar{3}m$ (225)	4a ($m\bar{3}m$)	12	$a/\sqrt{2}$	$a/\sqrt{2}$
BCC	V (43420)	$Im\bar{3}m$ (229)	2a ($m\bar{3}m$)	8	$\sqrt{3}a/2$	$\sqrt{3}a/2$
SC	$\alpha-$Po (43211)	$Pm\bar{3}m$ (221)	1a ($m\bar{3}m$)	6	a	a
Diamond	C (diamond) (28857)	$Fd\bar{3}m$ (227)	8a ($\bar{4}3m$)	4	$a/\sqrt{2}$	$\sqrt{3}a/4$

The "oxides dataset" is composed by six cubic oxides with chemical formula X_2O, XO, X_2O_3, XO_2, X_2O_5 and XO_3, where X goes also in this case from hydrogen to curium. The details of each of these structures are reported in Table S1.2, that also includes the formal oxidation number that is expected for X in the structure (we stress that the actual oxidation state is different from the formal charge, see SI Sec. S2). A visualization of the crystal structures is reported in SI Fig. S1.2.

For every material, the primitive cell is provided as input of the verification study (except when X is oxygen; in this case, the same cell is used as for all other oxides where X is different from oxygen, even if in the case of oxygen some of these cells might not be the smallest primitive cell, due to the increased symmetry). However, some codes might prefer to perform the actual calculation of the EOS on the cubic conventional cell, or use the actual primitive cell in the case of X = oxygen. The actual number of atoms in the simulation is reported inside the JSON files with the results of this verification study, available in Ref. 62.

In the following, we will often refer to quantities (energy, volume, etc.) per formula unit. To avoid ambiguity, we explicitly list here the number of atoms in the formula unit for each of our 10 prototypes: FCC (1), BCC(1), SC(1), Diamond (2), X_2O (3), XO (2), X_2O_3 (5), XO_2 (3), X_2O_5 (7), XO_3 (4). We highlight that these numbers also correspond to the number of atoms in the primitive cell, except for X_2O_3 and X_2O_5 that have 10 and 14 atoms in the primitive cell, respectively.

Finally, we report the central volumes for all 960 structures used for the calculation of the EOS data in SI Table S1.3. In order to compare results, the same central volumes (and the same volume range of $\pm 6\%$, with 7 points) should be used when generating additional datasets. To visualize the data, we report in SI Fig. S1.3 the distance of the X atom from its closest (oxygen) neighbor, across the whole periodic table and for the 10 prototypes.

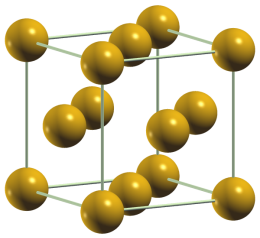

(a) FCC crystal (conventional cell).

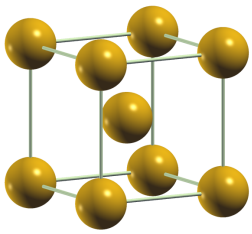

(b) BCC crystal (conventional cell).

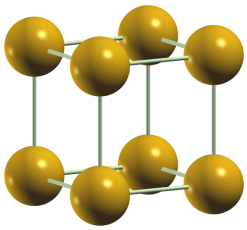

(c) SC crystal (conventional cell).

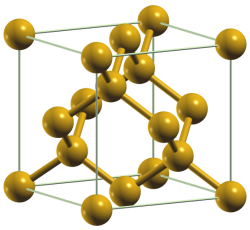

(d) Diamond crystal (conventional cell).

Figure S1.1. Conventional cells of the 4 unary prototypes used in this work. Images generated using XCrysDen[85].

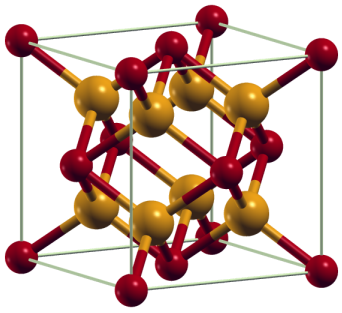

(a) X_2O crystal (conventional cell).

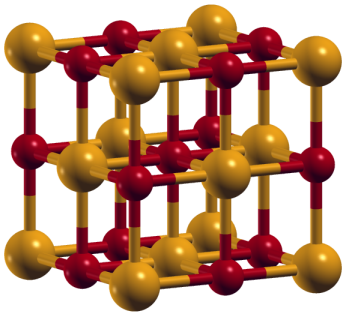

(b) XO crystal (conventional cell).

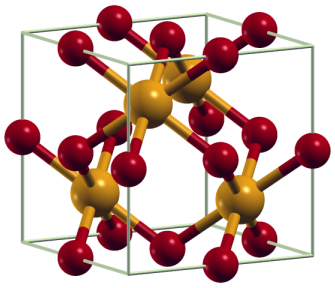

(c) X_2O_3 crystal (conventional cell).

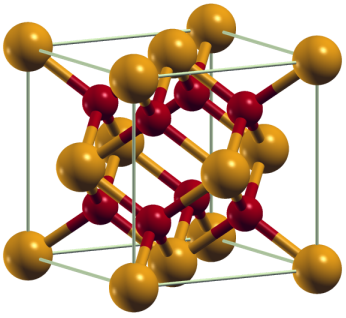

(d) XO_2 crystal (conventional cell).

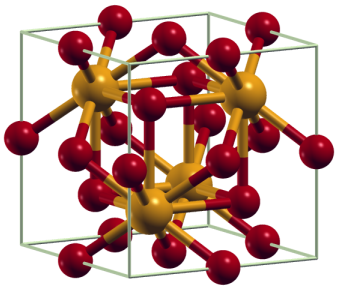

(e) X_2O_5 crystal (conventional cell).

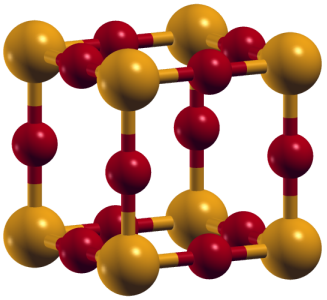

(f) XO_3 crystal (conventional cell).

Figure S1.2. Conventional cells of the 6 oxide prototypes used in this work. Oxygen atoms are represented as red atoms, while X atoms as gold atoms. Images generated using XCrysDen[85].

Table S1.2. Description of the crystal structure of the six cubic oxides, with a prototypical crystalline example and the corresponding ID from the ICSD database[84]. The quantity l is the length of the primitive-cell lattice vectors, a the cubic conventional-cell side, and d_{nn} is the distance of the X atom to its nearest-neighbor (oxygen) atom.

	Formal oxidation of X	Prototype (ICSD number)	Space group	Wyckoff site site symmetry of X	Coordination of X	l	d_{nn}
X_2O	+1	Na_2O (60435)	$Fm\bar{3}m$ (225)	X=8c, O=4a -43m	4	$a/\sqrt{2}$	$a\sqrt{3}/4$
XO	+2	NaCl (18189)	$Fm\bar{3}m$ (225)	X=4a, O=4b m-3m	6	$a/\sqrt{2}$	$a/2$
X_2O_3	+3	Ag_2O_3 (15999)	$Pn\bar{3}m$ (224)	X=4b, O=6d -3m	6	a	$a\sqrt{3}/4$
XO_2	+4	ZrO_2 (105553)	$Fm\bar{3}m$ (225)	X=4a, O=8c m-3m	8	$a/\sqrt{2}$	$a\sqrt{3}/4$
X_2O_5	+5	—	$Pn\bar{3}m$ (224)	X=4b, O=4c+6d -3m	6	a	$a\sqrt{3}/4$
XO_3	+6	ReO_3 (647352)	$Pm\bar{3}m$ (221)	X=1a, O=3d m-3m	6	a	$a/2$

Table S1.3. Table with the central volumes used for the calculation of the EOS datapoints. Volumes are expressed in Å^3 per formula unit (see definition of the formula unit in SI Sec. S1). The reference structures having these central volumes are available in Ref. 62.

	FCC	BCC	SC	Diamond	X_2O	X_2O_5	XO_2	X_2O_3	XO	XO_3
H	2.96383	2.96392	3.08364	6.84867	11.96463	51.67201	19.10477	30.91989	10.02535	31.07589
He	17.83621	18.12465	21.38414	64.32268	92.12727	56.39662	24.77499	47.12856	31.51877	43.04663
Li	20.21287	20.26593	20.40472	51.36159	24.72203	61.84374	24.92385	44.77362	16.82806	46.06591
Be	7.87403	7.81517	10.26455	29.37901	26.83653	57.32171	22.18348	38.79261	12.12488	39.00478
B	5.89415	6.14152	6.6991	16.62498	30.02954	54.37317	20.37072	35.98325	14.71073	33.62805
C	7.31505	6.69648	5.60717	11.39533	28.55083	58.60995	22.75464	42.26604	15.70062	32.91818
N	7.60577	7.23569	6.48497	18.35414	26.67062	57.22806	25.50994	45.6704	15.3358	39.68942
O	8.00192	7.7972	7.94802	21.36412	27.11225	57.93205	27.11223	47.87245	15.90618	44.79083
F	10.14406	10.08192	10.52097	29.004	30.96209	60.78463	30.83431	56.31851	18.85462	53.30451
Ne	24.26591	24.70382	29.68755	89.0995	95.7889	69.51806	38.90827	81.94501	47.11781	80.77935
Na	37.10691	36.99607	39.7588	108.85725	43.71875	74.35023	36.67184	70.84884	27.7619	82.17703
Mg	23.11539	22.93116	27.59134	80.79618	44.83726	69.448	30.59043	56.77165	19.2497	62.13962
Al	16.48998	16.92508	20.17082	55.21453	46.20985	63.07075	26.30127	49.23828	22.4582	49.74088
Si	14.4803	14.66715	16.23082	40.92143	42.69026	61.00716	24.05335	48.82219	24.59467	41.777
P	14.58744	14.29218	14.60552	41.27791	40.01409	65.27141	27.20059	56.43141	24.30168	37.00066
S	15.88301	15.73711	17.19755	48.58823	42.6917	67.07762	29.73936	58.62747	24.68481	39.1327
Cl	21.29569	21.46346	23.45819	67.51736	54.55214	75.16606	34.69697	67.62641	26.95723	52.00364
Ar	52.33201	53.50562	65.51497	198.12738	113.32949	92.69732	51.32183	103.20479	39.41786	68.32473
K	73.99534	73.80511	79.47128	224.24589	68.00111	99.39122	58.36793	113.79592	42.74207	136.60539
Ca	42.20189	42.15587	43.70466	160.093	56.09468	84.42406	42.31153	79.93599	28.18987	94.27512
Sc	24.6858	24.88426	26.11875	68.84236	43.1186	71.37218	32.98765	62.21668	22.3317	70.50445
Ti	17.39633	17.26807	18.40137	45.88764	36.3163	63.72954	28.1791	54.26031	19.61645	57.35797
V	13.9076	13.46008	14.68791	37.2808	32.71378	59.96306	26.57435	50.7807	18.31774	50.25823
Cr	11.89373	11.55544	12.80026	33.09544	30.44097	58.12757	25.42189	48.27373	17.6635	46.89194
Mn	10.75345	10.78666	11.9053	30.35903	29.56957	57.65839	24.64946	46.45968	17.2926	45.62581
Fe	10.26671	10.50643	11.65681	28.93599	29.39392	58.00272	24.1901	45.43045	17.13572	45.9389
Co	10.31329	10.54766	11.90016	29.77725	29.83543	58.94975	25.03188	45.30703	17.27042	47.13241
Ni	10.83846	10.90046	12.56525	33.01991	31.63922	60.71118	26.20001	47.99648	17.99342	49.20696
Cu	11.96066	12.00521	13.9456	38.3573	34.5396	64.24158	28.23319	51.90164	19.10594	52.00277
Zn	15.15266	15.35236	18.21695	49.37022	40.67075	68.51634	30.3891	56.63194	20.27908	56.55698
Ga	18.89945	19.1961	20.12767	50.86204	53.04849	67.83879	29.26061	55.49587	24.35231	57.48398
Ge	19.61105	19.26408	19.92661	47.84474	49.67078	69.75991	28.19282	60.60137	27.12181	51.09293
As	19.25156	19.06952	20.35448	57.08944	47.81491	72.02994	31.50589	65.30072	27.1941	47.3416
Se	20.38999	20.33796	22.67444	63.49704	49.91744	71.9333	33.07453	66.14337	28.35245	49.87193
Br	26.41028	26.78091	29.81278	86.15579	61.62718	77.98233	37.01169	73.66672	31.10869	58.2754
Kr	66.18624	67.66229	82.81744	250.49559	118.94061	96.19024	47.53319	97.16926	40.08181	67.9248
Rb	91.38789	91.27765	99.14298	283.10731	81.07467	114.34806	69.0703	134.5233	48.78267	109.64128

Table S1.3. (continued) Table with the central volumes used for the calculation of the EOS datapoints. Volumes are expressed in $Å^3$ per formula unit (see definition of the formula unit in SI Sec. S1). The reference structures having these central volumes are available in Ref. 62.

	FCC	BCC	SC	Diamond	X_2O	X_2O_5	XO_2	X_2O_3	XO	XO_3
Sr	54.91091	54.05117	57.38684	224.08214	70.15512	97.78005	51.29072	97.64817	35.05586	113.81785
Y	32.47792	33.03014	34.81815	87.6147	56.02664	82.48242	40.19378	76.25924	28.0575	88.92292
Zr	23.22672	22.85337	24.67007	61.95106	48.0859	71.98006	33.4764	65.13987	24.28322	72.31405
Nb	18.76368	18.12949	20.16049	51.64695	43.28804	65.77641	31.24816	60.07849	22.37503	61.62135
Mo	16.04515	15.79339	17.60535	46.04579	39.71891	62.89519	29.7259	56.76111	21.51546	55.61563
Tc	14.50906	14.62353	16.24577	42.51631	38.36272	62.29306	28.72035	54.60343	21.21284	53.12124
Ru	13.84099	14.24038	15.84808	40.6141	37.88283	63.27681	28.19283	53.64005	21.40643	52.5239
Rh	14.05529	14.47873	16.32474	41.91926	38.86199	65.4046	29.59307	54.41932	22.00732	54.2774
Pd	15.31609	15.44184	17.88203	49.04068	42.21056	68.95044	31.39346	59.01692	23.3105	58.57564
Ag	17.83932	18.00008	20.82095	60.08343	48.38454	74.95147	34.38486	65.63846	25.51029	65.19006
Cd	22.85103	23.39168	26.91335	74.58927	53.08317	80.62228	38.5362	73.25114	27.09207	73.17106
In	27.48501	27.76645	29.54359	76.27387	65.89698	78.42019	36.47078	70.18826	30.50678	74.75339
Sn	27.92759	27.62156	29.43402	73.68474	63.45403	76.77808	34.0064	72.49854	33.52195	67.66217
Sb	27.49335	27.16815	29.94869	85.55535	61.56831	78.86722	37.56726	78.6904	33.62451	60.24063
Te	28.31403	28.53875	32.78185	92.82855	62.89378	79.75651	39.06131	78.71778	34.89162	56.91725
I	35.12009	35.98158	41.54866	121.14185	72.20499	81.49821	41.44808	83.86273	38.00947	60.84655
Xe	87.15115	89.27395	109.89372	332.24175	137.22109	91.77459	47.37046	98.94124	45.25347	66.83409
Cs	117.71338	116.59594	128.22933	377.80616	96.47952	122.11939	63.56002	141.69282	53.27331	76.18877
Ba	64.22484	63.32039	61.52071	113.27682	79.80533	113.54449	60.31047	116.85012	43.27865	91.66471
La	36.95535	37.81167	37.01799	74.70356	65.16399	94.98527	47.88165	91.26986	34.42877	90.59307
Ce	26.53359	27.2707	24.80597	60.39358	56.09746	84.04452	40.7946	82.12996	31.03708	81.66735
Pr	24.09713	23.11993	20.26124	52.47588	52.30443	80.56703	39.81497	79.99604	30.07713	76.65652
Nd	22.76384	20.98371	18.16723	47.14628	50.5552	79.71193	39.09564	78.63461	29.46021	72.64543
Pm	22.24361	20.2416	17.37482	43.35196	49.83014	79.14646	38.53757	77.59916	29.02086	71.71784
Sm	22.8249	21.62656	17.16717	41.84622	49.72505	78.72225	38.07924	76.77967	28.71252	71.28495
Eu	24.97468	26.1259	17.68798	41.41038	49.99783	78.37384	37.68823	76.15461	28.5026	71.08958
Gd	27.96256	28.92878	20.74434	41.94188	50.44511	78.06943	37.3575	75.49738	28.36053	71.10647
Tb	30.53338	30.8832	27.62122	43.44373	51.03094	77.80866	37.10079	74.83874	28.25829	71.34317
Dy	32.47158	32.24109	31.62626	46.07452	51.787	77.66792	36.94349	74.27473	28.174	71.78804
Ho	33.88587	33.24726	34.02416	50.89551	52.71344	77.74286	36.8788	73.8801	28.09541	72.37003
Er	34.81162	33.9149	35.72581	160.65962	53.80493	78.00809	36.90264	73.68319	28.02352	73.17841
Tm	35.32142	34.35289	36.91694	163.2943	55.1443	78.45266	37.02748	73.68387	27.97309	74.23839
Yb	35.68954	34.45601	38.29539	164.06073	57.46052	79.24563	37.29979	73.91316	27.99156	75.71634
Lu	28.96169	29.57967	32.89043	101.18911	54.06305	78.94317	37.2627	72.22017	26.55736	78.07351
Hf	22.56668	22.30091	24.73374	70.20567	48.64474	71.33364	33.12187	64.18594	24.23282	70.82176
Ta	18.83578	18.29148	20.70598	56.84159	45.0229	65.63914	31.39846	59.96546	22.85916	61.7502
W	16.45344	16.14682	18.44138	49.57763	41.78609	62.77976	30.14777	57.13456	22.23519	56.04598
Re	15.0181	15.10498	17.14394	45.16071	40.19475	62.23732	29.3041	55.34484	22.11252	53.81481
Os	14.34475	14.78799	16.73456	42.93	39.57612	63.20103	28.80205	54.71102	22.54512	53.11224
Ir	14.51798	15.07236	17.01051	43.22586	40.36403	65.48808	30.42919	55.53976	23.42604	53.88197
Pt	15.65559	15.8485	18.10254	48.25544	43.22013	69.26345	32.29065	60.62094	24.64978	57.336
Au	17.96337	18.01979	20.75903	58.53091	49.44229	75.17109	35.00364	67.13364	26.87643	63.90256
Hg	32.36324	29.07647	30.07776	113.00826	56.10435	83.26519	39.30435	76.32712	29.80446	72.55805
Tl	31.19774	31.4643	34.37303	90.43011	72.24321	86.01923	40.72926	79.68706	33.96315	79.0134
Pb	32.13111	31.99849	34.45976	88.02959	70.3268	88.26763	39.60503	86.34487	36.51455	79.29789
Bi	31.77084	31.66197	35.18324	97.08873	69.26622	89.00017	42.09222	87.47546	36.02854	74.10038
Po	32.54441	32.88941	37.58851	104.9496	70.35802	85.35526	41.79777	84.65548	37.34068	70.91823
At	39.02559	39.94292	46.15152	133.91052	77.8056	84.55797	43.85025	88.77385	40.78895	71.68554
Rn	93.1132	95.57693	117.94773	355.33994	136.67664	91.11763	48.68438	101.57056	47.53838	72.06566
Fr	117.20593	116.47957	132.25863	384.39398	106.69693	114.96558	58.91507	131.0799	55.38287	79.53102
Ra	71.59113	70.96816	75.36362	339.34601	93.80196	121.53488	63.85	126.55639	47.84186	87.62984
Ac	45.55131	45.9684	50.16201	129.36355	80.39637	103.88226	52.95356	101.65853	38.99538	91.45268
Th	32.20115	32.67168	35.25242	92.51762	68.79224	89.10514	44.32081	87.47888	33.14217	84.96607
Pa	25.30196	24.73132	24.06085	61.37914	56.29059	79.83198	40.64908	78.8075	30.08799	77.67439
U	21.70953	20.2118	19.2531	49.63674	50.133	76.26324	39.02558	75.40504	28.35782	72.23741
Np	19.28905	17.78811	17.25306	42.95581	47.24644	74.80568	38.06636	73.6267	27.33128	70.29134
Pu	17.80178	16.59418	16.41493	40.17108	45.85351	74.2317	37.40308	72.67609	26.8416	68.83836
Am	17.36314	16.20862	16.14903	38.63027	45.41542	74.27276	36.96336	72.29916	26.66371	67.84802
Cm	17.48759	16.44718	16.39497	38.19162	45.8595	74.58951	36.65683	72.29245	26.79178	67.29113

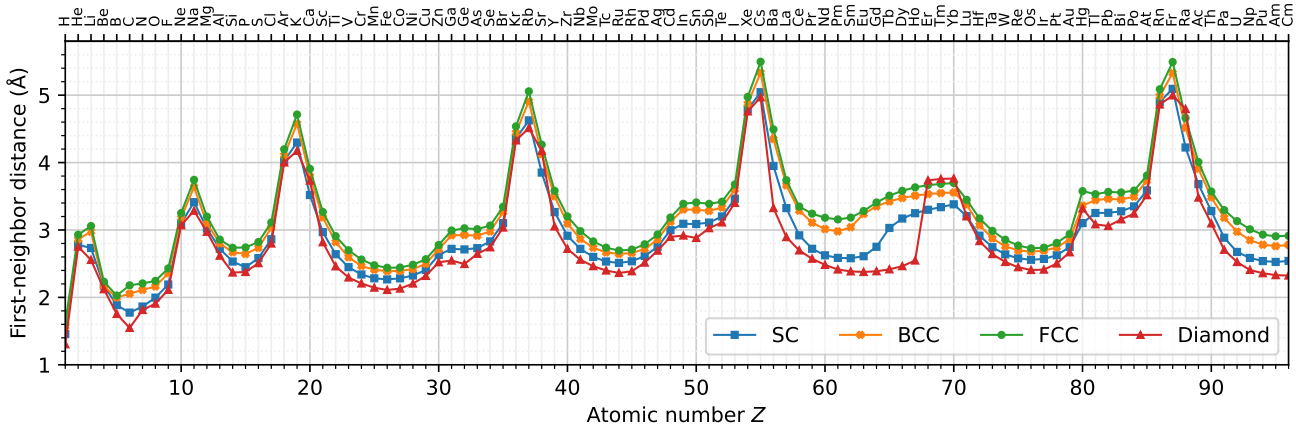

(a) First-neighbor distance for the unaries dataset.

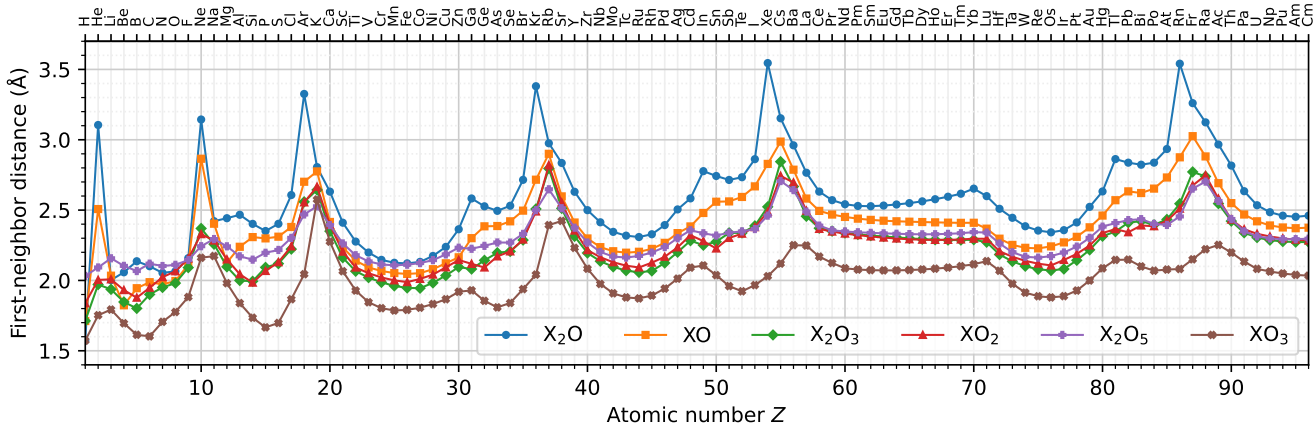

(b) First-neighbor distance of the X atom for the oxides dataset (the first neighbor is, in all cases considered here, an oxygen atom).

Figure S1.3. First-neighbor distance of the X atom to its closest neighbor for all 960 systems in our dataset.

S2 Hirshfeld-I charges

Six different oxide crystals are imposed, in order to force the element X into 6 different formal oxidation states. The hope is that this will bring each element into 6 chemically sufficiently different environments. In this section, we analyze whether this expectation has been realized. This is done by monitoring the Hirshfeld-I charges throughout this oxide set, as a proxy for the chemical environment.

S2.1 Hirshfeld-I atoms-in-molecules methodology

Atomic charges have been calculated within the context of an atoms-in-molecules (AIM) approach. The basic goal of these approaches is to divide the electrons, or more specifically the electron density, of a multi-atom system into subunits associated with chemical atoms. One can either start from the calculated wavefunctions (e.g., Mulliken charges[86,87]) or from the electron density distribution (EDD) (e.g., Hirshfeld[88] or Bader[89] charges). In this work, the iterative Hirshfeld approach (HI), which is an improvement of the Hirshfeld approach, is used. This approach alleviates the dependence on the chosen initial references of the original Hirshfeld method[58–60]. In Hirshfeld (and other stockholder) methods, the EDD in each point in space is divided over all the nearby AIM, in contrast to, for example, the Bader method[89], which assigns the entire electron density of a given point in space to a single AIM. This gives rise to smooth AIM which overlap in real-space. The Hirshfeld weights for an atom A are defined as:

$$w_A^H(r) = \frac{\rho_A^{AIM}(r)}{\rho_{mol}(r)}, \tag{S1}$$

where $\rho_A^{AIM}(r)$ and $\rho_{mol}(r)$ are the EDDs for the AIM and the molecule respectively. This however creates a circular reference, as the AIM EDD is calculated using the Hirshfeld weights. As a solution, Hirshfeld suggested the use of a reference EDD defined as the spherical average of the EDD of the free atom in a chosen reference state[88]. To make sure weights at every point in space remain normalized to unity, the molecular density is replaced by the sum of the atomic reference EDD, giving rise to a so-called *promolecular* EDD. Within this setup, one has to chose suitable atomic reference states, and it was found that for different atomic reference states, different atomic charges were obtained. This issue was resolved by Bultinck *et al.*[60], who proposed an extension of the scheme by iterative modification of the reference state. Starting with, for example, neutral reference EDDs, $\rho_A^0(r)$, the $w_A^H(r)$ are calculated. From these the AIM EDDs are calculated as:

$$\rho_A^{AIM}(r) = \frac{\rho_A^0(r)}{\rho_{promol}^0(r)}\rho_{mol}(r). \tag{S2}$$

With these AIM EDDs the atomic charge, x, is calculated through integration over the entire system. In the following step, the reference EDD is constructed as the linear interpolation of EDDs with atomic charge $I < x < I+1$, with I the integer value of the ionic charge lower than x. Using these reference EDDs, $\rho_A^x(r)$, new weights, AIM EDDs, and atomic charges are calculated. This scheme is then iterated to convergence of the atomic charges.

For periodic systems, the problem of the infinite size of the system is resolved by only considering the atoms of the unit cell for calculation of the charges and periodic copies which are "*nearby*"[58]. The Hirshfeld weights are calculated for all grid points (of an atom centered Becke grid[90]) associated with the atoms of the unit cell, and all other grid points which are located in the same spatial region. Atoms contributing to the weights are thus the unit cell atoms, as well as periodic copies within a limited range[58,59]. Furthermore, it was found that the EDDs of the valence electrons (i.e., all electrons not included in the frozen core) can be used without loss of quality compared to all-electron EDDs, while using a much coarser grid.

S2.2 Computational settings

In this work, HI-charges are calculated using the previous implementation for periodic systems,[58,59] as found in the HIVE package[91]. The calculations for generating the EDDs are performed using the VASP package. Reference atomic densities are calculated using a small unit cell of $20 \times 20 \times 20$ Å^3 for the cations, while a large $40 \times 40 \times 40$ Å^3 cell is used for the tail correction of the anions. The plane wave kinetic energy cut off is set to 1000 eV. The EDDs of the oxide and unary systems are obtained from static calculations using a $33 \times 33 \times 33$ Γ-centered k-point integration mesh and a kinetic energy cut off of 1000 eV, using the PBE functional as defined in S16.5. The atomic charges of the systems are calculated using the HI partitioning scheme with a charge convergence criterion of 1.0×10^{-4} electron. Charges are integrated on a logarithmic radial grid with atom-centered spherical shells of 1202 Lebedev–Laikov grid points[90,92].

S2.3 Discussion of Hirshfeld-I atomic charges and their relation to formal oxidation states

By imposing the topology of the oxides, every element X should exist in a predetermined formal oxidation state covering all integer values from +1 to +6. This formal oxidation state, however does not correspond one-to-one to the local configuration

of the charge density around element X that describes how element X binds to the surrounding oxygens. This is particularly relevant for those oxides that are ''*exotic*' (e.g., hydrogen in HO_3 has a formal oxidation state of +6, whereas even in a complete ionic picture hydrogen can only donate a single electron). In order to survey the actual chemical environment of every element X, we therefore calculated the Hirshfeld-I charges for X in all oxides and unaries (not shown), near the equilibrium volume[58–60]. As any other AIM scheme to define charges, Hirshfeld-I charges have their limitations. A common limitation all AIM schemes have to deal with is the fact that atomic charge is not a quantum mechanical observable. As such, there exists no absolute true value to find. The choice of the specific AIM scheme to calculate charges is therefore guided by the wish to satisfy other requirements. Attractive features of the Hirshfeld-I charges in this context are: They are (1) basis-set independent[93], (2) very robust, meaning charges are not structure dependent if the chemical environment remains the same, while very sensitive to changes in the chemical environment or oxidation state[94–96], (3) and large, though always smaller than the formal charge.

The results in SI Fig. S2.1 show the variation of the oxygen and metal charges over the periodic table as function of the formal oxidation state. These pictures reflect several trends that are intuitively expected: for X_2O (formal oxidation state +1), the elements with a HI charge closest to 1 are the alkali elements, while for XO (formal oxidation state +2) the elements with a HI charge closest to 2 are the earth-alkaline elements. On the other hand, the HI charges are clearly limited and are often about one half of the formal oxidation state. For instance, for XO_3 (formal oxidation state +6), the HI charges are often in the range 2.5-3.5.

Looking at the entire distribution of the atomic charges over the entire oxide dataset, (see SI Fig. S2.2) shows that the average metal charge gradually shifts to higher charges with increasing formal charge. In case of the oxygen charges, note that the oxygen charge decreases in size with increasing formal charge of the metal, which is a consequence of the fact that the formal charge is never actually fully transferred. Visualizing the results per formal oxidation state of the oxide system (see SI Fig. S2.3) shows an increasing trend, as expected. More interestingly, if the materials are split in two subsets – those with a 'reasonable' formal oxidation state for X and those with an 'exotic' formal oxidation stated for X (see caption of SI Fig. S2.3) – it becomes clear that for the 'reasonable' subset the calculated Hirshfeld-I charge is on average about half of the formal charge. In the case of the other subset, a lower value is found. Taken together, the different features of SI Fig. S2.3 consistently express that even though the nominal formal charges are not obtained, the six different crystal structures for the oxides give rise to systematically different chemical environments. This was exactly the purpose of imposing these six different oxide crystal structures.

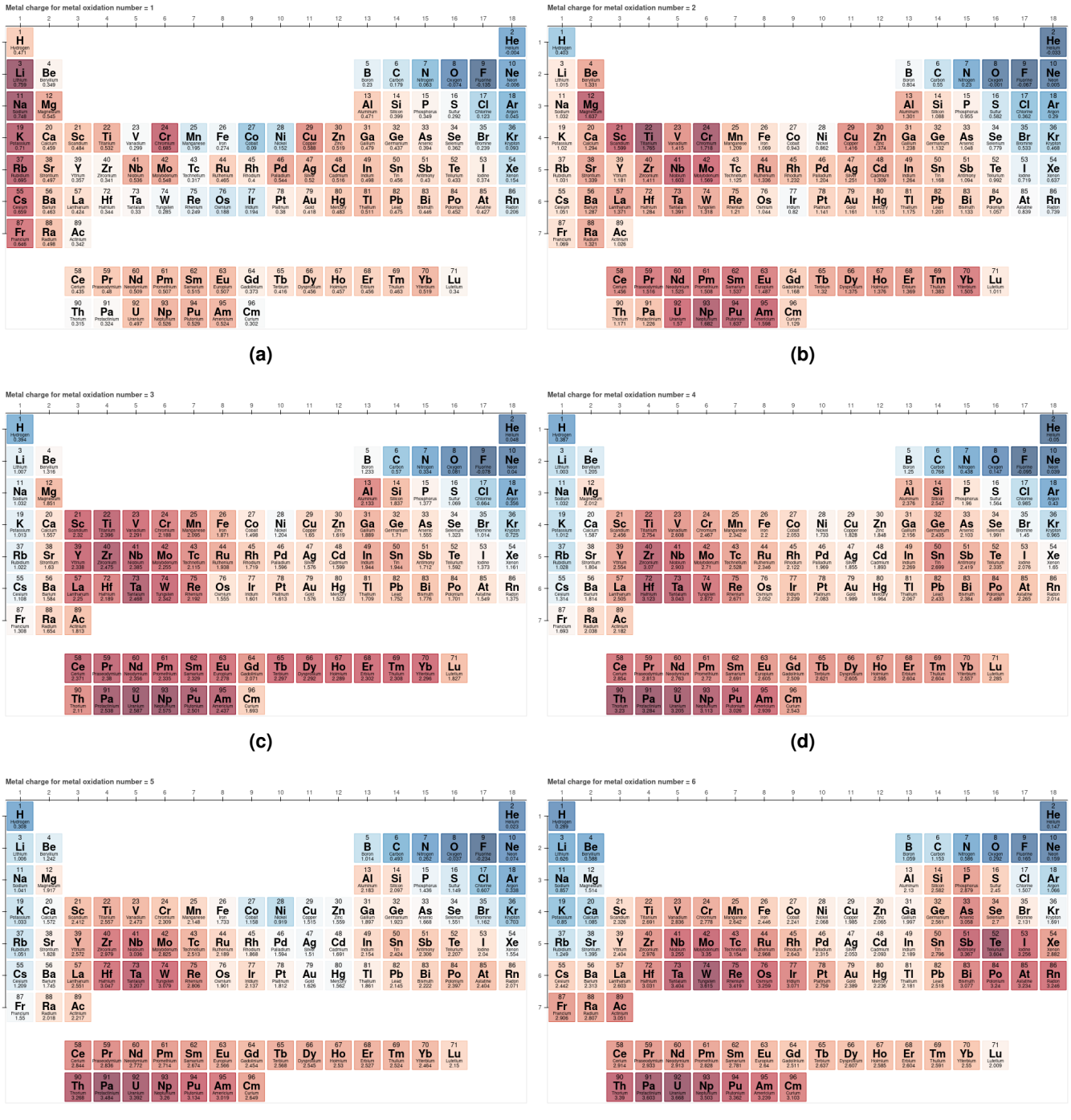

Figure S2.1. The average Hirshfeld-I charge on the metal atom for the oxides dataset according to the formal charge. Formal charge +1 (a), +2 (b), +3 (c), +4 (d), +5 (e), and +6 (f). Brownish colors indicate elements that have a Hirshfeld-I charge that is in line with their formal charge.

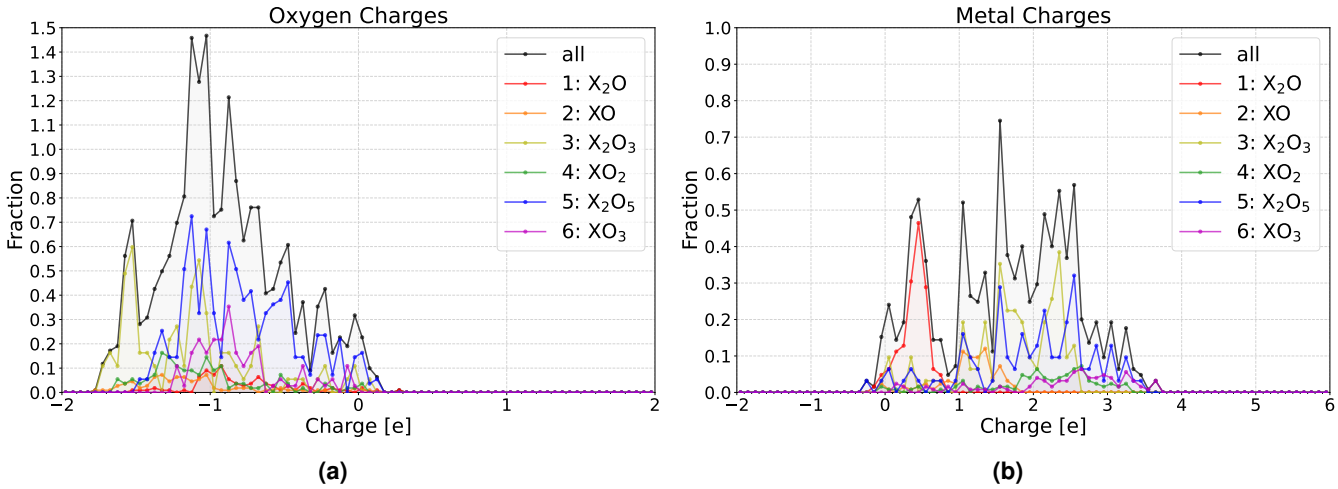

Figure S2.2. (a) Distribution of oxygen charges according to the Hirshfeld-I method for the oxides dataset. (b) Distribution of metal charges according to the Hirshfeld-I method for the oxides dataset.

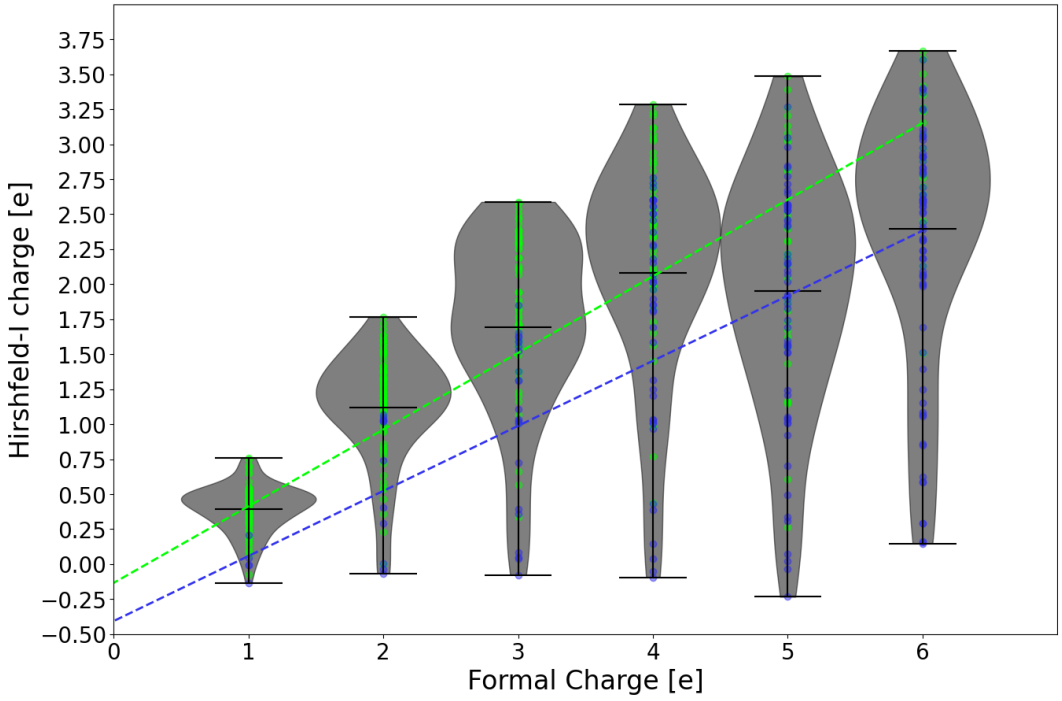

Figure S2.3. Violin plot of the HI charges of X in the oxides, as function of the formal oxidation state. Green dots and green linear fit: all oxides for which the formal oxidation state of X in this oxide is less than or equal to the maximal common formal oxidation state of X (as listed in Ref. 97). Blue dots and blue linear fit: all oxides for which the formal oxidation state of X in this oxide is larger than the maximal common formal oxidation state of X (as listed in Ref. 97). The green subset has therefore all oxides for which the formal oxidation state of X is 'reasonable', the blue subset represents oxides for which the formal oxidation state of X is 'exotic'.

S3 Determination of the weights of the metric ν based on the error propagation on the Birch–Murnaghan fit parameters

In this Section, we motivate the choice of weights $w_{V_0} = 1$, $w_{B_0} = 1/20$ and $w_{B_1} = 1/400$ discussed in the text for the ν metric.

When computing the EOS curves $E(V)$, the results from any simulation are affected by numerical noise, originating from many different sources (finiteness of the k-point integration mesh, basis set discretization, thresholds to stop the self-consistent convergence cycle, ...). When these points are fitted to a Birch–Murnaghan equation of state, the error propagates to the resulting fit parameters. This has been investigated in detail in Ref. 98, and several of the observations mentioned underneath are in line with the conclusions reached there. Intuitively, one can already expect that the numerical error will be larger for those parameters that are associated with higher-order derivatives. For instance, V_0 is the minimum of the EOS curve (i.e., the zero of the first derivative) is expected to be affected by a smaller error with respect to B_0 that is related to the curvature of the EOS curve close to the minimum (thus, to its second-order derivative). A first observation is that the error on all parameters will increase for increasing input noise on the energy datapoints. However, our goal in this section is not to quantify the error on each of these properties independently, but rather to understand if the error on pairs of fit parameters is related. In particular we will show that errors on B_0 (B_1) are typically 20 (400) times larger than those on V_0; by arbitrarily setting $w_{V_0} = 1$ (a change to this would result only in a global multiplicative factor), this will justify our final choice of weights.

We extract these relative weights using the following approach. We start from our reference AE dataset and consider, for each of the 960 materials, the fitted parameters V_0^{ref}, B_0^{ref} and B_1^{ref}. Rather than using the datapoints from the AE simulations, however, we generate a new "perfect" dataset (i.e., not affected by any numerical noise) by creating, for every curve, 7 fictitious points lying exactly on the Birch–Murnaghan curve, with the same volume spacing as discussed in the main text (spacing of 2% in volume between 94% and 106% of the tabulated central volume). This removes from our analysis any existing numerical noise of the AE simulations that is due to the numerical approximations in the two specific codes, rather than originating from the fitting procedure. We then select a reference average numerical error n_σ for the energy value of each point, and randomly displace each energy by a random value following a normal distribution with zero mean and standard deviation n_σ. We fit these noisy datapoints with the Birch–Murnaghan curve, thus obtaining fitted values of V_0, B_0 and B_1, that will be different from the initial reference ones V_0^{ref}, B_0^{ref} and B_1^{ref}. We therefore compute the relative errors on each of them with respect to their average (similar to what is done for ε and ν): e.g., for the minimum volume $\eta_{V_0} = (V_0 - V_0^{ref})/((V_0 + V_0^{ref})/2)$, for the bulk modulus $\eta_{B_0} = (B_0 - B_0^{ref})/((B_0 + B_0^{ref})/2)$ and for the derivative of the bulk modulus $\eta_{B_1} = (B_1 - B_1^{ref})/((B_1 + B_1^{ref})/2)$. We repeat the procedure for N_s random samples, and finally compute the average of the absolute value of the three relative errors η_{V_0}, η_{B_0} and η_{B_1} on the N_s samples (for each material):

$$\bar{\eta}_{V_0} = \sum_{i=1}^{N_s} \frac{|\eta_{V_0}(i)|}{N_s} \tag{S3}$$

and similarly for $\bar{\eta}_{B_0}$ and $\bar{\eta}_{B_1}$, where i denotes each of the individual independent random noise samples. The values $\bar{\eta}_{V_0}$, $\bar{\eta}_{B_0}$ and $\bar{\eta}_{B_1}$ quantify the typical average errors on the three fit parameters for a numerical noise of magnitude n_s. By producing histograms of the three quantities over the whole dataset of 960 structures, we obtain a peaked distribution that represents the range of values typical of our materials dataset ($V_0 \approx 3 - 400$ Å^3, $B_0 \approx 0.001 - 2.7$ eV/Å^3 and $B_1 \approx 0.4 - 12$). The position of the peak, as we expected, depends on the noise magnitude n_σ. As we discussed, however, we do not consider the histograms of these three quantities but we produce, instead, histograms for the two "relative" quantities

$$\frac{\bar{\eta}_{B_0}}{\bar{\eta}_{V_0}} \qquad \text{and} \qquad \frac{\bar{\eta}_{B_1}}{\bar{\eta}_{V_0}}. \tag{S4}$$

The positions of the peaks of these histograms will represent the quantities we wish to determine: the typical ratio of numerical error on pairs of fit parameters. The results of our simulations can be summarized as follows:

- $N_s = 100$ samples are already enough to converge the statistics and the histograms for our goal of identifying the peaks of the histograms;
- the positions of the peaks of $\bar{\eta}_{V_0}$, $\bar{\eta}_{B_0}$ and $\bar{\eta}_{B_1}$ are roughly proportional to the input noise n_σ; however, the position of the peaks of $\frac{\bar{\eta}_{B_0}}{\bar{\eta}_{V_0}}$ and $\frac{\bar{\eta}_{B_1}}{\bar{\eta}_{V_0}}$ are, to a good approximation, independent of n_σ for the noises that we considered (in the range $10^{-4} - 10^{-6}$ eV) (see also Ref. 98 for similar conclusions on the Δ metric);
- for our choice of volume range (94%–106%), the two histograms (see SI Fig. S3.1) display clear peaks at positions that can be rounded to 20 and 400, respectively. The peak positions are consistent when considering independently unaries and oxides (even if the spread of the peaks is different in the two cases). Hence, we choose the weights as $w_{V_0} = 1$, $w_{B_0} = 1/20$ and $w_{B_1} = 1/400$.

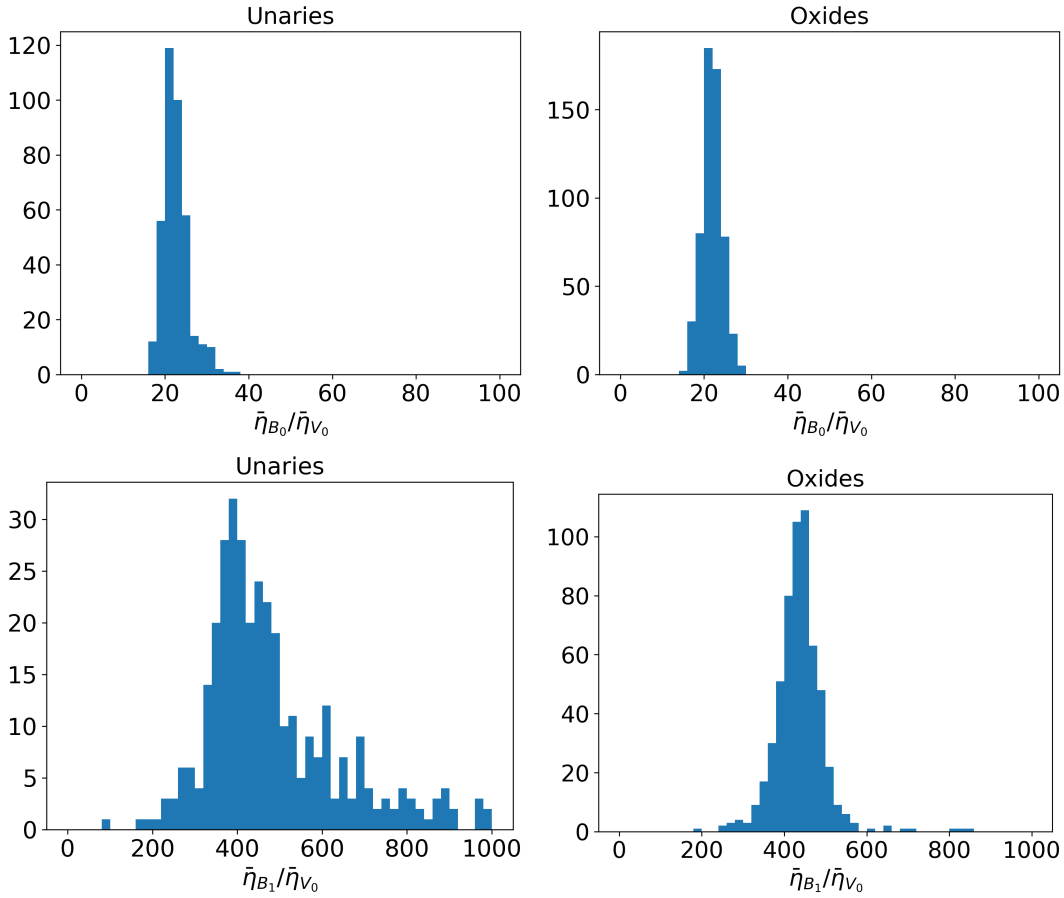

Figure S3.1. Histograms of the typical error ratios of B_0 vs. V_0 ($\bar{\eta}_{B_0}/\bar{\eta}_{V_0}$, top row) and of B_1 vs. V_0 ($\bar{\eta}_{B_1}/\bar{\eta}_{V_0}$, bottom row) for the unaries set (left column) and the oxides set (right column). The simulations were run for $N_s = 100$ random samples and a standard deviation on the error of the energy on the datapoints of $n_\sigma = 10^{-5}$ eV. The histograms indicate that the error of B_0 (B_1) is approximately 20 (400) times larger than the error on V_0, justifying our choice of weights for the metric ν.

- The peak positions are insensitive to the number of datapoints, as long as the total volume range is not modified. Instead, they change significantly if the volume range is changed. For instance, using a volume range of 90%–110% would result in values closer to 15 and 200 for the two ratios, respectively. This can also be intuitively explained: B_1, for instance, is related to the non-parabolicity of the Birch–Murnaghan curve away from its minimum. If we consider a very small volume range, the curve will be very close to parabolic, and we therefore expect a large error on B_1 since the fit has very little information on the non-parabolic behavior. For larger volume ranges, the curve starts to deviate significantly from a parabola, thus providing more information to the fitting algorithm on the actual value of B_1, in turn resulting into a smaller relative error on B_1 vs. B_0 or V_0.

- The stability of the fit, especially on B_1, is significantly affected by the choice of fitting algorithm. For instance, we realized that if one uses the `optimize.curve_fit` subroutine of SciPy (`https://www.scipy.org`), which is *not* the algorithm used in this work, the choice of the fitting starting point is very important, and we also observe that iterating the procedure a few times (using the results of the previous step as starting points for the next fit) improves the stability. Instead, the function used in this work (that is the same also used in Ref. 29, 30) is a non-iterative fitting algorithm that proves to be much more robust.

S4 Reference all-electron results for V_0, B_0 and B_1

This section reports the complete reference dataset of the EOS parameters obtained with the two all-electron codes FLEUR and WIEN2k, and the absolute value of their percentage difference (that we indicate with η). Moreover, it reports the averaged parameters among them, that constitutes our reference average dataset presented in this manuscript. Data is divided in 10 tables, one for each crystal structure (4 unaries and 6 oxides). The agreement for V_0 is within 0.3% for all materials except Cs_2O_5 (0.323%), Fr_2O_5 (0.645%), Ra_2O_5 (0.333%), NeO_3 (0.302%) and RbO_3 (0.343%). Not surprisingly, these are 5 crystals with very small bulk moduli B_0: it has been shown in Ref. 98 that the error in the volume scales inversely with the value of the bulk modulus.

Parameters are expressed per formula unit (see also SI Sec. S1). Note that, for X_2O_3 and for X_2O_5, the primitive cell has twice the number of atoms (10 and 14, respectively) than the number of atoms in the formula unit (5 and 7, respectively). This is reflected in a factor of 0.5 in the volumes reported in this table with respect to the volume of the unit cells in the input files available in Ref. 62.

Table S4.1. Table with all calculated EOS parameters for the FCC structures obtained with FLEUR and WIEN2k.

	FLEUR			WIEN2k			Abs. percentage difference [%]			Average set		
	V_0 [Å^3]	B_0 [eV/Å^3]	B_1	V_0 [Å^3]	B_0 [eV/Å^3]	B_1	$\lvert\eta(V_0)\rvert$	$\lvert\eta(B_0)\rvert$	$\lvert\eta(B_1)\rvert$	V_0 [Å^3]	B_0 [eV/Å^3]	B_1
H	2.9651	0.6768	3.2596	2.9646	0.6764	3.2598	0.017	0.048	0.007	2.9648	0.6766	3.2597
He	17.7867	0.0053	6.208	17.7585	0.0054	6.6423	0.159	0.404	6.759	17.7726	0.0053	6.4251
Li	20.2246	0.0862	3.3304	20.2243	0.0862	3.3298	0.001	0.001	0.019	20.2245	0.0862	3.3301
Be	7.8705	0.7437	3.4867	7.8728	0.7437	3.471	0.029	0.006	0.449	7.8716	0.7437	3.4789
B	5.8886	1.6978	3.7481	5.8945	1.6993	3.7554	0.099	0.088	0.196	5.8916	1.6985	3.7517
C	7.3221	0.9364	3.5885	7.3212	0.9358	3.5906	0.012	0.07	0.057	7.3216	0.9361	3.5896
N	7.6017	1.1174	4.1748	7.6009	1.1161	4.1633	0.011	0.119	0.276	7.6013	1.1167	4.169
O	7.9988	0.8755	4.7639	7.9987	0.8745	4.7427	0.002	0.115	0.446	7.9988	0.875	4.7533
F	10.1454	0.3137	5.6468	10.1486	0.3134	5.6241	0.031	0.111	0.404	10.147	0.3135	5.6355
Ne	24.2855	0.0079	7.5394	24.3201	0.0077	7.2489	0.142	1.852	3.929	24.3028	0.0078	7.3941
Na	37.1012	0.0482	3.6866	37.0968	0.0481	3.6838	0.012	0.025	0.076	37.099	0.0482	3.6852
Mg	23.1275	0.2192	3.9959	23.123	0.2193	3.9966	0.02	0.065	0.019	23.1252	0.2193	3.9963
Al	16.4943	0.4838	4.6231	16.4964	0.4838	4.6233	0.012	0.01	0.004	16.4954	0.4838	4.6232
Si	14.4856	0.5171	4.3331	14.4788	0.5174	4.3282	0.048	0.049	0.113	14.4822	0.5173	4.3307
P	14.5664	0.5752	3.9579	14.5607	0.5759	4.0276	0.039	0.112	1.744	14.5636	0.5756	3.9927
S	15.88	0.4921	4.308	15.8814	0.4917	4.3089	0.009	0.089	0.023	15.8807	0.4919	4.3085
Cl	21.2849	0.1893	5.442	21.2915	0.189	5.439	0.031	0.169	0.055	21.2882	0.1891	5.4405
Ar	52.3124	0.0047	6.8685	52.2404	0.0047	7.4623	0.138	0.284	8.287	52.2764	0.0047	7.1654
K	74.0038	0.0221	3.7672	74.0051	0.0221	3.7758	0.002	0.093	0.229	74.0044	0.0221	3.7715
Ca	42.1888	0.1084	3.2754	42.1998	0.1084	3.2907	0.026	0.002	0.465	42.1943	0.1084	3.283
Sc	24.6877	0.3188	3.1588	24.686	0.3187	3.1581	0.007	0.029	0.023	24.6869	0.3187	3.1584
Ti	17.3952	0.6709	3.4556	17.3939	0.6707	3.4529	0.008	0.021	0.079	17.3946	0.6708	3.4543
V	13.9046	1.0993	3.8722	13.9053	1.0994	3.8706	0.005	0.01	0.041	13.905	1.0993	3.8714
Cr	11.8849	1.4816	4.1479	11.887	1.4825	4.1167	0.018	0.059	0.756	11.8859	1.4821	4.1323
Mn	10.7458	1.7527	4.4245	10.7485	1.7506	4.4042	0.026	0.119	0.461	10.7471	1.7516	4.4144
Fe	10.2594	1.7835	4.6058	10.261	1.7813	4.6159	0.015	0.126	0.218	10.2602	1.7824	4.6109
Co	10.3081	1.5919	4.7528	10.3087	1.5909	4.7557	0.006	0.065	0.061	10.3084	1.5914	4.7542
Ni	10.8354	1.2626	4.8979	10.8344	1.2609	4.8916	0.009	0.134	0.129	10.8349	1.2617	4.8947
Cu	11.9534	0.8805	5.052	11.951	0.8795	5.0594	0.02	0.109	0.145	11.9522	0.88	5.0557
Zn	15.1641	0.4322	5.2768	15.1599	0.4331	5.2674	0.027	0.212	0.177	15.162	0.4326	5.2721
Ga	18.9499	0.3032	4.8071	18.9431	0.3038	4.8034	0.035	0.165	0.078	18.9465	0.3035	4.8053
Ge	19.5823	0.3927	4.3284	19.5826	0.3929	4.3261	0.002	0.053	0.054	19.5825	0.3928	4.3273
As	19.3209	0.493	4.3003	19.3143	0.4928	4.3653	0.034	0.038	1.5	19.3176	0.4929	4.3328
Se	20.3778	0.4333	4.6567	20.3779	0.4333	4.6647	0.0	0.017	0.172	20.3779	0.4333	4.6607
Br	26.4146	0.1723	5.5508	26.4204	0.172	5.5512	0.022	0.137	0.006	26.4175	0.1722	5.551
Kr	66.0139	0.004	7.5013	66.0696	0.004	7.2722	0.084	1.635	3.101	66.0418	0.004	7.3867
Rb	91.4121	0.0172	3.7661	91.4428	0.0172	3.7729	0.034	0.114	0.18	91.4275	0.0172	3.7695
Sr	54.882	0.0728	3.2918	54.9025	0.0727	3.296	0.037	0.07	0.129	54.8923	0.0728	3.2939
Y	32.4691	0.243	3.2686	32.474	0.2428	3.2699	0.015	0.062	0.04	32.4715	0.2429	3.2692
Zr	23.2137	0.5626	3.2904	23.2131	0.5624	3.288	0.002	0.037	0.072	23.2134	0.5625	3.2892
Nb	18.7683	1.0213	3.656	18.7673	1.021	3.6527	0.005	0.027	0.09	18.7678	1.0211	3.6544
Mo	16.0351	1.4875	4.0608	16.0351	1.4874	4.0598	0.0	0.013	0.024	16.0351	1.4875	4.0603
Tc	14.5123	1.8563	4.4992	14.513	1.8564	4.4999	0.005	0.006	0.015	14.5127	1.8564	4.4996
Ru	13.8362	1.9096	4.8614	13.837	1.9097	4.8617	0.006	0.001	0.006	13.8366	1.9096	4.8616
Rh	14.0519	1.6017	5.1987	14.049	1.6037	5.1824	0.021	0.122	0.313	14.0505	1.6027	5.1906
Pd	15.3284	1.0486	5.5494	15.3224	1.0488	5.5242	0.039	0.019	0.454	15.3254	1.0487	5.5368
Ag	17.8411	0.5681	5.8386	17.836	0.5676	5.8264	0.029	0.101	0.209	17.8386	0.5678	5.8325
Cd	22.8435	0.261	5.9936	22.839	0.2608	5.9998	0.02	0.088	0.103	22.8413	0.2609	5.9967

Table S4.1. (continued) Table with all calculated EOS parameters for the FCC structures obtained with FLEUR and WIEN2k.

	FLEUR			WIEN2k			Abs. percentage difference [%]			Average set		
	V_0 [Å^3]	B_0 [eV/Å^3]	B_1	V_0 [Å^3]	B_0 [eV/Å^3]	B_1	$\lvert\eta(V_0)\rvert$	$\lvert\eta(B_0)\rvert$	$\lvert\eta(B_1)\rvert$	V_0 [Å^3]	B_0 [eV/Å^3]	B_1
In	27.515	0.2215	5.0905	27.5052	0.2216	5.0854	0.035	0.071	0.1	27.5101	0.2216	5.0879
Sn	28.0234	0.2922	4.7449	27.9943	0.2929	4.7455	0.104	0.221	0.013	28.0088	0.2926	4.7452
Sb	27.4879	0.3654	4.5842	27.4913	0.3657	4.5711	0.012	0.088	0.288	27.4896	0.3656	4.5776
Te	28.28	0.334	4.8206	28.2775	0.3342	4.8406	0.009	0.048	0.415	28.2787	0.3341	4.8306
I	35.1036	0.1451	5.6049	35.1062	0.1451	5.6104	0.007	0.019	0.099	35.1049	0.1451	5.6076
Xe	87.0155	0.0034	7.1869	86.9985	0.0034	7.2278	0.02	0.624	0.567	87.007	0.0034	7.2074
Cs	117.3557	0.0122	3.51	117.3654	0.0122	3.5403	0.008	0.057	0.859	117.3606	0.0122	3.5251
Ba	64.1195	0.0505	2.4957	64.1086	0.0504	2.5043	0.017	0.153	0.342	64.114	0.0504	2.5
La	36.9471	0.1532	2.6241	36.9467	0.1531	2.6228	0.001	0.059	0.05	36.9469	0.1532	2.6234
Ce	26.5229	0.2379	4.2709	26.5218	0.2375	4.2942	0.004	0.143	0.544	26.5224	0.2377	4.2825
Pr	24.097	0.251	4.5955	24.0912	0.2506	4.6302	0.024	0.16	0.752	24.0941	0.2508	4.6129
Nd	22.7681	0.2337	4.9628	22.7614	0.2337	4.982	0.03	0.028	0.388	22.7648	0.2337	4.9724
Pm	22.2492	0.1997	5.214	22.2418	0.1993	5.1564	0.033	0.22	1.111	22.2455	0.1995	5.1852
Sm	22.8318	0.1497	5.0155	22.8251	0.1494	4.9396	0.029	0.202	1.525	22.8284	0.1496	4.9776
Eu	24.9932	0.1085	3.6911	24.9908	0.1082	3.7107	0.01	0.246	0.531	24.992	0.1083	3.7009
Gd	27.9899	0.0977	3.0674	27.9978	0.0973	3.0359	0.028	0.444	1.032	27.9939	0.0975	3.0517
Tb	30.5465	0.0974	2.9862	30.5577	0.0971	3.0003	0.037	0.258	0.47	30.5521	0.0972	2.9933
Dy	32.4704	0.0977	3.1108	32.4829	0.0975	3.102	0.039	0.23	0.286	32.4766	0.0976	3.1064
Ho	33.8849	0.0995	3.0456	33.8985	0.0994	2.995	0.04	0.052	1.674	33.8917	0.0995	3.0203
Er	34.8174	0.1052	2.8147	34.8284	0.1051	2.8416	0.031	0.067	0.951	34.8229	0.1052	2.8281
Tm	35.3264	0.1128	3.0333	35.3378	0.1126	3.0501	0.032	0.162	0.551	35.3321	0.1127	3.0417
Yb	35.7	0.1173	3.3001	35.7087	0.1171	3.3469	0.025	0.182	1.411	35.7044	0.1172	3.3235
Lu	28.9721	0.2626	3.4956	28.9707	0.2624	3.4779	0.005	0.083	0.509	28.9714	0.2625	3.4867
Hf	22.5694	0.634	3.3323	22.5658	0.6337	3.3262	0.016	0.053	0.184	22.5676	0.6339	3.3292
Ta	18.8409	1.1807	3.6978	18.8378	1.1801	3.6924	0.016	0.046	0.147	18.8394	1.1804	3.6951
W	16.4598	1.7535	4.0172	16.4559	1.753	4.0145	0.024	0.033	0.066	16.4579	1.7533	4.0159
Re	15.0194	2.2567	4.4466	15.0133	2.2579	4.4361	0.041	0.056	0.235	15.0163	2.2573	4.4414
Os	14.341	2.4281	4.7924	14.3407	2.4291	4.7851	0.002	0.042	0.153	14.3409	2.4286	4.7887
Ir	14.5054	2.1666	5.1036	14.5046	2.1674	5.1096	0.006	0.038	0.118	14.505	2.167	5.1066
Pt	15.6574	1.5446	5.4771	15.6545	1.5444	5.4614	0.019	0.014	0.287	15.656	1.5445	5.4692
Au	17.9802	0.8715	5.9562	17.9777	0.8706	5.9351	0.014	0.098	0.354	17.9789	0.871	5.9457
Hg	32.3647	0.0353	0.3443	32.3309	0.0351	0.4083	0.104	0.558	17.005	32.3478	0.0352	0.3763
Tl	31.144	0.1677	5.5108	31.1364	0.1678	5.5795	0.024	0.074	1.239	31.1402	0.1678	5.5451
Pb	32.0341	0.2464	4.7349	32.0321	0.2464	4.7442	0.006	0.014	0.196	32.0331	0.2464	4.7396
Bi	31.8128	0.3212	4.6441	31.8082	0.3215	4.6437	0.014	0.095	0.007	31.8105	0.3213	4.6439
Po	32.5569	0.3098	4.9427	32.5698	0.3097	4.9237	0.04	0.024	0.385	32.5633	0.3098	4.9332
At	39.0206	0.1488	5.7134	39.0407	0.1486	5.6808	0.052	0.114	0.573	39.0307	0.1487	5.6971
Rn	93.1794	0.0034	7.0782	93.1334	0.0034	6.4169	0.049	0.131	9.801	93.1564	0.0034	6.7476
Fr	117.1664	0.012	3.6076	117.1595	0.012	3.591	0.006	0.054	0.461	117.163	0.012	3.5993
Ra	71.6176	0.045	3.0685	71.6363	0.0448	2.9979	0.026	0.305	2.326	71.627	0.0449	3.0332
Ac	45.545	0.1491	2.7527	45.5563	0.1491	2.757	0.025	0.043	0.156	45.5507	0.1491	2.7548
Th	32.1793	0.3435	3.2867	32.1886	0.3438	3.306	0.029	0.086	0.585	32.1839	0.3437	3.2964
Pa	25.3021	0.5883	4.0176	25.2938	0.5883	4.023	0.033	0.004	0.135	25.2979	0.5883	4.0203
U	21.7185	0.7272	4.3875	21.7081	0.7275	4.3786	0.048	0.051	0.202	21.7133	0.7274	4.383
Np	19.2995	0.8519	4.8884	19.2896	0.8515	4.833	0.052	0.047	1.14	19.2945	0.8517	4.8607
Pu	17.8081	0.9555	5.3706	17.7962	0.9551	5.3544	0.067	0.047	0.302	17.8021	0.9553	5.3625
Am	17.3701	0.9257	5.5753	17.3574	0.9251	5.5301	0.074	0.063	0.814	17.3637	0.9254	5.5527

Table S4.2. Table with all calculated EOS parameters for the BCC structures obtained with FLEUR and WIEN2k.

	FLEUR			WIEN2k			Abs. percentage difference [%]			Average set		
	V_0 [Å^3]	B_0 [eV/Å^3]	B_1	V_0 [Å^3]	B_0 [eV/Å^3]	B_1	$\lvert\eta(V_0)\rvert$	$\lvert\eta(B_0)\rvert$	$\lvert\eta(B_1)\rvert$	V_0 [Å^3]	B_0 [eV/Å^3]	B_1
H	2.9668	0.6748	3.2642	2.9667	0.6747	3.2615	0.004	0.023	0.083	2.9668	0.6748	3.2629
He	18.0345	0.0051	6.3686	18.0262	0.0051	6.4241	0.046	0.903	0.868	18.0304	0.0051	6.3964
Li	20.2674	0.0867	3.3459	20.2675	0.0867	3.3469	0.0	0.009	0.029	20.2675	0.0867	3.3464
Be	7.8148	0.7736	3.3532	7.8167	0.7736	3.3517	0.024	0.001	0.044	7.8158	0.7736	3.3525
B	6.1368	1.4325	4.8875	6.1419	1.4311	4.9017	0.083	0.094	0.29	6.1394	1.4318	4.8946
C	6.6858	1.1343	4.407	6.6856	1.1346	4.4061	0.002	0.032	0.022	6.6857	1.1345	4.4066
N	7.2349	1.1666	4.0231	7.2346	1.1658	4.0177	0.004	0.068	0.133	7.2347	1.1662	4.0204
O	7.7864	0.9447	4.714	7.7862	0.9437	4.7018	0.002	0.106	0.258	7.7863	0.9442	4.7079
F	10.0832	0.3299	5.6206	10.0851	0.3292	5.5739	0.019	0.241	0.834	10.0841	0.3296	5.5972
Ne	24.6915	0.0076	7.6061	24.731	0.0074	7.1231	0.16	2.113	6.559	24.7112	0.0075	7.3646

Table S4.2. (continued) Table with all calculated EOS parameters for the BCC structures obtained with FLEUR and WIEN2k.

	FLEUR			WIEN2k			Abs. percentage difference [%]			Average set		
	V_0 [Å^3]	B_0 [eV/Å^3]	B_1	V_0 [Å^3]	B_0 [eV/Å^3]	B_1	$\lvert\eta(V_0)\rvert$	$\lvert\eta(B_0)\rvert$	$\lvert\eta(B_1)\rvert$	V_0 [Å^3]	B_0 [eV/Å^3]	B_1
Na	37.0174	0.0484	3.6882	37.0128	0.0484	3.6916	0.012	0.026	0.092	37.0151	0.0484	3.6899
Mg	22.9196	0.219	4.0661	22.9149	0.2191	4.0662	0.02	0.06	0.001	22.9173	0.2191	4.0662
Al	16.9245	0.4284	4.4411	16.9268	0.4285	4.4427	0.014	0.023	0.038	16.9257	0.4285	4.4419
Si	14.647	0.5803	4.4591	14.6434	0.5804	4.456	0.024	0.021	0.068	14.6452	0.5803	4.4575
P	14.2314	0.6049	3.892	14.229	0.6059	3.8879	0.017	0.158	0.105	14.2302	0.6054	3.89
S	15.761	0.5181	4.2791	15.7627	0.5179	4.2794	0.01	0.045	0.007	15.7618	0.518	4.2792
Cl	21.4514	0.1941	5.4296	21.458	0.1937	5.4297	0.031	0.184	0.003	21.4547	0.1939	5.4297
Ar	53.3552	0.0044	7.3192	53.3539	0.0044	7.3728	0.002	0.736	0.731	53.3545	0.0044	7.346
K	73.779	0.0223	3.7712	73.78	0.0223	3.7723	0.001	0.096	0.029	73.7795	0.0223	3.7717
Ca	42.1437	0.1035	2.7523	42.1573	0.1035	2.7487	0.032	0.033	0.131	42.1505	0.1035	2.7505
Sc	24.8867	0.3307	3.2537	24.885	0.3305	3.2528	0.007	0.039	0.027	24.8859	0.3306	3.2533
Ti	17.2672	0.6616	3.4022	17.2665	0.6615	3.4017	0.004	0.017	0.017	17.2668	0.6615	3.402
V	13.4602	1.1357	3.838	13.4613	1.1358	3.8385	0.008	0.004	0.012	13.4608	1.1358	3.8383
Cr	11.5473	1.6126	4.2448	11.5491	1.6125	4.248	0.016	0.005	0.077	11.5482	1.6126	4.2464
Mn	10.7794	1.7389	4.456	10.7822	1.738	4.4616	0.026	0.056	0.125	10.7808	1.7384	4.4588
Fe	10.4997	1.6736	4.6188	10.5013	1.6735	4.6099	0.015	0.005	0.194	10.5005	1.6736	4.6144
Co	10.5443	1.495	4.7437	10.5452	1.4937	4.7372	0.009	0.091	0.137	10.5448	1.4943	4.7404
Ni	10.8951	1.2393	4.903	10.8951	1.2385	4.8992	0.0	0.06	0.077	10.8951	1.2389	4.9011
Cu	12.0052	0.8671	5.0756	12.0038	0.8666	5.0746	0.011	0.05	0.019	12.0045	0.8668	5.0751
Zn	15.3775	0.4002	5.4873	15.3727	0.4011	5.471	0.031	0.225	0.298	15.3751	0.4007	5.4791
Ga	19.2084	0.2974	5.0478	19.2028	0.2979	5.0589	0.029	0.15	0.22	19.2056	0.2976	5.0534
Ge	19.2667	0.3987	4.5843	19.2723	0.3989	4.5973	0.029	0.046	0.282	19.2695	0.3988	4.5908
As	19.0548	0.5065	4.2725	19.0495	0.5069	4.3392	0.028	0.067	1.549	19.0522	0.5067	4.3058
Se	20.3606	0.448	4.6207	20.3594	0.4479	4.6208	0.006	0.018	0.0	20.36	0.448	4.6208
Br	26.7815	0.174	5.5415	26.7869	0.1737	5.5377	0.02	0.157	0.068	26.7842	0.1739	5.5396
Kr	67.4365	0.0038	7.1919	67.4904	0.0038	7.2803	0.08	0.46	1.222	67.4634	0.0038	7.2361
Rb	91.1283	0.0173	3.7748	91.1599	0.0173	3.7777	0.035	0.132	0.078	91.1441	0.0173	3.7762
Sr	54.0026	0.0719	3.734	54.0232	0.0718	3.7318	0.038	0.105	0.06	54.0129	0.0718	3.7329
Y	33.0276	0.241	2.9922	33.0333	0.2409	2.9913	0.017	0.065	0.029	33.0305	0.2409	2.9918
Zr	22.8452	0.546	3.1221	22.8444	0.5458	3.1202	0.004	0.038	0.059	22.8448	0.5459	3.1212
Nb	18.1416	1.059	3.6875	18.1414	1.0587	3.6867	0.001	0.026	0.021	18.1415	1.0588	3.6871
Mo	15.7921	1.6178	4.2092	15.793	1.618	4.2091	0.006	0.012	0.002	15.7926	1.6179	4.2092
Tc	14.6187	1.8252	4.5682	14.6204	1.8256	4.5726	0.011	0.023	0.097	14.6196	1.8254	4.5704
Ru	14.2348	1.7435	4.8713	14.2364	1.744	4.8808	0.011	0.03	0.195	14.2356	1.7438	4.876
Rh	14.4759	1.454	5.1586	14.4725	1.4559	5.1547	0.023	0.13	0.077	14.4742	1.4549	5.1566
Pd	15.4471	1.0243	5.5299	15.4415	1.0246	5.5276	0.037	0.032	0.042	15.4443	1.0245	5.5287
Ag	17.9841	0.552	5.716	17.9791	0.5514	5.7039	0.028	0.098	0.212	17.9816	0.5517	5.71
Cd	23.4219	0.2245	6.342	23.4172	0.2243	6.3645	0.02	0.082	0.354	23.4196	0.2244	6.3533
In	27.7854	0.2132	5.3173	27.7757	0.2133	5.2879	0.035	0.069	0.554	27.7806	0.2133	5.3026
Sn	27.6616	0.2938	4.767	27.633	0.2945	4.7405	0.103	0.25	0.557	27.6473	0.2941	4.7537
Sb	27.2242	0.3732	4.6094	27.2273	0.3736	4.5923	0.011	0.096	0.373	27.2258	0.3734	4.6009
Te	28.5165	0.3423	4.8563	28.514	0.3425	4.8599	0.009	0.056	0.074	28.5153	0.3424	4.8581
I	35.9846	0.1429	5.5984	35.989	0.1429	5.5666	0.012	0.054	0.571	35.9868	0.1429	5.5825
Xe	89.0428	0.0032	7.5311	89.0269	0.0032	7.3314	0.018	0.752	2.687	89.0349	0.0032	7.4312
Cs	116.8396	0.0122	3.4735	116.8439	0.0122	3.5064	0.004	0.141	0.942	116.8417	0.0122	3.4899
Ba	63.3089	0.0543	2.8828	63.3019	0.0542	2.8852	0.011	0.13	0.084	63.3054	0.0542	2.884
La	37.8179	0.1637	2.8455	37.8172	0.1636	2.8535	0.002	0.08	0.279	37.8176	0.1637	2.8495
Ce	27.3263	0.186	4.1491	27.3216	0.1858	4.1358	0.017	0.146	0.322	27.324	0.1859	4.1425
Pr	23.1417	0.1983	5.8764	23.1411	0.1983	5.7392	0.003	0.015	2.362	23.1414	0.1983	5.8078
Nd	21.0714	0.2006	6.9968	21.0642	0.1997	6.9853	0.034	0.476	0.165	21.0678	0.2002	6.991
Pm	20.3646	0.17	8.0253	20.3511	0.1695	8.0187	0.066	0.251	0.082	20.3579	0.1698	8.022
Sm	21.6574	0.078	8.0168	21.6344	0.0774	7.9884	0.106	0.789	0.355	21.6459	0.0777	8.0026
Eu	26.1365	0.0883	0.7888	26.1316	0.0881	0.7803	0.019	0.24	1.093	26.1341	0.0882	0.7846
Gd	28.9453	0.1044	2.3132	28.9495	0.104	2.3163	0.015	0.328	0.134	28.9474	0.1042	2.3147
Tb	30.8957	0.1109	2.8391	30.906	0.1106	2.8208	0.033	0.305	0.649	30.9008	0.1108	2.8299
Dy	32.2821	0.114	3.163	32.2951	0.1137	3.1523	0.04	0.251	0.34	32.2886	0.1138	3.1576
Ho	33.2601	0.1159	3.3954	33.2745	0.1157	3.314	0.043	0.136	2.428	33.2673	0.1158	3.3547
Er	33.9255	0.1178	3.5663	33.936	0.1177	3.542	0.031	0.11	0.684	33.9307	0.1177	3.5542
Tm	34.3535	0.1203	3.7116	34.3633	0.1202	3.7208	0.029	0.135	0.249	34.3584	0.1202	3.7162
Yb	34.635	0.1261	3.8441	34.6442	0.1259	3.8205	0.027	0.126	0.617	34.6396	0.126	3.8323
Lu	29.6266	0.2681	3.2169	29.6248	0.2679	3.2113	0.006	0.073	0.174	29.6257	0.268	3.2141
Hf	22.3067	0.6218	3.2861	22.3027	0.6214	3.2844	0.018	0.064	0.052	22.3047	0.6216	3.2853
Ta	18.2932	1.205	3.7558	18.2908	1.2046	3.7539	0.013	0.035	0.05	18.292	1.2048	3.7548
W	16.1467	1.8822	4.1745	16.1442	1.8818	4.1705	0.015	0.02	0.095	16.1455	1.882	4.1725
Re	15.1073	2.2046	4.5288	15.1016	2.2063	4.5158	0.038	0.076	0.286	15.1045	2.2055	4.5223
Os	14.7808	2.1925	4.7889	14.7809	2.1932	4.7823	0.001	0.035	0.139	14.7808	2.1928	4.7856

Table S4.2. (continued) Table with all calculated EOS parameters for the BCC structures obtained with FLEUR and WIEN2k.

	FLEUR			WIEN2k			Abs. percentage difference [%]			Average set		
	V_0 [Å^3]	B_0 [eV/Å^3]	B_1	V_0 [Å^3]	B_0 [eV/Å^3]	B_1	$\lvert\eta(V_0)\rvert$	$\lvert\eta(B_0)\rvert$	$\lvert\eta(B_1)\rvert$	V_0 [Å^3]	B_0 [eV/Å^3]	B_1
Ir	15.056	1.9137	5.0731	15.0553	1.9144	5.0693	0.004	0.039	0.075	15.0556	1.914	5.0712
Pt	15.8403	1.4858	5.4335	15.8376	1.4856	5.4384	0.017	0.015	0.089	15.839	1.4857	5.4359
Au	18.0432	0.8546	5.9833	18.041	0.854	5.9619	0.012	0.08	0.359	18.0421	0.8543	5.9726
Hg	29.249	0.0581	11.1694	29.2253	0.0584	11.0589	0.081	0.503	0.995	29.2372	0.0582	11.1142
Tl	31.4166	0.1647	5.4169	31.4121	0.165	5.3618	0.014	0.139	1.024	31.4144	0.1649	5.3894
Pb	31.9714	0.242	4.7531	31.9695	0.2423	4.7998	0.006	0.091	0.978	31.9704	0.2421	4.7765
Bi	31.6372	0.3248	4.6163	31.6321	0.3252	4.6367	0.016	0.131	0.441	31.6347	0.325	4.6265
Po	32.8474	0.3122	4.9521	32.8603	0.3123	4.951	0.039	0.023	0.023	32.8539	0.3123	4.9515
At	39.9964	0.1447	5.6798	40.0182	0.1446	5.6615	0.055	0.1	0.322	40.0073	0.1446	5.6706
Rn	95.493	0.0032	7.107	95.4013	0.0032	7.42	0.096	0.277	4.31	95.4471	0.0032	7.2635
Fr	116.5004	0.0118	3.5266	116.4842	0.0118	3.643	0.014	0.038	3.248	116.4923	0.0118	3.5848
Ra	70.9581	0.0473	3.2814	70.9756	0.0473	3.2125	0.025	0.07	2.122	70.9669	0.0473	3.247
Ac	45.938	0.1539	3.4041	45.9494	0.1538	3.3968	0.025	0.064	0.215	45.9437	0.1538	3.4005
Th	32.5629	0.3669	3.6094	32.5726	0.3669	3.6279	0.03	0.004	0.512	32.5677	0.3669	3.6186
Pa	24.8014	0.5641	3.652	24.7928	0.5655	3.6564	0.035	0.257	0.119	24.7971	0.5648	3.6542
U	20.2709	0.8144	4.9757	20.2615	0.814	4.9748	0.046	0.043	0.018	20.2662	0.8142	4.9752
Np	17.8121	1.0613	5.4074	17.8038	1.0624	5.3942	0.046	0.101	0.244	17.8079	1.0618	5.4008
Pu	16.5687	1.2318	5.8048	16.56	1.2319	5.8002	0.052	0.006	0.078	16.5643	1.2318	5.8025
Am	16.1958	1.2122	6.1435	16.1863	1.2124	6.1559	0.058	0.016	0.201	16.1911	1.2123	6.1497

Table S4.3. Table with all calculated EOS parameters for the SC structures obtained with FLEUR and WIEN2k.

	FLEUR			WIEN2k			Abs. percentage difference [%]			Average set		
	V_0 [Å^3]	B_0 [eV/Å^3]	B_1	V_0 [Å^3]	B_0 [eV/Å^3]	B_1	$\lvert\eta(V_0)\rvert$	$\lvert\eta(B_0)\rvert$	$\lvert\eta(B_1)\rvert$	V_0 [Å^3]	B_0 [eV/Å^3]	B_1
H	3.0874	0.6395	3.2502	3.0859	0.6375	3.2341	0.047	0.312	0.497	3.0867	0.6385	3.2421
He	21.4945	0.0037	6.3014	21.476	0.0037	6.8211	0.086	0.081	7.921	21.4853	0.0037	6.5613
Li	20.4075	0.0764	3.3063	20.4101	0.0765	3.312	0.013	0.064	0.173	20.4088	0.0765	3.3091
Be	10.2668	0.4705	3.3596	10.2677	0.4705	3.3576	0.009	0.007	0.057	10.2672	0.4705	3.3586
B	6.7003	1.4616	3.6331	6.7006	1.4619	3.6397	0.004	0.022	0.181	6.7005	1.4618	3.6364
C	5.583	2.0602	4.3081	5.5814	2.0606	4.3233	0.028	0.021	0.353	5.5822	2.0604	4.3157
N	6.481	1.2978	3.4544	6.4789	1.289	3.4364	0.032	0.678	0.522	6.4799	1.2934	3.4454
O	7.9532	1.0734	4.5927	7.9538	1.0704	4.5533	0.008	0.287	0.861	7.9535	1.0719	4.573
F	10.5176	0.3845	5.4747	10.5243	0.3834	5.404	0.063	0.296	1.3	10.5209	0.384	5.4394
Ne	29.7778	0.0052	6.1053	29.7126	0.0053	7.418	0.219	1.769	19.414	29.7452	0.0053	6.7616
Na	39.7536	0.0385	3.6918	39.7491	0.0385	3.7042	0.011	0.041	0.336	39.7514	0.0385	3.698
Mg	27.5827	0.1415	3.984	27.5785	0.1416	3.9843	0.015	0.04	0.007	27.5806	0.1416	3.9841
Al	20.1542	0.3544	4.4176	20.1561	0.3545	4.4195	0.01	0.028	0.044	20.1551	0.3545	4.4185
Si	16.2298	0.6282	4.4066	16.2288	0.6284	4.4058	0.006	0.026	0.02	16.2293	0.6283	4.4062
P	14.6578	0.6811	4.9192	14.6551	0.6815	4.9229	0.018	0.058	0.076	14.6564	0.6813	4.921
S	17.2218	0.522	4.1068	17.2177	0.5213	4.1069	0.024	0.125	0.004	17.2197	0.5216	4.1068
Cl	23.4607	0.2102	5.3804	23.4673	0.2098	5.377	0.028	0.2	0.063	23.464	0.21	5.3787
Ar	65.2384	0.003	7.5779	65.243	0.003	7.5506	0.007	0.241	0.361	65.2407	0.003	7.5643
K	79.3514	0.0173	3.7687	79.3575	0.0173	3.7676	0.008	0.109	0.029	79.3544	0.0173	3.7681
Ca	43.5743	0.0673	3.2681	43.5955	0.0672	3.278	0.049	0.078	0.303	43.5849	0.0672	3.2731
Sc	26.1489	0.2207	3.0076	26.1472	0.2206	3.0028	0.006	0.052	0.159	26.1481	0.2207	3.0052
Ti	18.4119	0.4871	3.4207	18.4145	0.4873	3.4201	0.014	0.035	0.017	18.4132	0.4872	3.4204
V	14.6788	0.8557	3.8363	14.6814	0.8555	3.839	0.017	0.026	0.069	14.6801	0.8556	3.8377
Cr	12.8052	1.1825	4.1204	12.8087	1.1813	4.0984	0.027	0.101	0.535	12.807	1.1819	4.1094
Mn	11.9003	1.3227	4.3317	11.8974	1.3262	4.3173	0.024	0.263	0.333	11.8988	1.3245	4.3245
Fe	11.6521	1.3003	4.5659	11.6506	1.3015	4.5003	0.013	0.095	1.447	11.6513	1.3009	4.5331
Co	11.8942	1.1472	4.7121	11.8924	1.149	4.6772	0.015	0.156	0.742	11.8933	1.1481	4.6946
Ni	12.5603	0.9185	4.8179	12.5578	0.9184	4.8409	0.02	0.004	0.475	12.559	0.9184	4.8294
Cu	13.936	0.642	5.0255	13.9339	0.6415	5.0067	0.015	0.082	0.375	13.935	0.6418	5.0161
Zn	18.1858	0.2984	5.2318	18.1722	0.2988	5.2246	0.075	0.134	0.137	18.179	0.2986	5.2282
Ga	20.1201	0.2876	4.8808	20.1145	0.2879	4.8731	0.027	0.124	0.157	20.1173	0.2877	4.877
Ge	19.9366	0.4203	4.6635	19.9469	0.4207	4.6681	0.052	0.076	0.099	19.9417	0.4205	4.6658
As	20.3702	0.4853	4.2814	20.3653	0.4852	4.282	0.024	0.009	0.015	20.3677	0.4853	4.2817
Se	22.6842	0.438	4.5607	22.6826	0.4378	4.5614	0.007	0.051	0.017	22.6834	0.4379	4.5611
Br	29.8252	0.1817	5.5123	29.8305	0.1814	5.5161	0.018	0.143	0.068	29.8279	0.1815	5.5142
Kr	82.6561	0.0026	7.5608	82.673	0.0026	7.6448	0.02	0.083	1.104	82.6645	0.0026	7.6028
Rb	98.963	0.0134	3.8286	98.9959	0.0134	3.8462	0.033	0.091	0.461	98.9794	0.0134	3.8374
Sr	57.1139	0.0441	3.3167	57.1441	0.0441	3.3067	0.053	0.128	0.3	57.129	0.0441	3.3117

Table S4.3. (continued) Table with all calculated EOS parameters for the SC structures obtained with FLEUR and WIEN2k.

	FLEUR			WIEN2k			Abs. percentage difference [%]			Average set		
	V_0 [Å^3]	B_0 [eV/Å^3]	B_1	V_0 [Å^3]	B_0 [eV/Å^3]	B_1	$\lvert\eta(V_0)\rvert$	$\lvert\eta(B_0)\rvert$	$\lvert\eta(B_1)\rvert$	V_0 [Å^3]	B_0 [eV/Å^3]	B_1
Y	34.8139	0.1623	2.999	34.82	0.1621	2.9973	0.017	0.083	0.057	34.817	0.1622	2.9981
Zr	24.7427	0.4236	3.5598	24.7436	0.4234	3.5602	0.003	0.056	0.012	24.7431	0.4235	3.56
Nb	20.1141	0.8088	3.8577	20.1157	0.8088	3.8587	0.008	0.002	0.026	20.1149	0.8088	3.8582
Mo	17.595	1.1805	4.1904	17.5976	1.1806	4.1953	0.015	0.009	0.117	17.5963	1.1806	4.1928
Tc	16.2338	1.3921	4.4901	16.2362	1.392	4.4906	0.015	0.005	0.011	16.235	1.3921	4.4903
Ru	15.837	1.3752	4.7774	15.8392	1.3746	4.7724	0.014	0.042	0.104	15.8381	1.3749	4.7749
Rh	16.3085	1.1425	5.0996	16.3021	1.1438	5.0755	0.04	0.12	0.474	16.3053	1.1431	5.0876
Pd	17.8659	0.7573	5.4482	17.8568	0.757	5.4601	0.051	0.036	0.218	17.8613	0.7572	5.4541
Ag	20.8117	0.418	5.8119	20.8039	0.4174	5.8181	0.037	0.157	0.106	20.8078	0.4177	5.815
Cd	26.926	0.1877	5.92	26.9212	0.1875	5.9102	0.018	0.088	0.165	26.9236	0.1876	5.9151
In	29.5572	0.1921	5.3733	29.5432	0.1921	5.4208	0.048	0.025	0.88	29.5502	0.1921	5.3971
Sn	29.4675	0.2884	4.8621	29.4386	0.2891	4.8783	0.098	0.243	0.332	29.453	0.2887	4.8702
Sb	30.0607	0.3417	4.6294	30.0661	0.3419	4.651	0.018	0.047	0.463	30.0634	0.3418	4.6402
Te	32.7941	0.3128	4.7768	32.7929	0.3129	4.7803	0.004	0.04	0.072	32.7935	0.3128	4.7785
I	41.5604	0.1396	5.6332	41.5659	0.1395	5.6517	0.013	0.052	0.329	41.5632	0.1395	5.6425
Xe	109.7961	0.0022	7.5385	109.8143	0.0022	7.1069	0.017	0.823	5.894	109.8052	0.0022	7.3227
Cs	128.3473	0.0096	3.7133	128.3708	0.0096	3.6686	0.018	0.075	1.213	128.3591	0.0096	3.6909
Ba	61.6074	0.0457	3.5585	61.6038	0.0456	3.5548	0.006	0.153	0.104	61.6056	0.0457	3.5566
La	36.7453	0.1485	3.6159	36.7448	0.1484	3.6219	0.001	0.077	0.168	36.7451	0.1485	3.6189
Ce	24.9216	0.3227	4.4791	24.9204	0.3227	4.4442	0.005	0.003	0.782	24.921	0.3227	4.4616
Pr	20.1536	0.5575	6.9047	20.148	0.5573	6.9101	0.028	0.041	0.079	20.1508	0.5574	6.9074
Nd	18.0792	0.7224	6.7109	18.0738	0.7229	6.6953	0.03	0.074	0.232	18.0765	0.7227	6.7031
Pm	17.3001	0.7216	6.8092	17.2963	0.7203	6.7693	0.022	0.173	0.587	17.2982	0.721	6.7893
Sm	17.198	0.6058	7.1606	17.195	0.6038	7.1047	0.018	0.333	0.783	17.1965	0.6048	7.1327
Eu	17.7969	0.395	8.4181	17.7934	0.3936	8.3252	0.02	0.368	1.11	17.7951	0.3943	8.3716
Gd	20.8194	0.0965	6.6479	20.7998	0.0964	6.6333	0.094	0.152	0.22	20.8096	0.0965	6.6406
Tb	27.8155	0.0665	2.5703	27.8244	0.0658	2.4522	0.032	1.078	4.703	27.8199	0.0662	2.5112
Dy	31.8504	0.0749	2.9649	31.864	0.0749	2.8942	0.042	0.079	2.411	31.8572	0.0749	2.9295
Ho	34.29	0.0784	3.1948	34.2982	0.0783	3.2963	0.024	0.126	3.126	34.2941	0.0783	3.2455
Er	35.9379	0.0788	3.783	35.9482	0.0786	3.8649	0.029	0.298	2.144	35.943	0.0787	3.824
Tm	37.2005	0.0756	4.2955	37.215	0.0755	4.3001	0.039	0.181	0.107	37.2078	0.0755	4.2978
Yb	38.635	0.0705	3.7553	38.6483	0.0703	3.8209	0.035	0.295	1.731	38.6416	0.0704	3.7881
Lu	32.9416	0.1821	3.0603	32.9384	0.1819	3.065	0.01	0.143	0.155	32.94	0.182	3.0627
Hf	24.7831	0.4561	3.4957	24.7792	0.4559	3.4795	0.016	0.055	0.464	24.7811	0.456	3.4876
Ta	20.668	0.8883	3.7951	20.6658	0.8878	3.7929	0.011	0.055	0.058	20.6669	0.888	3.794
W	18.3706	1.3303	4.149	18.3683	1.3298	4.1497	0.012	0.035	0.017	18.3695	1.3301	4.1494
Re	17.1636	1.6135	4.349	17.1586	1.6145	4.3436	0.029	0.059	0.123	17.1611	1.614	4.3463
Os	16.7309	1.6894	4.6804	16.7298	1.69	4.7023	0.006	0.038	0.467	16.7304	1.6897	4.6914
Ir	16.9953	1.5332	5.0268	16.9937	1.5338	5.0391	0.01	0.039	0.245	16.9945	1.5335	5.0329
Pt	18.0886	1.1568	5.4495	18.0835	1.1565	5.4557	0.028	0.026	0.115	18.0861	1.1567	5.4526
Au	20.7721	0.6615	5.6053	20.7671	0.6607	5.6111	0.024	0.125	0.102	20.7696	0.6611	5.6082
Hg	29.8599	0.0844	11.2909	29.8488	0.0845	11.2626	0.037	0.16	0.251	29.8543	0.0844	11.2768
Tl	34.3945	0.1364	5.3247	34.3936	0.1363	5.3359	0.003	0.077	0.211	34.3941	0.1363	5.3303
Pb	34.4761	0.2203	4.8671	34.4756	0.2202	4.9282	0.001	0.071	1.248	34.4758	0.2203	4.8976
Bi	35.2069	0.2878	4.7012	35.2032	0.2879	4.7136	0.011	0.027	0.263	35.2051	0.2878	4.7074
Po	37.5875	0.2835	4.8811	37.6035	0.2834	4.9108	0.043	0.043	0.608	37.5955	0.2834	4.8959
At	46.13	0.1384	5.6918	46.1581	0.1383	5.6884	0.061	0.136	0.06	46.1441	0.1384	5.6901
Rn	117.7392	0.0023	7.5597	117.5952	0.0023	7.9717	0.122	0.334	5.306	117.6672	0.0023	7.7657
Fr	132.168	0.0098	4.0616	132.1802	0.0099	3.9142	0.009	0.173	3.696	132.1741	0.0098	3.9879
Ra	75.3325	0.032	4.3286	75.3587	0.032	4.3646	0.035	0.242	0.83	75.3456	0.032	4.3466
Ac	49.8216	0.1151	3.5748	49.8365	0.1151	3.5859	0.03	0.054	0.309	49.8291	0.1151	3.5803
Th	35.3222	0.2654	3.3799	35.3421	0.2655	3.3812	0.056	0.056	0.038	35.3321	0.2654	3.3806
Pa	24.0207	0.5066	4.3883	24.0207	0.5061	4.3307	0.0	0.101	1.322	24.0207	0.5063	4.3595
U	19.1249	1.0627	6.5554	19.1199	1.0637	6.5604	0.026	0.093	0.077	19.1224	1.0632	6.5579
Np	17.2751	1.2937	7.4168	17.2717	1.2938	7.3939	0.02	0.008	0.309	17.2734	1.2938	7.4053
Pu	16.369	1.3884	7.0633	16.3653	1.3863	7.0169	0.023	0.152	0.659	16.3672	1.3874	7.0401
Am	16.1199	1.296	6.5926	16.1133	1.2914	6.5687	0.041	0.352	0.362	16.1166	1.2937	6.5807

Table S4.4. Table with all calculated EOS parameters for the Diamond structures obtained with FLEUR and WIEN2k.

	FLEUR			WIEN2k			Abs. percentage difference [%]			Average set		
	V_0 [Å^3]	B_0 [eV/Å^3]	B_1	V_0 [Å^3]	B_0 [eV/Å^3]	B_1	$\lvert\eta(V_0)\rvert$	$\lvert\eta(B_0)\rvert$	$\lvert\eta(B_1)\rvert$	V_0 [Å^3]	B_0 [eV/Å^3]	B_1
H	6.8313	0.5712	3.187	6.8309	0.5707	3.1744	0.005	0.083	0.395	6.8311	0.5709	3.1807
He	64.261	0.0017	6.4088	64.1688	0.0017	6.9241	0.144	2.148	7.73	64.2149	0.0017	6.6665
Li	51.373	0.0336	2.9432	51.4004	0.0337	2.9633	0.053	0.235	0.681	51.3867	0.0337	2.9533
Be	29.3729	0.2736	3.442	29.3751	0.2736	3.4413	0.008	0.001	0.019	29.374	0.2736	3.4417
B	16.6272	1.1051	3.5246	16.6255	1.1056	3.5309	0.01	0.039	0.178	16.6263	1.1054	3.5277
C	11.3933	2.7062	3.7134	11.3897	2.7041	3.7087	0.031	0.078	0.126	11.3915	2.7052	3.7111
N	18.3562	0.9779	3.3817	18.3504	0.9761	3.3695	0.032	0.192	0.36	18.3533	0.977	3.3756
O	21.3621	0.7423	4.4205	21.3637	0.7391	4.4212	0.007	0.429	0.017	21.3629	0.7407	4.4209
F	28.9918	0.2395	5.3704	29.0178	0.239	5.3299	0.09	0.209	0.756	29.0048	0.2392	5.3501
Ne	89.2362	0.0024	5.9601	89.0586	0.0024	7.3918	0.199	0.251	21.446	89.1474	0.0024	6.676
Na	109.1428	0.018	3.4482	109.1433	0.018	3.4443	0.0	0.024	0.114	109.1431	0.018	3.4462
Mg	80.8557	0.067	4.2292	80.8477	0.067	4.2271	0.01	0.036	0.049	80.8517	0.067	4.2281
Al	55.2517	0.2326	4.1733	55.2645	0.2328	4.1789	0.023	0.074	0.132	55.2581	0.2327	4.1761
Si	40.9112	0.5523	4.3107	40.9187	0.5525	4.3129	0.018	0.038	0.051	40.9149	0.5524	4.3118
P	41.3192	0.2689	2.5921	41.3174	0.2693	2.6067	0.004	0.116	0.562	41.3183	0.2691	2.5994
S	48.5624	0.2741	3.5373	48.5618	0.274	3.5419	0.001	0.067	0.131	48.5621	0.2741	3.5396
Cl	67.5006	0.1112	5.0519	67.5292	0.111	5.05	0.042	0.21	0.037	67.5149	0.1111	5.0509
Ar	197.137	0.0013	7.6557	197.2704	0.0013	7.5226	0.068	0.279	1.754	197.2037	0.0013	7.5891
K	223.7741	0.0075	3.2427	223.8349	0.0075	3.2341	0.027	0.048	0.265	223.8045	0.0075	3.2384
Ca	159.9347	0.0258	2.7288	160.004	0.0258	2.752	0.043	0.082	0.845	159.9694	0.0258	2.7404
Sc	68.9085	0.0529	5.6154	68.9217	0.0528	5.6117	0.019	0.204	0.066	68.9151	0.0529	5.6135
Ti	45.8349	0.2145	2.8216	45.8494	0.2145	2.8207	0.032	0.024	0.034	45.8422	0.2145	2.8211
V	37.2372	0.4015	4.1376	37.2429	0.4012	4.1531	0.015	0.091	0.374	37.2401	0.4014	4.1454
Cr	33.0699	0.6393	3.8386	33.0719	0.6377	3.8602	0.006	0.241	0.562	33.0709	0.6385	3.8494
Mn	30.3422	0.9094	4.1675	30.3443	0.9084	4.1932	0.007	0.106	0.615	30.3433	0.9089	4.1803
Fe	28.9258	0.9648	4.5131	28.9231	0.9701	4.4838	0.009	0.548	0.652	28.9244	0.9674	4.4985
Co	29.7685	0.8247	4.661	29.7703	0.8245	4.6504	0.006	0.019	0.228	29.7694	0.8246	4.6557
Ni	33.0094	0.5736	4.9039	33.0149	0.573	4.8377	0.017	0.107	1.359	33.0121	0.5733	4.8708
Cu	38.3545	0.3404	5.0518	38.3541	0.3404	5.009	0.001	0.017	0.852	38.3543	0.3404	5.0304
Zn	49.3719	0.1621	5.4829	49.3228	0.1626	5.4787	0.1	0.27	0.077	49.3474	0.1624	5.4808
Ga	50.8443	0.2224	5.0671	50.8317	0.2227	5.0464	0.025	0.151	0.409	50.838	0.2225	5.0568
Ge	47.8118	0.3676	4.8605	47.8414	0.3679	4.8634	0.062	0.099	0.06	47.8266	0.3677	4.862
As	57.0375	0.2887	3.7829	57.0294	0.2887	3.7836	0.014	0.012	0.019	57.0335	0.2887	3.7832
Se	63.5122	0.2416	4.0937	63.5093	0.2414	4.0976	0.005	0.062	0.095	63.5108	0.2415	4.0956
Br	86.1607	0.0936	5.1914	86.1815	0.0934	5.196	0.024	0.157	0.089	86.1711	0.0935	5.1937
Kr	249.6157	0.0012	7.5826	249.8003	0.0011	7.4128	0.074	0.481	2.264	249.708	0.0012	7.4977
Rb	282.6956	0.006	3.3031	282.8151	0.006	3.3219	0.042	0.085	0.566	282.7553	0.006	3.3125
Sr	223.7041	0.0166	2.8787	223.8602	0.0166	2.885	0.07	0.182	0.218	223.7821	0.0166	2.8818
Y	87.5058	0.0596	12.0946	87.5316	0.0594	12.1272	0.029	0.36	0.269	87.5187	0.0595	12.1109
Zr	61.9019	0.2261	3.0939	61.9182	0.226	3.0964	0.026	0.043	0.079	61.9101	0.2261	3.0951
Nb	51.5539	0.4169	4.2926	51.5685	0.4167	4.2936	0.028	0.046	0.022	51.5612	0.4168	4.2931
Mo	46.002	0.6665	4.1127	46.0131	0.6662	4.1135	0.024	0.044	0.021	46.0076	0.6663	4.1131
Tc	42.4877	0.9419	4.3428	42.496	0.9413	4.3456	0.02	0.061	0.063	42.4919	0.9416	4.3442
Ru	40.5816	1.0202	4.749	40.5911	1.0194	4.75	0.023	0.081	0.021	40.5864	1.0198	4.7495
Rh	41.9043	0.8031	5.1337	41.8966	0.8034	5.1526	0.018	0.037	0.368	41.9005	0.8032	5.1432
Pd	49.0237	0.4123	5.3756	49.0014	0.4126	5.3725	0.046	0.051	0.059	49.0125	0.4125	5.3741
Ag	60.1492	0.1879	5.6843	60.1277	0.1875	5.6848	0.036	0.222	0.01	60.1384	0.1877	5.6845
Cd	74.9104	0.0896	6.4878	74.9057	0.0894	6.4901	0.006	0.203	0.035	74.908	0.0895	6.489
In	76.4444	0.1326	5.427	76.4197	0.1328	5.4097	0.032	0.098	0.32	76.4321	0.1327	5.4183
Sn	73.7	0.2228	4.8941	73.6755	0.2233	4.8812	0.033	0.239	0.265	73.6878	0.223	4.8876
Sb	85.3537	0.1941	4.0543	85.3764	0.1942	4.0633	0.027	0.035	0.222	85.3651	0.1941	4.0588
Te	92.7994	0.1654	4.3252	92.8011	0.1654	4.3128	0.002	0.01	0.287	92.8003	0.1654	4.319
I	121.132	0.068	5.2277	121.1585	0.068	5.1889	0.022	0.069	0.744	121.1453	0.068	5.2083
Xe	331.7058	0.001	7.9642	332.0765	0.001	6.4733	0.112	1.189	20.653	331.8912	0.001	7.2187
Cs	377.4743	0.0042	3.1368	377.5496	0.0042	3.1689	0.02	0.005	1.019	377.512	0.0042	3.1528
Ba	113.1746	0.0514	7.9982	113.1653	0.0514	7.9943	0.008	0.094	0.048	113.17	0.0514	7.9963
La	74.6383	0.2717	6.127	74.6378	0.2717	6.1047	0.001	0.005	0.365	74.6381	0.2717	6.1158
Ce	60.3705	0.4629	5.5056	60.3688	0.4629	5.4716	0.003	0.003	0.619	60.3696	0.4629	5.4886
Pr	52.4385	0.5967	5.3371	52.4417	0.5958	5.3009	0.006	0.146	0.68	52.4401	0.5962	5.319
Nd	47.0989	0.705	5.2066	47.0994	0.7035	5.2084	0.001	0.213	0.036	47.0991	0.7042	5.2075
Pm	43.3021	0.7876	5.2688	43.3073	0.7853	5.2245	0.012	0.294	0.844	43.3047	0.7864	5.2467
Sm	41.8033	0.7644	5.6933	41.8077	0.7642	5.6341	0.01	0.031	1.046	41.8055	0.7643	5.6637
Eu	41.3631	0.6835	5.7182	41.367	0.6835	5.7299	0.009	0.009	0.204	41.3651	0.6835	5.724
Gd	41.8933	0.5828	5.6631	41.8952	0.5816	5.7741	0.005	0.209	1.941	41.8943	0.5822	5.7186
Tb	43.3904	0.4624	6.0834	43.3955	0.4602	6.1309	0.012	0.48	0.779	43.3929	0.4613	6.1071
Dy	46.0171	0.3281	6.7201	46.0237	0.3254	6.7199	0.014	0.824	0.003	46.0204	0.3268	6.72

Table S4.4. (continued) Table with all calculated EOS parameters for the Diamond structures obtained with FLEUR and WIEN2k.

	FLEUR			WIEN2k			Abs. percentage difference [%]			Average set		
	V_0 [Å^3]	B_0 [eV/Å^3]	B_1	V_0 [Å^3]	B_0 [eV/Å^3]	B_1	$\lvert\eta(V_0)\rvert$	$\lvert\eta(B_0)\rvert$	$\lvert\eta(B_1)\rvert$	V_0 [Å^3]	B_0 [eV/Å^3]	B_1
Ho	50.8449	0.1676	8.5397	50.8553	0.1662	8.4731	0.02	0.858	0.783	50.8501	0.1669	8.5064
Er	160.6478	0.0148	1.0607	160.7886	0.0148	1.1138	0.088	0.216	4.882	160.7182	0.0148	1.0872
Tm	163.2829	0.0176	2.3546	163.4196	0.0176	2.2266	0.084	0.151	5.589	163.3513	0.0176	2.2906
Yb	164.0753	0.0208	3.0708	164.1581	0.0207	3.1395	0.05	0.427	2.214	164.1167	0.0207	3.1052
Lu	101.2246	0.0756	1.2875	101.2119	0.0755	1.2857	0.012	0.169	0.141	101.2182	0.0755	1.2866
Hf	70.1618	0.1856	1.3045	70.1537	0.1854	1.2705	0.012	0.152	2.644	70.1577	0.1855	1.2875
Ta	56.8216	0.434	3.1658	56.8156	0.4334	3.1603	0.011	0.125	0.171	56.8186	0.4337	3.1631
W	49.5508	0.7463	3.7671	49.5502	0.7458	3.7655	0.001	0.064	0.042	49.5505	0.7461	3.7663
Re	45.1497	1.1074	4.1935	45.1479	1.1064	4.2016	0.004	0.088	0.193	45.1488	1.1069	4.1975
Os	42.896	1.2777	4.6029	42.9047	1.2781	4.622	0.02	0.031	0.415	42.9003	1.2779	4.6125
Ir	43.191	1.1503	5.0186	43.1961	1.1503	5.0315	0.012	0.001	0.257	43.1936	1.1503	5.0251
Pt	48.2347	0.7149	5.4439	48.2252	0.7152	5.4399	0.02	0.038	0.074	48.23	0.715	5.4419
Au	58.5475	0.3294	5.8992	58.5355	0.329	5.8941	0.021	0.114	0.085	58.5415	0.3292	5.8966
Hg	112.6094	0.0109	3.0526	112.5553	0.0109	3.0507	0.048	0.075	0.062	112.5823	0.0109	3.0516
Tl	90.2877	0.0871	5.3074	90.2882	0.0869	5.2158	0.001	0.152	1.74	90.2879	0.087	5.2616
Pb	88.087	0.1578	4.7587	88.0929	0.1578	4.768	0.007	0.014	0.195	88.09	0.1578	4.7633
Bi	96.9046	0.1791	4.3845	96.8998	0.1792	4.407	0.005	0.078	0.512	96.9022	0.1791	4.3957
Po	104.9406	0.1594	4.5595	104.9864	0.1594	4.5755	0.044	0.045	0.349	104.9635	0.1594	4.5675
At	133.7802	0.0686	5.3927	133.8686	0.0685	5.4205	0.066	0.144	0.514	133.8244	0.0685	5.4066
Rn	353.936	0.001	7.3908	353.8739	0.001	6.3754	0.018	0.07	14.753	353.9049	0.001	6.8831
Fr	384.0058	0.005	3.8935	384.0585	0.005	3.9506	0.014	0.057	1.457	384.0322	0.005	3.9221
Ra	339.2135	0.0078	2.2419	339.4608	0.0078	2.2052	0.073	0.009	1.65	339.3372	0.0078	2.2236
Ac	129.7348	0.079	2.8551	129.789	0.0789	2.8666	0.042	0.051	0.399	129.7619	0.0789	2.8609
Th	91.4342	0.1837	1.3304	91.4964	0.1841	1.3627	0.068	0.256	2.4	91.4653	0.1839	1.3465
Pa	61.0137	0.4614	8.1922	61.0251	0.461	8.1849	0.019	0.079	0.088	61.0194	0.4612	8.1885
U	49.5156	1.0105	5.6685	49.5244	1.0103	5.6705	0.018	0.024	0.036	49.52	1.0104	5.6695
Np	42.9415	1.3789	5.4786	42.9651	1.3746	5.5132	0.055	0.309	0.63	42.9533	1.3768	5.4959
Pu	40.3928	1.3883	5.1144	40.4223	1.3837	5.113	0.073	0.334	0.028	40.4076	1.386	5.1137
Am	38.9056	1.4247	5.3961	38.9465	1.4232	5.3762	0.105	0.106	0.37	38.9261	1.424	5.3862

Table S4.5. Table with all calculated EOS parameters for the X_2O structures obtained with FLEUR and WIEN2k.

	FLEUR			WIEN2k			Abs. percentage difference [%]			Average set		
	V_0 [Å^3]	B_0 [eV/Å^3]	B_1	V_0 [Å^3]	B_0 [eV/Å^3]	B_1	$\lvert\eta(V_0)\rvert$	$\lvert\eta(B_0)\rvert$	$\lvert\eta(B_1)\rvert$	V_0 [Å^3]	B_0 [eV/Å^3]	B_1
H	11.9643	1.2194	3.8782	11.9627	1.2122	3.8508	0.013	0.593	0.708	11.9635	1.2158	3.8645
He	92.2182	0.003	6.5355	92.1387	0.003	6.363	0.086	0.848	2.674	92.1785	0.003	6.4493
Li	24.7216	0.4951	3.8922	24.7224	0.4948	3.8849	0.003	0.051	0.189	24.722	0.4949	3.8885
Be	26.8278	0.672	3.2268	26.8396	0.6725	3.2323	0.044	0.071	0.172	26.8337	0.6722	3.2296
B	30.0246	0.4338	1.9828	30.0324	0.4342	1.9891	0.026	0.083	0.318	30.0285	0.434	1.986
C	28.5544	0.6939	3.606	28.5543	0.6934	3.6067	0.0	0.082	0.02	28.5543	0.6937	3.6064
N	26.6671	0.8843	4.2476	26.6692	0.8829	4.2274	0.008	0.158	0.477	26.6682	0.8836	4.2375
O	27.1117	0.8128	4.643	27.1151	0.8112	4.6361	0.012	0.195	0.149	27.1134	0.812	4.6396
F	30.9613	0.5015	5.0915	30.9701	0.4998	5.0535	0.028	0.35	0.749	30.9657	0.5006	5.0725
Ne	95.5957	0.0048	6.4474	95.7781	0.0048	6.4351	0.191	0.111	0.191	95.6869	0.0048	6.4413
Na	43.7236	0.2828	4.3085	43.6988	0.2823	4.304	0.057	0.176	0.107	43.7112	0.2826	4.3062
Mg	44.8566	0.3636	3.5867	44.867	0.3641	3.5958	0.023	0.119	0.256	44.8618	0.3638	3.5912
Al	46.2148	0.3543	5.2181	46.2185	0.3547	5.2263	0.008	0.103	0.157	46.2166	0.3545	5.2222
Si	42.6871	0.5304	4.3768	42.6717	0.5307	4.3761	0.036	0.058	0.016	42.6794	0.5306	4.3764
P	40.0302	0.6221	4.0297	40.0252	0.6222	4.0305	0.012	0.011	0.019	40.0277	0.6222	4.0301
S	42.6931	0.5406	4.1676	42.6992	0.5406	4.17	0.014	0.004	0.056	42.6962	0.5406	4.1688
Cl	54.5559	0.259	4.8178	54.5641	0.2589	4.8256	0.015	0.073	0.161	54.56	0.259	4.8217
Ar	113.1482	0.0104	7.1012	113.3687	0.0103	7.0708	0.195	0.965	0.428	113.2584	0.0103	7.086
K	67.9898	0.1685	4.4457	68.0148	0.1683	4.4542	0.037	0.17	0.19	68.0023	0.1684	4.45
Ca	56.0583	0.294	4.1293	56.1278	0.2942	4.1313	0.124	0.064	0.049	56.0931	0.2941	4.1303
Sc	43.1192	0.5698	4.2475	43.1212	0.5692	4.2448	0.005	0.108	0.064	43.1202	0.5695	4.2461
Ti	36.3134	0.917	4.3095	36.319	0.9163	4.2809	0.015	0.077	0.666	36.3162	0.9167	4.2952
V	32.7132	1.1231	4.3089	32.7181	1.1224	4.3032	0.015	0.06	0.134	32.7157	1.1228	4.306
Cr	30.4391	1.2713	4.503	30.4441	1.27	4.5116	0.016	0.105	0.192	30.4416	1.2706	4.5073
Mn	29.5701	1.2827	4.5671	29.5687	1.2914	4.5562	0.005	0.674	0.239	29.5694	1.2871	4.5616
Fe	29.3953	1.2616	4.3721	29.3919	1.2666	4.3648	0.012	0.393	0.167	29.3936	1.2641	4.3685
Co	29.8375	1.1673	4.6595	29.8338	1.1707	4.6512	0.012	0.29	0.179	29.8356	1.169	4.6553

Table S4.5. (continued) Table with all calculated EOS parameters for the X_2O structures obtained with FLEUR and WIEN2k.

	FLEUR			WIEN2k			Abs. percentage difference [%]			Average set		
	V_0 [Å^3]	B_0 [eV/Å^3]	B_1	V_0 [Å^3]	B_0 [eV/Å^3]	B_1	$\lvert\eta(V_0)\rvert$	$\lvert\eta(B_0)\rvert$	$\lvert\eta(B_1)\rvert$	V_0 [Å^3]	B_0 [eV/Å^3]	B_1
Ni	31.6423	0.9558	4.6902	31.6361	0.9569	4.7033	0.02	0.114	0.28	31.6392	0.9564	4.6967
Cu	34.5433	0.7418	4.7184	34.5343	0.7419	4.7268	0.026	0.025	0.177	34.5388	0.7418	4.7226
Zn	40.6708	0.5596	4.7335	40.6658	0.5616	4.7215	0.013	0.345	0.253	40.6683	0.5606	4.7275
Ga	53.0533	0.3085	4.6288	53.0323	0.3086	4.6322	0.04	0.025	0.073	53.0428	0.3085	4.6305
Ge	49.678	0.4595	4.336	49.6873	0.4593	4.3368	0.019	0.042	0.02	49.6827	0.4594	4.3364
As	47.8146	0.5655	4.3413	47.8113	0.5652	4.3407	0.007	0.046	0.014	47.8129	0.5654	4.341
Se	49.9179	0.5224	4.4535	49.9152	0.5223	4.4502	0.006	0.018	0.073	49.9165	0.5224	4.4519
Br	61.6268	0.2482	4.8783	61.6301	0.2478	4.8791	0.005	0.142	0.017	61.6285	0.248	4.8787
Kr	118.8829	0.0176	7.0604	119.0342	0.0174	7.0793	0.127	0.762	0.267	118.9586	0.0175	7.0698
Rb	81.0628	0.1414	4.6202	81.0934	0.1412	4.6227	0.038	0.137	0.054	81.0781	0.1413	4.6214
Sr	70.1388	0.2302	4.2927	70.1704	0.2299	4.2932	0.045	0.129	0.013	70.1546	0.2301	4.293
Y	56.0222	0.4471	4.3458	56.0328	0.4469	4.3441	0.019	0.053	0.039	56.0275	0.447	4.345
Zr	48.082	0.765	4.2783	48.092	0.7646	4.2836	0.021	0.054	0.124	48.087	0.7648	4.281
Nb	43.2779	1.0263	4.1765	43.2877	1.0261	4.1787	0.023	0.021	0.052	43.2828	1.0262	4.1776
Mo	39.7118	1.2512	4.4851	39.7221	1.2507	4.4942	0.026	0.045	0.204	39.717	1.251	4.4897
Tc	38.3641	1.3289	4.3659	38.3734	1.3284	4.372	0.024	0.035	0.14	38.3687	1.3286	4.3689
Ru	37.8808	1.3387	4.7519	37.8885	1.3381	4.7486	0.021	0.047	0.071	37.8847	1.3384	4.7502
Rh	38.8725	1.1497	5.0076	38.8557	1.1491	5.0267	0.043	0.057	0.38	38.8641	1.1494	5.0172
Pd	42.2211	0.8165	5.2311	42.2055	0.8157	5.2561	0.037	0.1	0.476	42.2133	0.8161	5.2436
Ag	48.3945	0.5213	5.2386	48.3817	0.5201	5.2363	0.027	0.231	0.045	48.3881	0.5207	5.2374
Cd	53.0867	0.462	5.0379	53.0788	0.4615	5.041	0.015	0.108	0.061	53.0827	0.4618	5.0395
In	65.9405	0.2698	4.9911	65.922	0.2695	4.9855	0.028	0.114	0.113	65.9313	0.2696	4.9883
Sn	63.5424	0.3822	4.6126	63.4925	0.3822	4.6161	0.079	0.004	0.076	63.5175	0.3822	4.6143
Sb	61.575	0.4688	4.5529	61.5859	0.4688	4.5507	0.018	0.002	0.049	61.5804	0.4688	4.5518
Te	62.9038	0.454	4.6217	62.9019	0.4539	4.6257	0.003	0.039	0.087	62.9029	0.4539	4.6237
I	72.1871	0.2464	5.112	72.1897	0.2463	5.0979	0.004	0.05	0.277	72.1884	0.2464	5.105
Xe	137.1579	0.0218	6.6205	137.2511	0.0217	6.6039	0.068	0.549	0.251	137.2045	0.0217	6.6122
Cs	96.4879	0.1281	4.9767	96.5047	0.1279	4.9601	0.017	0.151	0.335	96.4963	0.128	4.9684
Ba	79.8754	0.22	4.8493	79.9067	0.2209	4.3147	0.039	0.402	11.668	79.891	0.2204	4.582
La	65.133	0.4506	4.7153	65.1381	0.4503	4.7221	0.008	0.052	0.144	65.1355	0.4505	4.7187
Ce	56.1049	0.5813	4.7881	56.1018	0.5802	4.7804	0.006	0.19	0.162	56.1034	0.5807	4.7843
Pr	52.3072	0.6216	4.8786	52.311	0.6207	4.8708	0.007	0.139	0.16	52.3091	0.6212	4.8747
Nd	50.5575	0.6204	4.9753	50.5608	0.6194	4.9654	0.007	0.161	0.201	50.5591	0.6199	4.9703
Pm	49.8314	0.5958	5.0662	49.8362	0.5947	5.0576	0.01	0.172	0.171	49.8338	0.5952	5.0619
Sm	49.7266	0.5579	5.1019	49.7313	0.5567	5.0997	0.009	0.21	0.043	49.729	0.5573	5.1008
Eu	49.9993	0.5209	5.0533	50.0041	0.5196	5.0503	0.01	0.244	0.06	50.0017	0.5202	5.0518
Gd	50.4456	0.487	5.1332	50.4515	0.4857	5.1278	0.012	0.28	0.106	50.4486	0.4864	5.1305
Tb	51.0307	0.4492	5.2826	51.0372	0.4479	5.2677	0.013	0.297	0.282	51.034	0.4485	5.2752
Dy	51.7891	0.4087	5.3301	51.7947	0.4074	5.319	0.011	0.325	0.208	51.7919	0.408	5.3246
Ho	52.7175	0.3704	5.2574	52.7237	0.3693	5.248	0.012	0.314	0.18	52.7206	0.3699	5.2527
Er	53.812	0.337	5.0954	53.8172	0.3359	5.0945	0.01	0.31	0.017	53.8146	0.3364	5.0949
Tm	55.1527	0.3084	4.7068	55.1557	0.3076	4.7082	0.005	0.252	0.031	55.1542	0.308	4.7075
Yb	57.4653	0.299	4.091	57.4608	0.2985	4.0765	0.008	0.194	0.354	57.4631	0.2987	4.0837
Lu	54.0713	0.4225	4.6388	54.0704	0.4219	4.6408	0.002	0.136	0.043	54.0708	0.4222	4.6398
Hf	48.6449	0.7237	4.426	48.6479	0.7231	4.4245	0.006	0.078	0.035	48.6464	0.7234	4.4253
Ta	45.0212	1.0847	3.9429	45.0262	1.0841	3.9425	0.011	0.057	0.011	45.0237	1.0844	3.9427
W	41.7814	1.3209	4.1152	41.7834	1.3205	4.1209	0.005	0.029	0.137	41.7824	1.3207	4.118
Re	40.2033	1.5067	4.3146	40.1811	1.5088	4.3169	0.055	0.141	0.054	40.1922	1.5077	4.3157
Os	39.554	1.5636	4.6328	39.5539	1.5641	4.6374	0.0	0.031	0.098	39.554	1.5638	4.6351
Ir	40.3348	1.4184	4.9284	40.3367	1.4184	4.9339	0.005	0.001	0.111	40.3358	1.4184	4.9311
Pt	43.223	1.0804	5.2233	43.2256	1.0794	5.2067	0.006	0.097	0.318	43.2243	1.0799	5.215
Au	49.4523	0.6533	5.4252	49.4537	0.6526	5.4184	0.003	0.11	0.124	49.453	0.6529	5.4218
Hg	56.1764	0.4151	6.1521	56.1865	0.4145	6.1409	0.018	0.145	0.182	56.1814	0.4148	6.1465
Tl	72.2275	0.2376	5.0125	72.235	0.2374	5.0013	0.01	0.094	0.225	72.2312	0.2375	5.0069
Pb	70.3152	0.3426	4.7213	70.3244	0.3424	4.7241	0.013	0.051	0.058	70.3198	0.3425	4.7227
Bi	69.2388	0.4214	4.6665	69.2445	0.4214	4.6667	0.008	0.003	0.005	69.2416	0.4214	4.6666
Po	70.3131	0.4349	4.7168	70.3442	0.4346	4.723	0.044	0.049	0.131	70.3287	0.4348	4.7199
At	77.7713	0.2745	5.3469	77.811	0.2744	5.3608	0.051	0.018	0.261	77.7911	0.2744	5.3538
Rn	136.6646	0.0285	6.3787	136.6967	0.0284	6.4262	0.023	0.367	0.743	136.6806	0.0284	6.4025
Fr	106.7119	0.1192	5.1714	106.7044	0.1191	5.198	0.007	0.112	0.512	106.7081	0.1191	5.1847
Ra	93.8469	0.1755	4.7814	93.8575	0.1753	4.7883	0.011	0.117	0.145	93.8522	0.1754	4.7848
Ac	80.3641	0.3221	4.6124	80.3893	0.3213	4.7391	0.031	0.238	2.711	80.3767	0.3217	4.6758
Th	68.7644	0.473	3.5657	68.8144	0.4732	3.5385	0.073	0.047	0.767	68.7894	0.4731	3.5521
Pa	56.2942	0.7334	4.449	56.2904	0.7329	4.4338	0.007	0.064	0.342	56.2923	0.7331	4.4414
U	50.1356	0.9174	5.0222	50.1334	0.9169	5.0101	0.004	0.058	0.24	50.1345	0.9171	5.0162
Np	47.2514	1.0145	4.9791	47.246	1.014	4.9669	0.011	0.042	0.245	47.2487	1.0142	4.973

Table S4.5. (continued) Table with all calculated EOS parameters for the X_2O structures obtained with FLEUR and WIEN2k.

	FLEUR			WIEN2k			Abs. percentage difference [%]			Average set		
	V_0 [Å^3]	B_0 [eV/Å^3]	B_1	V_0 [Å^3]	B_0 [eV/Å^3]	B_1	$\lvert\eta(V_0)\rvert$	$\lvert\eta(B_0)\rvert$	$\lvert\eta(B_1)\rvert$	V_0 [Å^3]	B_0 [eV/Å^3]	B_1
Pu	45.8605	1.0171	5.0668	45.8533	1.0164	5.0567	0.016	0.065	0.201	45.8569	1.0168	5.0617
Am	45.4235	0.9482	5.2777	45.4157	0.9472	5.264	0.017	0.105	0.261	45.4196	0.9477	5.2709

Table S4.6. Table with all calculated EOS parameters for the XO structures obtained with FLEUR and WIEN2k.

	FLEUR			WIEN2k			Abs. percentage difference [%]			Average set		
	V_0 [Å^3]	B_0 [eV/Å^3]	B_1	V_0 [Å^3]	B_0 [eV/Å^3]	B_1	$\lvert\eta(V_0)\rvert$	$\lvert\eta(B_0)\rvert$	$\lvert\eta(B_1)\rvert$	V_0 [Å^3]	B_0 [eV/Å^3]	B_1
H	10.0288	1.0197	4.1229	10.0269	1.0187	4.1254	0.019	0.096	0.06	10.0278	1.0192	4.1242
He	31.5746	0.0241	6.0688	31.4823	0.0236	5.979	0.293	2.034	1.491	31.5284	0.0239	6.0239
Li	16.8226	0.4482	4.1939	16.8291	0.4481	4.1855	0.039	0.014	0.201	16.8258	0.4481	4.1897
Be	12.1214	1.5087	3.7923	12.1269	1.5059	3.7899	0.045	0.188	0.064	12.1241	1.5073	3.7911
B	14.7095	1.1486	3.5065	14.7115	1.1488	3.5147	0.014	0.021	0.235	14.7105	1.1487	3.5106
C	15.7031	1.0655	3.8408	15.7004	1.0641	3.8476	0.017	0.13	0.179	15.7018	1.0648	3.8442
N	15.3394	1.1522	4.1425	15.3367	1.1491	4.1256	0.018	0.269	0.409	15.3381	1.1507	4.134
O	15.9065	1.0734	4.5758	15.9076	1.0704	4.5541	0.007	0.282	0.475	15.9071	1.0719	4.5649
F	18.8546	0.6168	5.0487	18.8587	0.6139	5.0048	0.022	0.475	0.872	18.8567	0.6153	5.0267
Ne	47.0572	0.014	6.1749	47.0131	0.0139	7.3535	0.094	0.636	17.425	47.0352	0.0139	6.7642
Na	27.7686	0.2616	4.5297	27.7509	0.2609	4.553	0.064	0.249	0.512	27.7597	0.2612	4.5414
Mg	19.2493	0.9299	4.0911	19.2488	0.9299	4.0908	0.002	0.0	0.008	19.249	0.9299	4.0909
Al	22.4537	0.8324	4.02	22.4593	0.8331	4.0272	0.025	0.088	0.18	22.4565	0.8328	4.0236
Si	24.597	0.7636	4.0882	24.5864	0.7637	4.0907	0.043	0.018	0.061	24.5917	0.7636	4.0894
P	24.3034	0.882	4.2224	24.2986	0.8817	4.2236	0.02	0.039	0.029	24.301	0.8818	4.223
S	24.6841	0.8005	4.5574	24.6806	0.7995	4.522	0.014	0.123	0.781	24.6824	0.8	4.5397
Cl	26.9634	0.5433	5.0451	26.9539	0.5422	5.0464	0.035	0.209	0.026	26.9587	0.5428	5.0458
Ar	39.4369	0.0837	7.185	39.4264	0.0823	7.1055	0.027	1.673	1.112	39.4316	0.083	7.1453
K	42.7409	0.1465	4.4151	42.7499	0.1462	4.4275	0.021	0.211	0.28	42.7454	0.1464	4.4213
Ca	28.1871	0.6569	4.3376	28.1934	0.6562	4.3334	0.022	0.104	0.099	28.1903	0.6565	4.3355
Sc	22.3328	1.0934	4.4061	22.3321	1.0908	4.4344	0.003	0.237	0.639	22.3325	1.0921	4.4202
Ti	19.6186	1.3856	4.4556	19.6185	1.3844	4.4492	0.0	0.084	0.145	19.6186	1.385	4.4524
V	18.3189	1.5087	4.4803	18.3179	1.5086	4.5172	0.006	0.013	0.82	18.3184	1.5086	4.4988
Cr	17.6647	1.5352	4.5242	17.6637	1.5352	4.5357	0.006	0.004	0.252	17.6642	1.5352	4.53
Mn	17.2943	1.5225	4.5751	17.2922	1.5306	4.5411	0.012	0.532	0.745	17.2932	1.5265	4.5581
Fe	17.1387	1.473	4.6559	17.1333	1.4778	4.6697	0.031	0.326	0.296	17.136	1.4754	4.6628
Co	17.2745	1.3831	4.6192	17.2671	1.3867	4.6381	0.043	0.26	0.408	17.2708	1.3849	4.6286
Ni	17.9998	1.2811	4.5727	17.9903	1.2832	4.5995	0.053	0.166	0.584	17.995	1.2821	4.5861
Cu	19.1122	1.1037	4.704	19.1022	1.1037	4.7095	0.052	0.004	0.118	19.1072	1.1037	4.7068
Zn	20.2822	1.03	4.5327	20.2734	1.0351	4.4686	0.043	0.491	1.423	20.2778	1.0326	4.5006
Ga	24.3571	0.77	4.5886	24.3468	0.7711	4.5826	0.042	0.146	0.131	24.3519	0.7705	4.5856
Ge	27.1256	0.7045	4.2741	27.1194	0.7042	4.2781	0.023	0.055	0.093	27.1225	0.7043	4.2761
As	27.1939	0.8167	4.3448	27.1888	0.8159	4.3433	0.019	0.095	0.035	27.1913	0.8163	4.344
Se	28.3558	0.7367	4.6273	28.3506	0.7359	4.6188	0.018	0.104	0.183	28.3532	0.7363	4.6231
Br	31.1092	0.5211	5.1026	31.1041	0.5201	5.0963	0.016	0.199	0.125	31.1066	0.5206	5.0995
Kr	40.0823	0.1593	6.5465	40.0672	0.1578	6.5127	0.038	0.909	0.517	40.0747	0.1585	6.5296
Rb	48.774	0.1139	4.1311	48.7982	0.1137	4.1301	0.05	0.18	0.023	48.7861	0.1138	4.1306
Sr	35.0531	0.5281	4.4898	35.0564	0.5265	4.4609	0.009	0.302	0.645	35.0547	0.5273	4.4753
Y	28.0517	0.86	4.9381	28.0573	0.8587	4.9202	0.02	0.146	0.363	28.0545	0.8594	4.9292
Zr	24.2812	1.2219	4.7424	24.2888	1.2201	4.7201	0.032	0.149	0.471	24.285	1.221	4.7313
Nb	22.3729	1.4366	4.6054	22.3788	1.4347	4.6231	0.026	0.132	0.384	22.3758	1.4356	4.6143
Mo	21.5146	1.5081	4.7153	21.5198	1.5068	4.7072	0.024	0.088	0.173	21.5172	1.5075	4.7113
Tc	21.2137	1.4868	4.8848	21.2164	1.484	4.86	0.013	0.187	0.509	21.2151	1.4854	4.8724
Ru	21.4064	1.3422	4.9435	21.4083	1.3393	4.9313	0.009	0.213	0.247	21.4074	1.3407	4.9374
Rh	22.0167	1.2144	4.8158	21.9984	1.2166	4.8681	0.083	0.179	1.081	22.0076	1.2155	4.8419
Pd	23.3168	1.0706	4.9705	23.3018	1.0693	4.9961	0.065	0.123	0.513	23.3093	1.07	4.9833
Ag	25.5167	0.8029	5.2094	25.5018	0.8021	5.2142	0.058	0.102	0.092	25.5092	0.8025	5.2118
Cd	27.1002	0.7846	4.7875	27.0878	0.7843	4.7972	0.046	0.036	0.203	27.094	0.7845	4.7924
In	30.496	0.6391	4.6496	30.49	0.6384	4.6417	0.02	0.099	0.169	30.493	0.6388	4.6456
Sn	33.548	0.5765	4.4416	33.525	0.5762	4.4402	0.069	0.05	0.031	33.5365	0.5763	4.4409
Sb	33.6171	0.6861	4.4239	33.6237	0.6858	4.4269	0.02	0.052	0.068	33.6204	0.686	4.4254
Te	34.8875	0.6383	4.6109	34.886	0.6378	4.6086	0.004	0.083	0.051	34.8868	0.638	4.6097
I	38.0133	0.4712	5.0921	38.0111	0.4706	5.0889	0.006	0.112	0.062	38.0122	0.4709	5.0905
Xe	45.2557	0.2133	6.1876	45.2458	0.2129	6.1837	0.022	0.202	0.063	45.2507	0.2131	6.1857
Cs	53.2941	0.1183	5.7711	53.2989	0.1181	5.7773	0.009	0.227	0.107	53.2965	0.1182	5.7742

Table S4.6. (continued) Table with all calculated EOS parameters for the XO structures obtained with FLEUR and WIEN2k.

	FLEUR			WIEN2k			Abs. percentage difference [%]			Average set		
	V_0 [Å^3]	B_0 [eV/Å^3]	B_1	V_0 [Å^3]	B_0 [eV/Å^3]	B_1	$\lvert\eta(V_0)\rvert$	$\lvert\eta(B_0)\rvert$	$\lvert\eta(B_1)\rvert$	V_0 [Å^3]	B_0 [eV/Å^3]	B_1
Ba	43.3045	0.4311	4.5876	43.3073	0.431	4.4183	0.006	0.033	3.761	43.3059	0.431	4.503
La	34.4325	0.7778	4.5292	34.4298	0.7764	4.5246	0.008	0.175	0.101	34.4311	0.7771	4.5269
Ce	31.0414	0.9023	4.6582	31.0372	0.9003	4.6647	0.013	0.22	0.139	31.0393	0.9013	4.6615
Pr	30.0816	0.8992	4.6956	30.0777	0.8974	4.6907	0.013	0.192	0.105	30.0796	0.8983	4.6932
Nd	29.4646	0.8822	4.7199	29.4607	0.8804	4.7153	0.013	0.208	0.097	29.4626	0.8813	4.7176
Pm	29.0241	0.8616	4.7484	29.0207	0.8596	4.7463	0.012	0.233	0.045	29.0224	0.8606	4.7474
Sm	28.7161	0.8377	4.7656	28.7124	0.8357	4.7699	0.013	0.243	0.09	28.7142	0.8367	4.7678
Eu	28.5061	0.8124	4.7745	28.5022	0.8105	4.7721	0.014	0.241	0.052	28.5041	0.8115	4.7733
Gd	28.364	0.7891	4.766	28.36	0.7872	4.7647	0.014	0.242	0.027	28.362	0.7882	4.7653
Tb	28.2618	0.7685	4.7563	28.2574	0.7665	4.7574	0.016	0.261	0.022	28.2596	0.7675	4.7568
Dy	28.1783	0.75	4.7596	28.1735	0.7481	4.753	0.017	0.256	0.139	28.1759	0.7491	4.7563
Ho	28.1001	0.7344	4.7882	28.0949	0.7324	4.7761	0.019	0.274	0.252	28.0975	0.7334	4.7821
Er	28.0269	0.7191	4.9937	28.0211	0.7171	4.9779	0.021	0.275	0.317	28.024	0.7181	4.9858
Tm	27.9773	0.7028	5.1303	27.9707	0.7009	5.1177	0.024	0.278	0.247	27.974	0.7018	5.124
Yb	27.9965	0.691	5.0336	27.9894	0.689	5.0221	0.025	0.287	0.228	27.993	0.69	5.0278
Lu	26.561	0.8479	4.6385	26.5595	0.845	4.5987	0.006	0.337	0.861	26.5602	0.8465	4.6186
Hf	24.2304	1.1902	4.4648	24.2354	1.1868	4.4419	0.021	0.284	0.515	24.2329	1.1885	4.4534
Ta	22.8568	1.4431	4.4312	22.8591	1.4385	4.4351	0.01	0.319	0.087	22.8579	1.4408	4.4332
W	22.2354	1.5447	4.493	22.2348	1.5417	4.5216	0.003	0.196	0.635	22.2351	1.5432	4.5073
Re	22.1188	1.53	4.7283	22.1111	1.5266	4.7251	0.035	0.226	0.067	22.1149	1.5283	4.7267
Os	22.5394	1.382	4.6547	22.5302	1.3821	4.6798	0.041	0.008	0.539	22.5348	1.382	4.6672
Ir	23.4107	1.2768	4.5815	23.4035	1.2743	4.5829	0.03	0.193	0.031	23.4071	1.2755	4.5822
Pt	24.653	1.1661	4.956	24.6495	1.1628	4.9088	0.014	0.285	0.957	24.6513	1.1644	4.9324
Au	26.884	0.9036	5.1788	26.8798	0.9014	5.1689	0.016	0.239	0.192	26.8819	0.9025	5.1738
Hg	29.8152	0.7005	5.1745	29.8155	0.6989	5.1586	0.001	0.227	0.306	29.8153	0.6997	5.1665
Tl	33.9607	0.5069	5.3898	33.9589	0.5061	5.3972	0.006	0.153	0.138	33.9598	0.5065	5.3935
Pb	36.5108	0.541	4.5438	36.5132	0.5404	4.5519	0.007	0.11	0.177	36.512	0.5407	4.5478
Bi	36.0231	0.6541	4.5053	36.027	0.6533	4.5014	0.011	0.13	0.087	36.025	0.6537	4.5033
Po	37.3309	0.62	4.6192	37.3438	0.6191	4.613	0.035	0.142	0.134	37.3374	0.6196	4.6161
At	40.7663	0.4652	5.04	40.7823	0.4647	5.0333	0.039	0.118	0.134	40.7743	0.4649	5.0367
Rn	47.5395	0.2419	5.9434	47.5348	0.2416	5.9545	0.01	0.105	0.186	47.5372	0.2417	5.9489
Fr	55.3905	0.1352	6.0272	55.3942	0.135	5.9933	0.007	0.143	0.564	55.3924	0.1351	6.0103
Ra	47.8458	0.383	4.5804	47.8477	0.3827	4.5779	0.004	0.081	0.055	47.8467	0.3828	4.5792
Ac	38.9873	0.6251	4.8161	38.9974	0.6243	4.8117	0.026	0.129	0.091	38.9924	0.6247	4.8139
Th	33.1438	0.9923	4.6506	33.1544	0.9913	4.651	0.032	0.105	0.008	33.1491	0.9918	4.6508
Pa	30.0924	1.1906	4.7538	30.0863	1.1886	4.7462	0.02	0.172	0.159	30.0894	1.1896	4.75
U	28.3623	1.2826	4.9096	28.3541	1.2803	4.9094	0.029	0.173	0.004	28.3582	1.2814	4.9095
Np	27.337	1.3071	4.9982	27.3281	1.3048	4.9926	0.033	0.175	0.113	27.3326	1.3059	4.9954
Pu	26.8478	1.2777	4.9579	26.8393	1.2751	4.9494	0.032	0.208	0.17	26.8436	1.2764	4.9537
Am	26.6697	1.1967	5.0224	26.6613	1.1941	5.0078	0.032	0.218	0.291	26.6655	1.1954	5.0151

Table S4.7. Table with all calculated EOS parameters for the X_2O_3 structures obtained with FLEUR and WIEN2k. Note that for X_2O_3 the primitive cell includes two formula units, therefore the volume of the primitive cells are twice those reported in this table.

	FLEUR			WIEN2k			Abs. percentage difference [%]			Average set		
	V_0 [Å^3]	B_0 [eV/Å^3]	B_1	V_0 [Å^3]	B_0 [eV/Å^3]	B_1	$\lvert\eta(V_0)\rvert$	$\lvert\eta(B_0)\rvert$	$\lvert\eta(B_1)\rvert$	V_0 [Å^3]	B_0 [eV/Å^3]	B_1
H	30.9245	0.9742	4.1995	30.9217	0.9724	4.1695	0.009	0.177	0.718	30.9231	0.9733	4.1845
He	47.1431	0.2595	5.2575	47.1461	0.2587	5.2709	0.006	0.3	0.254	47.1446	0.2591	5.2642
Li	44.7336	0.5089	4.3172	44.7367	0.5078	4.3366	0.007	0.206	0.449	44.7351	0.5084	4.3269
Be	38.7978	1.0917	3.8856	38.8015	1.0919	3.8876	0.01	0.016	0.052	38.7996	1.0918	3.8866
B	35.986	1.4594	4.1701	35.9842	1.4596	4.1679	0.005	0.015	0.051	35.9851	1.4595	4.169
C	42.2741	0.9343	4.2434	42.264	0.9326	4.2485	0.024	0.181	0.121	42.269	0.9335	4.246
N	45.6783	0.9213	4.1362	45.6711	0.919	4.1271	0.016	0.244	0.22	45.6747	0.9202	4.1316
O	47.8736	0.8285	4.5295	47.8768	0.8264	4.5414	0.007	0.248	0.262	47.8752	0.8275	4.5355
F	56.315	0.4841	4.9766	56.3304	0.4827	4.9561	0.027	0.293	0.413	56.3227	0.4834	4.9664
Ne	81.8629	0.1066	6.0494	81.9923	0.1062	6.0019	0.158	0.343	0.789	81.9276	0.1064	6.0257
Na	70.8511	0.2753	4.7539	70.8657	0.2746	4.7694	0.021	0.266	0.326	70.8584	0.275	4.7616
Mg	56.7704	0.7007	4.1435	56.7772	0.7002	4.1412	0.012	0.084	0.054	56.7738	0.7005	4.1424
Al	49.236	1.1625	4.104	49.2432	1.1616	4.0874	0.015	0.079	0.406	49.2396	1.162	4.0957
Si	48.8101	0.9431	4.4684	48.8317	0.9432	4.4565	0.044	0.012	0.265	48.8209	0.9431	4.4624
P	56.4376	0.83	3.7806	56.4351	0.8301	3.7929	0.004	0.022	0.324	56.4364	0.83	3.7867

Table S4.7. (continued) Table with all calculated EOS parameters for the X_2O_3 structures obtained with FLEUR and WIEN2k. Note that for X_2O_3 the primitive cell includes two formula units, therefore the volume of the primitive cells are twice those reported in this table.

	FLEUR			WIEN2k			Abs. percentage difference [%]			Average set		
	V_0 [Å^3]	B_0 [eV/Å^3]	B_1	V_0 [Å^3]	B_0 [eV/Å^3]	B_1	$\lvert\eta(V_0)\rvert$	$\lvert\eta(B_0)\rvert$	$\lvert\eta(B_1)\rvert$	V_0 [Å^3]	B_0 [eV/Å^3]	B_1
S	58.6338	0.8245	4.2644	58.6316	0.8239	4.2687	0.004	0.072	0.101	58.6327	0.8242	4.2665
Cl	67.6299	0.5154	4.6231	67.6207	0.5144	4.6235	0.014	0.192	0.009	67.6253	0.5149	4.6233
Ar	103.3083	0.0941	6.1314	103.0547	0.0928	6.1536	0.246	1.368	0.361	103.1815	0.0934	6.1425
K	113.7512	0.1322	4.8095	113.8347	0.1314	4.7542	0.073	0.643	1.156	113.7929	0.1318	4.7819
Ca	79.9187	0.4827	4.2747	79.952	0.4818	4.2531	0.042	0.187	0.505	79.9354	0.4822	4.2639
Sc	62.2171	0.9875	4.1264	62.2188	0.9857	4.1316	0.003	0.18	0.125	62.218	0.9866	4.129
Ti	54.2653	1.2872	4.2609	54.2653	1.2857	4.2705	0.0	0.124	0.225	54.2653	1.2864	4.2657
V	50.7853	1.3819	4.3248	50.7844	1.3805	4.3385	0.002	0.106	0.316	50.7849	1.3812	4.3316
Cr	48.2812	1.4506	4.4339	48.2774	1.4491	4.4106	0.008	0.104	0.528	48.2793	1.4498	4.4223
Mn	46.4692	1.4967	4.4412	46.4617	1.495	4.4826	0.016	0.117	0.927	46.4655	1.4959	4.4619
Fe	45.4403	1.5025	4.5024	45.4306	1.4997	4.5556	0.021	0.183	1.174	45.4354	1.5011	4.529
Co	45.3153	1.4251	4.5484	45.3104	1.4248	4.6432	0.011	0.02	2.061	45.3128	1.425	4.5958
Ni	48.0044	1.261	4.6359	47.9962	1.2603	4.6506	0.017	0.054	0.317	48.0003	1.2606	4.6432
Cu	51.9027	1.0066	4.7609	51.8978	1.0057	4.7406	0.009	0.091	0.427	51.9003	1.0062	4.7507
Zn	56.6289	0.8189	4.5974	56.6257	0.819	4.6004	0.006	0.017	0.066	56.6273	0.819	4.5989
Ga	55.4953	0.9913	4.5884	55.4958	0.9943	4.5666	0.001	0.3	0.477	55.4955	0.9928	4.5775
Ge	60.6049	0.73	4.2266	60.6019	0.7308	4.234	0.005	0.106	0.173	60.6034	0.7304	4.2303
As	65.2932	0.7837	4.123	65.2859	0.7832	4.1109	0.011	0.06	0.295	65.2896	0.7834	4.1169
Se	66.1429	0.8055	4.4136	66.139	0.8049	4.4079	0.006	0.074	0.13	66.141	0.8052	4.4107
Br	73.6693	0.5575	4.6624	73.6681	0.5567	4.6642	0.002	0.155	0.039	73.6687	0.5571	4.6633
Kr	97.2445	0.1904	5.9427	97.0775	0.1898	5.9929	0.172	0.338	0.841	97.161	0.1901	5.9678
Rb	134.4961	0.0993	4.638	134.5853	0.0989	4.5802	0.066	0.431	1.254	134.5407	0.0991	4.6091
Sr	97.6375	0.3849	4.3226	97.6505	0.3833	4.288	0.013	0.419	0.803	97.644	0.3841	4.3053
Y	76.2574	0.8312	4.1782	76.2704	0.83	4.1718	0.017	0.144	0.153	76.2639	0.8306	4.175
Zr	65.1262	1.2312	4.2528	65.1443	1.2287	4.2429	0.028	0.206	0.233	65.1353	1.23	4.2479
Nb	60.0739	1.4053	4.4022	60.0915	1.4011	4.3813	0.029	0.301	0.476	60.0827	1.4032	4.3918
Mo	56.764	1.5114	4.5021	56.7746	1.5067	4.5127	0.019	0.309	0.235	56.7693	1.509	4.5074
Tc	54.6125	1.5611	4.635	54.6158	1.5566	4.6305	0.006	0.293	0.097	54.6142	1.5588	4.6327
Ru	53.6513	1.5425	4.7636	53.6557	1.5389	4.7383	0.008	0.232	0.531	53.6535	1.5407	4.7509
Rh	54.4294	1.3851	4.9213	54.4362	1.3818	4.9118	0.012	0.243	0.192	54.4328	1.3834	4.9165
Pd	59.0205	1.1373	4.9308	59.0323	1.1323	4.9546	0.02	0.439	0.482	59.0264	1.1348	4.9427
Ag	65.6516	0.7953	5.1613	65.6206	0.7943	5.2033	0.047	0.122	0.81	65.6361	0.7948	5.1823
Cd	73.2672	0.6162	4.772	73.237	0.6149	4.7708	0.041	0.2	0.026	73.2521	0.6156	4.7714
In	70.1969	0.8227	4.73	70.1828	0.8224	4.7426	0.02	0.033	0.265	70.1899	0.8226	4.7363
Sn	72.5032	0.6721	4.5856	72.4984	0.6718	4.6004	0.007	0.049	0.323	72.5008	0.672	4.593
Sb	78.7081	0.6836	4.1929	78.6962	0.684	4.2098	0.015	0.062	0.402	78.7022	0.6838	4.2013
Te	78.7118	0.7413	4.4639	78.7029	0.7409	4.4648	0.011	0.046	0.02	78.7074	0.7411	4.4643
I	83.8484	0.5737	4.5637	83.8531	0.573	4.5871	0.006	0.121	0.513	83.8508	0.5733	4.5754
Xe	98.9794	0.31	5.323	98.8933	0.3107	5.3487	0.087	0.225	0.481	98.9363	0.3104	5.3359
Cs	141.7132	0.0674	4.656	141.6551	0.0668	4.6011	0.041	0.821	1.185	141.6842	0.0671	4.6285
Ba	116.9524	0.2999	4.0229	116.8908	0.2987	4.0183	0.053	0.41	0.114	116.9216	0.2993	4.0206
La	91.2708	0.6932	4.1976	91.2459	0.6913	4.1854	0.027	0.267	0.291	91.2583	0.6923	4.1915
Ce	82.1366	0.8156	4.3598	82.1175	0.8134	4.3545	0.023	0.27	0.123	82.1271	0.8145	4.3572
Pr	80.0007	0.7894	4.2958	79.9816	0.7872	4.2844	0.024	0.274	0.264	79.9912	0.7883	4.2901
Nd	78.6464	0.7766	4.2778	78.6287	0.7744	4.2787	0.023	0.275	0.021	78.6375	0.7755	4.2783
Pm	77.6099	0.7663	4.3216	77.5946	0.7642	4.3067	0.02	0.272	0.346	77.6022	0.7652	4.3141
Sm	76.7961	0.743	4.8794	76.7794	0.7433	4.7507	0.022	0.049	2.674	76.7878	0.7432	4.8151
Eu	76.1735	0.7259	4.6623	76.1549	0.7251	4.6603	0.024	0.121	0.042	76.1642	0.7255	4.6613
Gd	75.5171	0.7288	4.4706	75.5026	0.7272	4.4696	0.019	0.23	0.021	75.5098	0.728	4.4701
Tb	74.8558	0.7341	4.3895	74.8446	0.7319	4.3812	0.015	0.289	0.19	74.8502	0.733	4.3853
Dy	74.2909	0.7354	4.3659	74.2807	0.7333	4.3659	0.014	0.288	0.0	74.2858	0.7343	4.3659
Ho	73.8918	0.7338	4.3761	73.8805	0.7318	4.3757	0.015	0.28	0.01	73.8862	0.7328	4.3759
Er	73.6922	0.7326	4.4017	73.6825	0.7304	4.3895	0.013	0.291	0.278	73.6874	0.7315	4.3956
Tm	73.6919	0.7323	4.4322	73.682	0.7303	4.4116	0.013	0.279	0.466	73.687	0.7313	4.4219
Yb	73.9288	0.733	4.446	73.9166	0.731	4.4426	0.017	0.272	0.078	73.9227	0.732	4.4443
Lu	72.2151	0.8785	4.1655	72.2114	0.8759	4.137	0.005	0.285	0.686	72.2132	0.8772	4.1513
Hf	64.1744	1.2941	4.2666	64.1849	1.2906	4.2325	0.016	0.271	0.803	64.1797	1.2924	4.2495
Ta	59.9565	1.5197	4.3765	59.9691	1.5129	4.4043	0.021	0.449	0.634	59.9628	1.5163	4.3904
W	57.1312	1.6598	4.501	57.1375	1.6527	4.5284	0.011	0.428	0.606	57.1343	1.6563	4.5147
Re	55.3469	1.7309	4.6669	55.3467	1.7244	4.633	0.0	0.38	0.729	55.3468	1.7277	4.65
Os	54.7045	1.7241	4.7074	54.7071	1.7189	4.7395	0.005	0.304	0.679	54.7058	1.7215	4.7234
Ir	55.5158	1.5999	4.9172	55.5223	1.5939	4.9521	0.012	0.377	0.706	55.519	1.5969	4.9346
Pt	60.6142	1.3074	4.965	60.618	1.3007	4.9076	0.006	0.512	1.162	60.6161	1.304	4.9363

Table S4.7. (continued) Table with all calculated EOS parameters for the X_2O_3 structures obtained with FLEUR and WIEN2k. Note that for X_2O_3 the primitive cell includes two formula units, therefore the volume of the primitive cells are twice those reported in this table.

	FLEUR			WIEN2k			Abs. percentage difference [%]			Average set		
	V_0 [Å^3]	B_0 [eV/Å^3]	B_1	V_0 [Å^3]	B_0 [eV/Å^3]	B_1	$\lvert\eta(V_0)\rvert$	$\lvert\eta(B_0)\rvert$	$\lvert\eta(B_1)\rvert$	V_0 [Å^3]	B_0 [eV/Å^3]	B_1
Au	67.1428	0.9521	5.1003	67.1253	0.9508	5.094	0.026	0.13	0.123	67.1341	0.9515	5.0971
Hg	76.3437	0.6274	5.2434	76.3363	0.6261	5.2385	0.01	0.202	0.095	76.34	0.6268	5.2409
Tl	79.6519	0.6227	5.1432	79.6413	0.6214	5.1441	0.013	0.205	0.017	79.6466	0.6221	5.1436
Pb	86.3031	0.5101	4.7628	86.3052	0.5092	4.7552	0.002	0.172	0.159	86.3041	0.5097	4.759
Bi	87.4478	0.6536	4.3813	87.4317	0.6531	4.3924	0.018	0.073	0.252	87.4397	0.6533	4.3868
Po	84.6231	0.7351	4.5946	84.6348	0.7344	4.6058	0.014	0.099	0.242	84.6289	0.7348	4.6002
At	88.73	0.5904	4.6807	88.7566	0.5891	4.6865	0.03	0.227	0.124	88.7433	0.5897	4.6836
Rn	101.5721	0.365	5.1878	101.5709	0.3641	5.1632	0.001	0.238	0.474	101.5715	0.3646	5.1755
Fr	131.0978	0.1168	6.5295	131.0934	0.1164	6.5221	0.003	0.317	0.113	131.0956	0.1166	6.5258
Ra	126.57	0.2555	3.6805	126.5766	0.2551	3.6673	0.005	0.154	0.359	126.5733	0.2553	3.6739
Ac	101.6614	0.6194	4.2103	101.6647	0.6183	4.2073	0.003	0.184	0.071	101.6631	0.6188	4.2088
Th	87.4641	0.948	4.1382	87.4822	0.9464	4.1251	0.021	0.166	0.318	87.4731	0.9472	4.1317
Pa	78.803	1.0796	4.4284	78.7995	1.0775	4.429	0.004	0.193	0.014	78.8012	1.0786	4.4287
U	75.4245	1.0761	4.4572	75.3927	1.0739	4.4608	0.042	0.198	0.08	75.4086	1.075	4.459
Np	73.6416	1.044	4.474	73.6127	1.0415	4.4507	0.039	0.234	0.522	73.6272	1.0427	4.4624
Pu	72.689	1.0017	4.4654	72.6582	0.9993	4.4542	0.042	0.245	0.252	72.6736	1.0005	4.4598
Am	72.3128	0.9563	4.4404	72.2816	0.9534	4.4424	0.043	0.3	0.044	72.2972	0.9548	4.4414

Table S4.8. Table with all calculated EOS parameters for the XO_2 structures obtained with FLEUR and WIEN2k.

	FLEUR			WIEN2k			Abs. percentage difference [%]			Average set		
	V_0 [Å^3]	B_0 [eV/Å^3]	B_1	V_0 [Å^3]	B_0 [eV/Å^3]	B_1	$\lvert\eta(V_0)\rvert$	$\lvert\eta(B_0)\rvert$	$\lvert\eta(B_1)\rvert$	V_0 [Å^3]	B_0 [eV/Å^3]	B_1
H	19.1041	0.9886	4.4002	19.1051	0.9874	4.3784	0.005	0.112	0.496	19.1046	0.988	4.3893
He	24.7738	0.4151	4.9973	24.7801	0.414	5.0015	0.025	0.261	0.084	24.777	0.4146	4.9994
Li	24.9191	0.5833	4.5324	24.9255	0.582	4.5315	0.026	0.218	0.02	24.9223	0.5827	4.5319
Be	22.1853	1.1333	4.0661	22.1855	1.1321	4.081	0.001	0.102	0.365	22.1854	1.1327	4.0735
B	20.3748	1.6109	4.1373	20.3723	1.6108	4.2092	0.012	0.006	1.722	20.3735	1.6109	4.1732
C	22.7585	1.047	4.6709	22.7543	1.0455	4.6565	0.019	0.15	0.308	22.7564	1.0462	4.6637
N	25.5102	1.0007	4.2193	25.5107	0.9983	4.2054	0.002	0.237	0.329	25.5104	0.9995	4.2123
O	27.1117	0.8128	4.643	27.1151	0.8112	4.6361	0.012	0.195	0.149	27.1134	0.812	4.6396
F	30.8344	0.5107	5.0475	30.8418	0.5096	5.029	0.024	0.21	0.367	30.8381	0.5102	5.0382
Ne	38.8875	0.2055	5.5634	38.927	0.2048	5.5996	0.102	0.357	0.649	38.9073	0.2052	5.5815
Na	36.6709	0.3314	4.858	36.6768	0.331	4.8468	0.016	0.11	0.232	36.6738	0.3312	4.8524
Mg	30.5882	0.7416	4.2473	30.5926	0.7409	4.2539	0.014	0.088	0.156	30.5904	0.7413	4.2506
Al	26.2983	1.2942	4.1561	26.3035	1.2938	4.1228	0.02	0.034	0.804	26.3009	1.294	4.1394
Si	24.0509	1.6607	4.4006	24.0582	1.6583	4.3757	0.031	0.143	0.568	24.0545	1.6595	4.3882
P	27.2019	1.1431	3.972	27.203	1.1436	3.9725	0.004	0.037	0.014	27.2024	1.1434	3.9723
S	29.7407	1.0067	4.3765	29.7406	1.0057	4.3799	0.001	0.101	0.077	29.7406	1.0062	4.3782
Cl	34.7015	0.6007	4.6766	34.6937	0.5995	4.6801	0.022	0.2	0.076	34.6976	0.6001	4.6784
Ar	51.4099	0.1218	5.896	51.2673	0.12	5.9689	0.278	1.443	1.229	51.3386	0.1209	5.9324
K	58.3457	0.1498	4.8304	58.3829	0.1492	4.7535	0.064	0.451	1.605	58.3643	0.1495	4.792
Ca	42.2986	0.4966	4.3355	42.3157	0.4958	4.3255	0.04	0.161	0.23	42.3072	0.4962	4.3305
Sc	32.9873	1.0554	4.196	32.989	1.0541	4.1913	0.005	0.125	0.113	32.9882	1.0548	4.1937
Ti	28.18	1.5524	4.2615	28.1816	1.5501	4.2753	0.005	0.146	0.322	28.1808	1.5512	4.2684
V	26.5771	1.6382	4.348	26.5779	1.637	4.348	0.003	0.073	0.0	26.5775	1.6376	4.348
Cr	25.4246	1.6982	4.4151	25.4254	1.6974	4.4057	0.003	0.048	0.212	25.425	1.6978	4.4104
Mn	24.6547	1.7286	4.5104	24.6524	1.7261	4.4758	0.009	0.149	0.768	24.6536	1.7273	4.4931
Fe	24.1923	1.7217	4.5792	24.1948	1.7217	4.5589	0.01	0.004	0.445	24.1936	1.7217	4.569
Co	25.0334	1.5883	4.6597	25.0339	1.5852	4.6012	0.002	0.19	1.265	25.0337	1.5868	4.6305
Ni	26.2014	1.3758	4.6785	26.201	1.3732	4.6827	0.002	0.186	0.09	26.2012	1.3745	4.6806
Cu	28.2325	1.0744	4.8111	28.2337	1.0735	4.7965	0.004	0.077	0.304	28.2331	1.0739	4.8038
Zn	30.3911	0.8892	4.6934	30.3948	0.8943	4.6318	0.012	0.567	1.322	30.3929	0.8917	4.6626
Ga	29.2617	1.1499	4.5457	29.2617	1.1538	4.5364	0.0	0.336	0.205	29.2617	1.1518	4.5411
Ge	28.1887	1.2379	4.8179	28.1928	1.2393	4.8238	0.014	0.115	0.123	28.1908	1.2386	4.8209
As	31.4994	1.0361	4.3961	31.4982	1.0355	4.3968	0.004	0.059	0.017	31.4988	1.0358	4.3965
Se	33.0737	1.0352	4.4845	33.0731	1.0343	4.4866	0.002	0.084	0.047	33.0734	1.0348	4.4855
Br	37.0141	0.687	4.6868	37.0133	0.6861	4.6828	0.002	0.126	0.085	37.0137	0.6866	4.6848
Kr	47.5877	0.2579	5.6502	47.4971	0.2573	5.717	0.19	0.256	1.175	47.5424	0.2576	5.6836
Rb	69.0447	0.1033	4.3636	69.0998	0.103	4.3199	0.08	0.316	1.007	69.0722	0.1032	4.3418
Sr	51.2847	0.3871	4.3007	51.2917	0.3848	4.2482	0.014	0.586	1.229	51.2882	0.3859	4.2744

Table S4.8. (continued) Table with all calculated EOS parameters for the XO_2 structures obtained with FLEUR and WIEN2k.

	FLEUR			WIEN2k			Abs. percentage difference [%]			Average set		
	V_0 [Å^3]	B_0 [eV/Å^3]	B_1	V_0 [Å^3]	B_0 [eV/Å^3]	B_1	$\lvert\eta(V_0)\rvert$	$\lvert\eta(B_0)\rvert$	$\lvert\eta(B_1)\rvert$	V_0 [Å^3]	B_0 [eV/Å^3]	B_1
Y	40.1873	0.8753	4.2095	40.1943	0.874	4.1958	0.018	0.143	0.325	40.1908	0.8747	4.2027
Zr	33.4686	1.4743	4.2079	33.478	1.4713	4.2167	0.028	0.198	0.209	33.4733	1.4728	4.2123
Nb	31.239	1.6335	4.3451	31.252	1.628	4.3382	0.042	0.333	0.16	31.2455	1.6307	4.3416
Mo	29.7234	1.7418	4.4573	29.7334	1.7348	4.4573	0.034	0.405	0.001	29.7284	1.7383	4.4573
Tc	28.7198	1.8001	4.56	28.7254	1.7926	4.584	0.02	0.416	0.524	28.7226	1.7963	4.572
Ru	28.1945	1.7909	4.7167	28.1996	1.7856	4.7313	0.018	0.296	0.308	28.1971	1.7882	4.724
Rh	29.5939	1.5728	4.7758	29.6002	1.5673	4.7972	0.022	0.348	0.446	29.597	1.57	4.7865
Pd	31.3974	1.2834	4.9725	31.386	1.2848	4.995	0.036	0.114	0.452	31.3917	1.2841	4.9838
Ag	34.3903	0.9025	5.2622	34.3764	0.9016	5.2774	0.041	0.099	0.288	34.3834	0.9021	5.2698
Cd	38.5422	0.6591	4.7544	38.531	0.6578	4.7653	0.029	0.192	0.23	38.5366	0.6585	4.7599
In	36.4766	0.9455	4.6414	36.4691	0.9446	4.6685	0.021	0.097	0.581	36.4729	0.9451	4.655
Sn	34.006	1.1609	4.9709	34.0051	1.1605	4.9878	0.003	0.041	0.339	34.0055	1.1607	4.9794
Sb	37.5677	0.9799	4.5478	37.5693	0.9813	4.5626	0.004	0.148	0.325	37.5685	0.9806	4.5552
Te	39.0619	1.0064	4.5042	39.058	1.0061	4.513	0.01	0.026	0.196	39.06	1.0062	4.5086
I	41.4434	0.7736	4.7091	41.4428	0.773	4.7119	0.001	0.078	0.061	41.4431	0.7733	4.7105
Xe	47.3899	0.4415	5.3366	47.3444	0.4433	5.4017	0.096	0.405	1.212	47.3671	0.4424	5.3691
Cs	63.6155	0.1033	6.9633	63.4962	0.1028	6.9827	0.188	0.511	0.279	63.5558	0.1031	6.973
Ba	60.3646	0.2815	3.8593	60.3195	0.2798	3.8481	0.075	0.592	0.29	60.3421	0.2806	3.8537
La	47.8855	0.7007	4.1796	47.8733	0.6983	4.1676	0.025	0.341	0.288	47.8794	0.6995	4.1736
Ce	40.7984	1.0903	4.4621	40.7886	1.0874	4.4623	0.024	0.263	0.005	40.7935	1.0888	4.4622
Pr	39.8174	1.0643	4.4128	39.8086	1.0617	4.4028	0.022	0.246	0.228	39.813	1.063	4.4078
Nd	39.1005	1.0453	4.4041	39.0925	1.0427	4.41	0.021	0.255	0.135	39.0965	1.044	4.407
Pm	38.5441	1.0286	4.4341	38.5368	1.0261	4.4292	0.019	0.242	0.112	38.5405	1.0273	4.4317
Sm	38.0857	1.013	4.459	38.0793	1.0107	4.4551	0.017	0.225	0.087	38.0825	1.0118	4.4571
Eu	37.6948	0.998	4.486	37.6888	0.9956	4.4768	0.016	0.244	0.205	37.6918	0.9968	4.4814
Gd	37.3643	0.9834	4.4994	37.3584	0.9809	4.4928	0.016	0.254	0.147	37.3613	0.9822	4.4961
Tb	37.1076	0.9704	4.5185	37.1023	0.9679	4.5133	0.014	0.251	0.114	37.1049	0.9692	4.5159
Dy	36.9475	0.9587	4.5719	36.9424	0.9564	4.5531	0.014	0.249	0.412	36.9449	0.9576	4.5625
Ho	36.8832	0.9462	4.5853	36.8779	0.9437	4.5884	0.014	0.266	0.066	36.8806	0.9449	4.5868
Er	36.9058	0.9307	4.6314	36.9012	0.9285	4.6125	0.012	0.243	0.409	36.9035	0.9296	4.6219
Tm	37.0337	0.9136	4.6459	37.0297	0.9111	4.6289	0.011	0.275	0.367	37.0317	0.9124	4.6374
Yb	37.3044	0.8918	4.6678	37.302	0.889	4.6382	0.007	0.317	0.638	37.3032	0.8904	4.653
Lu	37.2627	0.9423	4.4232	37.2645	0.9377	4.3581	0.005	0.493	1.482	37.2636	0.94	4.3906
Hf	33.1129	1.5399	4.2753	33.1213	1.5352	4.2269	0.025	0.306	1.139	33.1171	1.5375	4.2511
Ta	31.3877	1.7212	4.3956	31.3989	1.7135	4.3468	0.036	0.448	1.116	31.3933	1.7174	4.3712
W	30.1401	1.8549	4.4921	30.1503	1.8454	4.4611	0.034	0.514	0.693	30.1452	1.8502	4.4766
Re	29.302	1.9467	4.5924	29.3054	1.9363	4.5742	0.012	0.536	0.397	29.3037	1.9415	4.5833
Os	28.7919	1.9837	4.6927	28.7983	1.9744	4.7051	0.022	0.467	0.264	28.7951	1.9791	4.6989
Ir	30.4115	1.7468	4.7763	30.4126	1.7437	4.7606	0.004	0.174	0.33	30.4121	1.7453	4.7684
Pt	32.2848	1.4621	4.8523	32.2874	1.4594	4.9045	0.008	0.188	1.07	32.2861	1.4608	4.8784
Au	35.0077	1.0997	5.1214	34.9994	1.0985	5.1277	0.024	0.104	0.123	35.0036	1.0991	5.1246
Hg	39.3052	0.7079	5.3755	39.3012	0.7066	5.3712	0.01	0.187	0.08	39.3032	0.7073	5.3733
Tl	40.7151	0.7341	5.128	40.7096	0.7328	5.1192	0.014	0.183	0.173	40.7123	0.7334	5.1236
Pb	39.5779	0.8213	5.1176	39.5785	0.8198	5.1216	0.002	0.179	0.078	39.5782	0.8206	5.1196
Bi	42.0748	0.8352	4.7393	42.0715	0.8359	4.7633	0.008	0.078	0.506	42.0731	0.8356	4.7513
Po	41.7815	1.0096	4.6195	41.7881	1.009	4.6295	0.016	0.059	0.215	41.7848	1.0093	4.6245
At	43.8292	0.8115	4.7375	43.84	0.8101	4.7418	0.025	0.171	0.09	43.8346	0.8108	4.7397
Rn	48.688	0.5281	5.1751	48.6812	0.5268	5.2224	0.014	0.245	0.909	48.6846	0.5275	5.1988
Fr	58.9193	0.2152	6.6161	58.9098	0.2146	6.5983	0.016	0.302	0.269	58.9146	0.2149	6.6072
Ra	63.8562	0.245	4.0447	63.8576	0.2443	4.0173	0.002	0.266	0.681	63.8569	0.2446	4.031
Ac	52.961	0.6276	4.1684	52.9626	0.6262	4.1593	0.003	0.233	0.218	52.9618	0.6269	4.1639
Th	44.3164	1.1695	4.2589	44.317	1.1676	4.2538	0.001	0.161	0.118	44.3167	1.1685	4.2563
Pa	40.6558	1.2618	4.4602	40.6367	1.2592	4.461	0.047	0.209	0.019	40.6463	1.2605	4.4606
U	39.0326	1.2693	4.4209	39.017	1.2666	4.4192	0.04	0.216	0.037	39.0248	1.268	4.42
Np	38.0753	1.2668	4.3893	38.0608	1.264	4.3925	0.038	0.218	0.073	38.0681	1.2654	4.3909
Pu	37.4111	1.2489	4.3823	37.3982	1.2462	4.3877	0.035	0.217	0.122	37.4047	1.2476	4.385
Am	36.9689	1.2262	4.4039	36.9576	1.224	4.3911	0.031	0.182	0.293	36.9632	1.2251	4.3975

Table S4.9. Table with all calculated EOS parameters for the X_2O_5 structures obtained with FLEUR and WIEN2k. Note that for X_2O_5 the primitive cell includes two formula units, therefore the volume of the primitive cells are twice those reported in this table.

	FLEUR			WIEN2k			Abs. percentage difference [%]			Average set		
	V_0 [Å^3]	B_0 [eV/Å^3]	B_1	V_0 [Å^3]	B_0 [eV/Å^3]	B_1	$\lvert\eta(V_0)\rvert$	$\lvert\eta(B_0)\rvert$	$\lvert\eta(B_1)\rvert$	V_0 [Å^3]	B_0 [eV/Å^3]	B_1
H	51.6294	0.8182	4.3453	51.7182	0.8239	4.3852	0.172	0.69	0.915	51.6738	0.821	4.3653
He	56.3417	0.6362	4.7394	56.4553	0.6425	4.7791	0.201	0.994	0.836	56.3985	0.6393	4.7593
Li	61.7966	0.6087	4.5281	61.8956	0.6113	4.5471	0.16	0.43	0.418	61.8461	0.61	4.5376
Be	57.3047	0.9393	4.1197	57.3444	0.9407	4.1334	0.069	0.148	0.332	57.3245	0.94	4.1265
B	54.302	1.0186	4.46	54.4447	1.0179	4.4191	0.262	0.063	0.922	54.3733	1.0182	4.4396
C	58.5562	0.848	4.2161	58.6738	0.8484	4.234	0.201	0.045	0.422	58.615	0.8482	4.2251
N	57.1867	0.9674	4.4911	57.2811	0.9708	4.5012	0.165	0.355	0.225	57.2339	0.9691	4.4962
O	57.9311	0.9	4.6713	57.9351	0.8985	4.6548	0.007	0.168	0.354	57.9331	0.8993	4.6631
F	60.7621	0.7563	4.8447	60.8233	0.7607	4.8564	0.101	0.59	0.241	60.7927	0.7585	4.8506
Ne	69.4511	0.4887	5.1137	69.6022	0.4915	5.1213	0.217	0.582	0.148	69.5266	0.4901	5.1175
Na	74.3059	0.4769	4.7841	74.4106	0.4781	4.8105	0.141	0.255	0.55	74.3582	0.4775	4.7973
Mg	69.4193	0.7455	4.3021	69.4767	0.7453	4.3147	0.083	0.036	0.291	69.448	0.7454	4.3084
Al	63.0377	1.0719	4.259	63.1058	1.0703	4.2765	0.108	0.15	0.411	63.0717	1.0711	4.2677
Si	60.9727	1.0315	4.7012	61.0475	1.0294	4.715	0.123	0.209	0.292	61.0101	1.0305	4.7081
P	65.2299	0.8903	3.9471	65.3124	0.892	3.9802	0.126	0.189	0.836	65.2712	0.8911	3.9636
S	67.0295	0.8935	4.4347	67.1274	0.8935	4.4582	0.146	0.001	0.527	67.0785	0.8935	4.4465
Cl	75.0965	0.609	4.7508	75.2581	0.609	4.7688	0.215	0.013	0.378	75.1773	0.609	4.7598
Ar	92.6409	0.3001	5.2998	92.7488	0.2994	5.3155	0.116	0.222	0.296	92.6949	0.2997	5.3077
K	99.2928	0.292	4.9391	99.4761	0.2912	4.9178	0.184	0.292	0.432	99.3844	0.2916	4.9284
Ca	84.343	0.5819	4.4055	84.4983	0.5804	4.4132	0.184	0.256	0.173	84.4206	0.5812	4.4094
Sc	71.3552	1.0096	4.2325	71.3945	1.0062	4.2369	0.055	0.334	0.104	71.3749	1.0079	4.2347
Ti	63.7312	1.3162	4.3146	63.7342	1.3152	4.3386	0.005	0.075	0.554	63.7327	1.3157	4.3266
V	59.9657	1.4409	4.4135	59.9707	1.4397	4.4362	0.008	0.083	0.514	59.9682	1.4403	4.4248
Cr	58.1277	1.4509	4.4705	58.138	1.4498	4.5016	0.018	0.071	0.693	58.1328	1.4504	4.486
Mn	57.6635	1.3952	4.4933	57.6622	1.3981	4.4952	0.002	0.205	0.044	57.6628	1.3967	4.4942
Fe	58.0099	1.3256	4.5461	58.0067	1.3268	4.5607	0.006	0.091	0.322	58.0083	1.3262	4.5534
Co	58.9632	1.2372	4.597	58.9484	1.2374	4.6365	0.025	0.019	0.856	58.9558	1.2373	4.6168
Ni	60.7197	1.1182	4.6844	60.7143	1.1173	4.7029	0.009	0.078	0.395	60.717	1.1177	4.6936
Cu	64.2484	0.9439	4.7478	64.2421	0.9437	4.7662	0.01	0.017	0.386	64.2452	0.9438	4.757
Zn	68.5304	0.8318	4.594	68.5102	0.8328	4.5959	0.029	0.114	0.041	68.5203	0.8323	4.595
Ga	67.8213	0.9273	4.6796	67.8565	0.9261	4.6807	0.052	0.135	0.024	67.8389	0.9267	4.6802
Ge	69.7066	0.7774	4.867	69.8102	0.7694	4.8949	0.148	1.028	0.57	69.7584	0.7734	4.8809
As	71.9941	0.8625	4.0293	72.0367	0.8609	4.0588	0.059	0.189	0.729	72.0154	0.8617	4.0441
Se	71.9194	0.9264	4.5298	71.9473	0.9244	4.5397	0.039	0.214	0.217	71.9333	0.9254	4.5347
Br	77.9119	0.6787	4.7881	78.0608	0.674	4.8076	0.191	0.692	0.408	77.9864	0.6764	4.7978
Kr	96.0582	0.3196	5.2297	96.2602	0.3198	5.3234	0.21	0.049	1.775	96.1592	0.3197	5.2766
Rb	114.2322	0.2223	4.9166	114.4592	0.2207	4.9278	0.198	0.731	0.227	114.3457	0.2215	4.9222
Sr	97.7166	0.4839	4.5013	97.8478	0.4819	4.5021	0.134	0.43	0.018	97.7822	0.4829	4.5017
Y	82.4459	0.897	4.249	82.5133	0.892	4.2659	0.082	0.566	0.397	82.4796	0.8945	4.2574
Zr	71.9732	1.3408	4.2528	71.9948	1.3377	4.2563	0.03	0.231	0.084	71.984	1.3393	4.2545
Nb	65.7734	1.6474	4.4277	65.7879	1.6447	4.4301	0.022	0.164	0.056	65.7806	1.6461	4.4289
Mo	62.8934	1.7154	4.542	62.9126	1.7113	4.5574	0.03	0.237	0.34	62.903	1.7134	4.5497
Tc	62.293	1.6359	4.6314	62.3109	1.6309	4.653	0.029	0.308	0.466	62.3019	1.6334	4.6422
Ru	63.2791	1.4887	4.6938	63.3034	1.4832	4.7046	0.038	0.371	0.23	63.2912	1.486	4.6992
Rh	65.4019	1.3136	4.8313	65.4303	1.3084	4.8172	0.043	0.398	0.292	65.4161	1.311	4.8243
Pd	68.9615	1.0903	4.9216	68.9624	1.0874	4.9847	0.001	0.274	1.275	68.962	1.0889	4.9531
Ag	74.9618	0.8092	5.1026	74.9662	0.8077	5.1501	0.006	0.182	0.927	74.964	0.8085	5.1263
Cd	80.6206	0.7111	4.7591	80.6172	0.7098	4.7957	0.004	0.181	0.765	80.6189	0.7105	4.7774
In	78.3932	0.8719	4.7637	78.4544	0.8693	4.7632	0.078	0.307	0.012	78.4238	0.8706	4.7634
Sn	76.7786	0.894	5.0442	76.7939	0.8933	5.0783	0.02	0.081	0.673	76.7863	0.8936	5.0612
Sb	78.8791	0.7853	4.539	78.8806	0.7814	4.555	0.002	0.498	0.352	78.8798	0.7834	4.547
Te	79.8046	0.9293	4.3291	79.7168	0.9277	4.3669	0.11	0.166	0.87	79.7607	0.9285	4.348
I	81.504	0.8227	4.8772	81.4993	0.8197	4.9065	0.006	0.365	0.599	81.5016	0.8212	4.8918
Xe	91.6333	0.4815	5.3822	91.8801	0.4737	5.4721	0.269	1.634	1.656	91.7567	0.4776	5.4272
Cs	121.9143	0.1738	5.2303	122.3085	0.1715	5.3148	0.323	1.321	1.603	122.1114	0.1727	5.2726
Ba	113.5269	0.3849	4.3234	113.6812	0.385	4.3606	0.136	0.031	0.858	113.604	0.3849	4.342
La	94.9581	0.7667	4.2541	94.9984	0.7626	4.2465	0.042	0.534	0.177	94.9783	0.7647	4.2503
Ce	84.057	1.0214	4.4626	84.0371	1.0194	4.4566	0.024	0.189	0.134	84.047	1.0204	4.4596
Pr	80.5775	1.0583	4.5515	80.5673	1.0538	4.5465	0.013	0.422	0.11	80.5724	1.0561	4.549
Nd	79.7192	1.0307	4.513	79.7149	1.0258	4.5214	0.005	0.478	0.186	79.717	1.0283	4.5172
Pm	79.1496	1.0028	4.5156	79.1526	0.9977	4.5126	0.004	0.511	0.068	79.1511	1.0003	4.5141
Sm	78.7225	0.9798	4.525	78.7291	0.9745	4.5138	0.008	0.54	0.247	78.7258	0.9771	4.5194
Eu	78.3774	0.9602	4.5203	78.3874	0.955	4.5222	0.013	0.541	0.043	78.3824	0.9576	4.5213

Table S4.9. (continued) Table with all calculated EOS parameters for the X_2O_5 structures obtained with FLEUR and WIEN2k. Note that for X_2O_5 the primitive cell includes two formula units, therefore the volume of the primitive cells are twice those reported in this table.

	FLEUR			WIEN2k			Abs. percentage difference [%]			Average set		
	V_0 [Å^3]	B_0 [eV/Å^3]	B_1	V_0 [Å^3]	B_0 [eV/Å^3]	B_1	$\lvert\eta(V_0)\rvert$	$\lvert\eta(B_0)\rvert$	$\lvert\eta(B_1)\rvert$	V_0 [Å^3]	B_0 [eV/Å^3]	B_1
Gd	78.0692	0.944	4.5315	78.0849	0.9387	4.5326	0.02	0.572	0.025	78.0771	0.9414	4.532
Tb	77.807	0.9295	4.5399	77.8254	0.9238	4.5438	0.024	0.623	0.085	77.8162	0.9267	4.5418
Dy	77.6645	0.914	4.5574	77.6873	0.9081	4.5529	0.029	0.641	0.101	77.6759	0.911	4.5552
Ho	77.7345	0.8983	4.5733	77.7641	0.8921	4.5623	0.038	0.697	0.241	77.7493	0.8952	4.5678
Er	77.994	0.8825	4.5511	78.031	0.8763	4.5675	0.047	0.706	0.359	78.0125	0.8794	4.5593
Tm	78.4333	0.8673	4.5836	78.4806	0.8608	4.5863	0.06	0.747	0.059	78.457	0.8641	4.585
Yb	79.2082	0.8474	4.5908	79.2775	0.8403	4.6004	0.088	0.837	0.21	79.2428	0.8438	4.5956
Lu	78.899	0.9398	4.2826	78.9755	0.9322	4.2655	0.097	0.811	0.401	78.9373	0.936	4.274
Hf	71.3247	1.3956	4.2383	71.3384	1.3902	4.2458	0.019	0.386	0.177	71.3315	1.3929	4.242
Ta	65.6343	1.7753	4.4054	65.6399	1.7704	4.3963	0.009	0.276	0.205	65.6371	1.7729	4.4008
W	62.7772	1.9062	4.532	62.7855	1.8999	4.5308	0.013	0.33	0.026	62.7813	1.9031	4.5314
Re	62.2379	1.8535	4.6588	62.2409	1.8466	4.6216	0.005	0.37	0.801	62.2394	1.85	4.6402
Os	63.1798	1.7092	4.711	63.1881	1.7068	4.701	0.013	0.14	0.211	63.1839	1.708	4.706
Ir	65.4381	1.5167	4.7973	65.452	1.5128	4.7629	0.021	0.258	0.719	65.445	1.5147	4.7801
Pt	69.2398	1.2701	4.9084	69.2855	1.2607	4.9261	0.066	0.745	0.361	69.2627	1.2654	4.9172
Au	75.1453	0.9546	5.0926	75.2167	0.9514	5.0949	0.095	0.33	0.045	75.181	0.953	5.0937
Hg	83.2401	0.7022	5.0343	83.3029	0.7024	5.0494	0.075	0.028	0.3	83.2715	0.7023	5.0418
Tl	85.9046	0.6975	5.1118	86.0649	0.6935	5.1201	0.186	0.581	0.164	85.9848	0.6955	5.116
Pb	88.1344	0.6034	5.3275	88.3242	0.5935	5.3272	0.215	1.659	0.004	88.2293	0.5984	5.3274
Bi	88.9437	0.7332	4.0945	89.0038	0.7276	4.0997	0.068	0.767	0.129	88.9737	0.7304	4.0971
Po	85.3582	0.9552	4.5318	85.3152	0.9522	4.5434	0.05	0.316	0.255	85.3367	0.9537	4.5376
At	84.5589	0.9026	4.9844	84.5313	0.9017	5.0107	0.033	0.101	0.528	84.5451	0.9021	4.9975
Rn	91.0625	0.6154	5.25	91.1349	0.6095	5.2841	0.079	0.967	0.648	91.0987	0.6124	5.267
Fr	114.5881	0.2189	5.5915	115.33	0.2141	5.4186	0.645	2.239	3.14	114.959	0.2165	5.505
Ra	121.342	0.3304	4.0905	121.7472	0.3296	4.0304	0.333	0.249	1.481	121.5446	0.33	4.0604
Ac	103.833	0.6871	4.1775	103.935	0.6835	4.1724	0.098	0.531	0.123	103.884	0.6853	4.1749
Th	89.1023	1.1342	4.2096	89.0962	1.1331	4.1991	0.007	0.097	0.25	89.0992	1.1337	4.2043
Pa	79.84	1.4886	4.4293	79.8243	1.4859	4.4356	0.02	0.187	0.141	79.8321	1.4873	4.4324
U	76.2789	1.5023	4.5904	76.262	1.4994	4.5882	0.022	0.197	0.049	76.2704	1.5008	4.5893
Np	74.8246	1.4333	4.6339	74.8049	1.4301	4.6511	0.026	0.226	0.37	74.8147	1.4317	4.6425
Pu	74.2557	1.3472	4.668	74.2348	1.3439	4.6778	0.028	0.246	0.212	74.2452	1.3456	4.6729
Am	74.2991	1.2649	4.6179	74.2773	1.261	4.6534	0.029	0.304	0.765	74.2882	1.2629	4.6356

Table S4.10. Table with all calculated EOS parameters for the XO_3 structures obtained with FLEUR and WIEN2k.

	FLEUR			WIEN2k			Abs. percentage difference [%]			Average set		
	V_0 [Å^3]	B_0 [eV/Å^3]	B_1	V_0 [Å^3]	B_0 [eV/Å^3]	B_1	$\lvert\eta(V_0)\rvert$	$\lvert\eta(B_0)\rvert$	$\lvert\eta(B_1)\rvert$	V_0 [Å^3]	B_0 [eV/Å^3]	B_1
H	31.0974	0.7662	4.3422	31.0812	0.7635	4.477	0.052	0.348	3.056	31.0893	0.7648	4.4096
He	43.0362	0.2461	5.777	43.0829	0.2483	5.6076	0.108	0.909	2.977	43.0595	0.2472	5.6923
Li	46.0735	0.3228	4.8151	46.1048	0.3246	4.6981	0.068	0.559	2.462	46.0892	0.3237	4.7566
Be	38.9692	0.7063	4.2122	39.015	0.7037	4.1621	0.117	0.368	1.197	38.9921	0.705	4.1872
B	33.6256	1.2128	4.1217	33.6321	1.1989	4.1092	0.019	1.149	0.304	33.6288	1.2059	4.1154
C	32.9199	1.0243	4.6901	32.9186	1.0098	4.5753	0.004	1.429	2.478	32.9192	1.017	4.6327
N	39.7156	0.6921	4.0531	39.7033	0.6898	4.1545	0.031	0.333	2.469	39.7094	0.691	4.1038
O	44.7719	0.5504	4.6516	44.7872	0.5481	4.529	0.034	0.427	2.671	44.7796	0.5493	4.5903
F	53.3173	0.3437	4.6918	53.332	0.3417	4.7362	0.028	0.59	0.943	53.3246	0.3427	4.714
Ne	80.6186	0.0702	6.326	80.8624	0.0692	6.1871	0.302	1.456	2.22	80.7405	0.0697	6.2565
Na	82.1541	0.1189	4.9724	82.1439	0.1186	4.9454	0.012	0.264	0.544	82.149	0.1187	4.9589
Mg	62.132	0.3612	4.3723	62.1455	0.3609	4.3455	0.022	0.073	0.615	62.1388	0.361	4.3589
Al	49.7391	0.7581	4.0806	49.7487	0.7566	4.1651	0.019	0.196	2.051	49.7439	0.7574	4.1228
Si	41.775	1.2466	4.1317	41.7833	1.2431	4.2167	0.02	0.278	2.036	41.7792	1.2448	4.1742
P	37.0088	1.5954	4.8477	37.0111	1.592	4.6945	0.006	0.211	3.212	37.0099	1.5937	4.7711
S	39.1632	0.7555	5.2971	39.1265	0.7516	5.1875	0.094	0.522	2.091	39.1449	0.7535	5.2423
Cl	52.0045	0.4789	4.1771	52.0067	0.4767	4.2557	0.004	0.456	1.863	52.0056	0.4778	4.2164
Ar	68.3345	0.1759	5.35	68.3174	0.1771	5.5269	0.025	0.649	3.253	68.3259	0.1765	5.4385
K	136.4836	0.0344	3.5149	136.5856	0.0342	3.3773	0.075	0.668	3.992	136.5346	0.0343	3.4461
Ca	94.2769	0.1921	3.7084	94.2875	0.192	3.6879	0.011	0.037	0.553	94.2822	0.192	3.6982
Sc	70.4995	0.5058	3.9364	70.4966	0.5042	3.974	0.004	0.321	0.953	70.498	0.505	3.9552
Ti	57.3444	0.8781	4.3143	57.355	0.876	4.3055	0.019	0.236	0.205	57.3497	0.877	4.3099
V	50.2251	1.1391	4.5198	50.2553	1.1308	4.4765	0.06	0.732	0.961	50.2402	1.1349	4.4982

Table S4.10. (continued) Table with all calculated EOS parameters for the XO_3 structures obtained with FLEUR and WIEN2k.

	FLEUR			WIEN2k			Abs. percentage difference [%]			Average set		
	V_0 [Å^3]	B_0 [eV/Å^3]	B_1	V_0 [Å^3]	B_0 [eV/Å^3]	B_1	$\lvert\eta(V_0)\rvert$	$\lvert\eta(B_0)\rvert$	$\lvert\eta(B_1)\rvert$	V_0 [Å^3]	B_0 [eV/Å^3]	B_1
Cr	46.8589	1.233	4.499	46.89	1.2176	4.5732	0.066	1.264	1.637	46.8745	1.2253	4.5361
Mn	45.5937	1.2028	4.6744	45.6179	1.19	4.6931	0.053	1.073	0.4	45.6058	1.1964	4.6838
Fe	45.9306	1.0758	4.418	45.9407	1.0669	4.6464	0.022	0.828	5.04	45.9357	1.0713	4.5322
Co	47.1356	0.9313	4.6138	47.1399	0.9221	4.7596	0.009	0.997	3.112	47.1378	0.9267	4.6867
Ni	49.2114	0.7975	4.5683	49.1988	0.794	4.5601	0.026	0.446	0.178	49.2051	0.7957	4.5642
Cu	52.032	0.6615	4.7907	51.9946	0.6598	4.8197	0.072	0.254	0.604	52.0133	0.6606	4.8052
Zn	56.5539	0.51	4.8311	56.5475	0.5042	4.8693	0.011	1.13	0.787	56.5507	0.5071	4.8502
Ga	57.4651	0.6141	3.9238	57.4753	0.6127	3.8033	0.018	0.231	3.118	57.4702	0.6134	3.8636
Ge	51.0658	0.9322	4.8882	51.0822	0.9286	4.8481	0.032	0.395	0.824	51.074	0.9304	4.8682
As	47.3103	0.9137	5.6161	47.328	0.9092	5.6125	0.037	0.49	0.064	47.3192	0.9114	5.6143
Se	49.8196	0.622	4.8896	49.8512	0.6189	4.7816	0.063	0.502	2.232	49.8354	0.6205	4.8356
Br	58.2493	0.5035	3.8363	58.2633	0.5047	3.824	0.024	0.231	0.322	58.2563	0.5041	3.8301
Kr	68.1298	0.288	4.9759	67.9841	0.2902	5.1714	0.214	0.767	3.853	68.057	0.2891	5.0737
Rb	109.4539	0.0249	6.5277	109.83	0.0243	6.5778	0.343	2.583	0.766	109.642	0.0246	6.5527
Sr	113.8178	0.1147	2.2512	113.8533	0.1147	2.2317	0.031	0.039	0.872	113.8356	0.1147	2.2415
Y	88.919	0.3429	2.646	88.9188	0.3427	2.6422	0.0	0.04	0.143	88.9189	0.3428	2.6441
Zr	72.318	0.7345	3.7521	72.3267	0.7328	3.7631	0.012	0.237	0.292	72.3223	0.7336	3.7576
Nb	61.6154	1.0919	4.3643	61.6314	1.0919	4.4308	0.026	0.006	1.513	61.6234	1.0919	4.3975
Mo	55.6153	1.2978	4.5454	55.623	1.3043	4.5636	0.014	0.499	0.399	55.6191	1.301	4.5545
Tc	53.0875	1.3235	4.7967	53.1162	1.3292	4.6584	0.054	0.434	2.924	53.1019	1.3264	4.7276
Ru	52.4879	1.2256	4.913	52.5121	1.2283	4.8498	0.046	0.215	1.295	52.5	1.2269	4.8814
Rh	54.2637	0.9672	4.6691	54.2621	0.9685	4.778	0.003	0.135	2.305	54.2629	0.9679	4.7236
Pd	58.5895	0.6781	4.7836	58.5867	0.6744	4.8875	0.005	0.541	2.15	58.5881	0.6763	4.8355
Ag	65.2063	0.4996	4.9996	65.262	0.4935	4.9242	0.085	1.217	1.519	65.2342	0.4966	4.9619
Cd	73.1689	0.3373	4.9495	73.1353	0.3365	5.0666	0.046	0.231	2.337	73.1521	0.3369	5.0081
In	74.7851	0.4046	4.284	74.7503	0.404	4.3676	0.046	0.156	1.932	74.7677	0.4043	4.3258
Sn	67.673	0.707	4.8118	67.6622	0.7072	4.8366	0.016	0.027	0.516	67.6676	0.7071	4.8242
Sb	60.1815	0.8776	6.2938	60.2192	0.8806	6.3417	0.063	0.339	0.758	60.2004	0.8791	6.3177
Te	56.862	0.7705	5.6677	56.8786	0.7774	5.5722	0.029	0.888	1.699	56.8703	0.7739	5.6199
I	60.8603	0.7432	9.8642	60.8584	0.746	9.9571	0.003	0.377	0.937	60.8594	0.7446	9.9106
Xe	66.9651	0.5598	6.4488	66.8746	0.5665	6.5357	0.135	1.205	1.34	66.9198	0.5631	6.4922
Cs	76.1784	0.3058	7.0098	76.228	0.3056	7.0215	0.065	0.062	0.166	76.2032	0.3057	7.0156
Ba	91.0973	0.1157	6.022	91.3362	0.1153	6.0249	0.262	0.359	0.048	91.2168	0.1155	6.0234
La	90.844	0.1802	3.5885	90.9006	0.1783	3.6395	0.062	1.07	1.41	90.8723	0.1793	3.614
Ce	81.6513	0.3135	3.725	81.6541	0.3109	3.7659	0.003	0.816	1.091	81.6527	0.3122	3.7454
Pr	76.695	0.439	3.0101	76.6722	0.4366	3.0716	0.03	0.547	2.021	76.6836	0.4378	3.0408
Nd	72.6543	0.5687	4.2977	72.6395	0.5653	4.245	0.02	0.601	1.235	72.6469	0.567	4.2714
Pm	71.7295	0.5647	4.3037	71.7155	0.5607	4.2733	0.019	0.707	0.709	71.7225	0.5627	4.2885
Sm	71.3021	0.5462	4.186	71.2831	0.5422	4.2366	0.027	0.725	1.202	71.2926	0.5442	4.2113
Eu	71.1028	0.5274	4.2174	71.0851	0.5238	4.2258	0.025	0.689	0.201	71.0939	0.5256	4.2216
Gd	71.1241	0.5097	4.1273	71.1003	0.5054	4.2162	0.033	0.838	2.131	71.1122	0.5075	4.1718
Tb	71.3606	0.4928	4.0561	71.3371	0.4881	4.1711	0.033	0.96	2.795	71.3489	0.4904	4.1136
Dy	71.7907	0.4779	4.0567	71.769	0.4734	4.1482	0.03	0.951	2.231	71.7799	0.4757	4.1024
Ho	72.3773	0.4655	4.1498	72.3619	0.461	4.1411	0.021	0.981	0.209	72.3696	0.4633	4.1455
Er	73.1611	0.4543	4.1914	73.1581	0.4493	4.1808	0.004	1.105	0.251	73.1596	0.4518	4.1861
Tm	74.231	0.4379	4.2278	74.2329	0.4341	4.2371	0.003	0.861	0.221	74.2319	0.436	4.2325
Yb	75.6957	0.4108	4.3898	75.7015	0.4084	4.3044	0.008	0.591	1.964	75.6986	0.4096	4.3471
Lu	78.0854	0.3904	3.7515	78.0821	0.3889	3.7498	0.004	0.378	0.044	78.0838	0.3897	3.7506
Hf	70.8313	0.7648	3.5613	70.8216	0.7623	3.7227	0.014	0.324	4.431	70.8264	0.7635	3.642
Ta	61.7472	1.1622	4.4019	61.75	1.1618	4.4099	0.005	0.04	0.181	61.7486	1.162	4.4059
W	56.0537	1.4388	4.4241	56.0402	1.4475	4.5265	0.024	0.606	2.287	56.047	1.4431	4.4753
Re	53.7964	1.4943	4.7861	53.8075	1.5047	4.6142	0.021	0.694	3.658	53.802	1.4995	4.7002
Os	53.0758	1.4408	4.8712	53.0989	1.4474	4.751	0.043	0.454	2.499	53.0874	1.4441	4.8111
Ir	53.8628	1.1966	5.0594	53.8613	1.1995	5.1765	0.003	0.244	2.288	53.8621	1.1981	5.118
Pt	57.352	0.8618	5.7438	57.3201	0.8643	5.4607	0.056	0.299	5.053	57.3361	0.8631	5.6022
Au	63.9782	0.6137	5.0155	63.9457	0.6118	4.9955	0.051	0.316	0.4	63.962	0.6127	5.0055
Hg	72.6361	0.3996	5.0268	72.6256	0.3987	5.0425	0.014	0.227	0.312	72.6309	0.3992	5.0346
Tl	79.0415	0.342	5.0814	79.0379	0.339	4.9592	0.005	0.893	2.433	79.0397	0.3405	5.0203
Pb	79.2776	0.3794	3.8982	79.265	0.3774	3.9039	0.016	0.543	0.146	79.2713	0.3784	3.9011
Bi	74.0582	0.5105	5.3345	74.0287	0.5086	5.3135	0.04	0.375	0.394	74.0434	0.5096	5.324
Po	70.8958	0.5272	5.0055	70.8765	0.5255	5.0621	0.027	0.318	1.124	70.8861	0.5263	5.0338
At	71.73	0.5069	3.8506	71.7022	0.5063	3.8325	0.039	0.131	0.47	71.7161	0.5066	3.8416
Rn	72.1705	0.6647	6.1163	72.063	0.6635	6.4004	0.149	0.19	4.54	72.1167	0.6641	6.2583
Fr	79.526	0.4316	6.6797	79.5124	0.4302	6.6962	0.017	0.324	0.247	79.5192	0.4309	6.688
Ra	87.7112	0.2318	8.0555	87.7466	0.2294	8.1243	0.04	1.042	0.85	87.7289	0.2306	8.0899

Table S4.10. (continued) Table with all calculated EOS parameters for the XO_3 structures obtained with FLEUR and WIEN2k.

	FLEUR			WIEN2k			Abs. percentage difference [%]			Average set		
	V_0 [Å^3]	B_0 [eV/Å^3]	B_1	V_0 [Å^3]	B_0 [eV/Å^3]	B_1	$\lvert\eta(V_0)\rvert$	$\lvert\eta(B_0)\rvert$	$\lvert\eta(B_1)\rvert$	V_0 [Å^3]	B_0 [eV/Å^3]	B_1
Ac	91.3919	0.2075	5.8257	91.492	0.2046	5.6485	0.11	1.398	3.09	91.442	0.206	5.7371
Th	84.9418	0.3566	5.4148	84.985	0.353	5.3017	0.051	1.021	2.11	84.9634	0.3548	5.3583
Pa	77.7028	0.5786	5.6105	77.7052	0.577	5.6618	0.003	0.275	0.91	77.704	0.5778	5.6362
U	72.2283	0.929	4.2343	72.2313	0.9266	4.2328	0.004	0.259	0.034	72.2298	0.9278	4.2335
Np	70.2882	0.8987	4.1862	70.2877	0.8955	4.2317	0.001	0.362	1.08	70.288	0.8971	4.209
Pu	68.8403	0.8615	4.2029	68.8377	0.8588	4.2618	0.004	0.318	1.391	68.839	0.8602	4.2323
Am	67.8603	0.8185	4.1875	67.8468	0.8165	4.3118	0.02	0.245	2.926	67.8536	0.8175	4.2497

S5 Simulation parameters for FLEUR and WIEN2k

The AE codes used for producing the reference results in this work implement the (linearized) augmented-plane-wave + local orbitals ((L)APW+LO) method. This method is named after a family of different, but related basis sets, each having different characteristics and demands on cutoff parameters. It is based on a partitioning of the unit cell into muffin-tin (MT) spheres at the atom positions and an interstitial region in between the spheres. The MT sphere radii hereby have to be adapted to each structure to avoid overlapping spheres, but are typically chosen to be nearly touching, because large spheres reduce demands on the LAPW basis set cutoff parameter. The exact choice of the radii typically differs between (L)APW+LO codes.

The choice of the core/valence electron separation is related to the MT sphere radii. To avoid instabilities in the calculations and to obtain precise results, the extent of the core-electron states beyond the MT sphere boundary has to be limited. The AE codes employed here share the same core/valence separation for many structures, but differ in this choice for a considerable amount of other structures. Taking into account the overall excellent agreement between the results from the two codes it can be deduced that there is no significant dependence of the results on the differing description of physics for core and valence electrons, as long as the core/valence separation is within a reasonable range.

The valence electrons are represented by the (L)APW+LO basis chosen by the respective code. The different possible choices of basis sets nevertheless share a common set of parameters with which they are specified. These are cutoff parameters for the basis set size and the angular momentum expansion in the MT spheres, as well as energy parameters defining the linearization centers for each atom. Additionally, the local orbital setup has to be defined for each MT sphere. The two AE codes employed in this work make use of different kinds of (L)APW+LO basis sets and their choices for the setup aspects discussed here differ strongly.

A sketch on the parameter setup recipes is provided in the following two subsections. A detailed list of the setup parameter choices for each structure is available in the supplementary data, as referenced in the respective sections below. Moreover, these parameters are implemented for both FLEUR and WIEN2k in the `aiida-common-workflows` package (version `v1.0.0` and above) through the protocol `verification-PBE-v1`.

S5.1 FLEUR

The FLEUR code[31,32] is an open-source implementation of the all-electron full-potential linearized augmented-plane-wave (FLAPW) method[99,100]. The calculations with this code make use of a conventional LAPW basis in combination with local orbitals (LOs) of different types to describe semicore states[101] and to eliminate the linearization error for the valence states[102–104]. The employed setup profile defines global parameters, identical for all calculations and element-specific parameters. Further parameters are automatically adapted to each investigated structure.

In the context of this profile, global parameters are the reciprocal LAPW basis set cutoff parameter $K_{\max} = 5.0\ a_0^{-1}$ and the plane-wave cutoff parameters $G_{\max} = G_{\max,\mathrm{XC}} = 25.0\ a_0^{-1}$, where a_0 is the Bohr radius. The latter cutoff parameter covers the expansions of the plane-wave part of the density and the potential, the interstitial-region indicator function, and the exchange-correlation contribution to the potential. The Fermi–Dirac smearing and the k-point density are also fixed to the common choices of this work. Element-specific setup aspects include the core-valence separation of the electron states and the LO setup. The radii of the MT spheres centered on atom α, R^{α}_{MT}, are adapted to the smallest unit cell within an equation-of-states (EOS) workflow. For this, element-specific initial MT sphere radii are expanded to cover up to about 92% of the distance between the atoms, with a limit of a maximal MT radius of 2.66 a_0. The procedure also implies an adaption of the angular momentum cutoffs in the spheres to $l^{\alpha}_{\max} \approx K_{\max} R^{\alpha}_{\mathrm{MT}}$. A detailed description of the different parameters is available in the FLEUR user guide[31,32].

The parameter profile is the result of an iterative refinement process aiming at precision and stability on the basis of the structures investigated in this work, i.e., structures with a wide range of neighboring atom distances. However, it is not designed to provide an absolute convergence of the total energy, which may still be affected by structure-adapted numerical parameters like the MT radii. The determination of these parameters for each structure on the basis of the smallest unit cell solves this issue for the EOS workflow. Comparing the total-energy results from the EOS workflows for different structures may also yield reasonable numbers, but these do not reflect the precision capabilities of the code when used in an adequate way to perform such a comparison, see also discussion in SI Sec. S18.

With the exception of the k-point integration-mesh generation, the used parameter profile is implemented in the openly available releases of FLEUR starting with the MaX-R6.1 release. The results presented here have been obtained using the development version as of 2022/03/31. The profile is employed by invoking the FLEUR input generator with the command line option "`-profile oxides_validation`". Beyond using this profile, the AiiDA common workflows package[36] protocol "`verification-pbe-v1`" in combination with AiiDA-FLEUR[105,106] also sets the k-point integration mesh.

The resulting parametrization for each structure is discussed in the `all-electron-setups` folder of the supplementary data available in Ref. 62, in particular in the files

- `setup-oxides-verification-PBE-v1-fleur.json`

- `setup-unaries-verification-PBE-v1-fleur.json`

that are documented in the file `all-electron-data.md`.

In an ongoing effort the data from this work is also used to define further FLEUR parameter profiles for different precision levels and computational effort. This is done by reducing in a controlled way cutoff parameters and changing other aspects of the setup and relating the corresponding results to those presented here.

S5.2 WIEN2k

The WIEN2k calculations[33,34] employ the (linearized) augmented plane wave + local orbitals ((L)APW+lo) method[107] with additional local orbitals[101] (LOs) for states with an energy 1 Ry below the Fermi energy (semicore states) and high-derivative LOs (HDLOs)[108] for all "chemical" l values (except when there is already a semicore LO). The APW+lo basis set is used for all "chemical" l values (s, p, d or f - depending on the atom), while LAPW is used for higher angular momentum up to $l_{\max} = 10$.

The WIEN2k calculations have been initialized (see the WIEN2k users guide[33]) for the smallest volume of each case using:

```
init_lapw -b -prec 3 -nokshift -fermits 0.0045 -red 3 -numk -1 0.0317506
```

For subsequent volumes we use:

```
init_lapw -b -prec 3 -nokshift -fermits 0.0045 -red Element:RMT -numk 0 kx ky kz -fft ix iy iz
```

where `Element:RMT`, `kx ky kz`, and `ix iy iz` are inserted from the output of the first volume to ensure identical parameters.

This high-precision setup limits the maximal atomic sphere radius R^{α}_{MT} to 2.35 a_0, but otherwise sets the sphere sizes automatically depending on nearest neighbor distances and type of atom (largest for f elements, intermediate for d elements and smallest for sp elements). Also the plane wave cutoff $R^{\alpha}_{\mathrm{MT,\,min}} K_{\max}$ is set automatically depending on the type of atom and the smallest atomic sphere radius $R^{\alpha}_{\mathrm{MT,\,min}}$ and varies from 7.08 (H_2O_5) to 11. All states with an energy above -6 Ry or with a charge density of more than 0.01 e^- outside the atomic sphere are considered as valence states and treated scalar-relativistically, while lower energy states are considered as core and solved numerically with a radial symmetric Dirac equation. Note that with this choice the definition of core states for an element may change depending on its R^{α}_{MT} and this makes the calculation of formation energies in certain cases unrealistic as discussed also in SI Sec. S18. An SCF cycle was considered converged when both the change in total energy was less than 10^{-6} Ry and the change in the electron charge density within R^{α}_{MT} was less than 10^{-6} e.

The charge density and potential inside spheres is expanded into lattice harmonics up to $L_{\max} = 6$ and for the non-spherical Hamiltonian matrix elements the angular momentum of the wave functions is restricted to $l^{ns}_{\max} = 8$. In the interstitial region the density/potential is expanded into a Fourier series with cutoff parameter $G_{\max} = 25\ a_0^{-1}$ (except for alkali metals, noble gases, and Hg, where $G_{\max} = 40\ a_0^{-1}$).

The resulting parametrization for each structure is discussed in the `all-electron-setups` folder of the supplementary data available in Ref. 62, in particular in the files

- `setup-oxides-verification-PBE-v1-wien2k.json`
- `setup-unaries-verification-PBE-v1-wien2k.json`

that are documented in the file `all-electron-data.md`.

S6 Dependence of the metrics on the size of the simulation cell and on bond stiffness

The equation of state is often expressed in terms of the absolute energy E and volume V of the simulation cell, but other times quantities "per-formula-unit" or "per-atom" are considered. We want here to demonstrate that the new metrics ε and ν, introduced here, are intrinsic quantities, i.e., they are independent of the simulation cell size (while the original Δ metric is extensive).

Dependence on the number of atoms in the simulation cell: We first show that the original metric Δ is an extensive quantity that depends linearly on the number of atoms (or, equivalently, on the volume) of the simulation cell.

Let us consider a supercell where the number of atoms is increased by a factor of C. The volume and the total energy (assuming $E_0 = 0$) will scale accordingly as

$$E' = CE, \quad V' = CV. \tag{S5}$$

The integrand in Eq. (3) for the Δ metric will scale as

$$[E'_a(V') - E'_b(V')]^2 \, dV' = C^3 [E_a(V) - E_b(V)]^2 \, dV \tag{S6}$$

and the denominator as

$$V'_M - V'_m = C(V_M - V_m). \tag{S7}$$

The effect of increasing the number of atoms on the Δ metric is

$$\begin{aligned} \Delta'(a,b) &= \sqrt{\frac{1}{V'_M - V'_m} \int_{V'_m}^{V'_M} [E'_a(V') - E'_b(V')]^2 \, dV'} = \sqrt{\frac{C^3}{C(V_M - V_m)} \int_{V_m}^{V_M} [E_a(V) - E_b(V)]^2 \, dV} \\ &= C \sqrt{\frac{1}{V_M - V_m} \int_{V_m}^{V_M} [E_a(V) - E_b(V)]^2 \, dV} = C\Delta(a,b). \end{aligned} \tag{S8}$$

Thus, Δ scales *linearly* with the number of atoms in the simulation cell. This shortcoming is typically addressed by computing the Δ metric renormalized per atom.

For the ε metric we proceed in the same manner to demonstrate, instead, its independence from the simulation cell size.

$$\begin{aligned} \varepsilon'(a,b) &= \sqrt{\frac{\int_{V'_m}^{V'_M} [E'_a(V') - E'_b(V')]^2 \, dV'}{\sqrt{\left(\int_{V'_m}^{V'_M} [E'_a(V') - \langle E'_a \rangle]^2 \, dV'\right) \left(\int_{V'_m}^{V'_M} [E'_b(V') - \langle E'_b \rangle]^2 \, dV'\right)}}} \\ &= \sqrt{\frac{C^3 \int_{V_m}^{V_M} [E_a(V) - E_b(V)]^2 \, dV}{\sqrt{\left(C^3 \int_{V_m}^{V_M} [E_a(V) - \langle E_a \rangle]^2 \, dV\right) \left(C^3 \int_{V_m}^{V_M} [E_b(V) - \langle E_b \rangle]^2 \, dV\right)}}} \\ &= \sqrt{\frac{\int_{V_m}^{V_M} [E_a(V) - E_b(V)]^2 \, dV}{\sqrt{\left(\int_{V_m}^{V_M} [E_a(V) - \langle E_a \rangle]^2 \, dV\right) \left(\int_{V_m}^{V_M} [E_b(V) - \langle E_b \rangle]^2 \, dV\right)}}} = \varepsilon(a,b). \end{aligned} \tag{S9}$$

Since C cancels out, we have proven that ε is independent of the number of atoms in a simulation cell considered.

Analogously, it is also easy to see that ν is also an intrinsic quantity, independent of the number of atoms in the simulation cell: indeed, ν is defined as a function of the relative errors of the parameters V_0, B_0 and B_1, that are all intrinsic quantities.

We stress that this means that, while for Δ is recommended to report it normalized (e.g., per atom, or per formula unit), ε and ν should *not* be normalized.

Sensitivity to the value of the bulk modulus: Let us compare the metrics obtained comparing results for two different materials. We assume that the first material has bulk modulus B_0 and the second is identical except for its bulk modulus, that is scaled by factor of C, i.e., $B'_0 = CB_0$. We assume that there is no other difference between the two materials (same V_0 and B_1) and we are considering the same simulation volume (or number of atoms in the simulation cell). The total energy of the second material will then scale as

$$E' = CE \tag{S10}$$

according to Eq. (1) and assuming $E_0 = 0$ (minimum energy of both materials have been shifted to zero). The integrand in Eq. (3) for the Δ metric scales as

$$[E'_a(V) - E'_b(V)]^2 \, dV = C^2 [E_a(V) - E_b(V)]^2 \, dV. \tag{S11}$$

Following similar steps as for the number of atoms above, we arrive to the conclusion that Δ scales also *linearly* with the bulk modulus, while the ε metric is insensitive to the it. Similarly, also ν is insensitive to the reference value of the bulk modulus of the material, since it only depends on the relative change of the bulk modulus B_0 between the two systems, that does not depend on the factor C.

We stress that this fact does not mean that ε or ν will not capture a difference between bulk moduli when comparing two computational approaches a and b. It means, instead, that two datasets with a similar discrepancy in the bulk moduli (say 2%) will result in the same ε or ν irrespective of overall stiffness of their chemical bonds (i.e., their bulk modulus). We highlight that this shortcoming of the Δ metric was already recognized in the literature and addressed by defining a modified metric Δ_1 in Ref. 63.

S7 Sensitivity of Δ, ε and ν to perturbations of the EOS parameters and choice of thresholds for excellent and good agreement

Any of the three metrics Δ, ε or ν expresses the difference between two EOS curves by a single number. It is not *a priori* obvious, however, when those numbers can be considered small or large, and which features of the EOS have the largest impact on the value. In this section, we address these points.

In SI Fig. S7.1 we compare the EOS of a hypothetical material with the EOS obtained after four different perturbations of the material (see caption for details). The values for Δ, ε and ν that express the difference between the original and perturbed EOS are listed for each case. Analyzing these results allows to associate typical orders of magnitude to each of the metrics, and quantify their variation with respect to changes in V_0, B_0, and B_1.

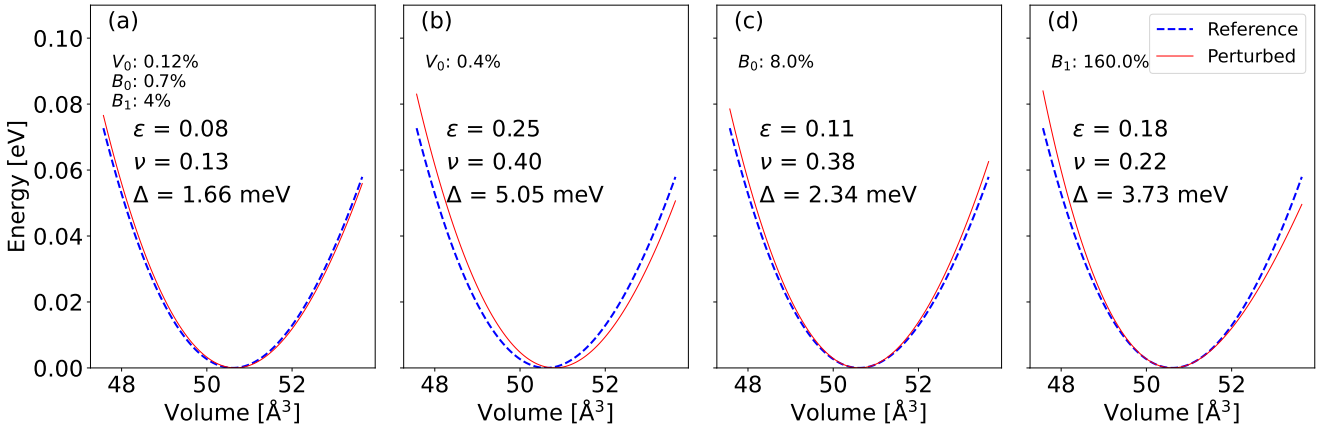

Figure S7.1. EOS for a hypothetical material with $V_0 = 50.61$ Å^3 per formula unit, $B_0 = 0.71$ eV/Å^3, and $B_1 = 4.67$ ("reference" curve, dashed blue), compared with the EOS where a perturbation has been applied to some of the EOS-defining parameters ("perturbed" curve, solid red). Each panel reports the resulting value for the three metrics ε, ν and Δ obtained comparing the two curves. The perturbed parameters and the magnitude of the perturbation are also indicated in each panel. In particular, in panel (a) a perturbation of 0.12% is applied to V_0, of 0.7% to B_0 and of 4% to B_1. Panels (b), (c) and (d) present the cases when a perturbation is applied independently to V_0 (0.4%), B_0 (8%) or B_1 (160%), respectively, while the other parameters are kept unchanged.

The hypothetical reference material that is used in SI Fig. S7.1 has $V_0 = 50.61$ Å^3 per formula unit, $B_0 = 0.71$ eV/Å^3, and $B_1 = 4.67$. These values are obtained as averages over the entire crystals set and thus represent a hypothetical "average" EOS.

In panel (a), a perturbation is applied to all three parameters, namely 0.12% to V_0, of 0.7% to B_0 and of 4% to B_1. These values are twice the standard deviations of the discrepancies between the two AE codes in our reference dataset, see Fig. 1 in the main text. Since the two EOS curves are almost undistinguishable, this result highlights the high level of agreement between our two AE codes. Based on this observation, we define a qualitative range of $\varepsilon \lesssim 0.06$ or $\nu \lesssim 0.1$ for which we consider two codes display excellent agreement. The threshold of $\varepsilon = 0.06$ (approximately) corresponds to a determination coefficient $R^2 \approx 1 - \varepsilon^2 = 0.9964$ when one EOS curve is considered as a fit to the other.

In panels (b), (c) and (d), instead, a larger perturbation is applied to only one of the three parameters V_0, B_0 or B_1, respectively. The perturbation to V_0 is chosen as 0.4%, and the magnitude of the perturbations for B_0 and B_1 is scaled following the inverse ratios 1/20/400 of the weights for the ν metric (see SI Sec. S3). This results in visually similar discrepancies between the two curves. This is an expected result, and is another way to interpret the results discussed in SI Sec. S3 for the weights of ν. Indeed, those weights were obtained by inferring the error propagated on the fitted parameters from a given amount of random noise on the datasets; the inverse weights can be conversely interpreted, intuitively, as the relative magnitude of the perturbation to each of the parameters required to induce similar changes to the EOS curve. These panels help us make a number of observations:

- All metrics (Δ and ε intrinsically, and ν by explicit definition of the weights) give a much stronger importance to changes of the equilibrium volume V_0 than to changes of the other parameters. This is a positive feature of the metrics, as the EOS shape is mostly sensitive to V_0 as well. The metric ν has the additional advantage, as already discussed, that weights can be tuned to give more importance to other parameters, if an application requires it.

- With our definitions of ε and ν, the two metric often return similar values for a given pair of EOS curves, with ε typically

slightly smaller (in the SI Sec. S8, we actually identify an approximate proportionality ratio between the two, valid for small values of the metrics).

- The values of the metrics on these last three panels allow us to define threshold values for noticeable, but still relatively small, changes between two EOS curves: $\varepsilon \lesssim 0.2$ or $\nu \lesssim 0.33$. Therefore, we take the ranges of $0.06 < \varepsilon \lesssim 0.20$ or $0.10 < \nu \lesssim 0.33$ as the signature for good (but not excellent) agreement between two codes. The upper end of this range $\varepsilon = 0.20$ (approximately) corresponds to a determination coefficient $R^2 \approx 1 - \varepsilon^2 = 0.96$ when one EOS curve is considered as a fit to the other.

- We can assign an intuitive meaning to the metric ν. If two EOS only differ in the equilibrium volume, its numerical value corresponds to the percentage error on the equilibrium volume between the two curves. If also B_0 and B_1 change, then ν will also take into account the discrepancies on these two parameters, rescaled so that similar contributions to ν result to similar quantitative changes to the EOS curve (in the volume range of interest, $\pm 6\%$ in this work).

- We note that in panels (b), (c) and (d) the value of ν is not exactly 0.4 as one might naively expect, because the perturbation that we apply refers to the reference curve, but the ν metric is defined in a symmetric way, with percentage differences with respect to the average of the two curves.

- SI Fig. S7.2, finally, illustrates the clear disagreement between EOS curves when $\varepsilon \geq 1.0$ or $\nu \geq 1.65$ (these values are used as upper limit for the colorbars of the figures in SI Sec. S9). As a note, $\varepsilon = 1$ is an estimator for the situation where the coefficient of determination $R^2 \approx 1 - \varepsilon^2$ starts to be negative (even if the approximation $R^2 \approx 1 - \varepsilon^2$ does not hold exactly anymore for such large values of ε). We highlight that a negative R^2 value indicates that a horizontal line at the average value of the data provides a better fit than the actual fit function. It is clear from SI Fig. S7.2 that in such cases there is no agreement at all between the results of two codes. Therefore, when $\varepsilon > 1.0$ or $\nu > 1.65$, two codes are said to be clearly different in SI Sec. S9.

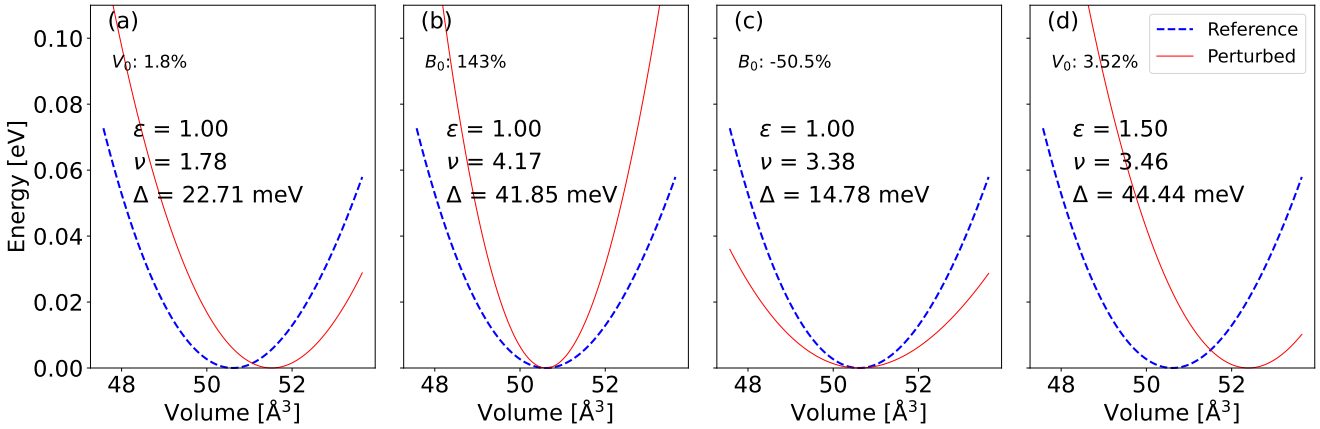

Figure S7.2. EOS for a hypothetical material with $V_0 = 50.61$ Å^3 per formula unit, $B_0 = 0.71$ eV/Å^3, and $B_1 = 4.67$ ("reference" curve, dashed blue), compared with the EOS where a perturbation has been applied to some of the EOS-defining parameters ("perturbed" curve, solid red). With respect to SI Fig. S7.1, we highlight here typical values for the metrics for large changes of the parameters that make the EOS curves clearly different. Each panel reports the resulting value for the three metrics ε, ν and Δ obtained comparing the two curves. The perturbed parameters and the magnitude of the perturbation are also indicated in each panel. In particular, in panel (a) a perturbation is applied to V_0 to obtain a value of $\varepsilon = 1$; panels (b) and (c) apply a (positive and negative, respectively) perturbation to B_0 resulting in $\varepsilon = 1$, and finally in panel (d) an even larger perturbation is applied to V_0 to obtain a value of $\varepsilon = 1.5$.

S8 Mutual correlation between the metrics

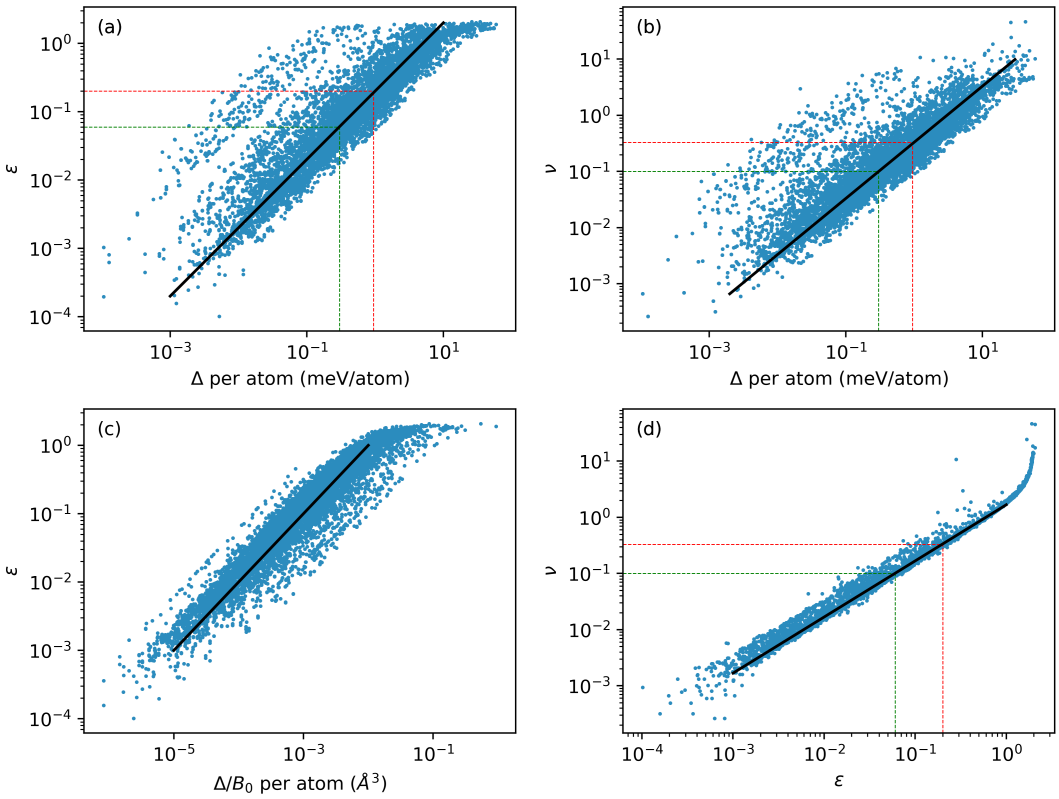

Figure S8.1. Cross-correlation between the Δ, ε, and ν metrics for the entire data (unaries and oxides) presented in the main text. Black lines are helpers to indicate a linear relation between the quantities (slope of 1 in a log-log plot). Dashed lines on ε and ν axes show the "excellent" (green) and "good" (red) agreement thresholds recommended in the main text. From the plots, these correspond to values of Δ of approximately 0.3 and 0.95 meV/atom, respectively.

In order to assess the correlation between the various metrics, we present in SI Fig. S8.1 for all codes mentioned in the main text their Δ, ε or ν with respect to the reference EOS, for each of the unaries and oxides. These Δ, ε or ν are plotted against one of the other metrics. The results support the presence of an approximately linear correlation between the three metrics (Δ, ε, and ν). However, there is more scattering in the correlation between ε and Δ (and, similarly, between ν and Δ), while ε and ν agree more consistently on a global scale.

We first note that the scattering between ε and Δ can be reduced by normalizing Δ by the bulk modulus, similar to the Δ_1 metric introduced in Ref. 63, as shown in SI Fig. S8.1(c). We then observe that the new metrics ε and ν are instead almost linearly correlated when their values are $\lesssim 1$; for larger discrepancies, the values of ν tend to grow faster than the values of ε, i.e., ε becomes relatively less sensitive to further small changes to the EOS curves if they are already significantly different.

This almost linear correlation can be justified with some approximations. Let us consider the simple case of two parabolic EOS curves with the same B_0, differing only in the equilibrium volume V_0. This is a valid approximation, since we discussed above that both metrics are mostly sensitive to changes of V_0 rather than B_0 or B_1. If we call $2V_R = V_M - V_m$ the volume range for the integration in ε (see also Eq. (4) in the main text for the definition of V_m and V_M) and $\tilde{V}$ the average volume of the two curves (with actual minima for $V_0 = \tilde{V} \pm \Delta V$), we obtain $\nu = 200\frac{\Delta V}{\tilde{V}}$. We now consider the limit in which $\Delta V \ll V_R$ (i.e., of a small discrepancy of the two curves in the volume range of interest, corresponding to the regime of small ε and ν in which our data show an almost linear relation between the two metrics).

It is then straightforward to show that $\varepsilon \approx 2\sqrt{15}\frac{\Delta V}{V_R}$. Indeed, writing the two curves as $E_{1,2}(V) = A(V - \tilde{V} \pm \Delta V)^2$, with A an appropriate coefficient (the same for both curves with our assumptions of same bulk modulus), we get that the integral in the

numerator of ε, $\langle[E_1(V)-E_2(V)]^2\rangle$, is given by:

$$\frac{1}{2V_R}\int_{\tilde{V}-V_R}^{\tilde{V}+V_R}[A(V-\tilde{V}-\Delta V)^2-A(V-\tilde{V}+\Delta V)^2]^2dV=\frac{1}{V_R}\int_{\tilde{V}}^{\tilde{V}+V_R}[A(V-\tilde{V}-\Delta V)^2-A(V-\tilde{V}+\Delta V)^2]^2dV \tag{S12}$$

$$=\frac{1}{V_R}\int_{\tilde{V}}^{\tilde{V}+V_R}[4A(V-\tilde{V})\Delta V]^2dV=\frac{16A^2\Delta V^2V_R^2}{3}. \tag{S13}$$

Similarly, we can obtain (using our assumption $\Delta V \ll V_R$) that

$$\langle E_1(V)\rangle=\frac{1}{2V_R}\int_{\tilde{V}-V_R}^{\tilde{V}+V_R}A(V-\tilde{V}-\Delta V)^2dV\approx\frac{1}{V_R}\int_{\tilde{V}}^{\tilde{V}+V_R}A(V-\tilde{V})^2dV=\frac{AV_R^2}{3}, \tag{S14}$$

and $\langle E_2(V)\rangle=\langle E_1(V)\rangle$. Using similar steps, one can also obtain $\langle[E_1(V)-\langle E_1\rangle]^2\rangle=\langle[E_2(V)-\langle E_2\rangle]^2\rangle\approx\frac{4}{45}A^2V_R^4$. Putting all results together, we obtain the final result $\varepsilon\approx 2\sqrt{15}\frac{\Delta V}{V_R}$.

Finally, considering our choice of a $\pm 6\%$ volume range ($V_R\approx 0.06\tilde{V}$) gives $\varepsilon\approx\frac{100}{3}\sqrt{15}\frac{\Delta V}{\tilde{V}}$. Therefore, the two metrics are linearly dependent with the ratio of

$$\frac{\nu}{\varepsilon}\Big|_{\Delta V}=\frac{6}{\sqrt{15}}\approx 1.55, \tag{S15}$$

which also matches well with the ratio of ν and ε calculated for a specific value of V_0 perturbation shown in SI Fig. S7.1(b).

A similar analysis can be performed for two parabolic EOS curves with the same V_0, but differing in B_0. In this case, $\nu=10\frac{\Delta B_0}{\tilde{B}_0}$, where $\tilde{B}_0$ is the average B_0 of the two curves and $\pm\Delta B_0$ is the difference from the average value for the two curves. It can be shown, similarly to the case of differing V_0, that in this case $\varepsilon\approx 3\frac{\Delta B_0}{\tilde{B}_0}$. The resulting ratio of the two metrics now becomes

$$\frac{\nu}{\varepsilon}\Big|_{\Delta B_0}\approx\frac{10}{3}\approx 3.33, \tag{S16}$$

which also matches well with the ratio of ν and ε in SI Fig. S7.1(c). The difference by a factor of 2 between (S15) and (S16) shows that, compared to ε, ν is 2 times more sensitive to B_0 variation relative to V_0 variation.

To assess the typical ratio of ν and ε in our dataset, in SI Fig. S8.2 we show a cross-correlation plot between ν and ε for the entire dataset of calculated crystals. One can see that for smaller values of the metrics ($\nu<1$), the relation is approximately linear, and a numerical fit gives the slope of $\frac{\nu}{\varepsilon}\approx 1.65$, which is close to 1.55 found in Eq. (S15). This is expected, as both metrics give larger weight to V_0 errors compared to B_0 or B_1 errors, and in our dataset errors on V_0 (once rescaled with these weights) dominate over B_0 and B_1 errors. This is also visible, for instance, from the histograms of Fig. 1 in the main text, where the ratios of the standard deviation of the histograms on V_0, B_0 and B_1 do not follow the 1, $\frac{1}{20}$, $\frac{1}{400}$ ratio of ν.

The cross correlation plots allow to establish a data-driven relation between different metrics. For instance, the two boundaries $\varepsilon=0.06$ and 0.2 selected in this project as "excellent" and "good" agreement between two EOSs, and the corresponding thresholds for ν (0.10 and 0.33) have been chosen according to these cross correlations. In addition, we can see from SI Fig. S8.1a that these thresholds translate, for Δ, approximately $\Delta\approx 0.3$ and 0.95 meV/atom. This result is comparable with the average Δ across AE codes $\langle\Delta\rangle=0.5-0.9$ meV/atom obtained in the earlier benchmark[29,30] for monoelemental solids, and is consistent with the conclusion obtained there that $\Delta=1$ meV/atom is a threshold under which one can speak about good agreement (for materials with bulk moduli that are not particularly small). This consistency between former and present benchmarks is about the metric; we refer to SI Sec. S15 for a demonstration of consistency regarding the crystal set, and an illustration of the added value of the present benchmark study.

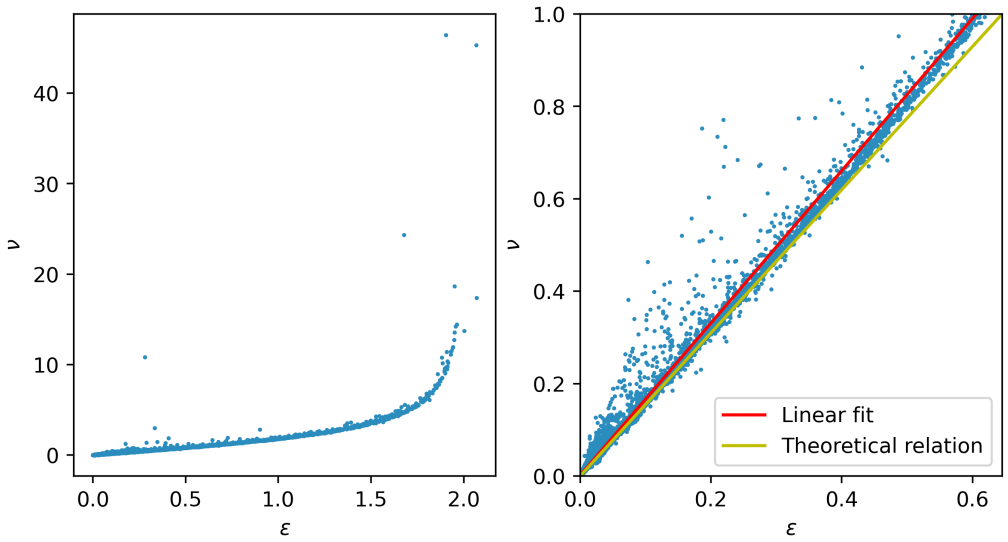

Figure S8.2. Cross-correlation between the ε and ν metrics on a linear-axes plot. Left panel: all data; right panel: zoom on the data with $\nu < 1$ where the relation is approximately linear, together with a linear fit of the data (red) resulting in a slope of ≈ 1.65, and a line with a slope ≈ 1.55 (yellow curve) taken from the parabolic model.

S9 Detailed results for all computational approaches

In this section, we report the comparison of each of the computational approaches considered in the main text with the average all-electron reference dataset, using both metrics ε and v. For each metric, the same colorbar is used for all approaches, based upon the ranges of agreement identified in SI Sec. S7 (in addition, the ratio of the threshold values for ε and v is in agreement with their approximate linear relationship, see SI Sec. S8):

- "excellent agreement" ($\varepsilon \leq 0.06$, $v \leq 0.10$): a very dark shade of blue (not evolving very much over this narrow interval);
- "good agreement" ($0.06 < \varepsilon \leq 0.20$, $0.10 < v \leq 0.33$): color evolving from a dark shade of blue to yellow as the values of ε or v increase;
- threshold for good agreement ($\varepsilon = 0.20$, $v = 0.33$): yellow;
- "noticeably different" ($0.20 < \varepsilon \leq 1.0$, $0.33 < v \leq 1.65$): color evolving from yellow to red as the values of ε or v increase;
- "clearly different" ($\varepsilon > 1.0$, $v > 1.65$): one uniform darker shade of red, regardless of the value.

Crystals that were not computed are left in white. The caption of every plot mentions the number of crystals belonging to each of these categories. The results for all the codes are shown in SI Figs. S9.1 to S9.11.

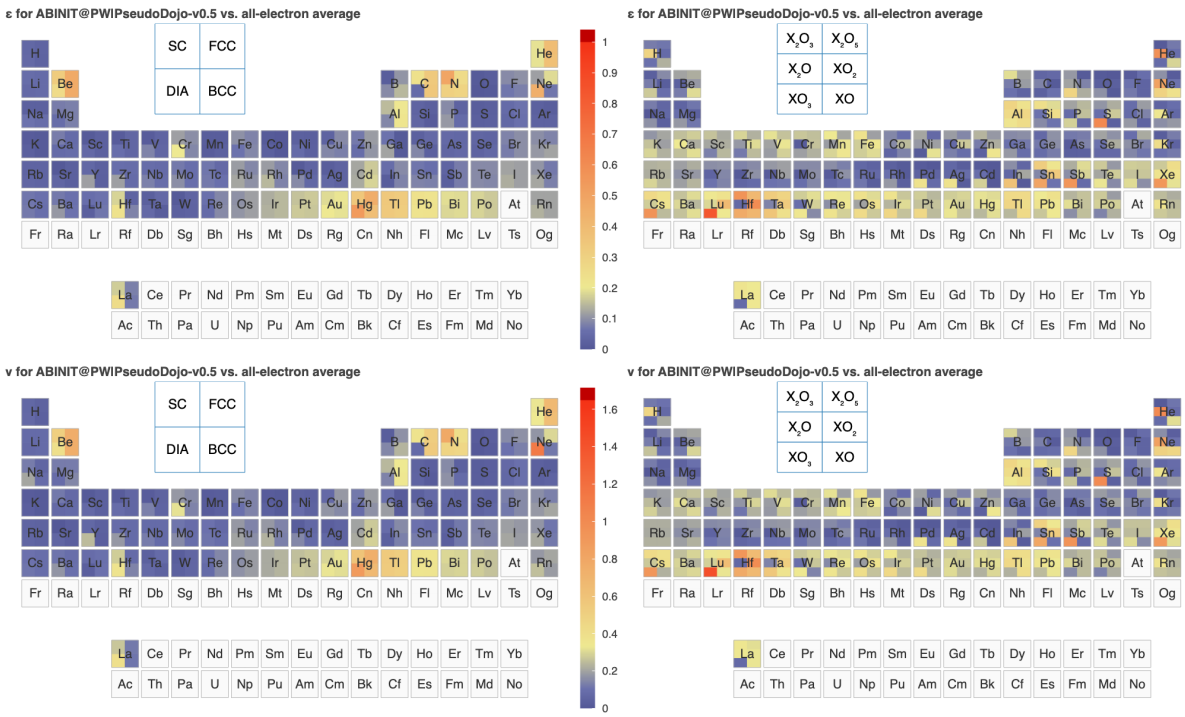

Figure S9.1. Value of the comparison metrics ε (top) and v (bottom) for `ABINIT@PW|PseudoDojo-v0.5` with respect to the average all-electron reference dataset. Left panels: unaries; right panels: oxides. 720 out of 960 crystals were calculated. The number of crystals that land in the excellent, good, noticeably different, and clearly different agreement ranges for the ε metric are 232, 377, 111, 0, respectively. For the v metric, they are 244, 378, 98, 0, respectively.

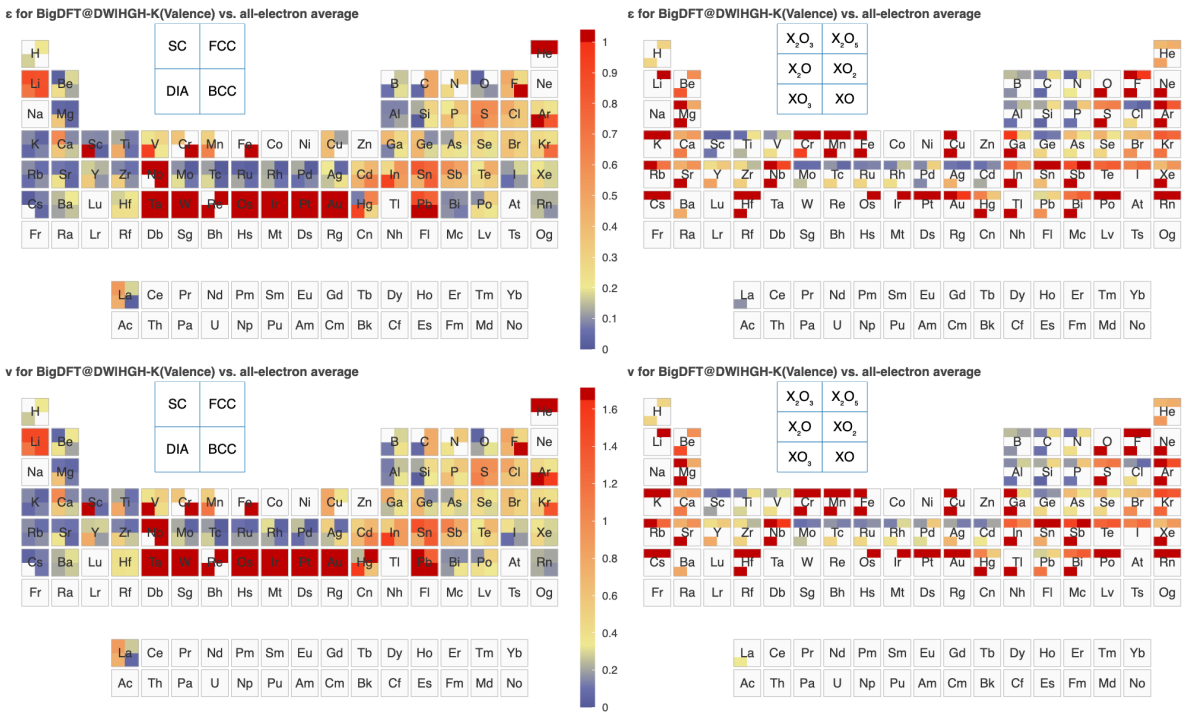

Figure S9.2. Value of the comparison metrics ε (top) and v (bottom) for `BigDFT@DW|HGH-K(Valence)` with respect to the average all-electron reference dataset. Left panels: unaries; right panels: oxides. 402 out of 960 crystals were calculated. The number of crystals that land in the excellent, good, noticeably different, and clearly different agreement ranges for the ε metric are 45, 97, 173, 87, respectively. For the v metric, they are 29, 106, 173, 94, respectively.

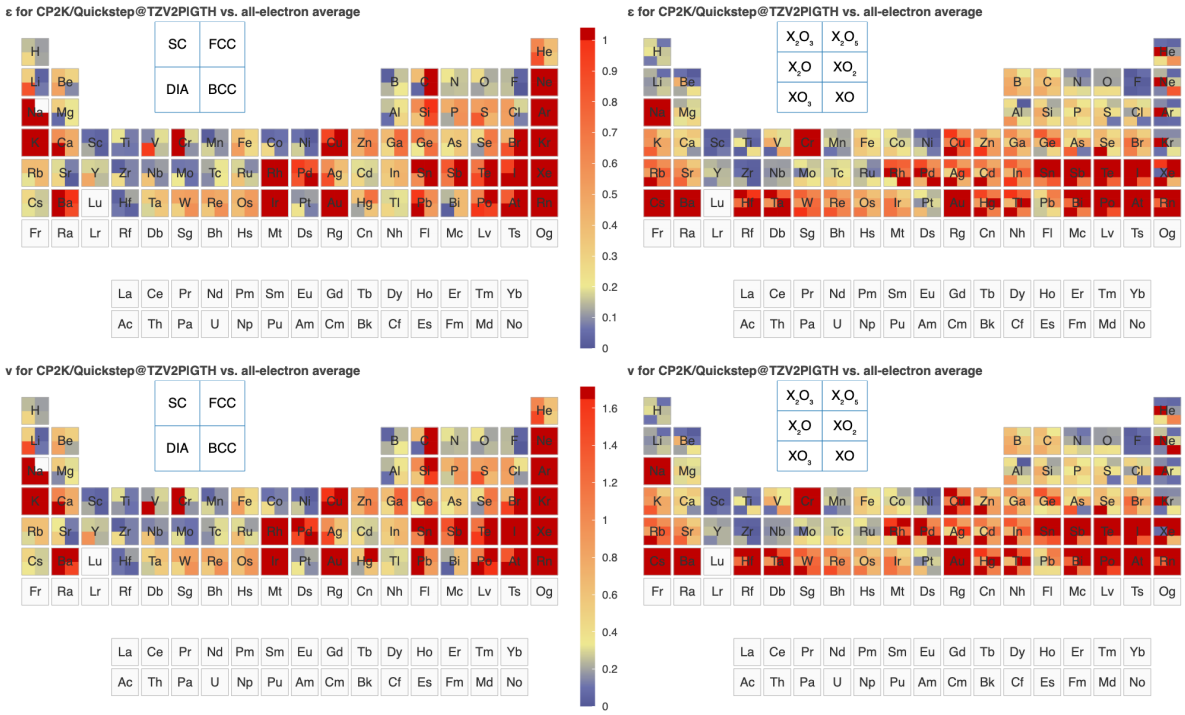

Figure S9.3. Value of the comparison metrics ε (top) and v (bottom) for `CP2K/Quickstep@TZV2P|GTH` with respect to the average all-electron reference dataset. Left panels: unaries; right panels: oxides. 709 out of 960 crystals were calculated. The number of crystals that land in the excellent, good, noticeably different, and clearly different agreement ranges for the ε metric are 57, 171, 317, 164, respectively. For the v metric, they are 55, 169, 302, 183, respectively.

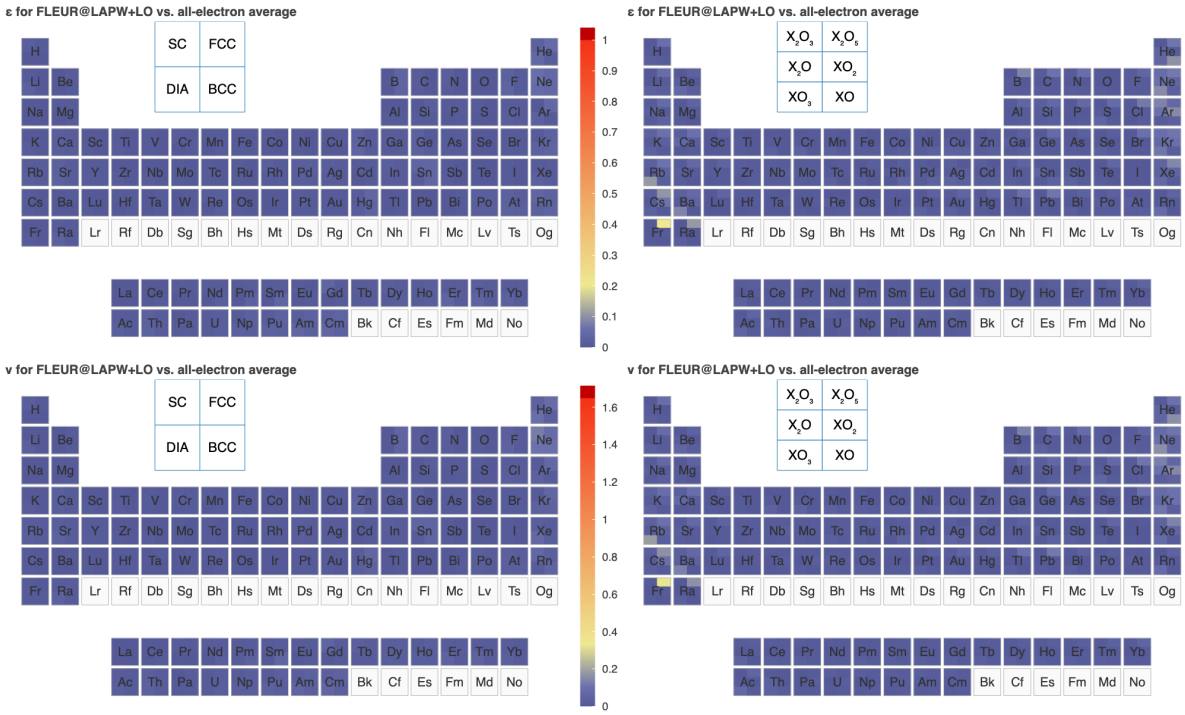

Figure S9.4. Value of the comparison metrics ε (top) and v (bottom) for `FLEUR@LAPW+LO` with respect to the average all-electron reference dataset. Left panels: unaries; right panels: oxides. 960 out of 960 crystals were calculated. The number of crystals that land in the excellent, good, noticeably different, and clearly different agreement ranges for the ε metric are 936, 23, 1, 0, respectively. For the v metric, they are 938, 22, 0, 0, respectively.

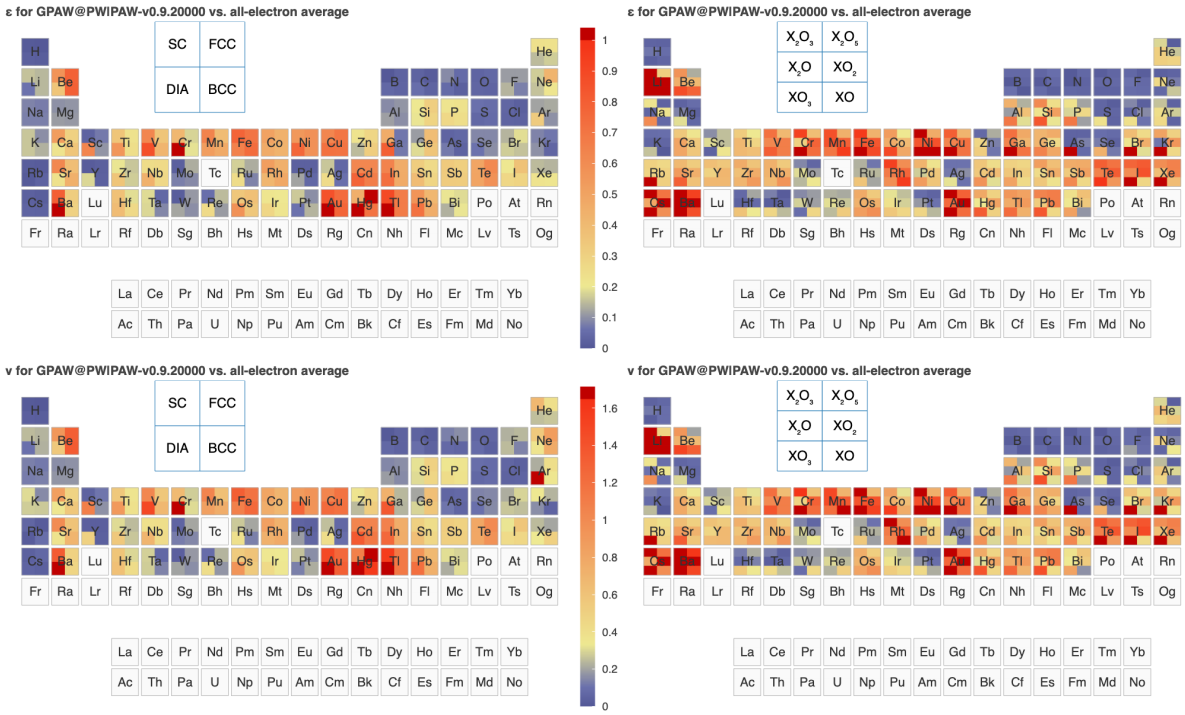

Figure S9.5. Value of the comparison metrics ε (top) and v (bottom) for `GPAW@PW|PAW-v0.9.20000` with respect to the average all-electron reference dataset. Left panels: unaries; right panels: oxides. 670 out of 960 crystals were calculated. The number of crystals that land in the excellent, good, noticeably different, and clearly different agreement ranges for the ε metric are 130, 156, 350, 34, respectively. For the v metric, they are 128, 155, 347, 40, respectively.

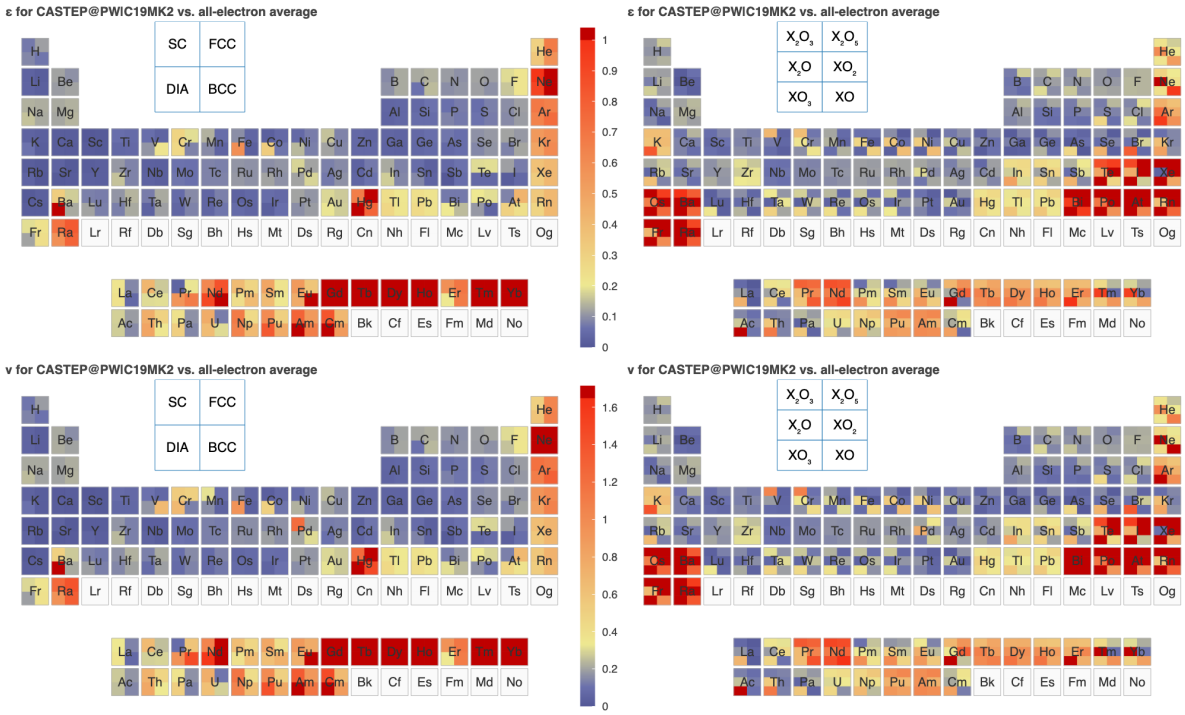

Figure S9.6. Value of the comparison metrics ε (top) and v (bottom) for `CASTEP@PW|C19MK2` with respect to the average all-electron reference dataset. Left panels: unaries; right panels: oxides. 960 out of 960 crystals were calculated. The number of crystals that land in the excellent, good, noticeably different, and clearly different agreement ranges for the ε metric are 197, 410, 277, 76, respectively. For the v metric, they are 206, 399, 267, 88, respectively.

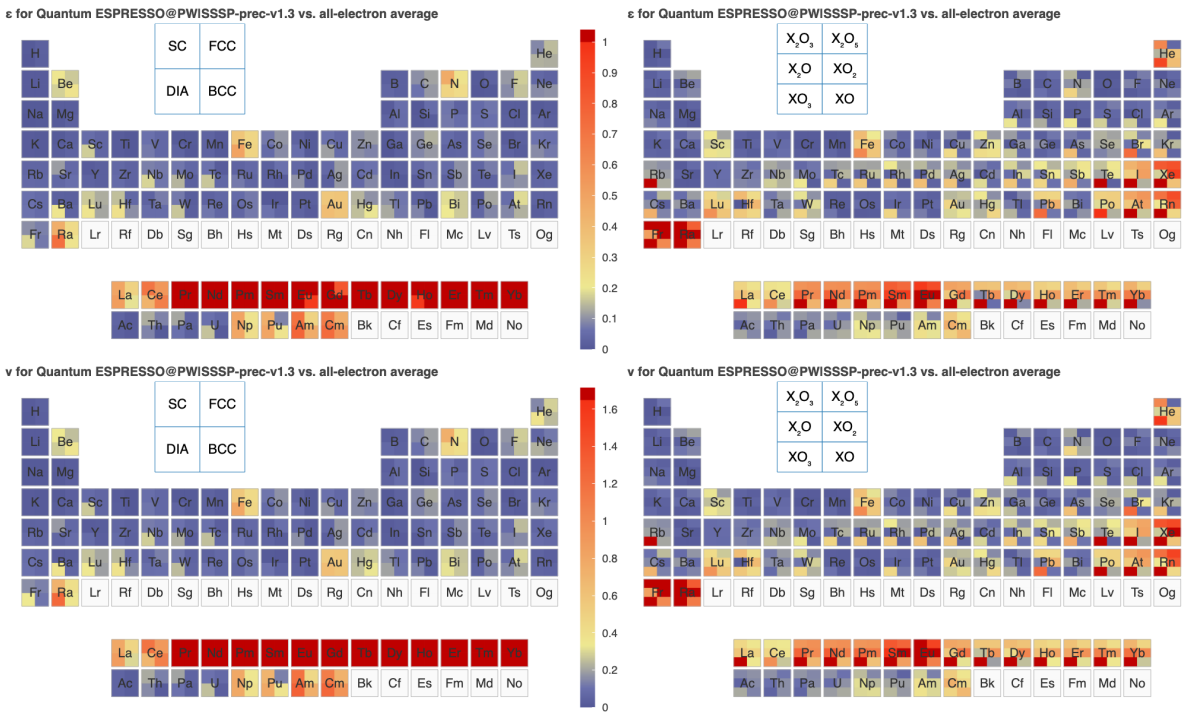

Figure S9.7. Value of the comparison metrics ε (top) and v (bottom) for `Quantum ESPRESSO@PW|SSSP-prec-v1.3` with respect to the average all-electron reference dataset. Left panels: unaries; right panels: oxides. 960 out of 960 crystals were calculated. The number of crystals that land in the excellent, good, noticeably different, and clearly different agreement ranges for the ε metric are 388, 300, 199, 73, respectively. For the v metric, they are 395, 300, 184, 81, respectively.

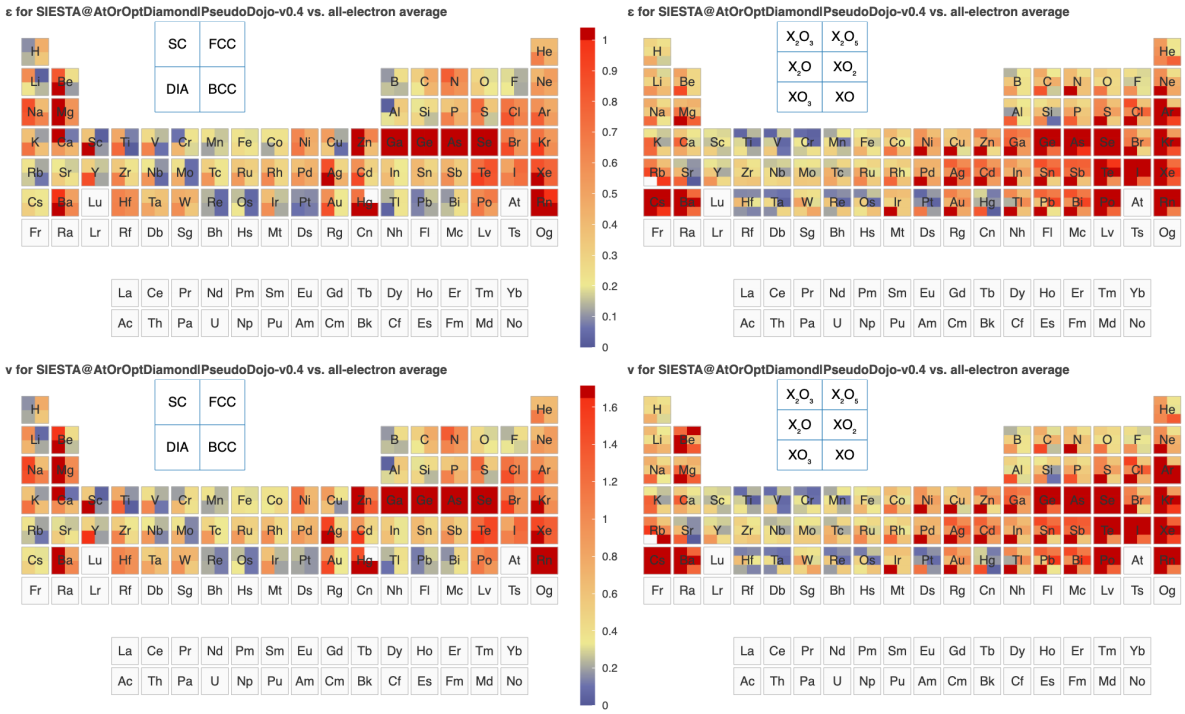

Figure S9.8. Value of the comparison metrics ε (top) and v (bottom) for `SIESTA@AtOrOptDiamond|PseudoDojo-v0.4` with respect to the average all-electron reference dataset. Left panels: unaries; right panels: oxides. 698 out of 960 crystals were calculated. The number of crystals that land in the excellent, good, noticeably different, and clearly different agreement ranges for the ε metric are 30, 117, 444, 107, respectively. For the v metric, they are 18, 137, 424, 119, respectively.

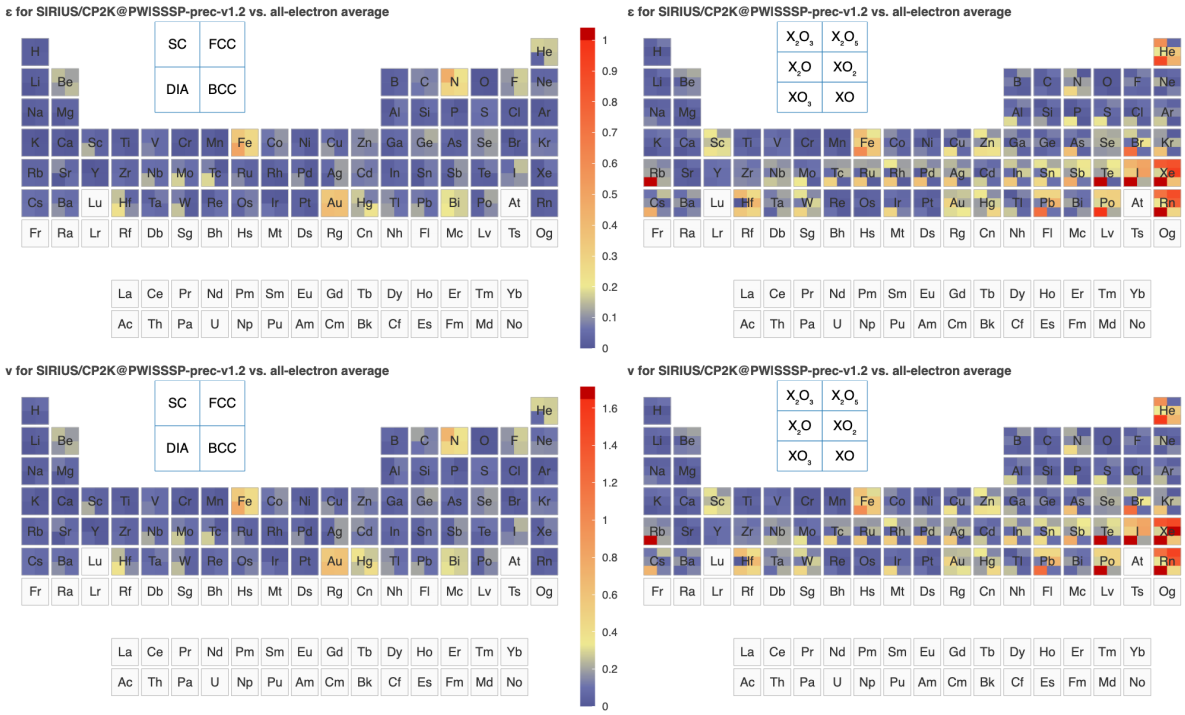

Figure S9.9. Value of the comparison metrics ε (top) and ν (bottom) for `SIRIUS/CP2K@PW|SSSP-prec-v1.2` with respect to the average all-electron reference dataset. Left panels: unaries; right panels: oxides. 700 out of 960 crystals were calculated. The number of crystals that land in the excellent, good, noticeably different, and clearly different agreement ranges for the ε metric are 363, 251, 81, 5, respectively. For the ν metric, they are 374, 247, 72, 7, respectively.

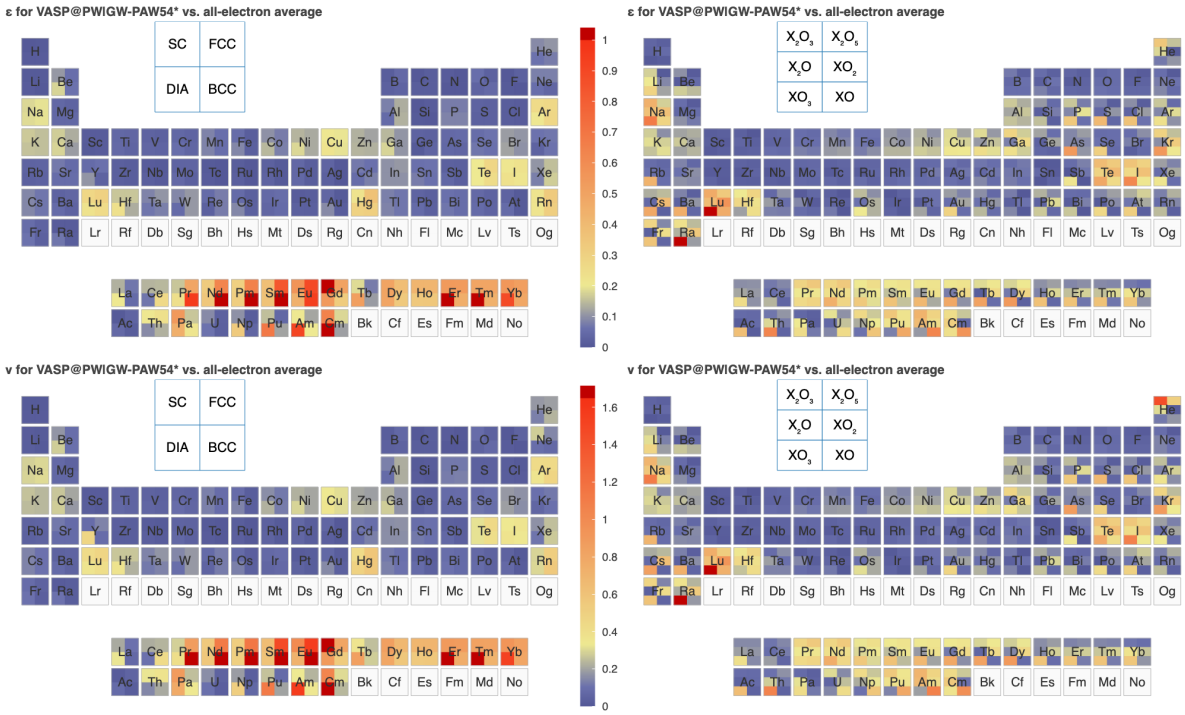

Figure S9.10. Value of the comparison metrics ε (top) and ν (bottom) for `VASP@PW|GW-PAW54*` with respect to the average all-electron reference dataset. Left panels: unaries; right panels: oxides. 960 out of 960 crystals were calculated. The number of crystals that land in the excellent, good, noticeably different, and clearly different agreement ranges for the ε metric are 403, 348, 200, 9, respectively. For the ν metric, they are 419, 341, 189, 11, respectively.

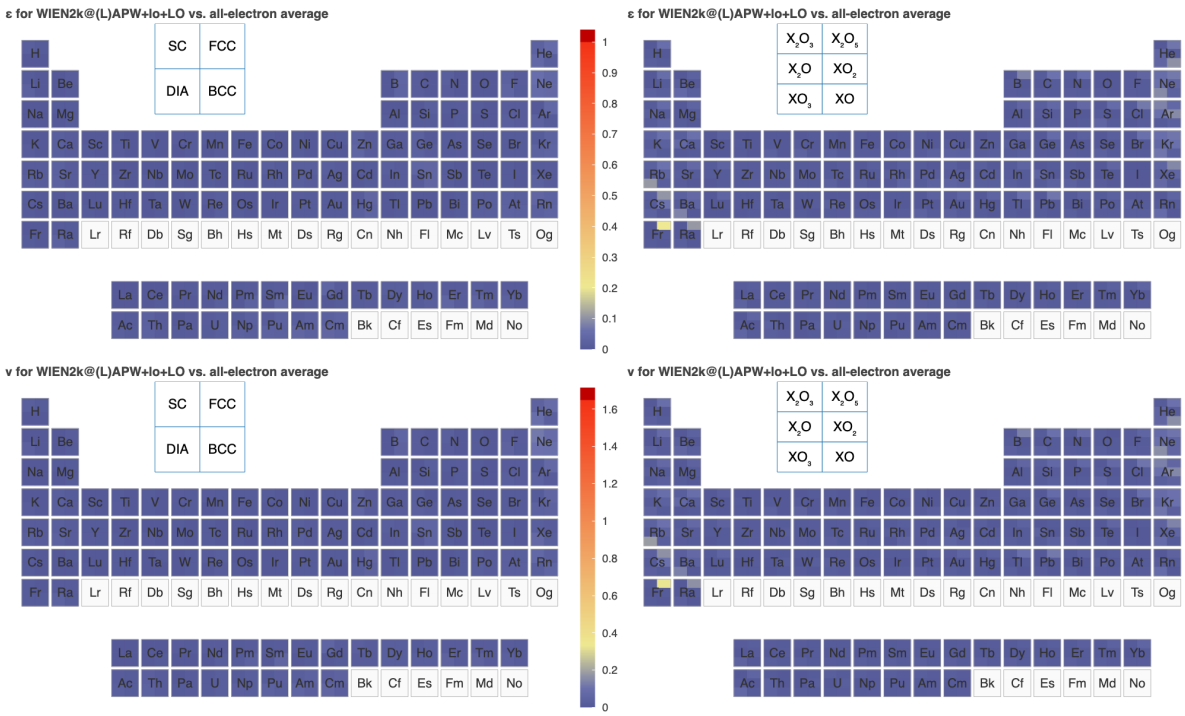

Figure S9.11. Value of the comparison metrics ε (top) and ν (bottom) for `WIEN2k@(L)APW+lo+LO` with respect to the average all-electron reference dataset. Left panels: unaries; right panels: oxides. 960 out of 960 crystals were calculated. The number of crystals that land in the excellent, good, noticeably different, and clearly different agreement ranges for the ε metric are 936, 23, 1, 0, respectively. For the ν metric, they are 938, 22, 0, 0, respectively.

S10 Smearing and k-point convergence

For the study presented in this paper, a fixed choice of k-point integration mesh and smearing has been implemented. In particular, the k-point mesh is a uniform regular grid including the Γ point, that guarantees a linear spacing of 0.06 Å^{-1} in each of the three reciprocal-space directions, and the smearing is a Fermi–Dirac type with broadening of 0.0045 Ry. This choice of parameters is essential in order to compare with the reference dataset presented in this manuscript, as explained in Box 3 of our recommendations. In this section, we present the reasoning for our choice of parameters.

The Fermi–Dirac smearing is widely used in the community and it is implemented in all the codes that participate in the study. The choice of the broadening has been made according to the recommendation of Ref. 66: the smearing parameter should not be too small to avoid sampling errors, nor too large to prevent systematic deviations due to the dependency of the total energy on the smearing broadening. The latter problem is explained in details in Ref. 66, that shows the quadratic dependence of the free energy with respect to the Fermi–Dirac smearing temperature. The problem of sampling error is instead demonstrated in SI Fig. S10.1, where we analyze a FCC aluminum crystal (conventional cell with 4 atoms) with an atom displaced by 0.1 Å with respect to its equilibrium position. The figure reports the magnitude of the force on the displaced atom as a function of the k-point integration mesh and smearing broadening. The instability of the force for very small broadening is clearly visible. Approaching the zero limit of the smearing, it becomes more and more necessary to have a dense k-point integration mesh in order to maintain 0.001 eV/Å convergence on the forces. The sampling error is not a peculiar feature of the Fermi–Dirac smearing; any other smearing type suffers from this drawback, as demonstrated in Ref. 66. Our choice of smearing broadening (0.0045 Ry ≈ 61 meV) lays on the extreme right of SI Fig. S10.1 and in this region a k-point integration mesh of $36 \times 36 \times 36$ is sufficient to obtain a converged value of the force within 0.001 eV/Å. At the same time, 0.0045 Ry is a small enough value to reduce to a minimum issues due to the dependency of the total energy on the smearing broadening. In any case, for the goal of verification, the exact value is not so important, as long as all codes perform the very same choice of smearing and k-point integration mesh.

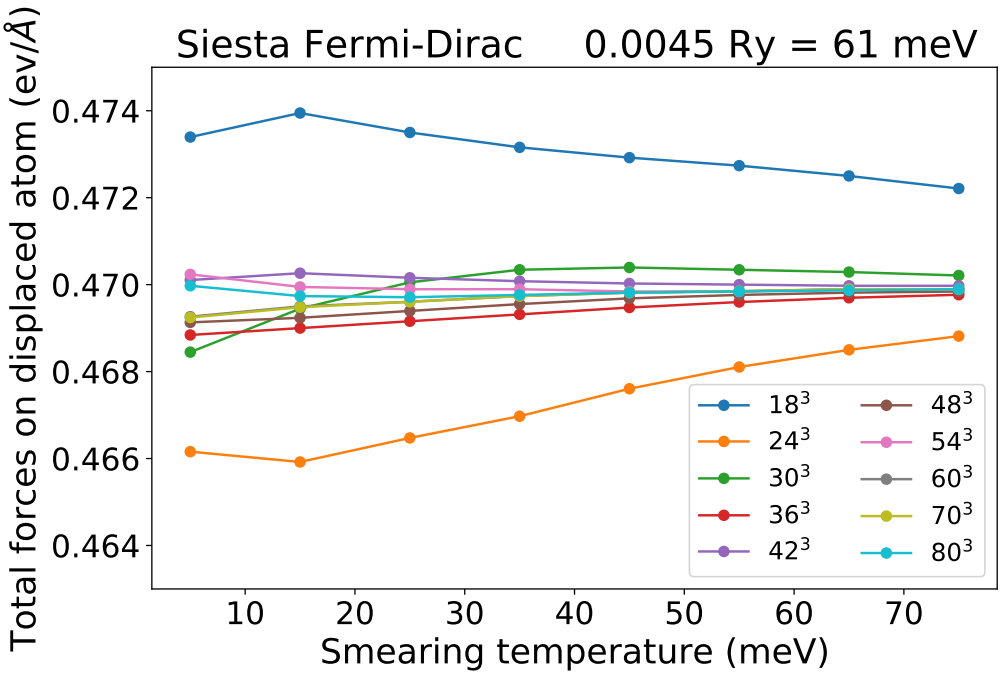

Figure S10.1. Total force on a displaced atom as a function of the smearing temperature and the k-point integration mesh. The system under investigation is an FCC Al with an atom displaced by 0.1 Å in the x direction. The volume per atom is 16.47 Å^3, for which a distance of 0.06 Å^{-1} between k-points correspond to a $26 \times 26 \times 26$ mesh. The smearing is a Fermi–Dirac smearing. Calculations of the forces are made with SIESTA and DZP (double-zeta polarized) basis set.

With our choice of the smearing broadening, we expect a rapid convergence of the electronic-structure properties with respect to the the k-point density. We test this assumption looking at the effect of the k-point integration mesh on the estimation of the EOS parameters. Using WIEN2k results, we compare calculations with k-point distance of 0.06 Å^{-1} and 0.045 Å^{-1} for all materials in the study. The comparison is reported in SI Fig. S10.2. This figure shows an overall discrepancy that is

significantly smaller with respect to the FLEUR-WIEN2k comparison presented in Fig. 1 in the main text (note that the x-axis range is half of the one in Fig. 1). Looking at the histograms, we can estimate that the overall agreement is at least a factor of 2 better for B_1 with respect to the FLEUR-WIEN2k comparison, more than a factor of 4 better for B_0 and even one order of magnitude better for V_0. The same conclusion cannot be drawn looking at the standard deviations reported in the figure, due to the presence of two important outliers: RbO_3 (3.7% difference in V_0, -142.29% difference in B_0 and 149.35% difference in B_1) and HeO (0.16% difference in V_0, 3.33% difference in B_0 and -7.90% difference in B_1). RbO_3 and HeO are the only two materials that are not converged with a k-point distance of 0.06 $Å^{-1}$. All other materials are converged within 0.07% of V_0. It is interesting to notice that, even though RbO_3 and HeO are not converged, their discrepancy is not so dramatic when comparing FLEUR and WIEN2k (Fig. 1 in the main text). This, once more, justifies our recommendation of adopting the same k-point integration mesh for all computational approaches.

For completeness, we mention that the k-point mesh comparison of SI Fig. S10.2 has been performed on the crystal-structure set described in the main text for the unaries. For the oxides set, instead, we present results of a previous iteration of the volume refinement. Therefore the structures used for the oxides calculation in SI Fig. S10.2 have central volumes that slightly differs with respect to the ones used in the main text.

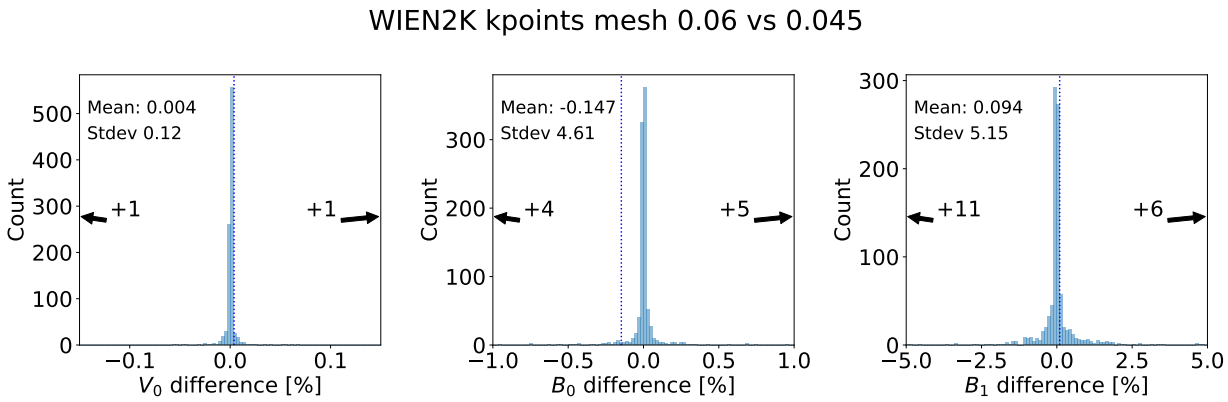

Figure S10.2. Histograms of the percentage difference between the results obtained with a k-point integration mesh with linear density 0.06 $Å^{-1}$ and 0.045 $Å^{-1}$ for the three EOS parameters V_0, B_0, and B_1. Results are obtained with WIEN2k code. Numbers close to the arrows indicate outliers beyond the x-axis range.

S11 Band structure of erbium in the diamond crystal structure

In SI Fig. S11.1 we show the band structure of erbium in the diamond crystal structure, obtained using the initial crystal structure (see SI Table S1.3) with conventional cubic lattice parameter of 8.6296 Å. The simulation has been run with the QUANTUM ESPRESSO code (version 7.0) using the PBE pseudopotential from the SSSP PBE Precision 1.2 library. 78, and the recommended cutoffs of 40 Ry and 320 Ry for the wavefunctions and charge density, respectively. A $9 \times 9 \times 9$ k-point integration mesh is chosen (note: this is less dense than the mesh recommended in the main text, but sufficient to demonstrate qualitatively the key features of the band structure, that is the goal of this section), and a Fermi–Dirac smearing with 0.0045 Ry of broadening. Input and output files are available in Ref. 62.

The band structure clearly displays a set of "almost flat" bands (with a dispersion of ~ 0.1 eV) very close to the Fermi energy in the range between -0.2 eV and 0 eV, originating from the f states of erbium. For this specific calculation and volume, these f bands are just below the Fermi level, but their position can shift with volume and cross the Fermi level, significantly affecting the nature of the occupied states in the material. This explains the unconventional shape of the EOS displayed in the main text in Fig. 3.

An interesting note is that the location of the f bands, determining the lowest-energy minimum of the EOS, also depends on the value Z, i.e., on the column of the periodic table. For our choice of parameters (k-point integration mesh and smearing) erbium is at the boundary between elements favoring the minimum at lower volume (for smaller Z) and elements favoring the minimum at higher volume (for higher Z). This is clearly visible in SI Fig. S1.3a as a jump of the first-neighbor distance for the diamond structures for elements before and after erbium.

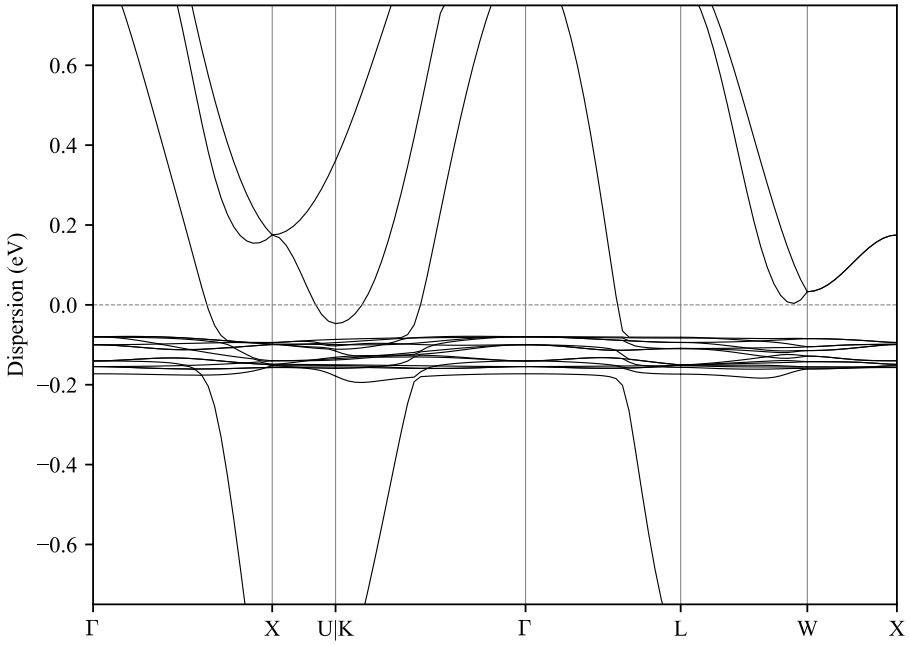

Figure S11.1. Band structure of erbium in the diamond crystal structure. The zero of energy is set at the Fermi level.

S12 Total energy versus free energy

Here we want to show a couple of examples where the exact choice of the energy to be computed in the EOS, namely the internal energy E, the free energy $E-TS$ (where $-TS$ is the smearing contribution) or the approximation $E-TS/2$, can significantly affect the EOS curves.

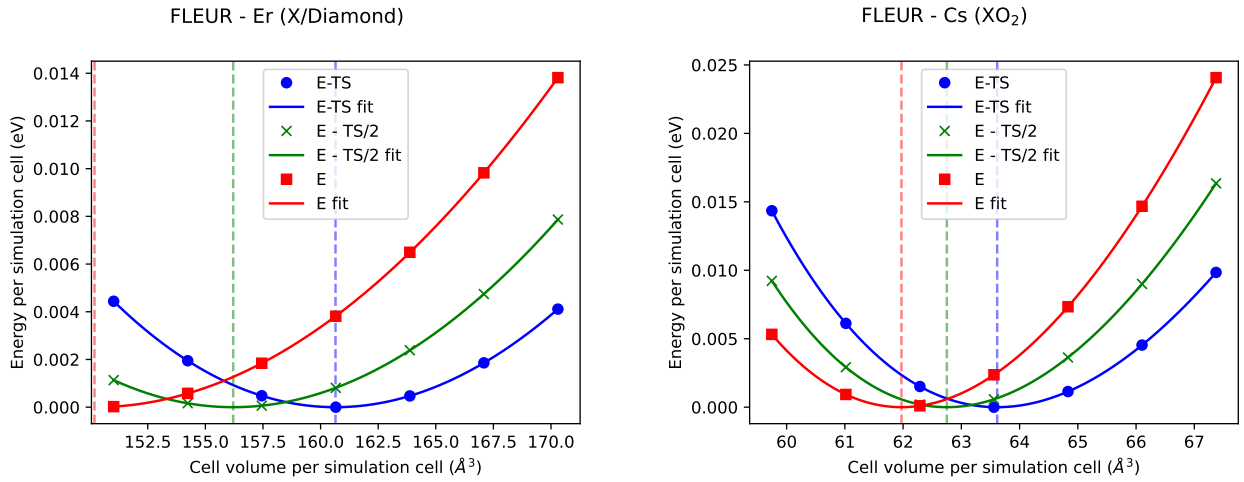

Figure S12.1. Comparison of EOS curves for two systems computed using the FLEUR code, using different quantities on the energy axis. Left panel: Er in the diamond structure; right panel: CsO_2.

While in many cases the choice of one of these three quantities does not have any effect on the curves (e.g., in the case of large-gap insulators), in SI Fig. S12.1 we show two EOS curves that we selected as they show a significant deviation (even larger deviations exist for other systems in our dataset). The first case is erbium in the diamond structure. We already discussed its band structure in SI Sec. S11: we expect that there are significant flat f bands (thus with high density of states) crossing the Fermi level as a function of volume; therefore, the $-TS$ contribution will also depend on volume, since it originates from the contribution of bands within a small energy range (comparable to the chosen smearing broadening) from the Fermi level.

One does not need, however, to consider such pathological cases: even other systems might show important discrepancies between the various curves if the density of states at the Fermi level changes significantly as a function of volume. This is illustrated for instance by CsO_2 (right panel in SI Fig. S12.1), whose band structure for two different volumes is reported in SI Fig. S12.2. Here, we see that bands with saddle points or almost-flat bands can be found within $\pm\sigma$ from the Fermi level (with σ being the value of smearing broadening recommended here). These bands shift with volume and therefore their contribution to $-TS$ will be a function of volume.

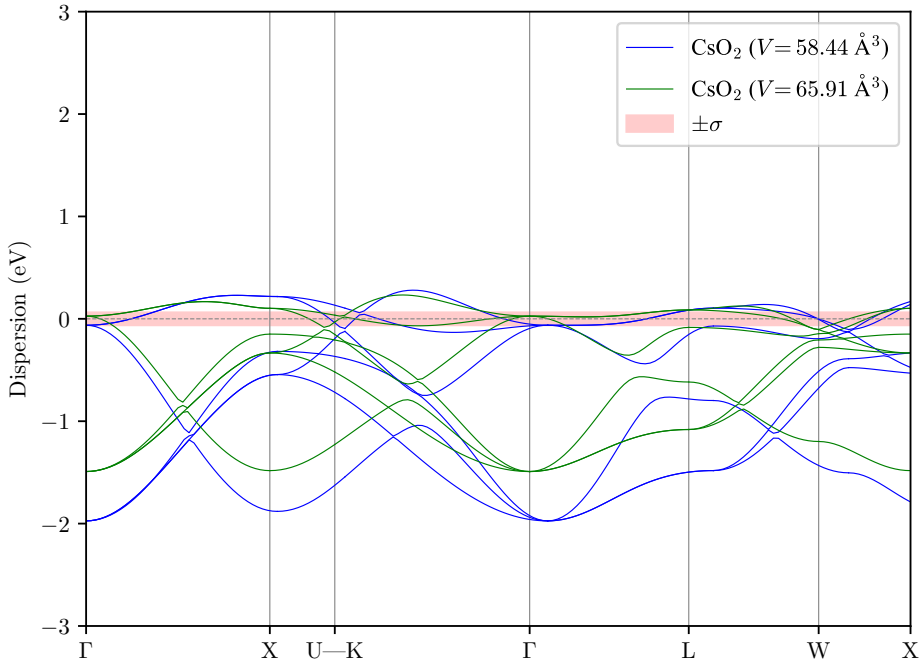

Figure S12.2. Band structure of CsO_2 for two different volumes computed with the QUANTUM ESPRESSO code. The shaded red area indicates an energy range of ± 0.0045 Ry, that is the smearing value recommended in this work.

S13 Code specific parameters for the pseudopotential codes

In this section, we discuss the technical choices adopted by each code for the verification work. These choices are implemented in the `aiida-common-workflows` package (version `v1.0.0` and above) through the protocol `verification-PBE-v1`, with the excepton of SIRIUS, whose protocol is the `verification-PBE-v1-sirius` available only for the CP2K code. We remind the reader that a number of parameters (such as the smearing type and broadening or the k-point integration mesh) have been fixed for all codes (see also Box 3 in the main text). We also remind that the parameters for the two all-electron codes are discussed instead in SI Sec. S5.

S13.1 ABINIT@PW|PseudoDojo-v0.5

The ABINIT calculations were performed with the version 9.6.2 of the code[13,42,43] and v0.2a2 of the `aiida-abinit` plugin. All calculations were run with `tolvrs = 1e-10`, Fermi–Dirac smearing (`occopt = 3`) of 0.0045 Rydberg (`tsmear = 0.00225`), a reasonable number of empty bands (`fband = 2`), and a minimal k-spacing of 0.06 Å^{-1}. Norm-conserving pseudopotentials from the PseudoDojo-v0.5 scalar-relativistic PBE standard library have been employed; the "high" stringency recommended energy cutoffs were used. The RMM-DIIS diagonalization algorithm[55](`rmm_diis = 1`) was used for calculations with norm-conserving scalar-relativistic PBE pseudopotentials because of its improved computational efficiency over the default CG method. Note that `rmm_diis = 1` means that the first four SCF iterations are performed with the CG method in order to obtain reasonably good trial states before changing to the RMM-DIIS method. RMM-DIIS is more efficient although less stable than the CG algorithm as there is no explicit orthogonalization while optimizing the trial states. This led to approximately a 0.7% error rate (108 out of 15460 total from all calculations performed in the process of this study) in the calculations, however in all cases, running the failed calculations with CG resulted in successful convergence.

S13.2 BigDFT@DW|HGH-K(Valence)

The version of the BigDFT code employed for these calculation is the 1.9.2. For the great majority of the structures presented here, the pseudopotentials employed in the calculations are norm-conserving Hartwigsen–Goedecker–Hutter[70] of the Krack family[72] (HGH-K). For this verification campaign, rather than choosing the most precise pseudopotentials for a given element, we employed the default pseudopotentials with the least possible number of valence electrons. We have therefore used a set which provides an overestimation of the precision error of this pseudopotential family. For comparison we have also included some of the semicore pseudopotentials, see SI Sec. S16.2. The BigDFT code formalism employs Daubechies wavelets basis sets to express the Kohn-Sham (KS) orbitals, which enable to reach precise converged results for a given pseudopotential with moderate effort with respect to the number of degrees of freedom employed. The wavelets grid spacing was set to a value of 0.3 a_0, with all the high-resolution degrees of freedom activated, and the k-point integration mesh correspond to a equivalent length of 94 a_0. Density mixing scheme was employed for electronic convergence, reached for a threshold voxel accuracy of 10^{-12} atomic units. Also, 120 empty Kohn–Sham states were included for each k-point. Symmetry operations were also included to limit the calculations to the irreducible k-points. At the time of developing the workflow, the BigDFT code was migrating its user interface into the PyBigDFT python module, which provides a user interface to the underlying executable. Therefore, to avoid issues in the API modifications, we fixed the PyBigDFT version to a beta release in the `aiida-bigdft` plugin, which activated limited features with respect to the stable version available nowadays. In particular, not all the structures which were defined with a non-orthogonal unit-cell were transformed in an orthogonal supercell, required by the code. This compatibility problem resulted in less structures treated by this approach. It is planned to release a stable version of the plugin compatible with the AiiDA 2.x API.

S13.3 CASTEP@PW|C19MK2

CASTEP is a plane-wave pseudopotential code[45], the 20.1.1 version is used in this work. Calculation parameters closely follow the "precision" setting in the initial common workflow implementation[36]. The cut off energy is fixed at 800 eV for all calculations since energy comparison is needed between different chemical systems. The reciprocal space sampling is done through Γ centered Monkhorst–Pack grids with a fixed spacing of 0.06 Å^{-1} (i.e., 0.00954929 2πÅ^{-1}), in line with other codes. On-the-fly generated (OTFG) core-corrected ultrasoft pseudopotentials from the library `C19` is used for the study except for the f-block elements (see section S16.3 for more details). The `C19` library is aimed for general use with a balance between precision and speed, and it has been the default potential library since CASTEP version 19.1.1. The modified pseudopotential generation strings for f-block elements are tabulated in Table S16.1. The energy convergence threshold for electronic minimization is set to 1×10^{-8} eV per atom.

S13.4 CP2K/Quickstep@TZV2P|GTH

The DFT module QUICKSTEP of the open-source simulation package CP2K is an implementation of the Gaussian and plane wave (GPW) and the all-electron Gaussian augmented plane wave approaches[46,47]. Therein, the Kohn-Sham orbitals are

represented by contracted Gaussian basis functions, whereas the electronic charge density is expanded in plane waves[109]. For the former, an accurate molecularly optimized triple-ζ basis set with two additional sets of polarization functions (TZV2P-MOLOPT) is employed[73], whereas for the latter a density cutoff of 2400 Ry is utilized, which differs from a conventional plane wave cutoff by a factor of four. Due to its GPW method, however, CP2K/QUICKSTEP is rather insensitive with respect to high density cutoffs. Furthermore, four multi-grids are used to ensure an efficient mapping of product Gaussians onto the real-space integration grids, so that wide and smooth Gaussian functions are mapped onto a coarser grid than narrow and sharp Gaussians. To control which product Gaussians are mapped onto which level of the multi-grid, a relative cutoff of 80 Ry is applied that defines the plane wave cutoff of a reference grid covered by a Gaussian with unit standard deviation. Separable and norm-conserving Goedecker–Teter–Hutter-type pseudopotentials including scalar relativistic effects are used to describe the interactions between the valence electrons and the ionic cores[71,72].

S13.5 `GPAW@PW|PAW-v0.9.20000`

GPAW[48,49] is an open-source DFT code developed at the Technical University of Denmark (DTU) and other universities and computer centers, originally created for combining a homogeneous grid basis set with the projector augmented wave (PAW) method. Today, the code also provides a linear combination of atomic orbitals (LCAO) basis[110] and a plane wave mode. The latter has been applied in this study with a plane-wave cutoff of 800 eV for all calculations, with the exception of systems containing noble gases, where a cutoff of 1200 eV combined with a tighter energy and density convergence was applied. As with other codes, Fermi–Dirac smearing of 0.06122 eV was used. Besides the mentioned parameters, default values (as per GPAW v. 21) were used for all other keywords needed to perform the calculation in order to ensure that the results reflect the most representative user experience. The applied PAW potentials, included in GPAW's PAW potential suite, were specifically created for the PBE exchange correlation functional, by applying GPAW's setup creator[111]. In particular, we use the pseudopotentials included in the setup release 0.9.20000 available at `https://wiki.fysik.dtu.dk/gpaw/setups/setups.html#atomic-paw-setups`. GPAW is tightly linked to the atomic simulation environment (ASE)[8,9], which handles the user interface and is developed independently.

S13.6 `Quantum ESPRESSO@PW|SSSP-prec-v1.3`

All calculations have been run using version 7.0 of the Quantum ESPRESSO code and version 3.5.1 of the AiiDA Quantum ESPRESSO plugin. For the results presented in the main text, all pseudopotentials were selected from the SSSP PBE Precision 1.3[76] library, with plane-wave cutoffs corresponding to the largest recommended value from the elements in each structure. In accordance with the `verification-PBE-v1` protocol, the Brillouin zone sampling was performed using Γ-centered meshes with a spacing of 0.06 Å and a Fermi–Dirac smearing of 0.0045 Ry. All other inputs parameters were set via the `precision` protocol as described in the SI of Ref. 37, most importantly the energy convergence threshold was set to a very strict $0.1 \cdot 10^{-9}$ Ry per atom. For the comparison with ABINIT and CASTEP discussed in S14, the pseudopotentials were selected from the PseudoDojo SR PBE standard set, version 0.4, in UPF format, after a small modification of the `.upf` files as described in S14. Plane-wave cutoffs were obtained from the "high" stringency hints provided by the PseudoDojo table, all other computational parameters were unchanged.

S13.7 `SIESTA@AtOrOptDiamond|PseudoDojo-v0.4`

The calculations presented in this work have been carried out with Siesta version Max-1.2.0 (`https://gitlab.com/siesta-project/siesta/-/tags/MaX-1.2.0`) powered by the `aiida-siesta` plugin version 1.2.0. Pseudopotentials from the PseudoDojo FR standard set, version 0.4, in PSML format, have been employed. The real-space cutoff for the representation of charge densities and potentials is fixed at 900 Ry. The recommended course of action regarding basis sets in Siesta is to perform an optimization considering the key features of the chemical environment of each system. In this project, we have not carried out the optimization for all 960 systems. Instead, we have attempted a partial, per element, optimization, considering only the unary diamond crystals at their central volume. The orbitals thus optimized for each element are then reused for all the other unary and oxide structures involving that element. The optimization starts from a TZDP basis with the addition of an extra f orbital. For alkali metals and alkaline earth metals the addition of a d orbital shell is also necessary. The optimization is performed with the Nelder–Mead algorithm (multidimensional optimization without derivatives), having as variables the first-zeta radius of each orbital and the split norm parameter that controls the ratio between the first and subsequent zetas. We foresee using the information garnered in this verification study to develop further heuristics and guide the development of fully automatic methods to generate basis sets taking into account appropriate chemical environment descriptors.

S13.8 `SIRIUS/CP2K@PW|SSSP-prec-v1.2`

SIRIUS is a domain-specific library, which implements pseudopotential plane wave and full potential linearized augmented plane wave methods and is designed for GPU acceleration[54]. As such it brings additional functionalities to CP2K such as

collinear and non-collinear magnetic systems with or without spin–orbit coupling. It is written in C++14 with the MPI, OpenMP, and CUDA/ROCm programming models. As shown previously, SIRIUS/CP2K allows for energy conserving *ab-initio* molecular dynamics simulations with a constant shift in the order of μHa compared to QUANTUM ESPRESSO reference calculations[47]. All SIRIUS/CP2K simulations were performed using the pseudopotentials of SSSP PBE Precision 1.2[80] together with a plane-wave cutoff of 55 a.u.$^{-1}$ for the density and potential, as well as 10 a.u.$^{-1}$ for $|\mathbf{k}+\mathbf{G}|$, respectively.

S13.9 `VASP@PW|GW-PAW54*`

All VASP results in this work have been obtained with VASP version 6.3.0 and AiiDA-VASP 2.2.0, using preferentially the GW VASP PBE potential set version 54.

The input parameters explicitly set for this work were (defaults in brackets): PREC = Accurate(Normal), EDIFF = 1E−7(1E−4), ALGO = Normal(Normal), NELM = 300(60), and LMAXMIX = 6(2). The last setting ensures that all electronic states up to quantum numbers $l = 6$ are included in the density mixer, and it is necessary to change this in order to converge some d-electron systems and most lanthanides. The plane wave cutoff was fixed at 1000 eV ($\sim$ 73.50 Ry) for all calculations. The PAW method was used[112].

We used the recommended GW potential sets, whenever possible, with exception of oxygen, where we chose the hard O_h_GW potential instead of the recommended O_GW since it improved results for the oxides dataset. This potential is required if short bonds to oxygen atoms are encountered. The recommended plane wave cutoff energy for this potential is 765 eV, however, for high precision studies we recommend to increase the cutoff in VASP by 30% yielding the employed 1000 eV. For the elements where no GW potential is supplied, we use the recommended standard PBE PAW potential. (The recommendations were taken from the VASP-wiki on April 22nd, 2022).

S14 Precision of plane-wave codes when using the same pseudopotential library

In order to assess how much codes implementing the same computational approaches agree among each other, we compare the ε metric among a subset of the plane-wave codes considered in this work, when using the same pseudopotential library. We consider two different cases. In the first case, we compare three different codes (ABINIT, QUANTUM ESPRESSO, and CASTEP) using the PseudoDojo v0.4 pseudopotential library. In the second case, we compare QUANTUM ESPRESSO and SIRIUS/CP2K using the SSSP PBE precision v1.2 pseudopotential library.

For the first case (PseudoDojo v0.4 library), an initial comparison highlighted some discrepancies among the codes for Cu, Zn, and Ne. After investigation, we found that these discrepancies stem from differences in the numerical treatment of the form factors, the local part of the pseudopotential, the model core charge density or the beta projectors with spherical Bessel functions (usage of spline or not, different integration methods, etc.).

While we have not precisely identified the main root of the effect, which would require additional investigation, it is clear that the treatment of the long range part of the pseudopotential is rather sensitive to the implementation details. For this reason, we manually truncated the radial mesh reported in the pseudopotential files (in UPF format, normally truncated at 10 Bobr) after 6 Bohr for all elements, as it is done in the psp8 format used by ABINIT, in order to have the same radial mesh in all codes. We verified that, except for the three cases mentioned above, this truncation had no visible effects on the results when compared to all-electron results. In the figures below, the tables for which the radial mesh has been truncated will be referred to as "trim" as a suffix to the approach label reported in the periodic-table titles.

Using this simple truncation to avoid numerical instabilities, we show in SI Figs. S14.1, S14.2 and S14.3 the six possible pairwise comparisons between the three codes. Remarkably, except for two noble gases, the agreement is excellent (we have used the same color scale for ε as in the main manuscript). This agreement is on average even better than the agreement between AE codes of this work (see Fig. 1 of the main text). We highlight however that this is expected, since the plane-wave codes use the same basis set and, in this SI Section, an almost identical set of numerical parameters, while the two AE codes differ in the details of the basis set and numerical parameters.

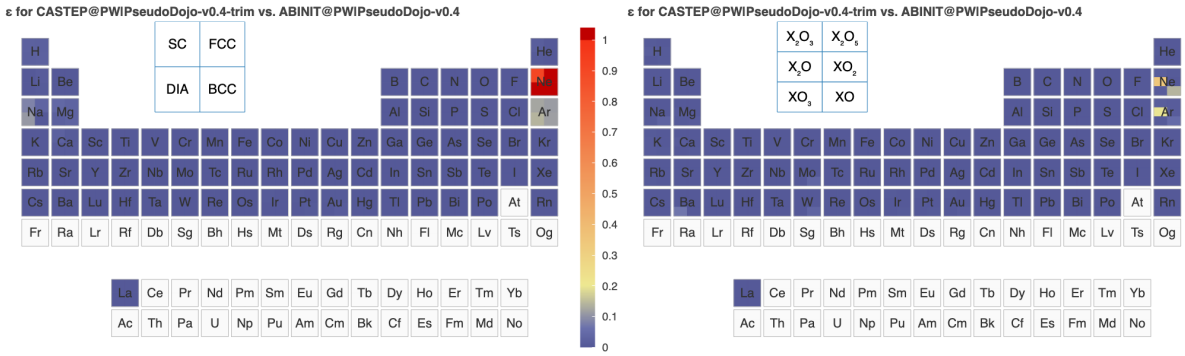

Figure S14.1. Value of the comparison metric ε between the CASTEP code (with truncated radial mesh) and the ABINIT code for the unaries and oxides set using the same PseudoDojo v0.4 library.

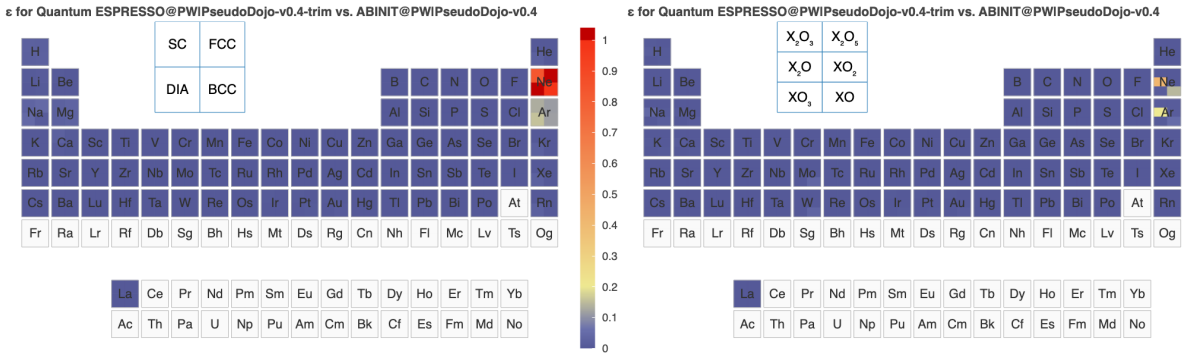

Figure S14.2. Value of the comparison metric ε between the QUANTUM ESPRESSO code (with truncated radial mesh) and the ABINIT code for the unaries and oxides set using the same PseudoDojo v0.4 library.

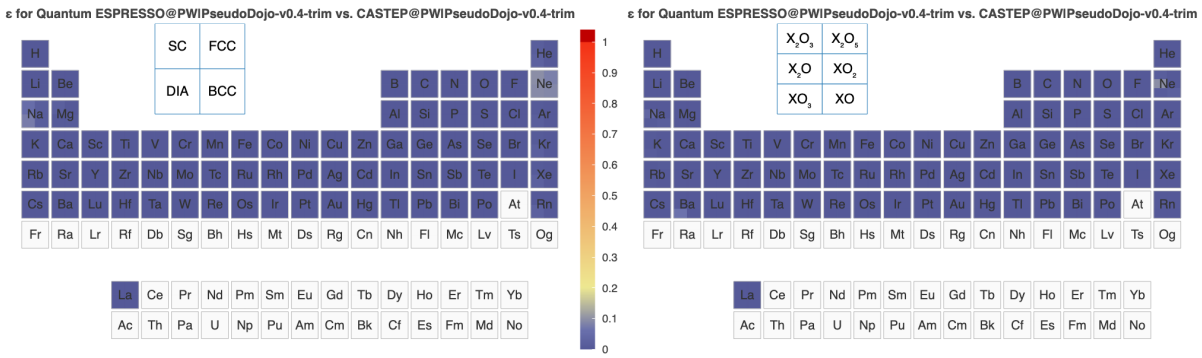

Figure S14.3. Value of the comparison metric ε between the QUANTUM ESPRESSO and CASTEP codes (both with truncated radial mesh) for the unaries and oxides set using the same PseudoDojo v0.4 library.

In the second case, we compared the SSSP PBE precision v1.2 pseudopotential library for QUANTUM ESPRESSO and SIRIUS/CP2K. The comparison of the ε metric is shown in SI Fig. S14.4. The match is very good for all systems except for Ba-diamond and RbO_3. We note here that in the main text, we used the SSSP PBE precision v1.3 for QUANTUM ESPRESSO, but we stress that it is equivalent to v1.2 for the subset of chemical elements considered in this section (the difference being that v1.3 also includes actinides).

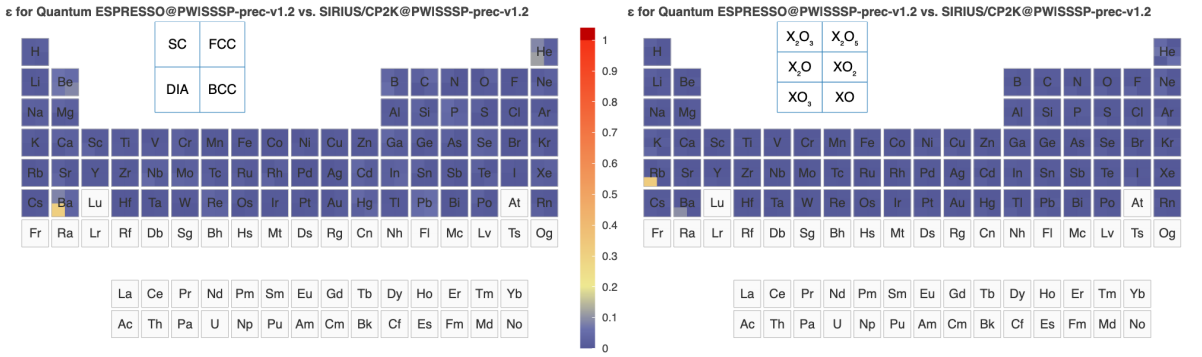

Figure S14.4. Value of the comparison metric ε between the QUANTUM ESPRESSO and SIRIUS/CP2K software for the unaries and oxides set using the same SSSP PBE precision v1.2 library.

The overall excellent agreement displayed in this SI Section demonstrates that different codes implementing the same computational approach (including, in addition to the basis set, also the pseudopotential library and other computational parameters) can reproduce the same results. In addition, our investigation helps identifying the remaining numerical aspects that might produce different outcomes and that merit further investigation, such as the truncation of the radial mesh discussed here.

S15 Transferability of conclusions from the previous smaller crystal set to the current 960 crystal set

In this section we want to show that even if two codes provide nearly identical results for the 71 crystal set of Refs. 29, 30, they will not necessarily provide identical results for the larger 960 crystal set of the present paper, demonstrating the value of the larger crystal-structure set.

To perform a quantitative comparison using the same computational approach, we use only data obtained as part of the present study. That means that we do not use the 71 crystal set (that has several crystals that are not part of the present set), but rather the set of 29 crystals common to both sets, as listed in SI Sec. S17, as a proxy for the 71 crystal set. SI Fig. S15.1 shows on the horizontal axis the ε averaged over these 29 crystals for any pair of approaches or codes used in this work, and on the vertical axis the ε for the same pairs but now averaged over all crystals (up to 960 crystals). The overall correlation in SI Fig. S15.1 shows that the 29 crystal set does indeed capture part of the information. However, as expected, the data points fall above the $y = x$ line, demonstrating that the large set probes relevant behavior that is not probed in the small sets previously used. In particular, there are code pairs (see shaded area in SI Fig. S15.1) that have a mutual $\varepsilon \leq 0.2$ for the 29 unaries (good agreement), yet have a larger ε for the large set (and similarly for $\varepsilon \leq 0.06$, that signals excellent agreement). SI Fig. S15.2 shows two examples when this happens: panels (a) and (c) demonstrate that while values for ε are small on the 29 crystals of the small set (boxed cases in SI Fig. S15.2(a,c)), other crystals outside this set may contribute to a larger average ε. This is typically the case for lanthanides, not included in the earlier 71-crystal benchmark (that stopped at Rn). Moreover, some elements lead to a low ε for the unaries, but to a larger ε for the oxides (e.g., Cs-Ba-Fr-Ra and Te-I-Xe-Bi-Po-At-Rn for CASTEP).

The overall conclusion of this analysis is that the 71-crystal set of unaries – or the 29-crystal set as its proxy – gives a fair first assessment of the comparative behavior of two DFT codes, while the complete 960-crystal set of unaries and oxides provides a more detailed comparison, both because more elements and more structures per element are included. Conclusions that were based on the benchmarks of Refs. 29, 30 will therefore still hold, yet can be refined. For testing newly developed pseudopotential libraries, a stepwise approach can be implemented: a first quick test on one unary per element will reveal the largest deviations; once these are fixed, the whole dataset of unaries and oxides can be used to hunt for smaller deviations.

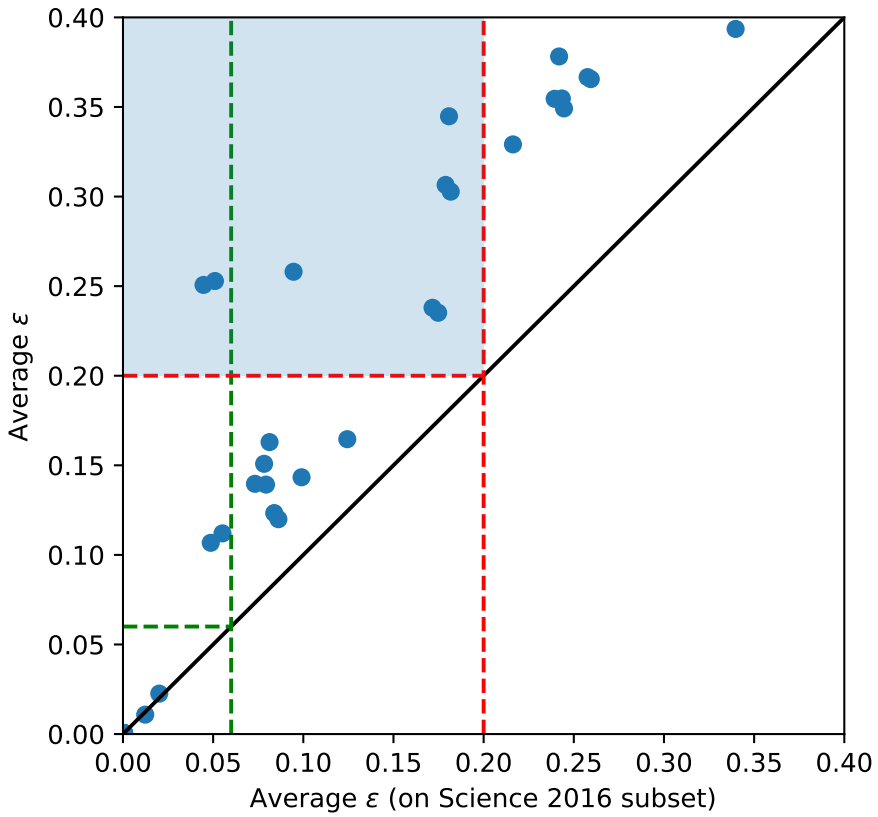

Figure S15.1. Vertical axis: ε averaged over all crystals of the unary and oxide set computed in this work, for all pairs of computational approaches considered in the main text. Horizontal axis: ε averaged over the 29 crystals from these 960 that appear as well in the 71 crystal set from Refs. 29, 30. The horizontal and vertical lines indicate the threshold values for excellent (green) and good (red) agreement, as discussed in the main text. The region above the horizontal red line and to the left of the vertical red line, highlighted by the shaded blue area, indicates pairs that are in good agreement according to the small crystal-structure set, but less so when considering the full set.

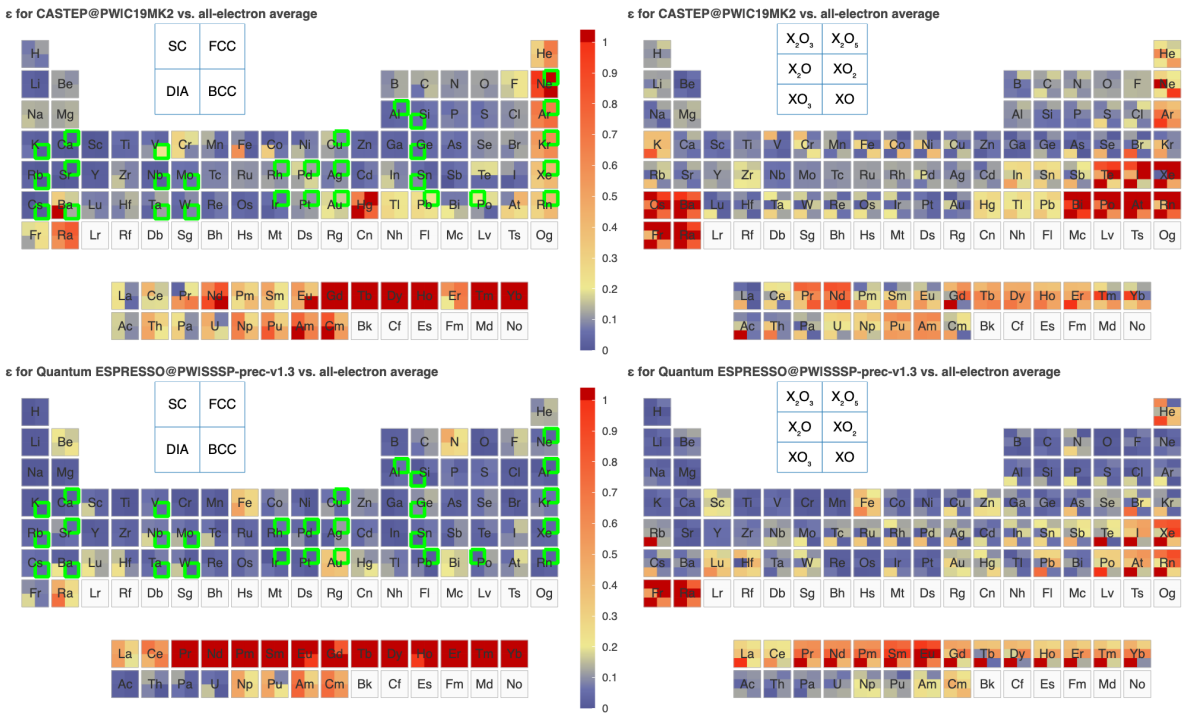

Figure S15.2. Same periodic tables for the comparison metric ε as in SI S9 for codes CASTEP and QUANTUM ESPRESSO, where the 29 crystal structures that appear also in the 71-crystal set of Ref. 29 are highlighted. While the 29 structures display values with excellent agreement, other structures result in a less good agreement. These two examples illustrate some of the cases in SI Fig. S15.1 for which the agreement is very good on the small crystal set, yet less good on the large crystal set.

S16 Additional pseudopotential datasets

This section discusses more in detail some additional datasets obtained using the same codes of the main text, but different basis sets or pseudopotential families, as well as the comparison with earlier versions of pseudopotentials, before those that were optimized here.

S16.1 ABINIT

During the process of computing the oxide verification equations of state using the initial standard norm-conserving scalar-relativistic PBE PseudoDojo (version 0.4)[68,113], we observed that the results for around 11 of the pseudopotentials were not in as good agreement with the all-electron equations of state as other elements from the same pseudopotential family. This led to an investigation into possible improvements to the pseudopotentials for Ba, Bi, I, Pb, Po, Rb, Rn, S, Te, Tl, and Xe. With the exception of S, we found that the accuracy of the pseudopotentials is significantly improved by including a projector for the f channel. In the original version, indeed, the local part of the pseudopotential was not able to reproduce the all-electron scattering properties of the f channel in the empty region.

A particularly severe case is the one of Ba which is shown in SI Fig. S16.1(a) where the pseudized f channel (black dashed line) does not reproduce well the all-electron reference. As a consequence, the EOS for the stable BCC phase of Ba is slightly off (SI Fig. S16.1(c)) but the one for BaO_3 is completely wrong, as shown in SI Fig. S16.1(d). This issue is fixed by the additional projector as shown in SI Fig. S16.1(b), which then gives excellent agreement with the all-electron EOS.

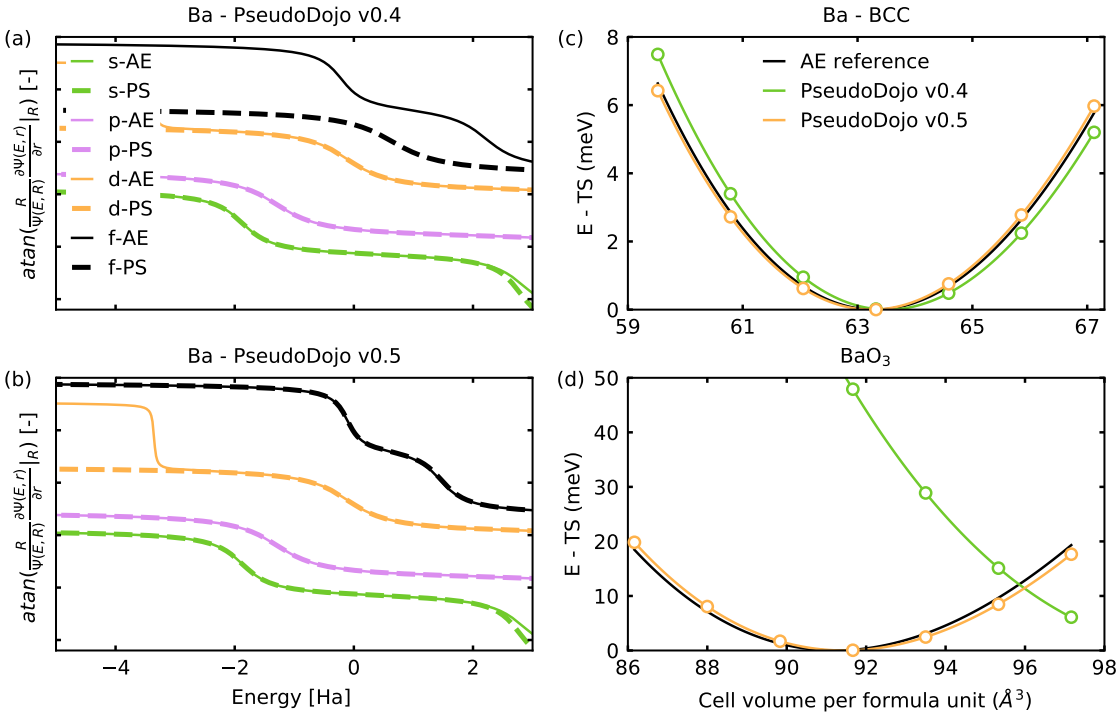

Figure S16.1. Comparison of the scattering properties of the all-electron (AE) atom and the pseudized (PS) Hamiltonian for two different Ba pseudopotentials generated without (with) an f projector. The subfigures (a) and (b) show the arctangent of the l-dependent logarithmic derivative computed for some R greater than the pseudization radius, where ψ is the solution of the non-local radial equation regular at the origin (a) without and (b) with f projector. Since the transferability of a pseudopotential is directly related to the capability of reproducing the AE logarithmic derivative over a wide range of energies, the version with f projector is expected to provide more accurate results and we provide two equation of state example in (c) for BCC barium and in (d) for BaO_3 where the pseudopotential with the additional projector is more accurate than the one without. This is true for all 10 cases tested in this study.

It should be noted that the inclusion of the f projector increases the computational cost associated to the application of the non-local part of the Hamiltonian V_{nl}. This is especially true if the computation of $V_{nl}|\psi\rangle$ is obtained by projecting the wavefunction over spherical Harmonics Y_{lm}. We stress, however, that in ABINIT the projection is implemented by expressing the sum over m in terms of Legendre polynomials (`useylm = 0` input variable, default option when norm-conserving pseudopotentials are employed). In this case, the computational cost of including an additional projector for l is not so high

because, contrary to the case when spherical harmonics are used, the number of floating point operations required to apply a projector does not scale with the total number of magnetic quantum numbers $2l+1$. This study led to the creation and adoption of 11 new pseudopotentials for Ba, Bi, I, Pb, Po, Rb, Rn, S, Te, Tl, and Xe in a new PseudoDojo (version 0.5). Because these pseudopotentials have not been subject to a convergence study with respect to all-electron results, 20 Hartree were added to the "high" stringency recommended cutoffs from ONCVPSP for safety.

In addition to norm-conserving pseudopotentials, we also investigated the JTH PAW PBE v1.1[63] table which has improved versions of the pseudopotentials for H, Li, Si, Cu, Zn, Ga, Cd, Sb, Lu, Os, Ir and Bi with respect to v1.0 used in the previous AiiDA common workflows study. Through testing, it was noted that the recommended kinetic energy cutoff values for these PAW pseudopotentials were not sufficient for the desired level of agreement with all-electron codes, so twice the "high" recommended cutoffs were used. The conjugate-gradient (CG) diagonalization algorithm was used for all calculations with PAW pseudopotentials. Note that there do exist pseudopotentials for lanthanide- and actinide-series elements in this PAW table but they have not been verified against all-electron reference results. Because of this and because the PAW potentials are included primarily as a point of comparison against the norm-conserving PseudoDojo family (which does not provide lanthanide nor actinide elements), these elements are not included in the reported results and analysis.

We therefore compare in SI Fig. S16.2 the performance of the three PBE pseudopotential libraries tested here using ABINIT: the norm-conserving PseudoDojo (version 0.4), the norm-conserving PseudoDojo (version 0.5) and the PAW JTH v1.1 tables. We conclude that PseudoDojo (version 0.5) is the most precise one and is therefore used in the main manuscript.

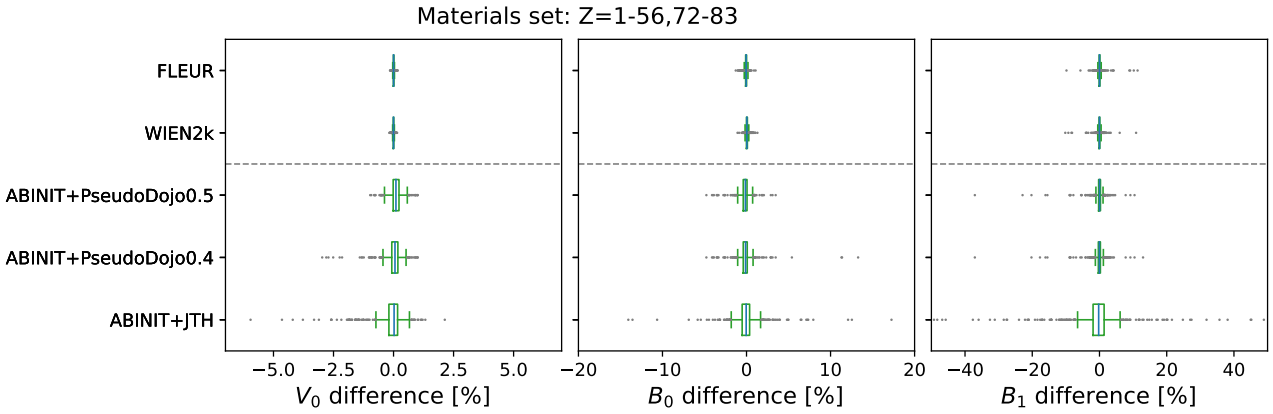

Figure S16.2. Comparison of the three tested PBE pseudopotential tables using the ABINIT software.

In summary, unary and oxide verification results were calculated for ABINIT with three sets of pseudopotentials: JTH PAW PBE v1.1, PseudoDojo norm-conserving standard scalar-relativistic PBE v0.4, and a new PseudoDojo norm-conserving standard scalar-relativistic PBE v0.5 based on v0.4 with improved potentials for the 10 elements listed above. The latter set is reported in the main text of the manuscript.

S16.2 BigDFT

Data production using BigDFT showed clear outliers in comparison to reference codes (FLEUR/WIEN2k) using HGH-K Valence only pseudopotentials. We therefore recalculated the EOS using semicore pseudopotentials for all the crystals for which this type of pseudopotential was available and that showed a difference in volume ≥ 0.2 Å^3 with respect to the reference AE data. The new calculations resulted, in most cases, in a significant shift towards a closer agreement with the reference AE, as shown in SI Fig. S16.3.

S16.3 CASTEP

A unique feature of CASTEP is that the pseudopotentials are typically generated on-the-fly during the calculations, although file-based potentials are still supported. Each on-the-fly generated (OTFG) potential is defined using a compact configuration string. An OTFG library is a collection of predefined configurations. Many such libraries are built into the CASTEP executable itself, with different focuses. In this study, the pseudopotentials used are provided by the `C19` library, except for the lanthanide and actinide elements. For these elements, a new set of pseudopotentials are generated to improve agreement with the all-electron reference data, which had not been available during the development of the original `C19` library.

The configuration strings for these elements are tabulated in Table S16.1. Each field is separated by "|". The first field is the local angular momentum channel. The second is the core radius in atomic units and the next three are the recommended cut off energies (Ha) corresponding to the *Coarse*, *Medium*, and *Fine* settings for CASTEP, which do not affect a calculation if a cut

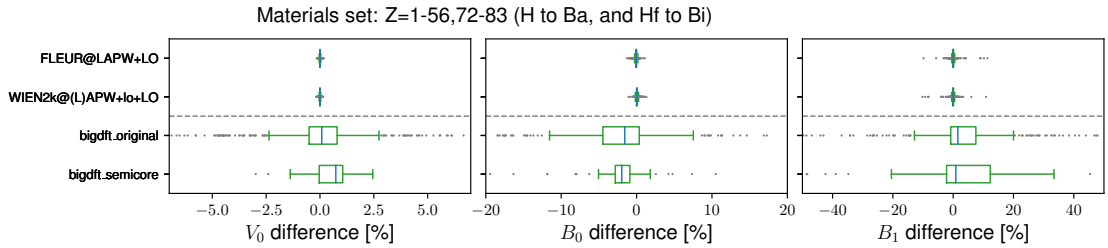

Figure S16.3. Comparative plot displaying the improvement obtained by using HGH-K (Semicore) pseudopotentials over Valence only pseudopotentials.

off energy is specified explicitly (as in this study). This is followed by the orbitals to be pseudized, which are separated by ":". Each orbital is defined by a *nl* number and may have suffixes to indicate what kind of projectors should be used. For example, "60U" indicates that a single ultrasoft projector should be used for the *6s* channel (the default is two ultrasoft projectors). The "NN" suffix indicates that two norm-conserving projectors should be included. The "U2U2" suffix indicates two ultrasoft projectors each with a core radius of 2.0. The "L" suffix pins the local channel, and the "P" suffix indicates that the pseudized channel is not represented by an explicit projector or a local channel. The parameter "qc" inside the brackets controls the smoothness of the potential. Occupations of atomic states can be further modified by settings inside a curly bracket.

Element	Old settings	New settings
La	`2|2.3|5|6|7|50U:60:51:52(qc=4.5)`	`2|2.3|5|6|7|50U:60:51:52:43{4f0.1}(qc=4.5)`
Ce	`2|2.1|9|10|11|50U:60:51:43:52L(qc=6)`	`2|2.2|8|9|10|50U:60:51:52:43{5d0.1}(qc=4.5)`
Pr	`2|2.1|9|10|11|50U:60:51:43(qc=6)`	`2|2.1|10|12|13|50U:60:51:52:43{5d0.1}(qc=5)`
Nd	`2|2.1|9|10|11|50U:60:51:43(qc=6)`	`2|2.1|10|12|13|50U:60:51:52:43{5d0.1}(qc=5)`
Pm	`2|2.1|10|12|13|50U:60:51:43(qc=6)`	`2|2.1|8|9|11|50U:60:51:52:43{5d0.1,4f4}(qc=5.5)`
Sm	`2|2.1|10|12|13|50U:60:51:43(qc=6)`	`2|2.1|9|10|12|50U:60:51:52:43{5d0.1,4f5}(qc=5.5)`
Eu	`2|2.1|10|12|13|50U:60:51:43(qc=6)`	`2|2.1|9|10|12|50U:60:51:52:43{5d0.1,4f6}(qc=5.5)`
Gd	`2|2.1|10|12|13|50U:60:51:52L:43(qc=6)`	`3|2.1|9|10|12|50U:60:51:52:43(qc=5.5)`
Tb	`2|2.1|10|12|13|50U:60:51:43(qc=6)`	`2|2.2|12|13|15|50U:60:51:52:43{5d0.1}(qc=5)`
Dy	`2|1.9|12|14|16|50U:60:51:43(qc=6.5)`	`2|2.0|12|13|15|50U:60:51:52:43{5d0.1}(qc=6.5)`
Ho	`2|1.9|12|14|16|50U:60:51:43(qc=6.5)`	`2|2.0|12|13|15|50U:60:51:52:43{5d0.1}(qc=6.5)`
Er	`2|2.1|10|12|13|50U:60:51:43{6s0.5}(qc=6)`	`2|2.1|10|12|13|50U:60:51:52:43{6s0.1,5d0.1}(qc=6)`
Tm	`2|2.1|10|12|13|50U:60:51:43{4f12}(qc=6)`	`2|2.1|10|12|13|50U:60:51:52:43{5d0.1,4f12}(qc=6)`
Yb	`2|2.1|10|12|13|50U:60:51:434f13(qc=6)`	`2|2.1|10|12|13|50U:60:51:52:43{5d0.1,4f13}(qc=6)`
Ac	`2|2.5|5|6|7|60U:70NN:61:62L`	`2|2.4|7|7|9|60U:70U2U2:61:62:53{6d0.1,5f0.1}(qc=5)`
Th	`2|2.5|7|7|9|60U:70NN:61:62`	`2|2.2|7|7|9|60U:70U2U2:61:62:53{5f0.1}(qc=5)`
Pa	`2|2.1|9|10|11|60U:70:61:53:62P(qc=6)`	`2|2.2|8|9|10|60U:70U2U2:61:62:53(qc=5)`
U	`2|2.1|10|12|13|60U:70:61:53:62P(qc=6)`	`2|2.2|8|9|10|60U:70U2U2:61:62:53(qc=5)`
Np	`2|2.1|10|12|13|60U:70:61:53:62P(qc=6)`	`2|2.2|9|10|12|60U:70U2U2:61:62:53(qc=5)`
Pu	`2|2.1|10|12|13|60U:70:61:53:62P{6d1,7s1}(qc=6)`	`2|2.2|9|10|12|60U:70U2U2:61:62:53{6d0.1}(qc=5.5)`
Am	`2|2.1|10|12|13|60U:70:61:53(qc=6)`	`2|2.2|9|10|12|60U:70U2U2:61:62:53{6d0.1}(qc=5.5)`
Cm	`2|2.1|10|12|13|60U:70:61:53:62L(qc=6)`	`2|2.2|9|10|12|60U:70U2U2:61:62:53(qc=5.5)`

Table S16.1. Configuration strings of the on-the-fly pseudopotential generation before and after the update for the lanthanide and actinide elements involved in this study.

Examples EOS curves for La and Ce are displayed in SI Fig. S16.4, showing that the updated pseudopotentials agree better with the all electron data. The improvements may vary for other elements with *f* electrons. One should note that a better fit to the all electron results does not necessarily mean smaller errors compared to the experimental results. This is due to the inherent self-interaction errors in semi-local DFT that are present in the description of *f* electrons.

For some elements, the improvements are achieved through the inclusion of additional orbital states and l channels/projectors such as La, where previously the *4f* channel was neglected. In other cases, the reference atomic calculations include partially occupied atomic states that are otherwise empty in the original configurations. For example `{5d0.1}` adds 0.1 electrons to the *5d* channel. In some cases, the updated potentials contain increased core radii and are made softer via a decreased "qc" value as far as possible. These modifications are applied consistently for elements that neighbors to each other in the periodic table. We also want to emphasize that the settings used in this study are one-shot updates based on the `C19` library, rather than the outcomes of iterative optimizations. With the help of the automated test framework and publicly available all-electron reference data, it should be easy to adjust the strings and test them rigorously for further improvements, as required.

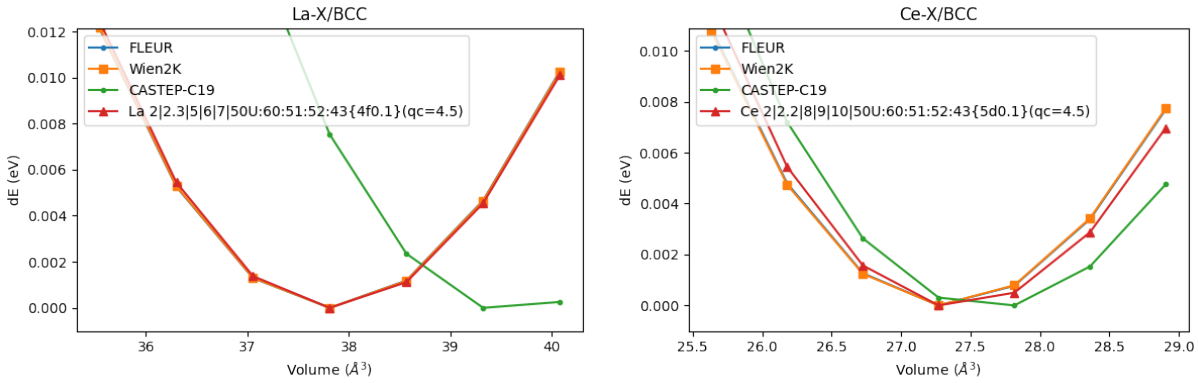

Figure S16.4. Comparing EOS curves of La and Ce in the BCC configuration. The updated pseudopotentials agree better with the all-electron data compared with those from the `C19`.

S16.4 Quantum ESPRESSO

SSSP[75] is a library of pseudopotentials that undergoes rigorous verification and ranking procedures. It contains two distinct families of pseudopotentials. The first family ("efficiency") is composed of relatively soft pseudopotentials that are still sufficiently precise for use in high-throughput calculations. The second family ("precision") contains pseudopotentials that are extremely precise with respect to all-electron references, even if more computationally expensive. In our QUANTUM ESPRESSO calculations, aiming at high precision, we have therefore used the SSSP "precision" library. Version 1.1.2 of SSSP, available before this work, was verified only on the unary configurations presented in Ref. 29, 30. With the additional results of this work, we have identified that certain pseudopotentials were not the best selection, and that more precise pseudopotentials are available in libraries that were not included in the previous generation of the SSSP library.

Element	SSSP precision v1.1.2	SSSP precision v1.3
Te	6|US |GBRV|v1|uspp	6|US | PSL|v1.0.0-low|ld1
Na	9|NC | PD|v4-std|oncvpsp3	9|PAW| PSL|v1.0.0-low|ld1
Cu	19|NC | PD|v4-std|oncvpsp3	11|PAW| PSL|v1.0.0-low|ld1
Cs	9|US |GBRV|v1|uspp	9|NC | PD|v4-str|oncvpsp3
Cd	12|US | PSL|v0.3.1|ld1	20|PAW| PSL|v1.0.0-high|ld1
Ba	10|PAW| PSL|v1.0.0-high|ld1	10|NC | PD|v5|oncvpsp4
As	5|US | PSL|v0.2|ld1	15|NC | PD|v4-std|oncvpsp3
I	17|PAW| PSL|v1.0.0-high|ld1	17|NC | PD|v4-std|oncvpsp3
Hg	20|NC |SG15|v0|oncvpsp3	12|US |GBRV|v1|uspp
Ne	8|NC |SG15|v0|oncvpsp3	8|PAW| PSL|v1.0.0-high|ld1
Ar	8|NC |SG15|v0|oncvpsp3	8|PAW| PSL|v1.0.0-high|ld1
Kr	8|NC |SG15|v0|oncvpsp3	18|PAW| PSL|v1.0.0-high|ld1
Xe	18|NC |SG15|v0|oncvpsp3	18|PAW| PSL|v1.0.0-high|ld1
Rn	18|NC |SG15|v0|oncvpsp3	18|PAW| PSL|v1.0.0-high|ld1
Ir	15|NC |GBRV|v1|uspp	31|US | PSL|v1.0.0-high|ld1

Table S16.2. List of pseudopotentials modified between SSSP v1.1.2 and SSSP v1.3. Each element in the table is composed of 5 strings separated by a | symbol, respectively: the number of electrons in the valence (Z), the type of pseudopotential (NC: norm-conserving, PAW: projector-augmented wave, US: ultrasoft), the source library (SG15: from Ref. 114, PSL: PSlibrary[82], GBRV: from Ref. 115, PD: PseudoDojo[68]), an internal version number that identifies the pseudopotential inside the given source library and the code used to generate them (oncvpsp3, oncvpsp4: version 3 and version 4 of the ONCVPSP code[113], ld1: the ld1.x code of Quantum ESPRESSO[51], uspp: the UltraSoft PseudoPotential (USPP) generation code[116]).

The pseudopotentials that were updated are summarized in Table S16.2. In particular, the pseudopotentials of the noble gases (Ne, Ar, Kr, Xe, Rn) were previously obtained using the SG15[114] library; in SSSP v1.3, we have replaced them with "PAW-high" pseudopotentials from the PSLibrary[82] based on our more recent verification results as they provide significantly better agreement with the all-electron reference EOS curves. An example of the improvement in the case of NeO_2 is shown in SI Fig. S16.5.

The pseudopotentials of I, Hg were obtained from SG15[114] as well. In SSSP v1.3, the pseudopotential of I is replaced with

the one from PseudoDojo library and the pseudopotential of Hg is replaced with the on from GBRV[115] library. It is not only because these two pseudopotentials from SG15 library are less precise, but also because these two pseudopotentials lead to the electronic step convergence issue during the calculation. Using new pseudopotentials makes all equation of state calculation finished without issues.

The SSSP v1.1.2 libraries for Ir have been updated with the latest pseudopotential from Pslibrary US v1.0.0 in the "high" family[82]. It should be noted that the original Ir pseudopotential from the GBRV library contains a ghost state at 10eV.

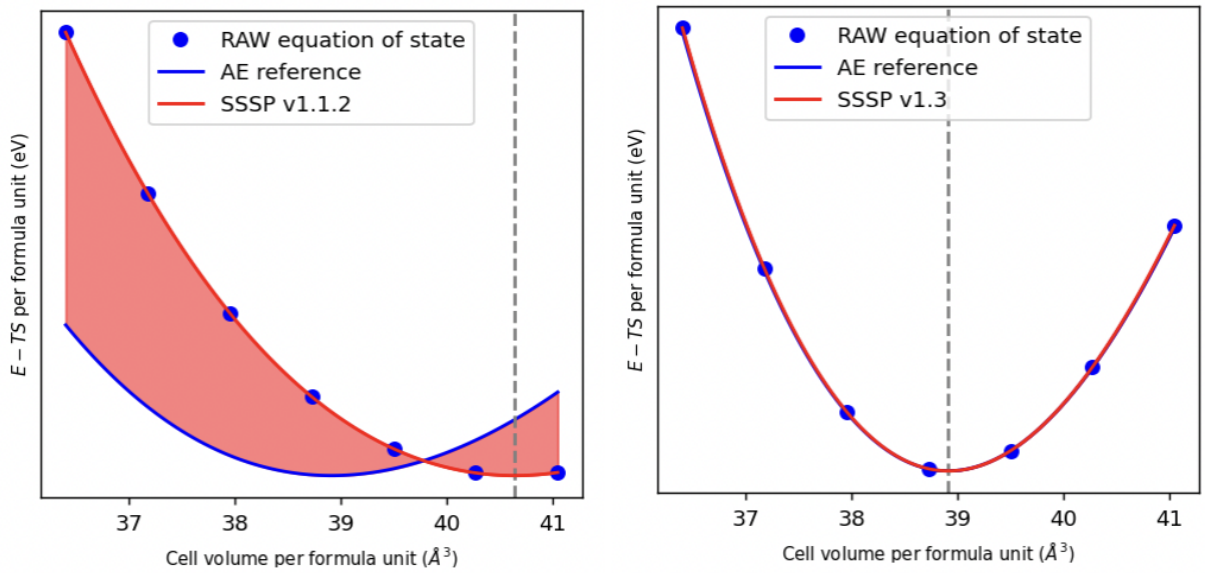

Figure S16.5. Left: EOS of NeO_2 using the Ne pseudopotential from `SSSP v1.1.2`. Right: EOS of NeO_2 using the Ne pseudopotential from `SSSP v1.3`.

For Ba, in SSSP v1.3 we select the new pseudopotential from the PseudoDojo v0.5 library[69] (generated in the context of this work, see SI Sec. S16.1) that includes an f projector.

For Te, Na, and Cu we consider in SSSP v1.3 the PAW or ultrasoft pseudopotentials from the PSlibrary[82] in the "low" family. These pseudopotentials have fewer semicore states and larger cut-off radii, making them possibly less accurate, but optimized for lower kinetic energy cut-offs. Tests on ten configurations, including oxides, revealed that some pseudopotentials from the "low" family are actually even more accurate than those from the "high" family (the latter have more semicore states and smaller cut-off radii). We note that PSlibrary suggests to use "high" pseudopotentials only for special applications, while "low" ones can yield sufficient precision for regular calculations. As an example of the results with the new pseudos, we show the results for TeO_2 for the two versions of SSSP in SI Fig. S16.6.

Starting from v1.3, the SSSP library also includes pseudopotentials for actinides (Th-Lr) developed in Ref. 81 as well as the pseudopotentials for Ac, At, Ra, and Fr from the "high" family of PSlibrary[82].

Finally, in the case of Cs, As, while the test of the SSSP v1.1.2 pseudopotentials on unaries was resulting in good-quality EOS curves, we obtained significant disagreements for oxides. We therefore replaced the corresponding pseudopotentials with others that provided more precise agreements. We illustrate the improvements in the case of Cs in SI Fig. S16.7.

S16.5 VASP

The lanthanides Pr, Nd, Pm, Sm, Eu, Gd, Tb, Dy, Ho, Er, Tm, and Yb were updated during the preparation of the data, since the initial ones showed quite significant deviations from the all-electron results. For elements containing $4f$ electrons, VASP recommends to use potentials with the f electrons placed in the frozen core, to avoid the well known self-interaction errors resulting from DFT. VASP therefore provides well-tested potentials with frozen f electrons for the lanthanides, with a valency of 2 or 3 (for Er, Eu, and Yb, both valences are available as separate potentials). Since this study has settled on treating f electrons explicitly as valence, we used the potentials that place all f electrons in the valence. Using semi-local functionals, these potentials lead to significant over-binding and too small unit cells (compared to experiment as well as compared to PAW potentials that place the f electrons in the core). However, the aim of this work is code comparison primarily. The lanthanide potentials used in this work have been generated by G. Kresse. They are using a much smaller core radius of 2.2 a.u. than the previous versions. Additionally, the reference electronic configuration was altered, by placing 0.5 electrons (instead of 1

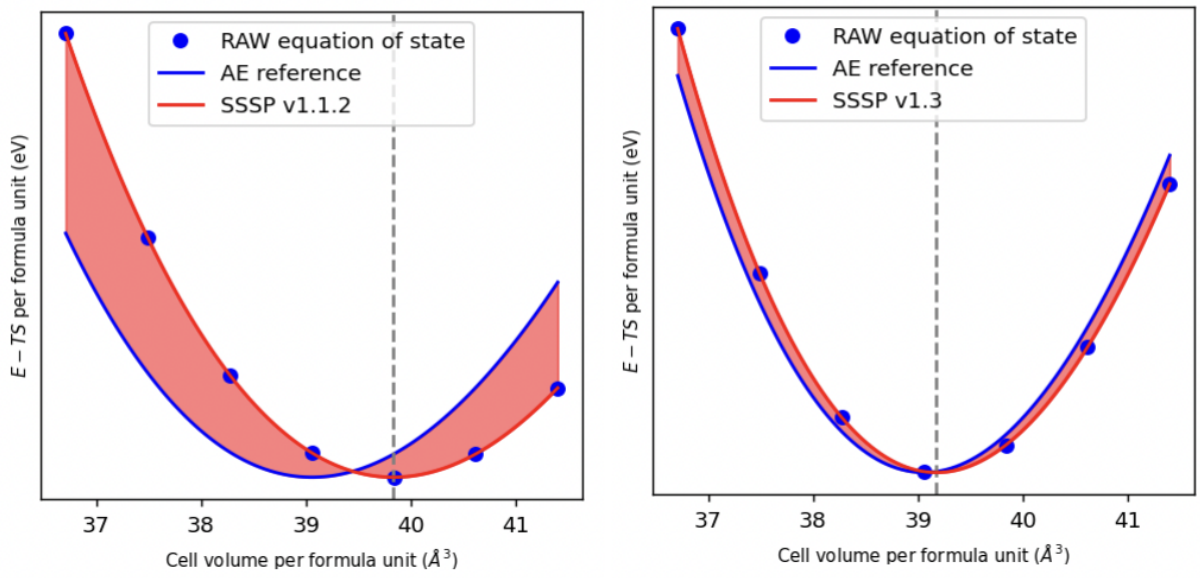

Figure S16.6. Left: EOS of TeO_2 using the Te pseudopotential from `SSSP v1.1.2`. Right: EOS of TeO_2 using the Te pseudopotential from `SSSP v1.3`.

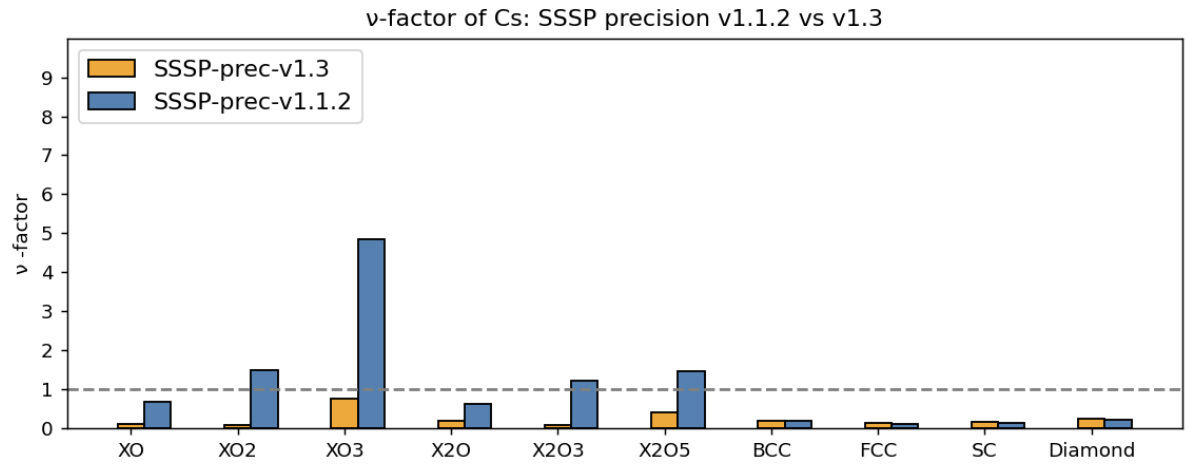

Figure S16.7. Comparison (via the ν metric) between QUANTUM ESPRESSO results and the all-electron reference from WIEN2k for the different crystal structures of Cs, revealing that while the old pseudopotential was already quite precise for unaries, only the new pseudopotential in SSSP v1.3 (from the PseudoDojo library) provides high precision results for oxides.

electron) from the $4f$ shell into the $5d$ shell. Generally, two projectors were used for the f shells. Due to contracting f shells towards the right of the series (Tm, Er, and Yb) a third projector was found to be necessary to obtain an accurate description of the f scattering properties. The new lanthanide potentials will be released on the VASP portal in the 6.4 PBE PAW potential set with an _h suffix. For future reference the specific potential mapping that was used is RECOMMENDED_ACWF_LANTH, where LANTH indicates that the new lanthanide potentials have been used.

For the unaries we have compared the elevated settings optimized for this study with the default settings of VASP (keeping only LMAXMIX = 6) and the chosen recommended GW potential set with the recommended PBE potential set. The resulting ε metrics are plotted in SI Fig. S16.8.

In the first panel of SI Fig. S16.8 we used the recommended PAW potentials for PBE (as given on the VASP website, for the lanthanides the new PAW potentials were used as detailed above), with the default cutoffs (dependent on the system) and precision setting (PREC = Normal). In panel (b) we used the same potentials, but PREC = Accurate and a plane wave cutoff of 800 eV alongside the other settings detailed in section S13.9, while panel (c) corresponds to the final results presented in the

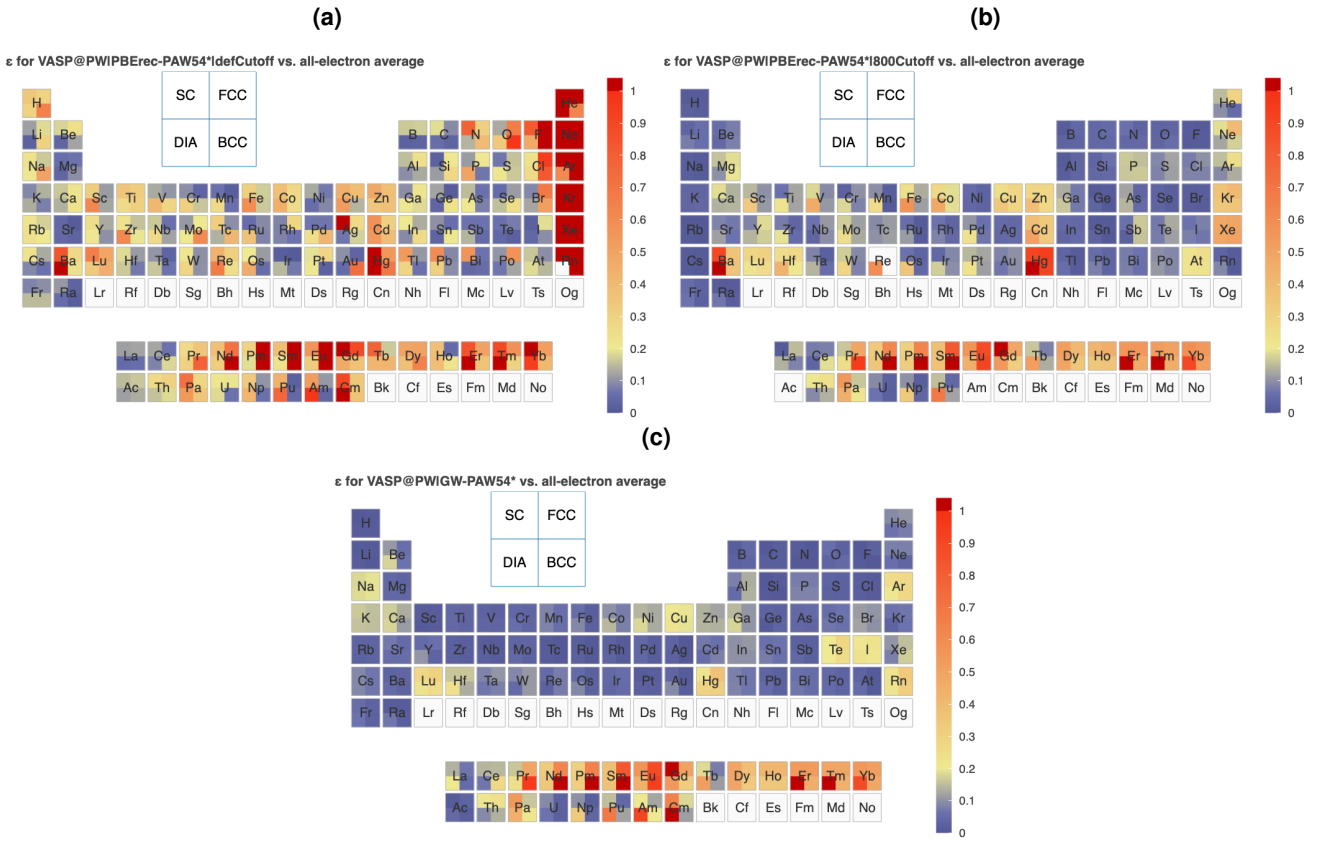

Figure S16.8. Value of the comparison metric ε for the unaries using three different settings for VASP with the averaged AE results as reference. The datasets in (a) and (b) use the recommended PBE potentials. Computational parameters are mostly left at default values in (a), while (b) increases the energy cutoff to 800 eV and adopts the other parameters described in section S13.9. In (c) we show the final dataset with recommended GW potentials, if available, and 1000 eV energy cutoff.

paper using the final settings (1000 eV) and the recommended GW potentials.

Clearly, changing the default parameters substantially improves the agreement with the AE reference calculations. The noble gases in particular are dramatically improved by using the more accurate settings. But many other weakly bonded structures are improved as well. If then also the GW potentials are used, some elements do improve again by quite a lot (Ba, Hg, Xe, Cd,...), while others improve only slightly (e.g., P, S, As,...) and some get slightly worse (e.g., Na, K, Rn,...). For the oxides, the improvement is significant for materials with short oxygen bonds, when using the O_h_GW potential instead of the standard PBE one (not shown).

S17 Consistency check with previous benchmarks for the all-electron data

All calculations in this work have been run independently and from scratch by expert users of the respective codes, following a strict protocol. As the all-electron calculations WIEN2k and FLEUR serve as references here, it is useful to compare them to results obtained for the same crystals in an earlier benchmark[29,30]. Table S17.1 shows this comparison for the parameters of the Birch-Murnaghan EOS: both for FLEUR and WIEN2k, there are only small relative differences between the parameters obtained in Refs. 29, 30 and the ones obtained in the present work. The only crystal with significant relative deviations is Ne (FCC), which is not surprising given its very shallow equation of state (small value of the bulk modulus, which is known[98] to lead to a large uncertainty in the volume). This demonstrates good agreement between the previous and current data, obtained from independent calculations.

A different view on the same data is represented in SI Fig. S17.1. It shows on the horizontal axis the difference between the FLEUR and WIEN2k results for these 29 crystals, expressed by the Δ metric, as obtained in Refs. 29, 30. On the vertical axis, the Δ metric for the same crystal and the same two codes is shown, now using the data obtained in the present work. Although the range on the horizontal axis does not extend much beyond the threshold of good agreement of $\Delta = 1$ meV/at that was used in Refs. 29, 30, the range on the vertical axis is significantly smaller.

The conclusion of this analysis is that although the agreement between the all-electron codes FLEUR and WIEN2k was already very good in Refs. 29, 30 ($\Delta \leq 1$ meV/at), and although the relative differences in the observable properties that can be derived from the EOS are very small (Tab. S17.1), the agreement between the two all-electron codes in the present work is definitely even better than it was in previous works (SI Fig. S17.1).

Table S17.1. Table comparing the V_0, B_0 and B_1 parameters for the subset of 29 structures of those suggested in Ref. 29, 30 that are also present in our set of unaries, namely those that have a cubic FCC, BCC, SC or Diamond structure and that were treated without spin polarization. In particular, Fe(BCC), Mn(FCC), Ni(FCC) and Cr(BCC) have not been included because they are treated including spin polarization in Ref. 29, 30; all other structures not shown here were not considered in a cubic structure in Ref. 29, 30. The table reports the absolute percentage error on each parameter with respect to the data for the same code and the same crystal reported in Ref. 29, 30.

		FLEUR			WIEN2k		
Element	Structure	V_0 error [%]	B_0 error [%]	B_1 error [%]	V_0 error [%]	B_0 error [%]	B_1 error [%]
Ag	FCC	0.01	1.59	1.98	0.06	0.86	6.97
Al	FCC	0.01	1.22	5.69	0.10	0.72	1.15
Ar	FCC	0.55	5.61	29.04	0.28	1.28	2.71
Au	FCC	0.20	1.62	10.40	0.02	0.27	2.95
Ba	BCC	0.16	2.18	9.86	0.26	0.05	30.67
Ca	FCC	0.11	0.24	5.91	0.00	1.50	0.59
Cs	BCC	0.19	0.39	4.82	0.20	1.45	38.97
Cu	FCC	0.16	0.06	0.71	0.05	0.10	4.14
Ge	Diamond	0.09	0.34	2.68	0.02	0.31	2.60
Ir	FCC	0.00	0.82	0.07	0.03	0.12	1.38
K	BCC	0.15	0.47	0.47	0.14	0.14	21.68
Kr	FCC	0.37	4.43	38.54	0.62	5.21	35.59
Mo	BCC	0.09	0.03	5.32	0.04	0.12	2.87
Nb	BCC	0.12	0.59	12.32	0.03	0.97	3.71
Ne	FCC	2.69	0.41	41.55	0.29	13.74	99.20
Pb	FCC	0.15	0.45	1.86	0.09	0.16	4.52
Pd	FCC	0.03	0.77	3.34	0.08	0.35	0.65
Po	SC	0.03	0.60	9.91	0.04	0.13	0.39
Pt	FCC	0.19	1.19	6.52	0.08	0.52	0.02
Rb	BCC	0.07	0.86	0.83	0.39	0.55	53.53
Rh	FCC	0.07	0.63	0.91	0.07	0.34	2.65
Rn	FCC	0.04	7.79	14.45	0.48	4.23	34.33
Si	Diamond	0.04	0.03	0.68	0.03	0.02	0.07
Sn	Diamond	0.01	0.47	3.56	0.06	0.71	4.94
Sr	FCC	0.71	3.27	37.98	0.68	3.43	5.89
Ta	BCC	0.02	1.62	8.91	0.03	1.11	1.17
V	BCC	0.07	1.20	1.87	0.07	0.16	2.31
W	BCC	0.04	0.72	6.96	0.03	0.04	2.63
Xe	FCC	0.11	4.06	6.18	0.36	2.00	12.28

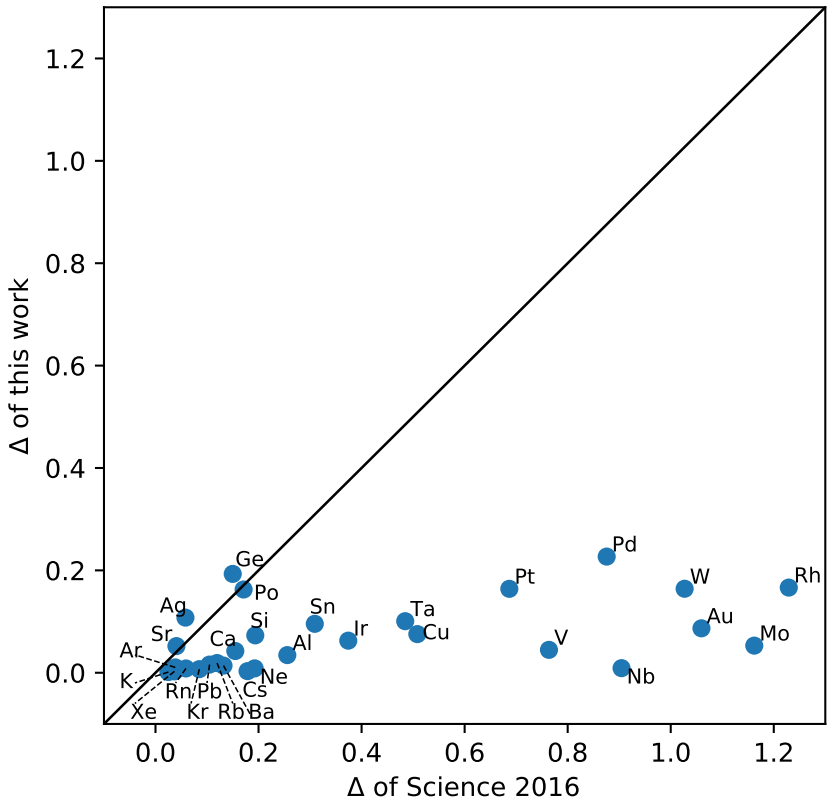

Figure S17.1. Correlation of the Δ metric on the 29 crystals listed in Tab. S17.1. x axis: Δ metric for these crystals between FLEUR and WIEN2k, using the results from Refs. 29, 30. y axis: same metric Δ for the same crystals and the same two codes, but using data from the present work. The black solid line indicates $y = x$. We note that $\Delta \leq 1$ meV/atom was considered in Ref. 29 to indicate a good agreement.

S18 Discrepancies of formation energies computed from the current dataset

In SI Fig. S18.1 we report a histogram of the difference of the formation energy obtained using the data for the two all-electron codes FLEUR and WIEN2k, computed from the minimum-energy value of the EOS data curves. The histogram is obtained considering the formation energy of all X_nO_m oxides, using the lowest-energy unary of element X and of oxygen as the two endpoints (in the case of oxygen, the lowest-energy non-magnetic unary in our dataset is the simple cubic structure). The majority of the datapoints are in the visible x axis range, i.e., with an (absolute) discrepancy smaller than 50 meV/atom. Nevertheless, several outliers are present: 52 out of the 576 materials considered have a discrepancy larger than 50 meV/atom. The most outstanding outliers are AtO_3, PoO_3, BiO_3, Am_2O, Pu_2O, AmO and PuO. They have a discrepancy larger than 1 eV/atom. For compounds containing Am and Pu, the discrepancy is also due by the fact that the unary identified as having lowest energy is different between the two codes.

As we discuss in the main text, the reason for this discrepancy is that our workflows have been designed to guarantee consistent simulation parameters among calculations for a given material at different volumes. However, when considering different structures, we did not enforce any consistency between simulation parameters, e.g., the choices of atomic radii for the AE codes might be different in different systems. Especially, changes to the core/valence separation from structure to structure may lead to larger discrepancies in this comparison, because the differing relativistic descriptions of core and valence electrons lead to different energy contributions. Therefore, we recommend not to use our dataset to generate plots like the one of SI Fig. S18.1 or, more generally, to avoid performing data analysis that considers energy differences between different structures. In this case, instead, one should design new appropriate workflows that can ensure the consistency of simulation parameters among all relevant calculations.

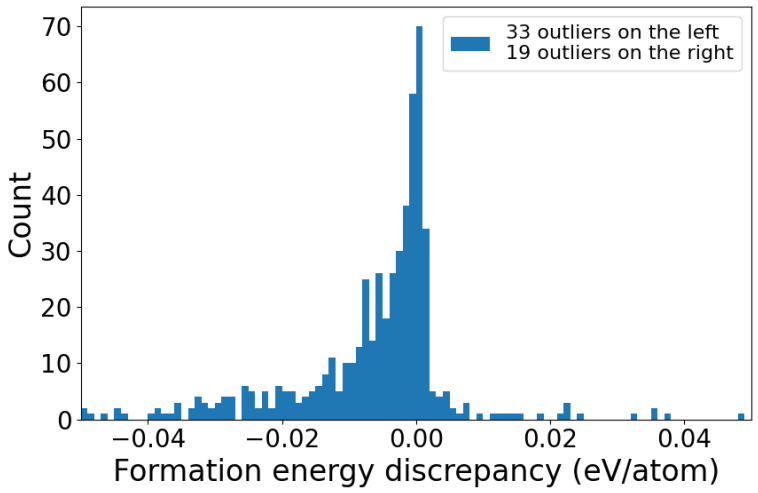

Figure S18.1. Histogram of the discrepancy between the formation energy obtained from our reference dataset for the two codes FLEUR and WIEN2k. We note that no correction is applied to the formation energies (as it is typically done, for instance, for oxygen[25]). However, since we are only considering differences in formation energies between two codes, these corrections cancel out so they do not need to be considered explicitly. The number of outliers outside of the visible x axis range is reported in the top right corner of the figure.

References

1. Alberi, K. *et al.* The 2019 materials by design roadmap. *J. Phys. D: Appl. Phys.* **52**, 013001, DOI: 10.1088/1361-6463/aad926 (2018).
2. Marzari, N., Ferretti, A. & Wolverton, C. Electronic-structure methods for materials design. *Nat. Mater.* **20**, 736–749, DOI: 10.1038/s41563-021-01013-3 (2021).
3. Pizzi, G., Cepellotti, A., Sabatini, R., Marzari, N. & Kozinsky, B. AiiDA: automated interactive infrastructure and database for computational science. *Comput. Mater. Sci.* **111**, 218–230, DOI: 10.1016/j.commatsci.2015.09.013 (2016).
4. Huber, S. P. *et al.* AiiDA 1.0, a scalable computational infrastructure for automated reproducible workflows and data provenance. *Sci. Data* **7**, DOI: 10.1038/s41597-020-00638-4 (2020).

5. Ong, S. P. *et al.* Python materials genomics (pymatgen): A robust, open-source python library for materials analysis. *Comput. Mater. Sci.* **68**, 314–319, DOI: https://doi.org/10.1016/j.commatsci.2012.10.028 (2013).

6. Jain, A. *et al.* Fireworks: a dynamic workflow system designed for high-throughput applications. *Concurr. Comput. Pract. Exp.* **27**, 5037–5059, DOI: 10.1002/cpe.3505 (2015).

7. Mathew, K. *et al.* Atomate: A high-level interface to generate, execute, and analyze computational materials science workflows. *Comput. Mater. Sci.* **139**, 140–152, DOI: 10.1016/j.commatsci.2017.07.030 (2017).

8. Bahn, S. R. & Jacobsen, K. W. An object-oriented scripting interface to a legacy electronic structure code. *Comput. Sci. Eng.* **4**, 56–66, DOI: 10.1109/5992.998641 (2002).

9. Hjorth Larsen, A. *et al.* The atomic simulation environment—a Python library for working with atoms. *J. Physics: Condens. Matter* **29**, 273002, DOI: 10.1088/1361-648X/AA680E (2017).

10. Curtarolo, S. *et al.* Aflow: An automatic framework for high-throughput materials discovery. *Comput. Mater. Sci.* **58**, 218–226, DOI: https://doi.org/10.1016/j.commatsci.2012.02.005 (2012).

11. Janssen, J. *et al.* pyiron: An integrated development environment for computational materials science. *Comput. Mater. Sci.* **163**, 24 – 36, DOI: https://doi.org/10.1016/j.commatsci.2018.07.043 (2019).

12. Armiento, R. *Database-Driven High-Throughput Calculations and Machine Learning Models for Materials Design*, 377–395 (Springer International Publishing, Cham, 2020).

13. Gonze, X. *et al.* The Abinit project: Impact, environment and recent developments. *Comput. Phys. Commun.* **248**, 107042, DOI: 10.1016/j.cpc.2019.107042 (2020).

14. Jain, A. *et al.* Commentary: The Materials Project: A materials genome approach to accelerating materials innovation. *APL Mater.* **1**, 011002, DOI: 10.1063/1.4812323 (2013).

15. Landis, D. D. *et al.* The Computational Materials Repository. *Comput. Sci. & Eng.* **14**, 51–57, DOI: 10.1109/MCSE.2012.16 (2012).

16. Kirklin, S. *et al.* The open quantum materials database (oqmd): assessing the accuracy of dft formation energies. *npj Comput. Mater.* **1**, 15010, DOI: 10.1038/npjcompumats.2015.10 (2015).

17. Merkys, A. *et al.* A posteriori metadata from automated provenance tracking: Integration of AiiDA and TCOD. *J. Cheminformatics* **9**, 56, DOI: 10.1186/s13321-017-0242-y (2017). 1706.08704v3.

18. Stevanović, V., Lany, S., Zhang, X. & Zunger, A. Correcting density functional theory for accurate predictions of compound enthalpies of formation: Fitted elemental-phase reference energies. *Phys. Rev. B* **85**, 115104, DOI: 10.1103/PhysRevB.85.115104 (2012).

19. Talirz, L. *et al.* Materials cloud, a platform for open computational science. *Sci. Data* **7**, DOI: 10.1038/s41597-020-00637-5 (2020).

20. Draxl, C. & Scheffler, M. Nomad: The fair concept for big data-driven materials science. *MRS Bull.* **43**, 676–682, DOI: 10.1557/mrs.2018.208 (2018).

21. Curtarolo, S. *et al.* Aflowlib.org: A distributed materials properties repository from high-throughput ab initio calculations. *Comput. Mater. Sci.* **58**, 227–235, DOI: https://doi.org/10.1016/j.commatsci.2012.02.002 (2012).

22. Wilkinson, M. D. *et al.* The FAIR guiding principles for scientific data management and stewardship. *Sci. Data* **3**, DOI: 10.1038/sdata.2016.18 (2016).

23. Andersen, C. W. *et al.* OPTIMADE, an API for exchanging materials data. *Sci. Data* **8**, DOI: 10.1038/s41597-021-00974-z (2021).

24. IEEE Standard for System, Software, and Hardware Verification and Validation. *IEEE Std 1012-2016 (Revision IEEE Std 1012-2012/ Incorporates IEEE Std 1012-2016/Cor1-2017)* 1–260, DOI: 10.1109/IEEESTD.2017.8055462 (2017).

25. Wang, A. *et al.* A framework for quantifying uncertainty in dft energy corrections. *Sci. Reports* **11**, 15496, DOI: 10.1038/s41598-021-94550-5 (2021).

26. Carbogno, C. *et al.* Numerical quality control for dft-based materials databases. *npj Comput. Mater.* **8**, 69, DOI: 10.1038/s41524-022-00744-4 (2022).

27. Poncé, S. *et al.* Verification of first-principles codes: Comparison of total energies, phonon frequencies, electron–phonon coupling and zero-point motion correction to the gap between abinit and qe/yambo. *Comput. Mater. Sci.* **83**, 341–348, DOI: https://doi.org/10.1016/j.commatsci.2013.11.031 (2014).

28. Pople, J. Nobel Lecture. NobelPrize.org, https://www.nobelprize.org/prizes/chemistry/1998/pople/lecture/.

29. Lejaeghere, K. *et al.* Reproducibility in density functional theory calculations of solids. *Science* **351**, aad3000, DOI: 10.1126/science.aad3000 (2016).

30. 71-crystal benchmark results from ref. 29 plus data collected later on, https://molmod.ugent.be/deltacodesdft.

31. The FLEUR project. https://www.flapw.de/.

32. Wortmann, D. *et al.* Fleur. Zenodo, DOI: 10.5281/zenodo.7576163 (2023).

33. Blaha, P. *et al.* Wien2k: An augmented plane wave plus local orbitals program for calculating crystal properties. http://www.wien2k.at/.

34. Blaha, P. *et al.* Wien2k: An apw+lo program for calculating the properties of solids. *J. Chem. Phys.* **152**, 074101, DOI: 10.1063/1.5143061 (2020).

35. Uhrin, M., Huber, S. P., Yu, J., Marzari, N. & Pizzi, G. Workflows in AiiDA: Engineering a high-throughput, event-based engine for robust and modular computational workflows. *Comput. Mater. Sci.* **187**, 110086, DOI: 10.1016/j.commatsci.2020.110086 (2021).

36. Huber, S. P. *et al.* Common workflows for computing material properties using different quantum engines. *npj Comput. Mater.* **7**, 136, DOI: 10.1038/s41524-021-00594-6 (2021).

37. Huber, S. P. *et al.* AiiDA common workflows (ACWF) package (2021). https://github.com/aiidateam/aiida-common-workflows.

38. Lejaeghere, K., Speybroeck, V. V., Oost, G. V. & Cottenier, S. Error Estimates for Solid-State Density-Functional Theory Predictions: An Overview by Means of the Ground-State Elemental Crystals. *Critical Rev. Solid State Mater. Sci.* **39**, 1–24, DOI: 10.1080/10408436.2013.772503 (2013).

39. Grosso, G. & Pastori Parravicini, G. *Solid State Physics* (Academic Press, Amsterdam, 2013), second edn.

40. Martin, R. M. *Electronic Structure: Basic Theory and Practical Methods* (Cambridge University Press, Cambridge, 2013), second edn.

41. Cohen, M. L. & Louie, S. G. *Fundamentals of Condensed Matter Physics* (Cambridge University Press, Cambridge, 2016).

42. Gonze, X. *et al.* Recent developments in the ABINIT software package. *Comput. Phys. Commun.* **205**, 106–131, DOI: 10.1016/j.cpc.2016.04.003 (2016).

43. Romero, A. H. *et al.* ABINIT: Overview and focus on selected capabilities. *The J. Chem. Phys.* **152**, 124102, DOI: 10.1063/1.5144261 (2020).

44. Ratcliff, L. E. *et al.* Flexibilities of wavelets as a computational basis set for large-scale electronic structure calculations. *The J. Chem. Phys.* **152**, 194110, DOI: 10.1063/5.0004792 (2020).

45. Clark, S. J. *et al.* First principles methods using CASTEP. *Zeitschrift für Kristallographie - Cryst. Mater.* **220**, DOI: 10.1524/zkri.220.5.567.65075 (2005).

46. The CP2K simulation package. https://www.cp2k.org.

47. Kühne, T. D. *et al.* CP2k: An electronic structure and molecular dynamics software package - quickstep: Efficient and accurate electronic structure calculations. *The J. Chem. Phys.* **152**, 194103, DOI: 10.1063/5.0007045 (2020).

48. Mortensen, J. J., Hansen, L. B. & Jacobsen, K. W. Real-space grid implementation of the projector augmented wave method. *Phys. Rev. B* **71**, 035109, DOI: 10.1103/PhysRevB.71.035109 (2005).

49. Enkovaara, J. *et al.* Electronic structure calculations with GPAW: a real-space implementation of the projector augmented-wave method. *J. Physics: Condens. Matter* **22**, 253202 (2010).

50. Giannozzi, P. *et al.* QUANTUM ESPRESSO: a modular and open-source software project for quantum simulations of materials. *J. Physics: Condens. Matter* **21**, 395502, DOI: 10.1088/0953-8984/21/39/395502 (2009).

51. Giannozzi, P. *et al.* Advanced capabilities for materials modelling with quantum ESPRESSO. *J. Physics: Condens. Matter* **29**, 465901, DOI: 10.1088/1361-648x/aa8f79 (2017).

52. Soler, J. M. *et al.* The SIESTA method for ab initio order-N materials simulation. *J. Physics: Condens. Matter* **14**, 2745–2779, DOI: 10.1088/0953-8984/14/11/302 (2002).

53. García, A. *et al.* Siesta: Recent developments and applications. *The J. Chem. Phys.* **152**, 204108, DOI: 10.1063/5.0005077 (2020).

54. The SIRIUS domain-specific library for electronic-structure calculations. https://github.com/electronic-structure/SIRIUS.

55. Kresse, G. & Furthmüller, J. Efficient iterative schemes for ab initio total-energy calculations using a plane-wave basis set. *Phys. Rev. B* **54**, 11169–11186, DOI: 10.1103/physrevb.54.11169 (1996).

56. Kresse, G. & Joubert, D. From ultrasoft pseudopotentials to the projector augmented-wave method. *Phys. Rev. B* **59**, 1758–1775, DOI: 10.1103/physrevb.59.1758 (1999).

57. Perdew, J. P., Burke, K. & Ernzerhof, M. Generalized gradient approximation made simple. *Phys. Rev. Lett.* **77**, 3865–3868, DOI: 10.1103/physrevlett.77.3865 (1996).

58. Vanpoucke, D. E. P., Bultinck, P. & Van Driessche, I. Extending Hirshfeld-I to bulk and periodic materials. *J. Comput. Chem.* **34**, 405–417, DOI: 10.1002/jcc.23088 (2013).

59. Vanpoucke, D. E. P., Van Driessche, I. & Bultinck, P. Reply to 'Comment on "Extending Hirshfeld-I to bulk and periodic materials" '. *J. Comput. Chem.* **34**, 422–427, DOI: 10.1002/jcc.23193 (2013).

60. Bultinck, P., Van Alsenoy, C., Ayers, P. W. & Carbó-Dorca, R. Critical analysis and extension of the hirshfeld atoms in molecules. *J. Chem. Phys.* **126**, 144111, DOI: 10.1063/1.2715563 (2007).

61. Birch, F. Finite elastic strain of cubic crystals. *Phys. Rev.* **71**, 809–824, DOI: 10.1103/PhysRev.71.809 (1947).

62. Bosoni, E. *et al.* How to verify the precision of density-functional-theory implementations via reproducible and universal workflows. *Mater. Cloud Arch.* DOI: https://doi.org/10.24435/materialscloud:s4-3h (2023). https://doi.org/10.24435/materialscloud:s4-3h.

63. Jollet, F., Torrent, M. & Holzwarth, N. Generation of projector augmented-wave atomic data: A 71 element validated table in the XML format. *Comput. Phys. Commun.* **185**, 1246–1254, DOI: 10.1016/j.cpc.2013.12.023 (2014).

64. Glantz, S. A., Slinker, B. K. & Neilands, T. B. *Selecting the "Best" Regression Model, in Primer of Applied Regression and Analysis of Variance, third edition* (McGraw-Hill Education, New York, 2017).

65. Marzari, N., Vanderbilt, D., De Vita, A. & Payne, M. C. Thermal Contraction and Disordering of the Al(110) Surface. *Phys. Rev. Lett.* **82**, 3296–3299, DOI: 10.1103/PhysRevLett.82.3296 (1999).

66. dos Santos, F. J. & Marzari, N. Fermi energy determination for advanced smearing techniques. *arXiv* **2212.07988**, DOI: 10.48550/ARXIV.2212.07988 (2022).

67. Gillan, M. J. Calculation of the vacancy formation energy in aluminium. *J. Phys.. Cond. Matter* **1**, 689, DOI: 10.1088/0953-8984/1/4/005 (1989).

68. van Setten, M. *et al.* The PseudoDojo: Training and grading a 85 element optimized norm-conserving pseudopotential table. *Comput. Phys. Commun.* **226**, 39–54, DOI: 10.1016/j.cpc.2018.01.012 (2018).

69. The PseudoDojo website. http://www.pseudo-dojo.org/.

70. Hartwigsen, C., Goedecker, S. & Hutter, J. Relativistic separable dual-space Gaussian pseudopotentials from H to Rn. *Phys. Rev. B* **58**, 3641–3662, DOI: 10.1103/PhysRevB.58.3641 (1998).

71. Goedecker, S., Teter, M. & Hutter, J. Separable dual-space Gaussian pseudopotentials. *Phys. Rev. B* **54**, 1703 (1996).

72. Krack, M. Pseudopotentials for H to Kr optimized for gradient-corrected exchange-correlation functionals. *Theor. Chem. Accounts* **114**, 145–152 (2005).

73. VandeVondele, J. & Hutter, J. Gaussian basis sets for accurate calculations on molecular systems in gas and condensed phases. *The J. chemical physics* **127**, 114105 (2007).

74. GPAW atomic PAW setups. https://wiki.fysik.dtu.dk/gpaw/setups/setups.html#atomic-paw-setups.

75. Prandini, G., Marrazzo, A., Castelli, I. E., Mounet, N. & Marzari, N. Precision and efficiency in solid-state pseudopotential calculations. *npj Comput. Mater.* **4**, DOI: 10.1038/s41524-018-0127-2 (2018).

76. Prandini, G. *et al.* A standard solid state pseudopotentials (sssp) library optimized for precision and efficiency. *Mater. Cloud Arch.* **2023.65** (2022). Version v11, https://doi.org/10.24435/materialscloud:f3-ym.

77. García, A., Verstraete, M. J., Pouillon, Y. n. & Junquera, J. The psml format and library for norm-conserving pseudopotential data curation and interoperability. *Comput. Phys. Commun.* **227**, 51 – 71, DOI: https://doi.org/10.1016/j.cpc.2018.02.011 (2018).

78. Topsakal, M. & Wentzcovitch, R. Accurate projected augmented wave (paw) datasets for rare-earth elements (re=la–lu). *Comput. Mater. Sci.* **95**, 263–270, DOI: https://doi.org/10.1016/j.commatsci.2014.07.030 (2014).

79. Prandini, G. *et al.* A standard solid state pseudopotentials (sssp) library optimized for precision and efficiency. *Mater. Cloud Arch.* **2021.76** (2021). Version v7, https://doi.org/10.24435/materialscloud:rz-77.

80. Prandini, G. *et al.* A standard solid state pseudopotentials (sssp) library optimized for precision and efficiency. *Mater. Cloud Arch.* **2022.159** (2022). Version v8, https://doi.org/10.24435/materialscloud:3v-xt.

81. Sachs, M. *et al.* Dft-guided crystal structure redetermination and lattice dynamics of the intermetallic actinoid compound uir. *Inorg. Chem.* **60**, 16686–16699 (2021).

82. Dal Corso, A. Pseudopotentials periodic table: From H to Pu. *Comput. Mater. Sci.* **95**, 337–350 (2014).

83. Thörnig, P. JURECA: Data Centric and Booster Modules implementing the Modular Supercomputing Architecture at Jülich Supercomputing Centre. *J. large-scale research facilities JLSRF* **7**, 182, DOI: 10.17815/jlsrf-7-182 (2021).

84. Igor Levin. NIST Inorganic Crystal Structure Database (ICSD), National Institute of Standards and Technology (2018).

85. Kokalj, A. Xcrysden—a new program for displaying crystalline structures and electron densities. *J. Mol. Graph. Model.* **17**, 176–179, DOI: https://doi.org/10.1016/S1093-3263(99)00028-5 (1999).

86. Mulliken, R. S. Electronic structures of molecules xi. electroaffinity, molecular orbitals and dipole moments. *J. Chem. Phys.* **3**, 573–585, DOI: 10.1063/1.1749731 (1935).

87. Mulliken, R. S. Electronic population analysis on lcao–mo molecular wave functions. i. *J. Chem. Phys.* **23**, 1833–1840, DOI: 10.1063/1.1740588 (1955).

88. Hirshfeld, F. L. Bonded-atom fragments for describing molecular charge densities. *Theor. Chim. Acta* **44**, 129–138, DOI: 10.1007/BF00549096 (1977).

89. Bader, R. F. W. A quantum theory of molecular structure and its applications. *Chem. Rev.* **91**, 893–928, DOI: 10.1021/cr00005a013 (1991).

90. Becke, A. D. A multicenter numerical integration scheme for polyatomic molecules. *J. Chem. Phys.* **88**, 2547–2553, DOI: 10.1063/1.454033 (1988).

91. Vanpoucke, D.E.P. HIVE-tools. https://github.com/DannyVanpoucke/HIVE4-tools.

92. Lebedev, V. I. & Laikov, D. A quadrature formula for the sphere of the 131st algebraic order of accuracy. *Doklady Math.* **59**, 477–481 (1988).

93. Bultinck, P., Ayers, P. W., Fias, S., Tiels, K. & Van Alsenoy, C. Uniqueness and basis set dependence of iterative hirshfeld charges. *Chem. Phys. Let.* **444**, 205–208, DOI: https://doi.org/10.1016/j.cplett.2007.07.014 (2007).

94. Wolffis, J. J., Vanpoucke, D. E. P., Sharma, A., Lawler, K. V. & Forster, P. M. Predicting partial atomic charges in siliceous zeolites. *Microporous Mesoporous Mater.* **277**, 184–196, DOI: 10.1016/j.micromeso.2018.10.028 (2019).

95. Bueken, B. *et al.* A Flexible Photoactive Titanium Metal–Organic Framework Based on a $[Ti_3^{IV}(\mu_3\text{-O})(O)_2(COO)_6]$ Cluster. *Angew. Chem. Int. Ed.* **54**, 13912–13917, DOI: 10.1002/anie.201505512 (2015).

96. Verstraelen, T., Sukhomlinov, S. V., Van Speybroeck, V., Waroquier, M. & Smirnov, K. S. Computation of charge distribution and electrostatic potential in silicates with the use of chemical potential equalization models. *J. Phys. Chem. C* **116**, 490–504, DOI: 10.1021/jp210129r (2012).

97. 2 - Chemical Periodicity and the Periodic Table. In Greenwood, N. & Earnshaw, A. (eds.) *Chemistry of the Elements*, 27–28, DOI: https://doi.org/10.1016/B978-0-7506-3365-9.50008-0 (Butterworth-Heinemann, Oxford, 1997), second edn.

98. Lejaeghere, K., Vanduyfhuys, L., Verstraelen, T., Van Speybroeck, V. & Cottenier, S. Is the error on first-principles volume predictions absolute or relative? *Comput. Mater. Sci.* **117**, 390–396, DOI: https://doi.org/10.1016/j.commatsci.2016.01.039 (2016).

99. Andersen, O. K. Linear methods in band theory. *Phys. Rev. B* **12**, 3060–3083, DOI: 10.1103/PhysRevB.12.3060 (1975).

100. Wimmer, E., Krakauer, H., Weinert, M. & Freeman, A. J. Full-potential self-consistent linearized-augmented-plane-wave method for calculating the electronic structure of molecules and surfaces: O_2 molecule. *Phys. Rev. B* **24**, 864–875, DOI: 10.1103/PhysRevB.24.864 (1981).

101. Singh, D. Ground-state properties of lanthanum: Treatment of extended-core states. *Phys. Rev. B* **43**, 6388–6392, DOI: 10.1103/PhysRevB.43.6388 (1991).

102. Michalicek, G., Betzinger, M., Friedrich, C. & Blügel, S. Elimination of the linearization error and improved basis-set convergence within the FLAPW method. *Comput. Phys. Commun.* **184**, 2670 – 2679, DOI: http://dx.doi.org/10.1016/j.cpc.2013.07.002 (2013).

103. Friedrich, C., Schindlmayr, A., Blügel, S. & Kotani, T. Elimination of the linearization error in *GW* calculations based on the linearized augmented-plane-wave method. *Phys. Rev. B* **74**, 045104, DOI: 10.1103/PhysRevB.74.045104 (2006).

104. Betzinger, M., Friedrich, C., Blügel, S. & Görling, A. Local exact exchange potentials within the all-electron FLAPW method and a comparison with pseudopotential results. *Phys. Rev. B* **83**, 045105, DOI: 10.1103/PhysRevB.83.045105 (2011).

105. Bröder, J., Wortmann, D. & Blügel, S. Using the AiiDA-FLEUR package for all-electron abinitio electronic structure data generation and processing in materials science. In *In Extreme Data Workshop 2018 Proceedings*, vol. 40 of *IAS Series*, p 43–48 (Forschungszentrum Jülich, Jülich, 2019).

106. Bröder, J. *et al.* JuDFTteam/aiida-fleur: AiiDA-FLEUR. Zenodo, DOI: 10.5281/zenodo.6420726 (2022).

107. Madsen, G. K. H., Blaha, P., Schwarz, K., Sjöstedt, E. & Nordström, L. Efficient linearization of the augmented plane-wave method. *Phys. Rev. B* **64**, 195134, DOI: 10.1103/PhysRevB.64.195134 (2001).

108. Karsai, F., Tran, F. & Blaha, P. On the importance of local orbitals using second energy derivatives for *d* and *f* electrons. *Comput. Phys. Commun.* **220**, 230, DOI: 10.1016/j.cpc.2017.07.008 (2017).

109. Lippert, G., Parrinello, M. & Hutter, J. A hybrid Gaussian and plane wave density functional scheme. *Mol. Phys.* **92**, 477–488 (1997).

110. Larsen, A. H., Vanin, M., Mortensen, J. J., Thygesen, K. S. & Jacobsen, K. W. Localized atomic basis set in the projector augmented wave method. *Phys. Rev. B* **80**, 195112, DOI: 10.1103/PhysRevB.80.195112 (2009).

111. Setup generation — GPAW (2022). https://wiki.fysik.dtu.dk/gpaw/setups/generation_of_setups.html.

112. Kresse, G. & Joubert, D. From ultrasoft pseudopotentials to the projector augmented-wave method. *Phys. Rev. B* **59**, 1758–1775, DOI: 10.1103/PhysRevB.59.1758 (1999).

113. Hamann, D. R. Optimized norm-conserving vanderbilt pseudopotentials. *Phys. Rev. B* **88**, 085117, DOI: 10.1103/physrevb.88.085117 (2013).

114. Schlipf, M. & Gygi, F. Optimization algorithm for the generation of oncv pseudopotentials. *Comput. Phys. Commun.* **196**, 36–44 (2015).

115. Garrity, K. F., Bennett, J. W., Rabe, K. M. & Vanderbilt, D. Pseudopotentials for high-throughput dft calculations. *Comput. Mater. Sci.* **81**, 446–452 (2014).

116. Vanderbilt, D. Soft self-consistent pseudopotentials in a generalized eigenvalue formalism. *Phys. Rev. B* **41**, 7892 (1990).